



University of **HUDDERSFIELD**

University of Huddersfield Repository

Zhang, Hao

Model Development and Stability Analysis for a Turbocharger Rotor System under Multi-Field Coupled Forces

Original Citation

Zhang, Hao (2012) Model Development and Stability Analysis for a Turbocharger Rotor System under Multi-Field Coupled Forces. Doctoral thesis, University of Huddersfield.

This version is available at <http://eprints.hud.ac.uk/id/eprint/17823/>

The University Repository is a digital collection of the research output of the University, available on Open Access. Copyright and Moral Rights for the items on this site are retained by the individual author and/or other copyright owners. Users may access full items free of charge; copies of full text items generally can be reproduced, displayed or performed and given to third parties in any format or medium for personal research or study, educational or not-for-profit purposes without prior permission or charge, provided:

- The authors, title and full bibliographic details is credited in any copy;
- A hyperlink and/or URL is included for the original metadata page; and
- The content is not changed in any way.

For more information, including our policy and submission procedure, please contact the Repository Team at: E.mailbox@hud.ac.uk.

<http://eprints.hud.ac.uk/>

Model Development and Stability Analysis for a Turbocharger Rotor System under Multi-Field Coupled Forces

Hao Zhang

A thesis submitted to the University of Huddersfield
in partial fulfilment of the requirements for
the degree of Doctor of Philosophy

April 2012

List of Contents

List of Contents.....	2
List of Tables.....	8
List of Figures.....	9
Abstract.....	16
Declaration.....	18
Copyright Statement	19
Acknowledgement	20
Publications.....	21
CHAPTER ONE INTRODUCTION.....	23
1.1 Introduction to the Rotating Machinery.....	24
1.2 Introduction to the Turbocharger	26
1.3 Background.....	27
1.3.1 Development of the research of the fluid lubrication	27
1.3.2 Development of the research of the rotordynamics	29
1.3.3 Research areas of the rotordynamics	31
1.3.3.1 The critical speeds calculation of the rotor bearing system	31
1.3.3.2 Calculation of the steady state response under the rotor imbalance	31
1.3.3.3 Balancing of the flexible rotor system.....	32
1.3.3.4 The stability analysis of the rotor bearing system	33

1.4 Motivation.....	34
1.5 Research Objectives.....	35
1.6 The Structure of the Thesis	36
CHAPTER TWO LITERATURE REVIEW	38
2.1 Review of the Research of the Fluid Lubrication	41
2.1.1 The linear models of hydrodynamic forces	41
2.1.1.1 The linear expression of the hydrodynamic force increment.....	41
2.1.1.2 The undetermined function matrix.....	42
2.1.1.3 Conventional expressions of the hydrodynamic force.....	42
2.1.1.4 Database approach	42
2.1.2 The limitation of the linear hydrodynamic force model	43
2.1.3 The nonlinear analytical model of the hydrodynamic force	44
2.1.4 The list of classical nonlinear models of the hydrodynamic force	45
2.1.4.1 The infinitely short bearing model.....	45
2.1.4.2 The Capone hydrodynamic force model.....	46
2.1.4.3 Zhang hydrodynamic force model	47
2.1.4.4 The comparison of the classical models	48
2.2 Review of the Research on the Dynamic Characteristics of the Rotor Bearing System.....	49
2.2.1 Critical speed calculations	49
2.2.2 Forced response estimation.....	52
2.2.3 The stability analysis.....	54

2.2.4 Approaches to the analysis of the dynamic performance and stability of the rotor bearing system.....	56
2.3 Review of the Research on Turbocharger Rotordynamics	57
2.4 Review of the Research of the Nonlinearity of the Vibration System.....	59
2.5 Review of the Research of the Modal Synthesis Method.....	61
2.6 Review of the Numerical Integration Approaches.....	63
2.7 Summary	64
CHAPTER THREE ANALYTICAL INVESTIGATION OF THE LUBRICATION OF FLOATING RING BEARINGS	65
3.1 Introduction to the Lubrication of Floating Ring Bearings	66
3.2 Theoretical modeling for the lubrication of a floating ring bearing	69
3.3 Simulation results and analysis.....	73
3.3.1 The equilibrium position.....	74
3.3.2 Oil film continuity	76
3.3.3 Inner oil film lubrication.....	79
3.3.4 Effects of external load on the oil flow rate into the inner oil film	83
3.3.5 Effects of inlet pressure on the oil flow rate into the inner oil film.....	86
3.4 Summary	89
CHAPTER FOUR THEORETICAL MODELLING FOR A TURBOCHARGER ROTOR SYSTEM.....	90
4.1 Finite Element Analysis of the Rotor System.....	96
4.1.1 Finite element method	96

4.1.2 Motion equations of the unit	96
4.2 Modeling of a Turbocharger in Rotordynamics	100
4.3 Hydrodynamic Fluid Forces in the Model	104
4.3.1 Linear force model	104
4.3.2 Nonlinear force model	107
4.4 Rub-impact Force	111
4.5 Summary	112
CHAPTER FIVE CALCULATION OF CRITICAL SPEEDS AND MODE SHAPES OF A TURBOCHARGER ROTOR SYSTEM	113
5.1 Modal Analysis for a Free Rotor	114
5.2 Modal Analysis for a Turbocharger Rotor System	116
5.3 Simulation and Analysis	120
5.4 Summary	137
CHAPTER SIX STABILITY ANALYSIS OF A TURBOCHARGER ROTOR SYSTEM UNDER MULTI-FIELD COUPLED FORCES	138
6.1 Introduction to the motion of the Turbocharger Rotor System	139
6.2 Stability Analysis of a Turbocharger Rotor System	139
6.2.1 Stability characteristics of the floating ring bearing	139
6.2.2 Influences of the rotor imbalance	140
6.2.3 Influences of the lubricant viscosity	149
6.2.4 Influences of bearing clearances	155
6.2.5 Influences of the lubricant feed pressure	164

6.3 Summary	170
CHAPTER SEVEN TURBOCHARGER TEST RIG DEVELOPMENT	172
7.1 Introduction to the Turbocharger Test Rig	173
7.2 The Turbocharger	174
7.3 Air Resource System	175
7.4 Lubrication System	176
7.5 Pipeline System	178
7.6 Sensors and Installation	180
7.7 Signal Acquisition System	187
7.8 The Entire Test Rig	188
CHAPTER EIGHT EXPERIMENTAL RESULTS AND ANALYSIS	190
8.1 Introduction to the Experiment Procedure	191
8.2 Experimental Results and Analysis	192
8.3 Summary	205
CHAPTER NINE CONCLUSIONS AND FUTURE WORK	206
9.1 Review of Research Objectives and Achievements	207
9.2 Conclusions	209
9.3 Contribution to Knowledge	213
9.4 Future Work	215
Appendices	218
Appendix A	218
Appendix B	220

Appendix C222

Reference223

List of Tables

Table 3. 1. Simulation Parameters	73
Table 5. 1. Parameters of a turbocharger rotor system for modal analysis	121
Table 5. 2. Natural frequencies of a free rotor	122
Table 5. 3. First ten orders of natural frequencies of a turbocharger rotor system.....	124
Table 6. 1. Simulation parameters in the rotor imbalance analysis.....	141
Table 6. 2. Simulation parameters in the lubricant viscosity analysis.....	149
Table 6. 3. Simulation parameters in the bearing clearances analysis	155
Table 6. 4. Simulation parameters in the lubricant feed pressure analysis.....	165
Table 7. 1. The typical specification of a KD2306 1U1 eddy current displacement transducer	182
Table 7. 2. Typical specification of the BR100_DDT_P photoelectric sensor.....	185

List of Figures

Figure 1. 1. The industrial application of the rotating machinery.....	24
Figure 1. 2. The structure of rotor and stator	25
Figure 1. 3. The structure of a typical automotive turbocharger.....	26
Figure 3. 1. Coordinate system of the floating ring bearing	69
Figure 3. 2. Outer equilibrium positions under different external loads.....	74
Figure 3. 3. Inner equilibrium positions under different external loads.....	75
Figure 3. 4. Outer equilibrium positions under different lubricant inlet pressure	76
Figure 3. 5. The start positions of the cavitation area in outer oil film under 10N, 20N and 30N external loads within 6000rad/s of the journal speed.....	77
Figure 3. 6. The start positions of the cavitation area in the inner oil film under 10N, 20N and 30N external loads within 6000rad/s of the journal speed.....	78
Figure 3. 7. The start positions of the cavitation area in the outer oil film under different lubricant inlet pressure	78
Figure 3. 8. Circumferential pressure distribution in the outer and inner oil films at a journal speed of 3000rad/s under 2×10^5 Pa lubricant feed pressure	79
Figure 3. 9. The pressure difference between the outer and inner oil film in the circumferential direction.....	80
Figure 3. 10. Inner oil film lubrication as the ring spins: (a)0° (b)20° (c)40° (d)60°	81

Figure 3. 11. The oil flow rate supplied to the inner oil film in one revolution of the ring.....	82
Figure 3. 12. The oil flow rate into the inner oil film in one revolution of the ring at journal speeds of 1000rad/s, 3000rad/s and 5000rad/s under 10N, 20N and 30N external loads: (a)10N load (b)20N load (c)30N load	84
Figure 3. 13. The mean oil flow rate into inner the oil film under different external loads	85
Figure 3. 14. The oil flow rate into the inner oil film in a revolution of the ring at journal speeds of 1000rad/s, 3000rad/s and 5000rad/s under 10^5 Pa, 2×10^5 Pa and 3×10^5 Pa inlet pressure: (a) 10^5 Pa (b) 2×10^5 Pa (c) 3×10^5 Pa	87
Figure 3. 15. The mean oil flow rate into the inner oil film under 10^5 Pa, 2×10^5 Pa and 3×10^5 Pa inlet pressure	88
Figure 4. 1. An elastic shaft segment unit in Finite Element analysis	97
Figure 4. 2. The model of a turbocharger rotor system: (a) Physical model (b) Finite element model.....	100
Figure 4. 3. Rotating disk with an imbalance mass	102
Figure 4. 4. Weak disturbance exerted on the journal.....	104
Figure 4. 5. Geometrical structure and system coordinates of the journal bearing....	105
Figure 4. 6. Rub-impact dynamics model of the floating ring bearing.....	111
Figure 5. 1. Dynamic coefficients simplification of the floating ring bearing.....	117
Figure 5. 2. Mode shapes of a turbocharger free rotor: (a) The first order (b) The	

second order (c) The third order (d) The fourth order	123
Figure 5. 3. A Campbell diagram of the turbocharger rotor system with an equivalent stiffness coefficient of 10^{10} N/m	127
Figure 5. 4. Turbocharger mode shapes with an equivalent bearing stiffness coefficient of 10^{10} N/m at the rotational speed of 8,000 rad/s	130
Figure 5. 5. A Campbell diagram of the turbocharger rotor system with an equivalent stiffness coefficient of 10^7 N/m	130
Figure 5. 6. Turbocharger mode shapes with an equivalent bearing stiffness coefficient of 10^7 N/m at the rotational speed of 8,000 rad/s	133
Figure 5. 7. A Campbell diagram of the turbocharger rotor system with an equivalent stiffness coefficient of 10^4 N/m	134
Figure 5. 8. Turbocharger mode shapes with an equivalent bearing stiffness coefficient of 10^4 N/m at the rotational speed of 8,000 rad/s	137
Figure 6. 1. Displacement of the turbocharger shaft under 10^{-5} kgm rotor imbalance at the turbine impeller: (a)Waterfall diagram (b)Bifurcation diagram	142
Figure 6. 2. Displacement of the turbocharger shaft under 2.5×10^{-5} kgm rotor imbalance at the turbine impeller: (a)Waterfall diagram (b)Bifurcation diagram	143
Figure 6. 3. Displacement of the turbocharger shaft under 5×10^{-5} kgm rotor imbalance at the turbine impeller: (a)Waterfall diagram (b)Bifurcation diagram	144
Figure 6. 4. The spectrum and trajectory of the turbocharger shaft at 3000rad/s: (a)	

under 10^{-5} kgm rotor imbalance (b)under 2.5×10^{-5} kgm rotor imbalance	
(c)under 5×10^{-5} kgm rotor imbalance	146

Figure 6. 5. The spectrum and trajectory of the turbocharger shaft at 6000rad/s: (a)

under 10^{-5} kgm rotor imbalance (b)under 2.5×10^{-5} kgm rotor imbalance	
(c)under 5×10^{-5} kgm rotor imbalance	148

Figure 6. 6. Displacement of the turbocharger shaft under 5cp lubricant viscosity:

(a)Waterfall diagram (b)Bifurcation diagram	150
---	-----

Figure 6. 7. Displacement of the turbocharger shaft under 35cp lubricant viscosity:

(a)Waterfall diagram (b)Bifurcation diagram	151
---	-----

Figure 6. 8. The spectrum and trajectory of the turbocharger shaft at 2000rad/s:

(a)under 5cp lubricant viscosity (b)under 35cp lubricant viscosity	153
--	-----

Figure 6. 9. The spectrum and trajectory of the turbocharger shaft at 6000rad/s:

(a)under 5cp lubricant viscosity (b)under 35cp lubricant viscosity	154
--	-----

Figure 6. 10. Displacement of the turbocharger shaft under 15μm inner bearing

clearance: (a)Waterfall diagram (b)Bifurcation diagram	156
--	-----

Figure 6. 11. Displacement of the turbocharger shaft under 25μm inner bearing

clearance: (a)Waterfall diagram (b)Bifurcation diagram	157
--	-----

Figure 6. 12. The spectrum and trajectory of the turbocharger shaft at 3000rad/s:

(a)under 15μm inner bearing clearance (b)under 25μm inner bearing clearance .	158
---	-----

Figure 6. 13. The spectrum and trajectory of the turbocharger shaft at 6000rad/s:

(a)under 15μm inner bearing clearance (b)under 25μm inner bearing clearance .	159
---	-----

Figure 6. 14. Displacement of the turbocharger shaft under 70μm outer bearing

clearance: (a)Waterfall diagram (b)Bifurcation diagram.....	160
Figure 6. 15. Displacement of the turbocharger shaft under 90 μ m inner bearing	
clearance: (a)Waterfall diagram (b)Bifurcation diagram.....	161
Figure 6. 16. The spectrum and trajectory of the turbocharger shaft at 3000rad/s:	
(a)under 70 μ m outer bearing clearance (b)under90 μ m outer bearing clearance. 163	
Figure 6. 17. The spectrum and trajectory of the turbocharger shaft at 6000rad/s:	
(a)under 70 μ m outer bearing clearance (b)under90 μ m outer bearing clearance. 164	
Figure 6. 18. Displacement of the turbocharger shaft under 2N static load on the ring:	
(a)Waterfall diagram (b)Bifurcation diagram	166
Figure 6. 19. Displacement of the turbocharger shaft under 5N static load on the ring:	
(a)Waterfall diagram (b)Bifurcation diagram	167
Figure 6. 20. The spectrum and trajectory of the turbocharger shaft at 3000rad/s:	
(a)under 2N static load (b)under 5N static load.....	168
Figure 6. 21. The spectrum and trajectory of the turbocharger shaft at 6000rad/s:	
(a)under 2N static load (b)under 5N static load.....	169
Figure 7. 1. The block diagram of the turbocharger test rig	174
Figure 7. 2. The GJ90C turbocharger.....	175
Figure 7. 3. The block diagram of the lubrication system	177
Figure 7. 4. CB-B gear lubrication pump.....	178
Figure 7. 5. Tescom 44-52-12243V Hydraulic control valve	178
Figure 7. 6. A photograph of the assembly flanges between the lubricant pipe and the	
turbocharger	180

Figure 7. 7. KAMAN KD2306 1U1 eddy current displacement transducer.....	182
Figure 7. 8. A photograph of the eddy current displacement transducers installed on the turbocharger	184
Figure 7. 9. A BR100_DDT_P cylindrical photoelectric sensor.....	184
Figure 7. 10. The speed nut for the light sensitive belt placement	186
Figure 7. 11. The rotational speed sensor fixed on a universal bracket	186
Figure 7. 12. USB-6251 BNC signal collection card.....	187
Figure 7. 13. A photograph of the turbocharger test rig.....	188
Figure 8. 1. The turbocharger shaft end motion at the compressor impeller side at 1,000r/min rotational speed: (a)X displacement (b)Spectrum of X displacement (c)Y displacement (d)Spectrum of Y displacement (e)Trajectory	194
Figure 8. 2. The turbocharger shaft end motion at the compressor impeller side at 5,000r/min rotational speed: (a)X displacement (b)Spectrum of X displacement (c)Y displacement (d)Spectrum of Y displacement (e)Trajectory	196
Figure 8. 3. The turbocharger shaft end motion at the compressor impeller side at 11,000r/min rotational speed: (a)X displacement (b)Spectrum of X displacement (c)Y displacement (d)Spectrum of Y displacement (e)Trajectory	198
Figure 8. 4. The turbocharger shaft end motion at the compressor impeller side at 15,000r/min rotational speed: (a)X displacement (b)Spectrum of X displacement (c)Y displacement (d)Spectrum of Y displacement (e)Trajectory	200
Figure 8. 5. Waterfall diagrams of the turbocharger shaft end motion at the compressor side: (a)X displacement (b)Y displacement.....	202

Figure 8. 6. Bifurcation diagrams of the turbocharger shaft end motion at the
compressor side: (a)X displacement (b)Y displacement203

Abstract

Automotive turbochargers have been widely applied in vehicles in order to increase the power output of internal combustion engines by increasing the air to fuel ratio entering the piston cylinders. Turbochargers use the exhaust flow to spin a turbine at speeds of up to 140,000 r/min. Under such extreme working conditions, even a weak vibration can lead to the bearing failure and the whole turbocharger destroyed. In order to guarantee a safe operation, it is necessary to carry out a theoretical research on the dynamics performance of turbochargers. Therefore, the primary objective of this research is to develop a dynamics model for the turbocharger rotor system under multi-field coupled forces and then to study the dynamic characteristics and the stability of its rotor system according to the simulation and experimental results.

A turbocharger is a special kind of rotating machinery because of the following aspects: Firstly, the turbocharger rotor system is supported by floating ring bearings. The impact of nonlinear multi-field coupled forces must be considered. Secondly, the turbocharger rotor system is a multi-span rotor bearing system that makes the modeling and simulation more complicated. Thirdly, the working speed range of the turbocharger covers multiple orders of critical speeds. This flexible rotor system cannot be studied using the conventional theory of rigid rotors.

In this thesis, the lubrication system of a turbocharger is initially investigated. The analytical expressions of the hydrodynamic pressure distribution in the floating ring bearing are derived using the infinitely long bearing theory, taking into account the oil inlet pressure and the cavitation area. The influences of external loads and oil inlet pressure on the oil flow rate into the inner clearance are analytically investigated, while considering the effect of the rotation of the ring. A finite element model is then developed for the turbocharger rotor system. In this model, the excitation forces considered include rotor imbalance, hydrodynamic forces, lubricant feed pressure and the dead weight. The dimensionless form of Capone hydrodynamic force model is extended into the floating ring bearing. Following model development, modal analysis is carried out on both a free rotor system and a turbocharger rotor system. The effects of the structural parameters and working conditions, such as the rotor imbalance, lubricant viscosity, bearing clearances and lubricant feed pressure, on the stability of the turbocharger rotor system are studied. A turbocharger test rig is then designed and developed to monitor the turbocharger shaft motion. The experimental data agree well with the simulation results from the theoretical model.

The primary contribution of the current research can be categorized into the following aspects: Firstly, the analytical expressions of the hydrodynamic pressure distribution have been solved. The equilibrium positions of the journal and ring have been deduced under

different external loads and lubricant feed pressure. The relationship between the oil flow rate and the rotational velocity of the shaft has been obtained. Secondly, Capone hydrodynamic force model is introduced and extended to simulate the dynamic performance of the floating ring bearing. The analytical expression of the hydrodynamic forces of double oil films have been derived based on the dimensionless form of the Reynolds Equations. Thirdly, the motion of the turbocharger shaft is simulated within a speed range of 0 to 8,000 rad/s. The influences of structural parameters and working conditions on the stability of the turbocharger rotor system are clearly understood.

It should be noted that the developed model still needs to be validated when turbocharger is operated at a relatively high speed, although it agrees well with experimental results within the speed range of 0 to 2,000 rad/s.

Declaration

No portion of the work referred to in this thesis has been submitted in support of an application for another degree or qualification of the University of Huddersfield or any other university or other institute of learning.

Copyright Statement

1. The author of this thesis (including any appendices and/or schedules to this thesis) owns any copyright in it (the “Copyright”) and he has given The University of Huddersfield the right to use such Copyright for any administrative, promotional, educational and/or teaching purposes.
2. Copies of this thesis, either in full or in extracts, may be made only in accordance with the regulations of the University Library. Details of these regulations may be obtained from the Librarian. This page must form part of any such copies made.
3. The ownership of any patents, designs, trade marks and any and all other intellectual property rights except for the Copyright (the “Intellectual Property Rights”) and any reproductions of copyright works, for example graphs and tables (“Reproductions”), which may be described in this thesis, may not be owned by the author and may be owned by third parties. Such Intellectual Property Rights and Reproductions cannot and must not be made available for use without the prior written permission of the owner(s) of the relevant Intellectual Property Rights and/or Reproductions.

Acknowledgement

I would like to express my deep and sincere gratitude to my main supervisor, Professor Andrew Ball. His wide knowledge and his logical way of thinking have been of great value for me. His understanding, encouragement and personal guidance have provided a good basis for the present thesis.

I am deeply grateful to my former supervisor, Dr. Zhanqun Shi for his important support throughout this work.

I wish to express my warm and sincere thanks to Dr. Fengshou Gu for his help during this experiment.

I would like to thank my parents for their encouragement and support during my study.

The financial support of the University of Huddersfield is gratefully acknowledged.

Publications

1. **Zhang H**, Shi ZQ, Song YM, Gu FS and Ball AD. (2012) Analytical investigation on the lubrication of floating ring bearing under the influences of external load and oil inlet pressure. Proceedings of the Institution of Mechanical Engineers, Part J: Journal of Engineering Tribology. (Under Review)
2. **Zhang H**, Shi ZQ, Gu FS and Ball AD. (2012) Stability analysis against turbocharger rotor system supported on floating ring bearings. The 25th International Congress on Condition Monitoring and Diagnostic Engineering Management, University of Huddersfield, United Kingdom, June 2012. (Under Review)
3. **Zhang H**, Shi ZQ, Gu FS and Ball AD. (2011) Stability analysis against turbocharger rotor system under coupling of multi-field nonlinear forces. Scientific Research and Essays. (Under Review)
4. **Zhang H**, Shi ZQ, Gu FS and Ball AD. (2011) Modelling of outer and inner film oil pressure for floating ring bearing clearance in turbochargers. The 9th International Conference on Damage Assessment of Structures, St. Anne's College, Oxford, United Kingdom, July 2011.
5. **Zhang H**, Shi ZQ, Gu FS and Ball AD. (2010) Bending vibration of an automotive turbocharger under the influence of rotor imbalance. CM 2010 and MFPT 2010 The 7th International Conference on Condition Monitoring and Machinery Failure Prevention Technologies, Ettington Chase, Stratford-upon-Avon, United Kingdom, June 2010.

6. **Zhang H**, Shi ZQ, Gu FS, Mishra R and Ball AD. (2009) Model-based fault detection for a turbocharger. Proceedings of COMADEM 2009 : Condition Monitoring and Diagnostic Engineering Management (COMADEM). ISBN 9788493206468.
7. **Zhang H** and Shi ZQ. (2009) Modelling for a turbocharger in rotordynamics. Proceedings of Computing and Engineering Annual Researchers' Conference 2009: CEARC'09. University of Huddersfield, United Kingdom, 2009. ISBN 9781862180857.

CHAPTER ONE

INTRODUCTION

This chapter provides an introduction to why this investigation is conducted. The application and development of the rotating machinery are firstly introduced. The structure and working principle of an automotive turbocharger is then described. After that, the research background related to the fluid lubrication and the rotordynamics are given in order to provide a foundation for this research. The motivation to study the dynamic characteristics of the turbocharger rotor system is stated. Finally, the project objectives and structure of the thesis are presented.

1.1 Introduction to the Rotating Machinery



The steam turbine generator set



The aero-generator



The hydroelectric generator set



The turbocharger



The nuclear generator set



The centrifugal pump

Figure 1. 1. The industrial application of the rotating machinery

Rotating machinery is mechanical equipment which operates on the basis of the rotor system, such as the steam turbine generator set, the hydroelectric generator set, the nuclear

generator set, the aero-generator, the turbocharger, the centrifugal pump, etc, which are shown in Figure 1.1. It generally comprises of the rotor, stator, bearing, seal, etc. The rotor spins inside the stator and the energy conversion is conducted through the media in the clearance between the rotor and stator [1], which is shown in Figure 1.2.

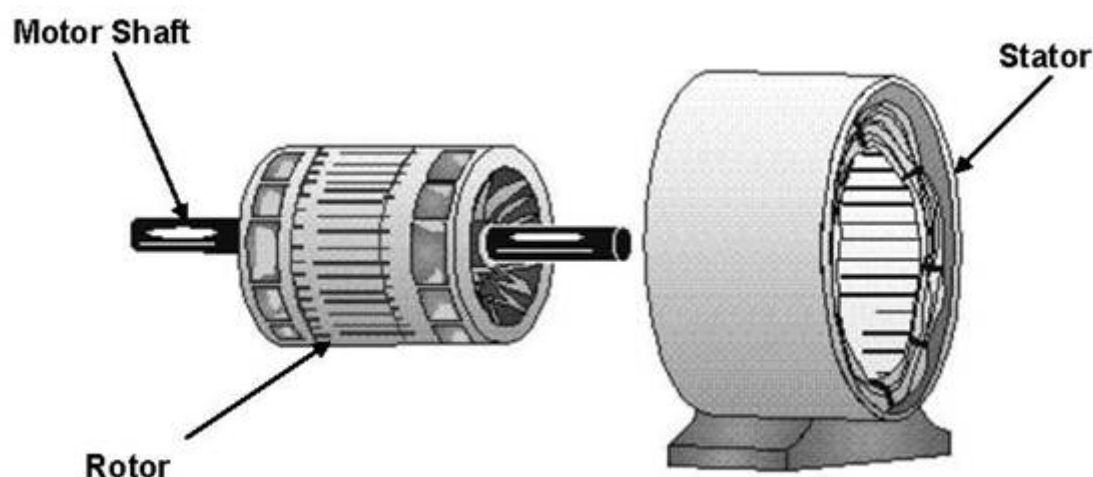


Figure 1. 2. The structure of rotor and stator

Modern rotating machinery has the characteristics of the speed, heavy load and automation, which improve the production efficiency and reduce costs. However, it also has the negative impact. Once the faults occur in the operating equipment, the economic losses might be incalculable. Therefore the criterion of rotating machinery is required more strictly nowadays in terms of the speed, volume, efficiency, stability, reliability, etc.

Rotating machinery is a complex nonlinear vibration system with multi-degrees of freedom. The operational stability is crucial for the safe operation of the whole equipment. In the actual rotor bearing system, the residual imbalance remains existence, although the rotors have been balanced. The imbalance excites the system to perform a stable synchronous motion. In fact this stable state might be affected by the existence of faults which could

excite a subsynchronous motion. The combination of the synchronous and subsynchronous motion lead to the system performing a complex trajectory and also give rise to a large alternating stress on the shaft. Long term operation in the unstable stage will threaten the service life of the equipment. Therefore there is an important theoretical and practical significance to the study of the influences of the parameters of the rotor system and working condition on its stability characteristics for safe operation of the rotating machinery.

1.2 Introduction to the Turbocharger

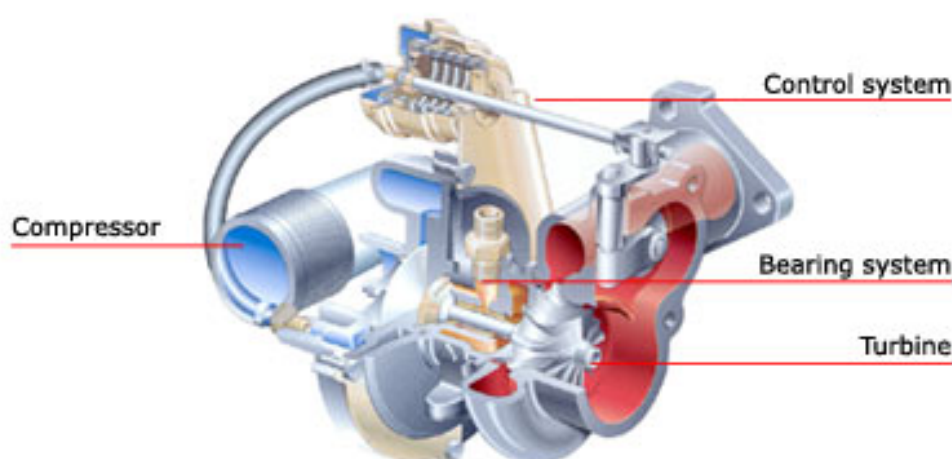


Figure 1. 3. The structure of a typical automotive turbocharger

Figure 1.3 shows the structure of a typical automotive turbocharger. (It is noted that Figure 1.3 is copied from the website of the BorgWarner Company and used without the permission from the BorgWarner Company) The turbocharger mainly comprises of turbine and compressor impellers linked by a shared shaft. The turbocharger is a centrifugal compressor powered by the exhaust gases. It utilizes the engine's exhaust to drive the

turbine wheel. Through the rotation of the coaxial compressor wheel, the ambient air is compressed and then delivered to engine cylinders. Therefore, the engine burns more air and fuel so that more mechanical power is created. In addition, the application of turbochargers reduces the exhaust gases emission and improves the efficiency of the engine [2]. The major advantage of the turbocharger is that the output power and torque of the engine can be significantly improved without increasing the displacement. Generally speaking, the output power and torque of a turbocharged engine could be improved 20% - 30% compared to a normal engine [2].

Turbochargers, as the best way to improve the performance of the engine, can be viewed as a milestone in the history of the engine's development [3]. In 1905, the first turbocharger was designed by Buchi, a Swiss engineer. At that period, turbochargers were applied in the aero-engines in order to improve the performance of the engine in a high altitude. In 1950s, racers tried to install the turbochargers in the automotive engines and the first turbocharged automotive engine was produced in 1960s. In recent years, with the requirement of the energy saving and environmental protection, turbochargers have been widely applied in automobiles.

1.3 Background

1.3.1 Development of the research of the fluid lubrication

From 1883 to 1885, B. Tower [4] conducted the first investigation on the fluid lubrication of the radial journal bearings on the railway. During the experiment, he noticed the existence of the hydrodynamic pressure in the oil holes. The experimental results about oil

film pressure distribution attracted the interests of the researchers. In 1886, according to the published experimental results, O. Reynolds [5] conducted an analytical research on the mechanism of the pressure distribution and derived the well-known Reynolds Equation for the oil film pressure that provided the theoretical foundation for a further research of the fluid lubrication. From the mathematical point of view, the core issue of the fluid lubrication is the solution of Reynolds Equation to reveal the oil film pressure distribution. Unfortunately, the attempt to derive the analytical solution is unsuccessful so far except for rare cases, the numerical calculation is still the most common approach [6, 7].

With the development of mathematical algorithms and the application of the fast computers, a considerable progress has been made on the research of the fluid lubrication and bearing techniques. The research field covers both static and dynamic characteristics of the bearing, both in the steady state and non-steady state. In 1931, Kingsbury [8] used the electrolyzer simulation method to calculate the oil film pressure distribution. In 1942, Christopherson [9] initially introduced the finite difference method to solve Reynolds Equation. In 1969, Reddi [10] adopted the finite element method to derive the oil film pressure distribution in the journal bearing.

From 1980s, researchers paid more attention to the stability analysis of the nonlinear rotor bearing system that becomes increasingly important for the high speed rotor systems. As far as the nonlinear analysis is concerned, the key issue is to derive a satisfied functional expression to reflect the dynamic characteristics of the nonlinear hydrodynamic force, which determines the accuracy of nonlinear dynamics design of the rotating machinery. To date, the general approach to solve the Reynolds Equation is to simplify the non-steady

state boundary of the oil film to the steady state boundary, such as Sommerfeld boundary condition, *Gümbel* boundary condition, Reynolds boundary condition, etc, which ignores the impact of the journal perturbation velocity on the oil film boundary [11]. As a result, the derived expression of the nonlinear hydrodynamic force is insufficient to meet the reality. It is necessary to develop a more reasonable theory of the fluid lubrication to meet the demand of the modern industry.

1.3.2 Development of the research of the rotordynamics

The development of rotordynamics is closely related to industrial development. In 1869, the first rotordynamic investigation was published by Rankine [12], who studied the equilibrium condition of an undamped homogeneous shaft under perturbation at its initial position. Without consideration of the influences of Coriolis Forces, he concluded that the shaft performs a stable motion below the first order critical speed, an unstable motion over the first order critical speed and an uncertain motion around the first order critical speed.

In 1919, H. Jeffcott [13] was invited to conduct the research of the rotordynamics. The model he studied was an elastic shaft without mass, both sides of which were rigidly hinged. A rigid disk with mass, imbalance and damping, was fixed in the middle of the shaft. This simplified model of the flexible rotor system is called ‘Jeffcott rotor’. From this research, he drew the following conclusion:

In a dynamic coordinate system rotating at the same velocity of the shaft, the position of the centroid of the disk will be changed rather than fixed. If the shaft speed is much lower than the critical speed, the centroid will be located outside the deflection; if the shaft speed

is much higher than the critical speed, the centroid will be located inside the deflection; if the shaft speed equals the critical speed, the eccentricity and deflection will place in a perpendicular position. Therefore, it is possible for a rotor system to keep stable even the shaft rotating in a supercritical state. In addition, the load of the bearing is even declined as increasing the shaft speed.

Based on this theory, in 1920s, numerous rotor systems were designed and produced, which operating speeds are far higher than the first order critical speeds. Unfortunately, the serious vibration always occurred in some of the equipment. In order to clarify the reasons of the accidents, experts conducted a series of experimental investigation. The results indicate that when the rotor system working over the first order critical speed, a dramatic motion will occur until the shaft reaches a certain speed. The angular frequency of the motion approximately equals the first order critical speed. The speed when the dramatic motion occurs can be viewed as the threshold speed of the instability of the rotor bearing system. In addition, the amplitude of the motion will become larger as increasing further the operating speed. This conclusion provides a foundation for the stability analysis of the rotor system [1].

Since the 1950s, the rapid development of the aviation industry, electric industry, shipbuilding industry, petroleum and chemical industry, etc, promoted the development of rotordynamics. More and more rotor systems were running in the flexible state, even working over the third and fourth order critical speeds. Therefore, more stable and reliable rotors are required to be designed and the theory of the rotordynamics needs to be further investigated.

1.3.3 Research areas of the rotordynamics

1.3.3.1 The critical speeds calculation of the rotor bearing system

In order to avoid the occurrence of the resonance for a rotor system, it is required to estimate its critical speed as accurately as possible. To date, the most popular approaches of the critical speed calculation are the transfer matrix method and the finite element method. The transfer matrix method has the advantage of simple solution, easy programming and being able to calculate the higher orders critical speeds. However, the accuracy of this approach is not satisfied, especially in the calculation of dynamic performance of the large-scale rotor system working at high speed. Also, numerical instability would be occurred. Compared to the transfer matrix method, the finite element method is a more accurate approach that also can avoid the numerical instability, which is usually occurred in the transfer matrix method. On the other hand, the disadvantage of the finite element method is that more computer resources will be occupied, and also difficult to program.

1.3.3.2 Calculation of the steady state response under the rotor imbalance

It is crucial for the design of a rotor bearing system to accurately estimate the deflection of the rotor, support and the load of the bearing under a given rotor imbalance. The classical approaches of calculation of the rotor imbalance response primarily include the transfer matrix method and the modal synthesis method. However, neither two approaches are accurate enough for the industrial calculation as a result of the difficulty of the estimation of the structural damping. In addition, the modal synthesis method is only suitable for

linear systems, which can not be used in the rotor bearing systems with nonlinear factors. In recent years, the finite element method gradually becomes popular in the forced response of the rotor system with the development of the computer and mathematical software.

1.3.3.3 Balancing of the flexible rotor system

Most of modern rotor systems work in the supercritical state so that the flexible deflection can not be ignored. It is, therefore, necessary to study the balancing techniques for the flexible rotor systems. The primary approaches include the mode decomposition method and the influence coefficient method.

In the mode decomposition method, the rotor is driven to spin at the 1st, 2nd, ... , n order critical speeds respectively and then a group of appropriate mass is used to achieve balancing. This method has an advantage of high sensitivity. However, it is difficult to obtain an accurate result. In addition, this method is unsuitable for the systems with significant damping. In the influence coefficient method, the dynamic flexibility matrices are required to be obtained under each balancing velocity to calculate the eccentricity and altitude degree of the unknown disks. This method will consume a long calculation time.

The academic research of balancing techniques for flexible rotor systems concentrates on two fields: firstly, the relationship of the rotor imbalance and the flexible deflection, supporting forces, vibration; secondly, the compensation method, the balancing criterion and their relationship.

1.3.3.4 The stability analysis of the rotor bearing system

The self-excited vibration of the rotor system can lead to a dramatic alternating stress on the shaft that may cause a failure of the equipment. The higher the rotor velocity, the more possible the vibration occurs, because most of the self-excited vibration occur in the supercritical state of the rotor.

To date, most of the stability analysis is conducted based on the Jeffcott model. The primary approaches for the stability analysis are listed as follows:

(I) Eigenvalue approach

In this approach, eigenvalues should be solved by the derived characteristic equation of the rotor system. When the real part of the eigenvalue is zero, the corresponding velocity can be viewed as the threshold velocity of the self-excited vibration and then the stability boundary of the system can be obtained. However, due to the difficulty to solve a higher order polynomial, it is not a good approach in terms of the numerical integration.

(II) Routh-Hurwitz criterion

In this approach, the roots of the characteristic equation are not required to solve. However, this approach is not suitable for a higher order characteristic equation, thus it can only be applied in a qualitative research on the stability of the simplified rotor bearing system.

(III) Numerical integration approach

In this approach, the motion of the rotor system is solved numerically and then the system stability can be determined by the system response. This approach is not only suitable for stability analysis, steady state forced response and critical speeds calculation, but also fit for the study of the transient system response. Also, it can be used for both linear and

nonlinear systems.

The disadvantage of the numerical integration approach is that a long calculation time will be consumed. In addition, the time step has to be short enough to ensure the calculation accuracy and stability, and also the integration period must be long enough to eliminate the impacts of the initial perturbation.

1.4 Motivation

A turbocharger is a rotating machine of the high speed and light load category. The rotational speed can reach 140,000r/min and over. At such a high speed, even a weak vibration can lead to the failure of its rotor system. In order to ensure the turbocharger operating safely under the extreme working conditions, it is therefore, crucial to conduct the research on the rotordynamics of the turbocharger rotor system.

The research of the vibration characteristics and the stability of the turbocharger rotor system mainly concentrate on two fields: Firstly, floating ring bearings. The extreme working condition of the turbocharger could not be withstood by the general journal bearings and ball bearings. As a result, most automotive turbochargers use floating ring bearings to support their rotor systems. When the shaft spins, double oil films connected by the supply holes on the ring are formed inside the bearing clearance. The pressure distribution and the stability of two oil films simultaneously affect the turbocharger rotor system that makes the vibration characteristics and stability more complex to analyze. Secondly, modeling of a multi-span rotor system. Compared to the Jeffcott rotor model, the turbocharger rotor system is a multi-span rotor bearing system which performs a complex

nonlinear behavior. In addition, the existence of double oil films increases the number of the degree of freedom of the rotor system. In this thesis, research will be conducted on the above two fields.

1.5 Research Objectives

The primary objective of this research is to study the dynamic performance of the turbocharger rotor system under nonlinear forces in order to provide a theoretical foundation for the design and application of the automotive turbocharger and to ensure that the turbochargers operate safely under extreme working conditions. On the other hand, work also involves investigation of the lubrication of floating ring bearings in order to study the influences of double oil films on the dynamic performance of the rotor system and derive the analytical expression of the nonlinear hydrodynamic fluid forces of two oil films.

In particular, the objectives can be categorized into several parts, as listed as follows:

Objective 1. To conduct a full literature review of current research in the areas of fluid lubrication, rotordynamics and turbocharger rotordynamics.

Objective 2. To investigate the fluid lubrication of floating ring bearings.

Objective 3. To develop a theoretical dynamics model for the turbocharger rotor system..

Objective 4. To analyze the dynamic performance of the turbocharger rotor system and to calculate the critical speeds and mode shapes.

Objective 5. To study the effects of working conditions on the dynamic performance and stability of the turbocharger rotor system.

Objective 6. To construct a turbocharger test rig to validate and verify the theoretical model.

1.6 The Structure of the Thesis

In the first chapter, the development of the rotating machinery and turbochargers are introduced. The research background of the rotordynamics is given. The motivation of the research on the turbocharger rotor system and the stability is briefly discussed. The research objectives and the structure of the thesis are listed.

In the second chapter, the literatures regarding fluid lubrication, rotordynamics and turbocharger rotordynamics are reviewed. The approaches of the research on the nonlinearity of the vibration system, the modal synthesis method and the numerical integration method are introduced.

In the third chapter, the lubrication system of a turbocharger is analytically studied. The effects of external loads and oil inlet pressure on the oil film pressure distribution and oil flow rate are investigated.

In the fourth chapter, a dynamics model is developed for the turbocharger rotor system using the finite element method. Linear and nonlinear hydrodynamic fluid forces are studied respectively. Rub-impact forces are considered in modeling.

In the fifth chapter, the modal analysis is conducted to the turbocharger rotor system. Critical speeds and mode shapes of the turbocharger rotor system are calculated and analyzed based on the linear dynamics model.

In the sixth chapter, motions of the turbocharger rotor system are simulated. The stability disciplines are analyzed under the influences of the rotor imbalance, the lubricant viscosity, bearing clearances and the lubricant feed pressure.

In the seventh chapter, a turbocharger test rig is developed to validate the theoretical model and investigate the motion discipline of turbocharger rotor system.

In the eighth chapter, the experimental data of the turbocharger shaft end motion at the compressor impeller side as well as the rotational speed of the shaft are monitored. The instability discipline of the turbocharger rotor system is studied according to the experimental and simulation results.

In the ninth chapter, the current research is concluded and makes suggestions for future work.

CHAPTER TWO

LITERATURE REVIEW

In this chapter, literature regarding the research of fluid lubrication and dynamic characteristics of the rotor bearing system has been reviewed. Literature regarding the turbocharger rotordynamics, which is a special nonlinear rotor bearing system supported by floating ring bearings, is studied. The key backgrounds of the theory involved in this research have been introduced, such as the nonlinear theory of the vibration system, the modal synthesis method and the numerical integration approach.

Nomenclature

x	Displacement in x direction (m)	Fh_x	Oil film force in x direction (N)
y	Displacement in y direction (m)	Fh_y	Oil film force in y direction (N)
z	Displacement in z direction (m)	Fh_t	Oil film force in tangential direction (N)
\bar{x}	Dimensionless displacement in x direction	Fh_r	Oil film force in radial direction (N)
\bar{y}	Dimensionless displacement in y direction	fh_t	Dimensionless oil film force in tangential direction
\bar{z}	Dimensionless displacement in z direction	fh_r	Dimensionless oil film force in radial direction
t	Time (s)	k_{xx}	Stiffness coefficients (N/m)
\bar{t}	Dimensionless time	k_{xy}	
ω	Rotational velocity (rad/s)	k_{yx}	
ϕ	Attitude angle (rad)	k_{yy}	
φ	Coordinate system in circumferential direction (rad)	c_{xx}	Damping coefficients (Ns/m)
P	Oil film pressure distribution (Pa)	c_{xy}	
\bar{P}	Dimensionless oil film pressure distribution	c_{yx}	
D	Diameter of the journal (m)	c_{yy}	

R	Radius of the journal (m)	K_1	Undetermined coefficients
L	Length of the bearing (m)	K_2	
H	Oil film thickness (m)	K_3	
h	Dimensionless oil film thickness	C	Oil film clearance (m)
μ	Lubricant viscosity (PaS)	ε	Eccentricity

2.1 Review of the Research of the Fluid Lubrication

The key issue of the research on the fluid lubrication is the study of the dynamic characteristics of hydrodynamic forces. From a mathematical point of view, the primary task of research of the fluid lubrication is the solution of Reynolds Equation. Linearization is the most popular method for the analysis of nonlinear hydrodynamic forces. Linear models are generally adequate to describe the static characteristics of the rotor systems supported by hydrodynamic bearings. However, linearization is insufficient to describe the nonlinear dynamic behaviors. Therefore, the nonlinear model should be developed for the analysis of nonlinear behaviors of the rotor system.

2.1.1 The linear models of hydrodynamic forces

2.1.1.1 The linear expression of the hydrodynamic force increment

The hydrodynamic force is viewed as a function of the displacement and velocity around the static equilibrium position. Through Taylor series expansion, the hydrodynamic force increment due to a perturbation can be expressed in Equation (2.1) [14].

$$\begin{bmatrix} \delta F h_x \\ \delta F h_y \end{bmatrix} = \begin{bmatrix} k_{xx} \\ k_{yx} \end{bmatrix} x + \begin{bmatrix} k_{xy} \\ k_{yy} \end{bmatrix} y + \begin{bmatrix} c_{xx} \\ c_{yx} \end{bmatrix} \dot{x} + \begin{bmatrix} c_{xy} \\ c_{yy} \end{bmatrix} \dot{y} \quad (2.1)$$

In the equation (2.1), $k_{xx}, k_{yx}, k_{xy}, k_{yy}$ and $c_{xx}, c_{yx}, c_{xy}, c_{yy}$ denote the stiffness and damping coefficients of the oil film respectively. Therefore, the dynamic characteristic of the oil film is simplified to such eight dynamic coefficients. Unfortunately, this approach is unsuitable for some situations when the system does not meet the perturbation condition.

2.1.1.2 The undetermined function matrix

In this approach, the expression of the hydrodynamic force is given in the equation (2.2) under the assumption of zero pressure on the boundary [15].

$$\begin{bmatrix} Fh_r \\ Fh_t \end{bmatrix} = - \begin{bmatrix} K_1 & K_2 \\ K_2 & K_3 \end{bmatrix} \begin{bmatrix} \partial \varepsilon / \partial t \\ (\partial \phi / \partial t - \omega/2) \varepsilon \end{bmatrix} = -K \begin{bmatrix} \partial \varepsilon / \partial t \\ (\partial \phi / \partial t - \omega/2) \varepsilon \end{bmatrix} \quad (2.2)$$

The nonlinear hydrodynamic force is simplified to three coefficients. However, this approach is only suitable for the case of $\partial \phi / \partial t = 0$, because the squeeze term is ignored.

2.1.1.3 Conventional expressions of the hydrodynamic force

The common approach of the solution is to simplify Reynolds Equation under the assumption of the infinitely long or short bearings. The simplified equation is integrated with respect to the eccentricity and attitude angle and then the results are modified, if necessary, by the coefficients of the turbulent flow and leakage. This approach shows a great accuracy and convergence in the case of small eccentricity, whereas under large eccentricity, the calculation error may appear to be very obvious.

2.1.1.4 Database approach

The key step of this approach is the definition of the numerical range of the squeeze term in the Reynolds Equation. The database that is established by the Castell method under Reynolds boundary condition, includes three groups of parameters, such as eccentricity, attitude angle and squeeze ratio. This approach has an advantage of fast calculation speed. However, it is difficult to achieve a great accuracy [16].

2.1.2 The limitation of the linear hydrodynamic force model

It has been demonstrated by numerous accidents of the rotating machinery caused by instability that the analytical results derived from the linear hydrodynamic force model are insufficient to predict dynamic performance of nonlinear rotor bearing systems in practice. In the linear model, the hydrodynamic force is expressed by the stiffness and damping coefficients. Although this model has been widely applied in rotating machinery under small perturbation, the actual rotor bearing system might not satisfy the condition of the small perturbation. As a result, the predicted result based on the linear model can not comprehensively reflect the mechanism of the oil film. In addition, the linear model lacks a clear link among such dynamic coefficients. It is, therefore, necessary to derive a more logical and accurate expression for the nonlinear hydrodynamic force to provide a theoretical support for the comprehensive dynamic analysis of rotating machinery.

To date, although a considerable achievement has been made in the research of rotor bearing system based on the linear model, it is still insufficient to analyze the mechanism of the oil film instability. Here take the plain journal bearing as an example to illustrate the oil film instability. The oil film instability, such as oil whirl and whip, is an unstable free vibration of the journal bearing. Under an insufficient unit loading, the shaft centerline dynamic motion is usually circular in the direction of rotation. Oil whirl occurs at the oil flow velocity within the bearing, usually 40% to 49% of the shaft speed. Oil whip occurs when the whirl frequency coincide with a shaft resonant frequency. It is the nonlinear hydrodynamic force that leads to the subsynchronous motion of the rotor system. The

analytical expression of the hydrodynamic force can not be derived from the linear Reynolds Equation. In order to study the mechanism of oil film instability and reveal the intrinsic link between oil film instability and the stability of rotor system, a reasonable expression of the nonlinear hydrodynamic force is required to be derived.

2.1.3 The nonlinear analytical model of the hydrodynamic force

The nonlinear analytical models of hydrodynamic forces can be categorized into the infinitely long/short bearing model and the finite length bearing model. To date, most of the research regarding oil film nonlinear behaviors is based on the simplified infinitely long/short model. Gardner [17] used the method of multiple scales to study the weakly nonlinear motion of the rotor system under the assumption of the infinite long/short bearing theory. The subcritical and supercritical bifurcations at the equilibrium position were studied. Russo [18] investigated the impacts of the turbulent flow on the stability of synchronous motion. Adams and Abu-Mahfouz [19] used numerical investigation method to study the nonlinear dynamic behaviors of the rotors supported by the cylindrical bearing and tilting pad bearing. With the aid of the spectrum, the trajectory and Poincare map, the way into chaos was analyzed. Based on the shooting method and Floquet theory, Yuan and Zhu [20] discussed the influences of the rotor imbalance on the instability of the rotor supported on cylindrical bearings. It was found that the unbalance of rotors has an important effect on the stability, and the larger the unbalance magnitude is, the more serious the effect is. Under the assumption of infinite short bearing theory, Chen [21] adopted the center manifold theorem to study the subsynchronous motion of the shaft

around the critical equilibrium position. Furthermore, the bifurcation set was obtained by Floquet theory. According to the research of the rotor supported by the oil film damper, Zhao et al [22, 23] illustrated the nonlinear dynamic behaviors, e.g. synchronous motion, quasi-periodic motion, sub-harmonic motion and chaos, and the bifurcation behaviors, e.g. limit point bifurcation, quasi-periodic bifurcation, double periodic bifurcation and sub-harmonic bifurcation.

2.1.4 The list of classical nonlinear models of the hydrodynamic force

In the following section, three classical nonlinear models of the hydrodynamic force are listed, which have been widely used in the nonlinear behaviors analysis of journal bearings.

2.1.4.1 The infinitely short bearing model

Under the assumption of the infinitely short bearing and half-sommerfeld boundary condition, the corresponding Reynolds Equation in the dimensionless form is given by equation (2.3) [24].

$$\frac{D}{L} \frac{d}{d\bar{z}} \left(H^3 \frac{dP}{d\bar{z}} \right) = -3\varepsilon \left(1 - 2 \frac{d\phi}{d\bar{t}} \right) \sin \varphi + 6 \frac{d\varepsilon}{d\bar{t}} \cos \varphi \quad (2.3)$$

With the boundary conditions: $\frac{\partial P}{\partial \bar{z}} \Big|_{\bar{z}=0} = 0$, $\frac{\partial P}{\partial \bar{z}} \Big|_{\bar{z}=\pm 1} = 0$, $P|_{\varphi=0} = P|_{\varphi=\pi} = 0$

The analytical expressions of the radial and tangential hydrodynamic forces in the dimensionless form are given by equations (2.4a) and (2.4b).

$$fh_r = 2 \left(\frac{L}{D} \right)^2 \left[\left(1 - 2 \frac{d\phi}{d\bar{t}} \right) \frac{2\varepsilon^2}{(1-\varepsilon^2)^2} + \frac{\pi(1+2\varepsilon^2)}{(1-\varepsilon^2)^{2.5}} \frac{d\varepsilon}{d\bar{t}} \right] \quad (2.4a)$$

$$fh_t = -2\left(\frac{L}{D}\right)^2 \left[\left(1 - 2\frac{d\phi}{d\bar{t}}\right) \frac{\pi\varepsilon}{2(1-\varepsilon^2)^{1.5}} + \frac{4\varepsilon}{(1-\varepsilon^2)^2} \frac{d\varepsilon}{d\bar{t}} \right] \quad (2.4b)$$

2.1.4.2 The Capone hydrodynamic force model

In 1991, Capone [25] developed a nonlinear model of hydrodynamic force under the assumption of the infinitely short bearing. The calculation results show a good accuracy and convergence.

The dimensionless form of Reynolds Equation under the assumption of the infinitely short bearing is given in equation (2.5).

$$\left(\frac{R}{L}\right)^2 \frac{\partial}{\partial \bar{z}} \left(h^3 \frac{\partial p}{\partial \bar{z}} \right) = \bar{x} \sin \varphi - \bar{y} \cos \varphi - 2(\bar{x} \cos \varphi + \bar{y} \sin \varphi) \quad (2.5)$$

The pressure distribution in the dimensionless form is expressed by equation (2.6)

$$p = \frac{1}{2} \left(\frac{L}{D}\right)^2 \left[\frac{(\bar{x} - 2\dot{\bar{y}}) \sin \varphi - (\bar{y} + 2\dot{\bar{x}}) \cos \varphi}{(1 - \bar{x} \cos \varphi - \bar{y} \sin \varphi)^3} \right] (4\bar{z}^2 - 1) \quad (2.6)$$

The hydrodynamic fluid forces are expressed as follows.

$$\begin{aligned} \begin{Bmatrix} Fh_x \\ Fh_y \end{Bmatrix} &= -\mu\omega \left(\frac{R^2}{C^2} \right) \left(\frac{L^2}{D^2} \right) (RL) \frac{\sqrt{(\bar{x} - 2\dot{\bar{y}})^2 + (\bar{y} + 2\dot{\bar{x}})^2}}{(1 - \bar{x} \cos \varphi - \bar{y} \sin \varphi)} \\ &\quad \begin{Bmatrix} 3\bar{x}V - \sin \alpha G - 2 \cos \alpha F \\ 3\bar{y}V - \cos \alpha G - 2 \sin \alpha F \end{Bmatrix} \\ V &= \frac{2 + (\bar{y} \cos \alpha - \bar{x} \sin \alpha)G}{(1 - \bar{x}^2 - \bar{y}^2)} \\ G &= \frac{\pi}{\sqrt{1 - \bar{x}^2 - \bar{y}^2}} - \frac{2}{\sqrt{1 - \bar{x}^2 - \bar{y}^2}} \tan^{-1} \left(\frac{\bar{y} \cos \alpha - \bar{x} \sin \alpha}{\sqrt{1 - \bar{x}^2 - \bar{y}^2}} \right) \\ F &= \frac{(\bar{x} \cos \alpha + \bar{y} \sin \alpha)}{(1 - \bar{x}^2 - \bar{y}^2)} \end{aligned}$$

$$\alpha = \tan^{-1}\left(\frac{\bar{y} + 2\dot{\bar{x}}}{\bar{x} - \dot{\bar{y}}}\right) - \frac{\pi}{2} \text{sign}\left(\frac{\bar{y} + 2\dot{\bar{x}}}{\bar{x} - \dot{\bar{y}}}\right) - \frac{\pi}{2} \text{sign}(\bar{y} + 2\dot{\bar{x}}) \quad (2.7)$$

2.1.4.3 Zhang hydrodynamic force model

In this model, the adopted form of Reynolds Equation is given in equation (2.8) [26, 27].

$$-\frac{1}{12\mu R^2} \frac{\partial}{\partial \varphi} \left(h^3 \frac{\partial p}{\partial \varphi} \right) - \frac{h^3}{12\mu} \frac{\partial^2 p}{\partial z^2} = \left(\frac{d\phi}{dt} - \frac{\omega}{2} \right) \varepsilon \sin \varphi + \frac{d\varepsilon}{dt} \cos \varphi \quad (2.8)$$

With the boundary condition: $P|_{\partial s} = 0$, where ∂s denotes the boundary of the oil film.

The analytical expressions of hydrodynamic forces in radial and tangential directions are given in (2.9).

$$\begin{aligned} \begin{bmatrix} f_r \\ f_t \end{bmatrix} &= \begin{bmatrix} C_{11} & C_{12} \\ C_{21} & C_{22} \end{bmatrix} \begin{bmatrix} \frac{d\varepsilon}{dt} \\ -\frac{1}{2} \left(1 - 2 \frac{d\phi}{dt} \right) \varepsilon \end{bmatrix} \\ C_{11} &= 4\lambda^2 \left[\frac{\varepsilon \frac{d\varepsilon}{dt} A \left[3A^2 + \frac{1}{4} (2 - 5\varepsilon^2) \left(1 - 2 \frac{d\phi}{dt} \right)^2 \varepsilon^2 \right]}{(1 - \varepsilon^2)^2 \left[A^2 - \frac{1}{4} \left(1 - 2 \frac{d\phi}{dt} \right)^2 \varepsilon^4 \right]^2} + \frac{1 + 2\varepsilon^2}{2(1 - \varepsilon^2)^{2.5}} \Delta \right] \\ C_{22} &= 4\lambda^2 \left[\frac{\varepsilon \frac{d\varepsilon}{dt} A \left[A^2 + \frac{1}{4} (\varepsilon^2 - 2) \left(1 - 2 \frac{d\phi}{dt} \right)^2 \varepsilon^2 \right]}{(1 - \varepsilon^2)^2 \left[A^2 - \frac{1}{4} \left(1 - 2 \frac{d\phi}{dt} \right)^2 \varepsilon^4 \right]^2} + \frac{1}{2(1 - \varepsilon^2)^{1.5}} \Delta \right] \\ C_{12} = C_{21} &= - \frac{A\lambda^2 \left(1 - 2 \frac{d\phi}{dt} \right)^3 \varepsilon^4}{\left[A^2 - \frac{1}{4} \left(1 - 2 \frac{d\phi}{dt} \right)^2 \varepsilon^4 \right]^2} \\ \lambda &= \frac{L}{D} = \frac{L}{2R} \end{aligned} \quad (2.9)$$

$$\Delta = \pi + 2 \tan^{-1} \left[\frac{\varepsilon \frac{d\varepsilon}{d\bar{t}}}{A(1 - \varepsilon^2)^{0.5}} \right]$$

$$A = \sqrt{\left(\frac{d\varepsilon}{d\bar{t}} \right)^2 + \frac{1}{4} \left(1 - 2 \left(\frac{d\phi}{d\bar{t}} \right)^2 \right)^2 \varepsilon^2}$$

2.1.4.4 The comparison of the classical models

It can be seen from the simplification process of Reynolds Equation that both the infinitely short bearing model and Capone hydrodynamic force model are based on the assumption of the infinitely short bearing theory, i.e. $\frac{\partial}{\partial \phi} \left(\frac{h^3}{\mu} \frac{\partial p}{\partial \phi} \right) = 0$. In the infinitely short bearing model, the impact of the centroid motion term is ignored, which is taken into account in the Capone hydrodynamic force model. In addition, the phase angle in the Capone model leads $\pi/2$ compared to the infinitely short bearing model. Zhang hydrodynamic force model is derived based on the finite-length Reynolds Equation. This model takes into account the rotational torque of journal, the instability force of the oil film, the squeeze force of the bearing and lubricant feed pressure. Although more factors are considered in Zhang model, the structural nonlinearity of Zhang model appears to be very complex in terms of the industrial simulation and analysis, especially for the dynamic relation among the three matrix coefficients.

2.2 Review of the Research on the Dynamic Characteristics of the Rotor Bearing System

Rotordynamics is a specialized branch of applied mechanics concerned with the behavior of rotating structures. Rotordynamics include factors such as dynamic response, vibration, strength, fatigue, stability, reliability, status monitoring, fault detection and control, etc [28~33]. The primary research objective of rotordynamics is to provide a theoretical foundation and a technical support pertaining to the design optimization, efficiency improvement, security guarantee and fault detection for rotors. Most of the academic papers regarding the research of rotordynamics concentrate on three fields, such as critical speed calculations, forced response estimation and stability analysis.

2.2.1 Critical speed calculations

The critical speed calculation of the rotor bearing system is an important issue in the research of rotordynamics. The rule of rotating machinery design requires a separation margin between the service speed and critical speed of the rotor. For example, in petroleum, chemical industry and natural gas industries, the rotor bearing system design of the centrifugal compressors and expanders adopt the standard 617 of the American Petroleum Institute (API617) [34], which is an uncontroversial technical standard for the specification for the axial and centrifugal compressors and expander compressors, and the rotor bearing system design of steam turbines adopt the standard 612 of the American Petroleum Institute (API612) [35], which is an uncontroversial technical standard for the specification for the special purposes steam turbines. The reason for creating separation margins is not

only to guarantee the stable operation of rotors under the fluctuation of the rotational speed, but also to tolerate a deviation between the predicted and the actual critical speed. Consequently the separation margin of critical speed should be corrected after the design of the rotor bearing system. If the separation margin does not meet the requirement, it will be necessary to optimize the structure of the system until it satisfies the standard.

Calculation of the critical speeds of the rotor bearing system uses both the transfer matrix method and the finite element method.

(I) Transfer matrix method

N.O.Myklestad and M.A.Prohl developed the initial parameter method for multi-disc torsional vibration into the shaft bending vibration, this extension is called the Prohl method [36]. In this method, the state vectors of cross sections of the rotor system, e.g. deflection, slope, bending moment and shear force, are transferred among the discretized nodes of the rotor system. The advantage of the Prohl method is that the matrix order does not increase as the system degree of freedom is increased, thus it fits for a chained system such as a rotor system.

However, the Prohl method is limited to rotors which are supported on isotropic bearings. In 1974, J. W. Lund [37] applied complex vectors in transfer matrices, with the consideration of system damping effects. The transfer matrix method could therefore be applied to an anisotropic rotor bearing system by solving complex characteristic values.

In 1978, G. C. Honer [38] developed the Riccati transfer matrix method. This approach transforms the two point boundary condition of the differential equation to a single point boundary condition in order to improve the numerical stability of the transfer matrix

method. In 1990, D. Kim and J. W. David [39, 40] improved the transfer matrix method and did not substitute values in the matrix multiplication. In the calculation, the matrix multiplication was transformed to the sum of several matrices and then the QR method, which is an approach to calculate the eigenvalues and eigenvectors of a matrix by a QR decomposition, writing the matrix as a product of an orthogonal matrix and an upper triangular matrix, multiply the factors in the other, and iterate, was utilized to solve the characteristic polynomial. This approach enables the whole eigenvalues to be calculated, and also prevents the problem of roots leakage.

(II) Finite element method

In 1970, the finite element method was initially introduced into rotordynamics. It is a direct variation approximation method based on the Rayleigh law [41, 42]. In the finite element method, a rotor bearing system is discretized into units such as the disk, the shaft segment and bearing, etc, which are linked at nodes. Through unit analysis, the relationship between the nodal force and the nodal displacement can be established. The motion equation of the rotor system is formed by the combination of all units. As a result, a continuous rotor system could be turned into a discretized system with finite degrees of freedom, and critical speeds could then be solved by a group of linearized algebraic equations.

Initially, the finite element method was only able to calculate the moment of inertia of the rotors. With the development of the numerical calculation method, the finite element model for the rotor system has been gradually improved. So far, the model has been extended, which include effects such as moment of inertia, gyroscopic moment, axial load, damping,

and shear deformation, etc.

2.2.2 Forced response estimation

According to the theory of rotordynamics, at a rotational speed of 3,000 r/min, the centrifugal force caused by 0.1 mm eccentricity is similar to the dead weight of the rotor [43] and can cause the undesirable vibration in rotating machinery.

Forced vibration caused by an external exciting force or torque is called force response and is a common fault of rotating machinery. In order to eliminate the effects on the rotor system, researchers have carried out an extensive research on the performance of forced response to the rotor bearing system.

Shiraki [44] utilized the approach of the modal response circular to draw a vector diagram of the vibration response in polar coordinates using the rotational speed as the reference variable. In 1988, J.Verhoeven [45] obtained the rotor imbalance response at a given speed and then applied Gaussian elimination to acquire the transformation matrix, from the imbalance response matrix to the imbalance mass matrix, to estimate the position of the imbalance on the rotor. In 1999, H.Irretier [46] introduced an imbalance factor to estimate the residual imbalance distribution on the rotor system. The imbalance factor includes the amplitude and the phase of imbalance. He also established a transformation matrix from the centrifugal force to an imbalance factor. Lyn M.Greenhill [47] noted that the rotor imbalance would have excited the reverse precession mode of a rotor supported on the bearings with an asymmetric main stiffness. After analyzing the effects of the principal stiffness, the cross stiffness and the damping of the Jeffcott rotor on such resonance

phenomena, he concluded that the more asymmetrical the principal stiffness is, the easier the resonance could be excited and that large damping could obviously inhibit the resonance. S.W.Hong [48] applied the matrix concentration method to reduce the dimension of the system matrix to obtain an imbalance response for the whole rotor system. This method greatly improves calculation speed especially for the rotor system motion equation with gyroscopic torque. Jun and Kim [49] made a precise study of the free bending vibration of a multi-step rotor using a Timoshenko beam model. The differential equation of motion for a continuous system was used and obtained solutions by applying boundary conditions. The shear force and bending moment distributions were obtained. A. C. Chasalevris and C. A. Papadopoulos [50] investigated the cross-coupled bending vibrations of a rotating shaft, with a breathing crack, mounted in resilient bearings. They found that the coupling could affect the forced response in both time and frequency domains and amplifies the higher harmonics in the vibration. In addition, the coupling due to a crack is negligible in respect to the coupling that the bearings introduce. Ehrich [51] investigated bifurcations in a high-speed rotor-bearing system and found that the rotor response was characterized by a sub-harmonic vibration phenomenon. Parkinson [52] provided an observation that the amplitude and phase of vibration response are severely affected by the location of mass unbalance, thus demanding a complex balancing scheme. Lin et al [53] have investigated the optimal weight design of rotor bearing systems. A Timoshenko rotor model with oil-lubricated support bearings was developed and it was found that the rotor weight can be significantly reduced with constraint conditions being satisfied. Aleyaasin et al [54] have used the dynamic stiffness matrix method to perform

the lateral vibration analysis of the rotor-bearing system. It was concluded that for the computation of the eigenvalues and mode shapes of the rotor-bearing system, the transfer matrix method should be chosen and for the frequency response computation, the dynamic stiffness matrix method will give results with great accuracy. Firoozian and Zhu [55] have used the transfer matrix method to study the lateral vibration of the rotor-bearing system. In their research, the transfer matrix method was modified by a combination of the transfer matrix method and the finite element method.

2.2.3 The stability analysis

Since the 1960s, it has been found that the conventional theory of the fluid lubrication has been insufficient to predict some faults in high speed rotating machines. In these instances, the shaft shows a great flexibility and the whirling motion becomes obvious. The relative eccentricity of the journal centerline might exceed 0.7~0.9, which is caused by the nonlinear oil film instabilities of the rotor bearing system. Numerous academic papers have been published in the research of the stability analysis of journal bearings.

A.C.Hagg [56], B.Sternlicht [57], J.W.Lund [58, 59] and J.Glienake [60] proposed a theory to describe dynamic characteristics of the journal bearing by using linearized coefficients such as stiffness and damping coefficients. In this theory, the hydrodynamic force is expressed by a function of the displacement and velocity around the equilibrium position. Reynolds Equation is solved to obtain the oil film pressure, which is then used to calculate the hydrodynamic fluid force. However, the condition of the weak perturbation is sometimes not satisfied, thus the linearized results might be insufficient to describe the oil

film motion. In order to reveal the mechanism of oil film instability, researchers have studied in depth the principle of the journal motion based on the research of the nonlinear rotor system differential motion equation [61~65]. The following three models are popular in nonlinear rotor bearing system research.

(I) A Jeffcott rotor supported on the rigid journal bearings

A Jeffcott rotor supported on rigid journal bearing is the most popular model in nonlinear rotor bearing system analysis because of its simplicity, although there is an obvious deviation in practical system analysis [66~68].

(II) A Jeffcott rotor supported on the elastic journal bearings

A Jeffcott rotor supported on elastic journal bearing is a multi-field coupling model in nonlinear rotor system dynamics analysis in which fluid and solid fields are involved [69, 70]. Goldman and Muszynska [71] studied the chaotic behavior of rotor/stator systems with rub-impacts. The analytical and numerical simulations show that the regular periodic vibration of the order of the synchronous, the subsynchronous and the chaos vibration are all accompanied by higher harmonics. Chu and Zhang [72] investigated the nonlinear vibration characteristics of a rub-impact Jeffcott rotor. They found that when the rotating speed is increased, the grazing bifurcation, the quasi-periodic motion and chaotic motion occur after the rub-impact. Chang-Jian and Chen [73~76] presented a series of papers on the nonlinear dynamics of rotor-bearing systems under nonlinear suspension and combined these with rub-impact effect, turbulent effect and micropolar lubricant. They found that many non-periodic responses occurred in the rotor-bearing systems. Fu et al [77] investigated the chaotic motions of a rotor system with a transverse crack by theoretical

and numerical approaches.

(III) A multi-span rotor supported on the elastic journal bearings

The coupling effects in this model between the rotor and the bearing are very complicated [78, 79], it is therefore difficult to analyse, especially for the coupling of the bending and torsional vibration as well as the coupling of the dynamic and static load distribution. Research on the elastic journal bearing still has a long way to go because the conventional dynamic theory is insufficient to depict the dynamic performance of a multi-dimensional nonlinear rotor bearing system.

2.2.4 Approaches to the analysis of the dynamic performance and stability of the rotor bearing system

Due to complex working conditions such as constraint, disturbance and load in the nonlinear rotor bearing system, there is, as yet, no unified approach. Different analysis methods are suitable for different conditions of the constraint and excitation. The common approaches are:

- Research on a weak nonlinear dynamic system, for example: the perturbation method, the Krylov-Bogoliubov method, the Krylov-Bogoliubov-Mitropolskii method, the multiple scale method, etc.
- Research on the asymptotic solution of single degree of freedom nonlinear dynamics system, for example: the generalized average method, the area average method, the Jacobi elliptic function method, the time transformation method, the parameter expansion method, the stroboscopic method, the incremental harmonic balance method,

etc.

- Research on the system with multi-degrees of freedom, for example: the improved average method, the multiple frequency perturbation approach, etc.
- Research on the response, bifurcation and chaos of nonlinear dynamic systems, for example: the average method, the multiple scale method, the generalized harmonic balance method, the least squares method, the singularity theory, the center manifold theory, the power series method, the Poincaré map, etc.

2.3 Review of the Research on Turbocharger Rotordynamics

The turbocharger rotor system is a special kind of rotor bearing system because of the following aspects. Firstly, the working speed range of an automotive turbocharger covers multiple orders of critical speeds. Therefore, rigid rotors are unsuitable for analyzing turbocharger rotor systems. Secondly, a turbocharger rotor is supported on the floating ring bearings which comprise of two fluid films in series. The inner and outer films affect each other which make the stability characteristics more complicated to study compared to a rotor supported on journal bearings with a single fluid film. Thirdly, turbocharger rotordynamics is a multi-field coupling topic which involves thermodynamics, fluid mechanics, rotordynamics, etc. For example, the stability of a rotor system might be affected by the high temperature from the exhaust gas and local temperature increases due to the mechanical power dissipated in the bearing. In addition, the exhaust pulse might also affect the bending and torsional vibration of the rotor system. To date, a significant amount of research on turbocharger rotor systems has been carried out.

Tatara [80] stated that as soon as whirl appears in the inner film, the ring begins to spin and the bearing could stabilize the rotor system. Tanaka and Hori [81] developed a dynamics model for a flexible rotor supported on floating ring bearings based on the infinitely short bearing theory. They then estimated the stable speed under different bearing parameters. By comparison of predicted and experimental results acquired by Hill [82], Dworski [83] and Tondl [84], it was demonstrated that the frequency of the oil film whirl was approximately one half of the sum of the shaft speed and the ring speed under medium pressure. Rohde and Ezzat [85] reported that floating ring bearings have the potential to reduce power loss of the automotive engine. Tatara [80] and Tanaka [87] carried out linear stability analysis of the floating ring rotor bearing system. It was found that unstable speed shows sensitivity to the outer bearing clearance and the thinner of the outer bearings clearance is, the wider speed range covered. Trippett and Dennis [86] concluded that oil film whirl and whip is caused by shear effects between the inner and outer fluid films and will eventually reach a stable limit cycle. Howard [88, 89] discussed the possibility of replacing oil film bearings with air bearings in a diesel truck turbocharger. Walton et al [90] developed a miniature test rig of a rotor system to simulate a turbocharger rotor system in the aero-engine which is supported on air bearings. The predicted results show good agreement with the experimental results in natural frequency, rotor displacement and the load capability of the thrust bearing. Aretakis et al [91] discussed the possibility of detecting the instabilities in the turbocharger rotor system by vibration and noise signals of the compressor impeller. By signal features extraction, a bi-parametric criterion was established for determination of whether the compressor of the turbocharger operates in the

stable stage. Chen et al [92] developed a model for a turbocharger turbine under pulsating inlet conditions. The one-dimensional unsteady flow method was applied to study the behavior of the turbine under the steady and the unsteady flow conditions. This model showed an improved prediction at off-design condition. Kreuz-Ihli et al [93] utilized a commercial Navier-stokes solver to study the vibration of radial inflow turbines under the unsteady flow and then validated the model by experimental data collected from a Laser-Doppler velocimeter. Peat et al [94] presented a model for the passive acoustic behavior of a turbine impeller of an automotive turbocharger. Based on the knowledge of the rotor vibration, the effects of the primary noises, such as the gas pulsation and the exhaust tailpipe orifice, on the behavior of the turbine was studied. Payri [95, 96] published a series of papers focusing on the investigation of the transient performance of turbocharged diesel engines and developed an action model for calculating the transient operation.

2.4 Review of the Research of the Nonlinearity of the Vibration System

The objective of the research on the nonlinearity of the vibration system is to reveal the discipline of the system motion under various parameters and initial conditions based on the mathematical model of the nonlinear vibration system. The stability and bifurcation analysis play key roles in the theoretical research of the system nonlinearity.

The stability analysis addresses the stability of trajectories of dynamical systems under small perturbations of initial conditions [97]. It studies the relationship among the topological properties of the trajectories of a cluster of similar systems. The bifurcation

analysis reveals the interrelation and transformation of the system states. The system parameters in the mathematical models of practical systems, such as differential equations, difference equations, integral equations and etc, might be affected by the working conditions. It is required to understand the impacts of the change of system parameters on the system performance. Bifurcation analysis has a greatly theoretical significance and practical value in the research of the nonlinear vibration system.

The approaches of the bifurcation analysis include the theoretical approach and numerical approach. Due to the limitation of the theoretical approach, the most popular way to study the bifurcation and stability of the nonlinear vibration system is the numerical approach. C. Padmanabhan and R. Singh [98] utilized the algorithm of the parameter extension to investigate the dynamic characteristics of a nonlinear, non-autonomous system. They found the subsynchronous motion, chaotic motion and the parameter range of the jumping phenomenon occurred. For the bifurcation analysis of a non-conservative, nonlinear system with large degrees of freedom, P. Sundamrarajan and S. T. Noah [99] adopted the modal synthesis method to separate the linear and nonlinear vectors. The shooting method was used to solve the system periodic solution and then the system stability and bifurcation is justified by the Floquet theory. L. Cherfils [100] developed an efficient algorithm of parameter extension for a large-scale nonlinear system, in which an adapted meshing approach and parallel calculation were introduced to improve the calculation efficiency. Blair et al [101] stated a novel algorithm combining the harmonic balance method and the continuation method, by which a series of periodic solution of the modified Holmes-Duffing Equation was derived. This approach can also be introduced into the

solution of strongly nonlinear systems. The key step of this approach is the Newton-Raphson iteration that requires the derivation of the Jacobi matrix. Hu [102] presented a curve fitting method to simulate the system periodic motion by the transient response without the calculation of the Jacobi matrix. Chen and Zheng [103, 104] defined the stability of the periodic solution of a nonlinear, non-autonomous system and then developed a numerical calculation approach to the stability of the periodic solution of the transient response. Lust, Roose et al [105] developed the Newton-Picard algorithm, in which the feature space of the single valued matrix of the periodic motion is separated into a stable subspace and an unstable subspace. In the stable subspace, Picard iteration is carried out and in the unstable subspace, Newton iteration is conducted. Obviously this algorithm is more efficient compared to the Newton-Raphson algorithm and the continuation-shooting algorithm. Van Noorden et al [106] introduced the Newton-Picard algorithm in the calculation of the cyclic chemical reaction. The high efficiency of this algorithm was demonstrated by the comparison with the directly numerical integration method, the Newton-Raphson algorithm and the Broyden quasi-Newton algorithm. Tiesinga et al [107] investigated the bifurcation of the incompressible fluid from the stable state to the quasi-periodic state within the range of the Reynolds number between 7500 and 10000. The influences of the Reynolds number of the fluid on the Hopf bifurcation were concluded.

2.5 Review of the Research of the Modal Synthesis Method

With the research of the stability in depth, the system with less degree of freedom is

insufficient to model the practical system. It is, therefore, necessary to carry out the research on the high dimensional system. As far as a high dimensional system is concerned, it is generally required to conduct the dimensionality reduction. The modal synthesis method is an efficient approach that has been widely applied in the study of the high dimensional system.

In 1960, Hurty [108] initially presented the fixed-interface modal synthesis method and in 1964, Gladwell [109] clearly clarified the idea of decomposition for a system. Since then, a variety of modal synthesis methods have been developed, most of which are based on the orthogonal modes of the subsystems. According to the boundary conditions of the subsystems, the modal synthesis method can be classified into the fixed-interface modal synthesis method, the free-interface modal synthesis method, the mixed-interface synthesis method and the loaded-interface modal synthesis method.

Tran [110, 111], Meirovitch [112], Craig [113~115] et al carried out respectively the review of study on the modal synthesis method. Kuhar and Stahle [116] stated that the free and fixed interface modal synthesis methods are equivalent to the dynamic coordinate transformation method with stiffness and inertial connection respectively. Kubomura [117-119] derived the formula of the free and fixed interface modal synthesis methods using the data of the 1st and 2nd order modes. Curnier [120] obtained the formula of the free, the fixed and the loaded interface modal synthesis methods and proved the accuracy under no modal truncation. Eagels [121] developed an approach to improve the precision of the modal vectors in the presence of the attachment modes of the subsystem. By the eigen analysis of heterogeneous and homogeneous finite element models of a high speed civil

transport, Farhatt and Geradin [122] proved that the fixed-interface modal synthesis method can be derived by the impedance equation. Thonon et al [123] utilized the modal expansion to establish the admittance equation of the free-interface modal synthesis method. Ohayon et al [124] extended the free and the fixed interface modal synthesis methods into the damping system and then developed an approach of the subsystems coupling by the singular value decomposition of the constraint matrix.

In the modal synthesis methods, subsystems are generally coupled by displacements of the points in the interface. In order to reduce the interface coordinates and the dimension of the coupled system, Bourquin [125, 126] developed the Poincaré-Steklov approach that is suitable for the fixed-interface modal synthesis method. Other common approaches include the GUYAN method, the SEREP method, the IRS method, etc [127].

2.6 Review of the Numerical Integration Approaches

The numerical calculation approach has developed rapidly since the 1950s. With the popularization of computers, many direct numerical integration methods have been developed, such as the Euler method, the Runge-Kutta method, the Adams linear multistep method, etc [128, 129]. With the aid of computers and related mathematical software, numerical approaches have been used to solve many ordinary differential equations of initial value cases in research and in practical applications.

Problems associated with the dynamics of mechanical systems can be expressed as the second order ordinary differential equations. The primary approaches for the solution of differential equations include direct numerical integration methods and the state space

method [130]. Direct integration methods include: the central difference method, the Houbolt method, the Wilson method, the Newmark method, etc. The state space method transforms the original equations into a group of the first order differential equations and then the reduced differential equations can be solved by the Taylor expansion method, the Runge-kutta method, the Adams multistep method or the shooting method [131, 132].

2.7 Summary

In this chapter, a comprehensive literature review with regard to the current research is carried out. Publications associated with the research on the fluid lubrication are initially reviewed. Both linear and nonlinear hydrodynamic force models are compared and studied, which provide a foundation of the investigation of the lubrication of the floating ring bearing. Literature associated with the research of rotordynamics and turbocharger rotordynamics are reviewed. The nonlinearity of the vibration system is introduced because the nonlinear behaviors of the rotor system are involved in the research. Modal synthesis method and numerical integration approach, as the popular methods in the analysis of rotor system behaviors, are also introduced.

CHAPTER THREE

ANALYTICAL INVESTIGATION OF THE LUBRICATION OF FLOATING RING BEARINGS

A turbocharger adopts floating ring bearings to support its rotor system. Floating ring bearings significantly affect the dynamic performance of turbochargers. In this chapter, the lubrication of floating ring bearings has been investigated analytically. Based on the simulation results, the influences of working conditions on the oil film pressure and the oil flow rate have been studied.

3.1 Introduction to the Lubrication of Floating Ring Bearings

Compared to a conventional journal bearing with single film, the lubrication procedure for a floating ring bearing is more complex. Lubricant is fed into the outer oil film from a fixed supply hole on the bearing shell, while the inner clearance is lubricated through a number of holes evenly distributed on the ring. Lubrication can be affected by working circumstances, such as the oil inlet pressure, external loads, the service speed, etc. An unreasonable design or operation can cause serious faults in the bearing or even the whole system. It is, therefore, worthwhile to investigate the floating ring bearing lubrication and to understand the effects of such working conditions on the lubrication procedure.

In this chapter, the infinitely long bearing theory is adopted to solve the steady state Reynolds Equation. Both oil inlet pressure and the starting and ending positions of the cavitation area are considered as the boundary conditions in order to obtain the analytical expressions of the pressure distribution of the outer and inner oil films in the floating ring bearing. The inner oil film lubrication model is developed according to the relationship between the oil flow rate and the pressure difference of a tube. Following model development, the effects of external loads and inlet pressure on the equilibrium positions of the journal and ring have been studied based on simulation results. The disciplines of inner oil film lubrication have been analyzed and the impacts of external loads and inlet pressure on the oil flow rate into the inner oil film have also been investigated.

Nomenclature

P_o	Pressure distribution in outer film (Pa)	θ_o	Circumferential coordinate starting from the line across the centers of the ring and bearing shell (Degree)
P_i	Pressure distribution in inner film (Pa)		
Ω_J	Rotational speed of the journal (rad/s)	θ_i	Circumferential coordinate starting from the line across the centers of the journal and ring (Degree)
Ω_R	Rotational speed of the ring (rad/s)		
η	Lubricant viscosity (Pa s)		
R_J	Radius of the journal (m)	θ_{start_o}	Starting position of outer film (Degree)
R_{Ro}	Outer radius of the ring (m)		
R_{Ri}	Inner radius of the ring (m)	θ_{start_i}	Starting position of inner oil film (Degree)
C_o	Outer clearance (m)		
C_i	Inner clearance (m)	θ_{end_o}	End position of outer oil film (Degree)
h_o	Outer oil film thickness (m)		
h_i	Inner oil film thickness (m)	θ_{end_i}	End position of inner oil film (Degree)
ε_o	Outer eccentricity ratio		
ε_i	Inner eccentricity ratio	Ψ	Coordinate starting from Y axis (Degree)
L	Length of the bearing (m)		

F_{X_o}	Outer fluid force in X direction (N)	f_{ε_o}	Radial component of outer fluid force (N)
F_{X_i}	Inner fluid force in X direction (N)	f_{ε_i}	Radial component of inner fluid force (N)
F_{Y_o}	Outer fluid force in Y direction (N)	f_{ϕ_o}	Tangential component of outer fluid force (N)
F_{Y_i}	Inner fluid force in Y direction (N)	f_{ϕ_i}	Tangential component of inner fluid force (N)
ρ	Density (kg/m ³)	P_{diff}	Pressure difference (Pa)
S	Friction coefficient	g	Gravitation constant (m/s ²)
T	Length of the tube (m)	m_R	Mass of the ring (kg)

3.2 Theoretical modeling for the lubrication of a floating ring bearing

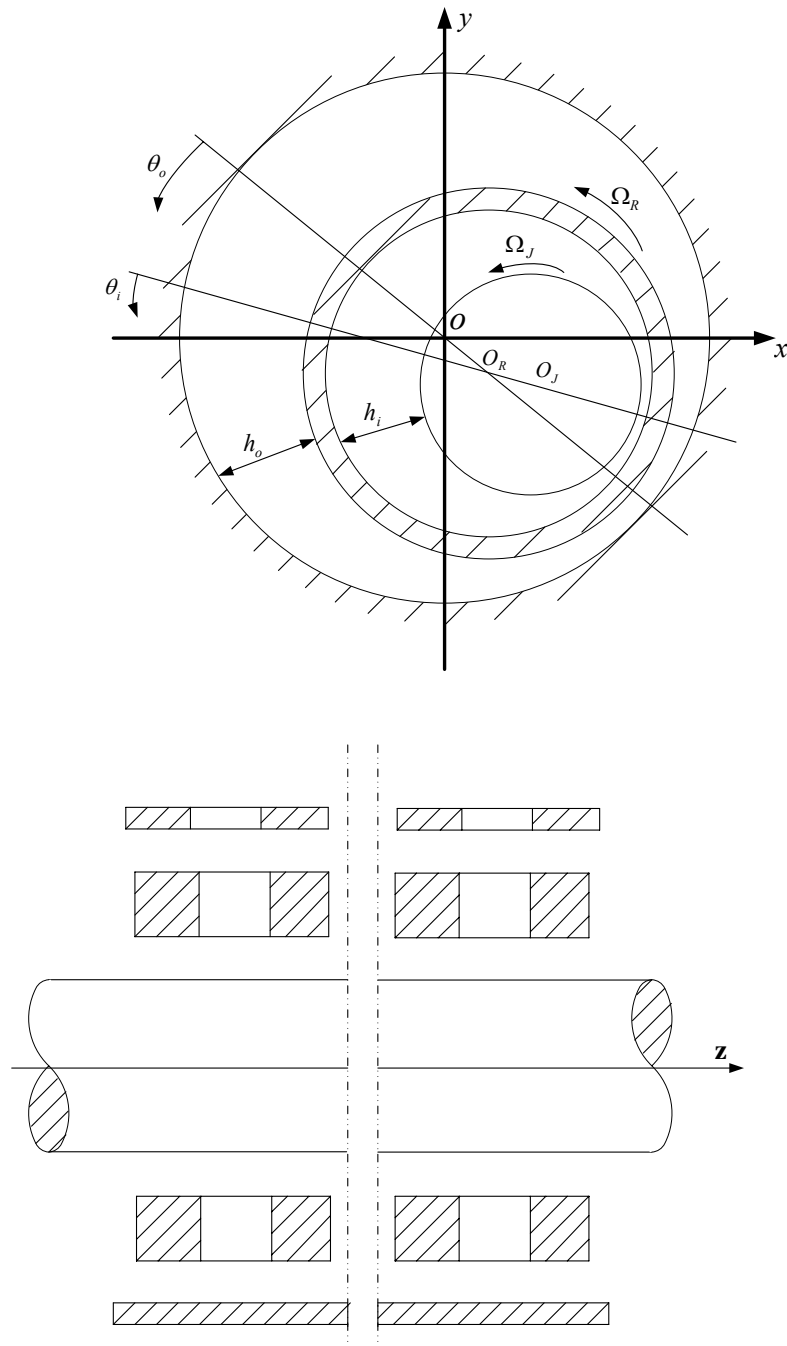


Figure 3. 1. Coordinate system of the floating ring bearing

Figure 3.1 illustrates the structure and the coordinate system of the floating ring bearing.

When the shaft spins, the ring will rotate as a result of the shear-driven torques. Double oil films will be formed in the inner and outer clearances respectively. Pressure distribution of both of oil films in the steady state can be described by the Reynolds Equations. In order to investigate oil film pressure in circumferential direction and the oil film rate from outer to inner clearances of the floating ring bearing, the pressure gradient in the axial direction will be ignored and the length of the bearing is assumed to be infinite in the solution of the oil film pressure distribution. As such, a simplified form of the Reynolds Equation in the steady state is given by Equations (3.1) and (3.2).

$$\frac{\partial}{\partial \theta_o} \left(\frac{h_o^3 \partial P_o}{\partial \theta_o} \right) = 6\eta \Omega_R R_{Ro}^2 \frac{\partial h_o}{\partial \theta_o} \quad (3.1)$$

$$\frac{\partial}{\partial \theta_i} \left(\frac{h_i^3 \partial P_i}{\partial \theta_i} \right) = 6\eta \left(\Omega_J + \frac{R_{Ri}}{R_J} \Omega_R \right) R_J \frac{\partial h_i}{\partial \theta_i} \quad (3.2)$$

where the oil film thickness h_o, h_i is given by

$$h_o = C_o (1 + \varepsilon_o \cos \theta_o) \quad (3.3)$$

$$h_i = C_i (1 + \varepsilon_i \cos \theta_i) \quad (3.4)$$

with the boundary conditions

$$P_o = P_{inlet} \quad , \quad \text{at } \Psi = 0 \quad (3.5)$$

$$P_{i,o} = 0 \quad , \quad \text{at } \theta_{start_i,o} \quad (3.6)$$

$$P_{i,o} = 0 \quad , \quad \text{at } \theta_{end_i,o} \quad (3.7)$$

$$\frac{\partial P_{i,o}}{\partial \theta_{i,o}} = 0 \quad , \quad \text{at } \theta_{end_i,o} \quad (3.8)$$

By substituting the above boundary conditions into equations (3.1) and (3.2), we get

$$\frac{\partial P_o}{\partial \theta_o} = 6\eta \Omega_R C_o^{-2} R_{Ro}^2 \varepsilon_o \left[\frac{\cos \theta_o}{(1 + \varepsilon_o \cos \theta_o)^3} - \frac{\cos \theta_{end_o}}{(1 + \varepsilon_o \cos \theta_o)^3} \right] \quad (3.9)$$

$$\frac{\partial P_i}{\partial \theta_i} = 6\eta \left(\Omega_J + \frac{R_{Ri}}{R_J} \Omega_R \right) C_i^{-2} R_J^2 \varepsilon_i \left[\frac{\cos \theta_i}{(1 + \varepsilon_i \cos \theta_i)^3} - \frac{\cos \theta_{end_i}}{(1 + \varepsilon_i \cos \theta_i)^3} \right] \quad (3.10)$$

Integrate (3.9) and (3.10) with respect to θ_o, θ_i respectively.

$$P_o = 6\eta \Omega_R C_o^{-2} R_{Ro}^2 \varepsilon_o \left[\int \frac{\cos \theta_o}{(1 + \varepsilon_o \cos \theta_o)^3} d\theta_o - \cos \theta_{end_o} \int \frac{1}{(1 + \varepsilon_o \cos \theta_o)^3} d\theta_o + C_{-o} \right] \quad (3.11)$$

$$P_i = 6\eta \left(\Omega_J + \frac{R_{Ri}}{R_J} \Omega_R \right) C_i^{-2} R_J^2 \varepsilon_i \left[\int \frac{\cos \theta_i}{(1 + \varepsilon_i \cos \theta_i)^3} d\theta_i - \cos \theta_{end_i} \int \frac{1}{(1 + \varepsilon_i \cos \theta_i)^3} d\theta_i + C_{-i} \right] \quad (3.12)$$

where C_{-o}, C_{-i} are integration constants.

Introducing the Sommerfeld substitution (3.13) [10], the solution form of the integrals in (3.11) and (3.12) can be derived by (3.14) and (3.15).

$$1 + \varepsilon \cos \theta = \frac{1 - \varepsilon^2}{1 - \varepsilon \cos \varphi} \quad (3.13)$$

$$\int \frac{\cos \theta}{(1 + \varepsilon \cos \theta)^3} d\theta = \frac{-3\varepsilon\varphi + 2(1 + \varepsilon^2)\sin \varphi - \varepsilon \sin \varphi \cos \varphi}{2(1 - \varepsilon^2)^{2.5}} \quad (3.14)$$

$$\int \frac{1}{(1 + \varepsilon \cos \theta)^3} d\theta = \frac{1}{(1 - \varepsilon^2)^{2.5}} \left(\varphi + \frac{\varepsilon^2}{2} \varphi - 2\varepsilon \sin \varphi + \frac{\varepsilon^2 \sin 2\varphi}{4} \right) \quad (3.15)$$

By substituting (3.13), (3.14), (3.15) and the boundary condition (3.5) into (3.11) and (3.12), the pressure distribution in outer and inner films can be derived as follows.

$$P_o = P_{inlet} + 3\eta \Omega_R R_{Ro}^2 C_o^{-2} \varepsilon_o (1 - \varepsilon_o^2)^{-1.5} / (1 - \varepsilon_o \cos \varphi_{end_o}) \left[2(\sin \varphi_o - \sin \varphi_{inlet_o})(1 + \varepsilon_o \cos \varphi_{end_o}) + (2 \cos \varphi_{end_o} + \varepsilon_o)(\varphi_{inlet_o} - \varphi_o) - \varepsilon_o (\sin \varphi_o \cos \varphi_o - \sin \varphi_{inlet_o} \cos \varphi_{inlet_o}) \right] \quad (3.16)$$

$$P_i = 6\eta \left(\Omega_J + \frac{R_{Ri}}{R_J} \Omega_R \right) R_J^2 C_i^{-2} (1 - \varepsilon_i^2)^{-1.5} \left[\frac{\varphi_i - \varepsilon_i \sin \varphi_i - \frac{\varepsilon_i^2}{2} \varphi_i - 2\varepsilon_i \sin \varphi_i + \frac{\varepsilon_i^2 \sin 2\varphi_i}{4}}{1 - \varepsilon_i \cos \varphi_{end_i}} \right] \quad (3.17)$$

$\varphi_{start_i,o}$, $\varphi_{end_i,o}$, φ_{inlet} should be within the range of $\pi < \varphi_{end_i,o} \leq \varphi_{inlet} + 2\pi$ and $\varphi_{end_i,o} < \varphi_{start_i,o} \leq \varphi_{inlet}$. It is noted that φ correspond to θ , and their relationship is expressed by the Sommerfeld substitution.

Hydrodynamic fluid forces in two films can be obtained by integrating the pressure distribution within the continuous oil film field, i.e. $\varphi_{start_i,o} < \varphi_{i,o} \leq \varphi_{end_i,o}$.

$$f_{\varepsilon_o} = -3\eta \Omega_R L R_{Ro}^3 C_o^{-2} \frac{\varepsilon_o (\cos \varphi_{end_o} - \cos \varphi_{start_o})^2}{(1 - \varepsilon_o^2)(1 - \varepsilon_o \cos \varphi_{end_o})} \quad (3.18)$$

$$f_{\phi_o} = 3\eta \Omega_R L R_{Ro}^3 C_o^{-2} \varepsilon_o (1 - \varepsilon_o^2)^{-1.5} (1 - \varepsilon_o \cos \varphi_{end_o})^{-1} \left[\begin{aligned} & (1 + 2\varepsilon_o \cos \varphi_{end_o}) (\varphi_{end_o} - \varphi_{start_o}) \\ & - 2(\varepsilon_o + \cos \varphi_{end_o}) (\sin \varphi_{end_o} - \sin \varphi_{start_o}) \\ & + (\sin \varphi_{end_o} \cos \varphi_{end_o} - \sin \varphi_{start_o} \cos \varphi_{start_o}) \end{aligned} \right] \quad (3.19)$$

$$f_{\varepsilon_i} = -3\eta \left(\Omega_J + \frac{R_{Ri}}{R_J} \Omega_R \right) L R_J^3 C_i^{-2} \frac{\varepsilon_i (1 - \cos \varphi_{end_i})^2}{(1 - \varepsilon_i^2)(1 - \varepsilon_i \cos \varphi_{end_i})} \quad (3.20)$$

$$f_{\phi_i} = 6\eta \left(\Omega_J + \frac{R_{Ri}}{R_J} \Omega_R \right) L R_J^3 C_i^{-2} (1 - \varepsilon_i^2)^{-0.5} (1 - \varepsilon_i \cos \varphi_{end_i})^{-1} (\sin \varphi_{end_i} - \varphi_{end_i} \cos \varphi_{end_i}) \quad (3.21)$$

Through the equilibrium position, the hydrodynamic fluid forces in X and Y directions are expressed in Equation (3.22) and (3.23).

$$F_{X_i,o} = f_{\varepsilon_i,o} \sin \phi_{i,o} + f_{\phi_i,o} \cos \phi_{i,o} \quad (3.22)$$

$$F_{Y_i,o} = -f_{\varepsilon_i,o} \cos \phi_{i,o} + f_{\phi_i,o} \sin \phi_{i,o} \quad (3.23)$$

Because in the equilibrium position, the force vectors exerted on the journal and the ring are supposed to be balanced, they should be solved iteratively.

The oil flow rate inside the supply holes distributed on the ring mainly depends upon the pressure difference on both sides of each hole [133], which is expressed in equation (3.24).

$$Q = \left(\frac{P_{diff}}{\rho g S T} \right)^{0.5} \quad (3.24)$$

The rotational speed ratio between the ring and the journal is assumed to keep constant in this thesis, ignoring the thermal effects of the mechanical power dissipated on the floating ring bearing. The empirical formula [134] is given in equation (3.25).

$$\frac{\Omega_R}{\Omega_J} = \frac{1}{1 + R_{Ro}^3 / R_J^3 C_i / C_o} \quad (3.25)$$

3.3 Simulation results and analysis

Table 3. 1. Simulation Parameters

Parameter	Value
Length of the bearing (L)	10mm
Outer clearance (C_o)	80 μ m
Inner clearance (C_i)	20 μ m
Radius of the journal (R_J)	5mm
Outer radius of the ring (R_{Ro})	7mm
Inner radius of the ring (R_{Ri})	$R_J + C_i$
Mass of the ring (m_R)	0.02kg
Lubricant viscosity (η)	0.012PaS
Lubricant density (ρ)	9.2×10^3 kg/m ³
Friction coefficient (S)	0.015

3.3.1 The equilibrium position

Whirling phenomena in floating ring bearing has not been considered in this thesis. Both the journal and the ring rotate at their respective equilibrium positions because the external load and hydrodynamic fluid forces balance each other. In this section, the influences of external load and lubricant feed pressure on the equilibrium positions of the journal and ring have been studied by means of simulation.

It should be noted that the outer equilibrium position denotes the relative position of the ring to the bearing shell and the inner equilibrium position denotes the relative position of the journal to the ring. The direction of the external load is considered to keep vertically downward.

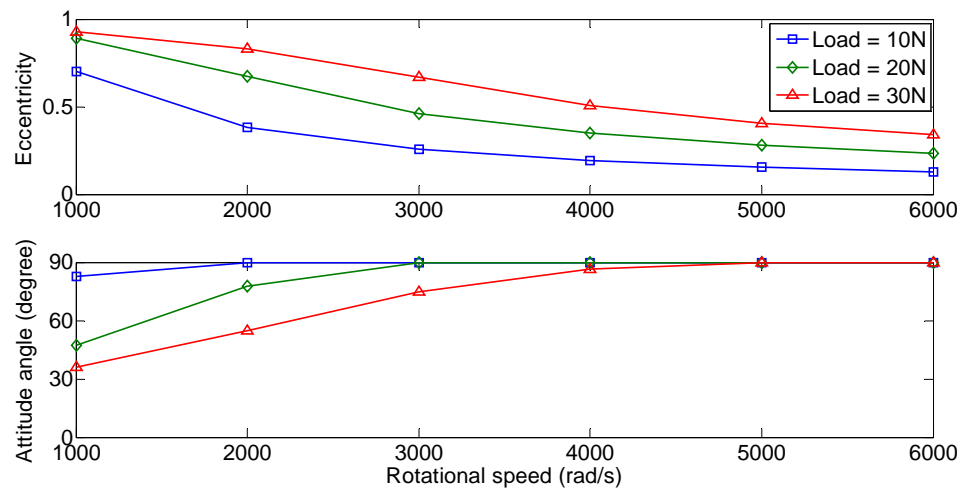


Figure 3. 2. Outer equilibrium positions under different external loads

Figure 3.2 shows the outer equilibrium positions, i.e. eccentricity and attitude angle (the deviation from the vertical of the line which connects the centre of the bearing from the centre of the ring), under different external loads exerted on the shaft within a journal

speed range of 1000 to 6000rad/s. A similar trend can be observed under different external loads in which the outer eccentricities decrease as the speed of the journal increases while the attitude angle becomes close to 90° . As a higher external load is exerted on the journal, the ring will rotate at a larger eccentricity to generate enough hydrodynamic fluid forces to support the load.

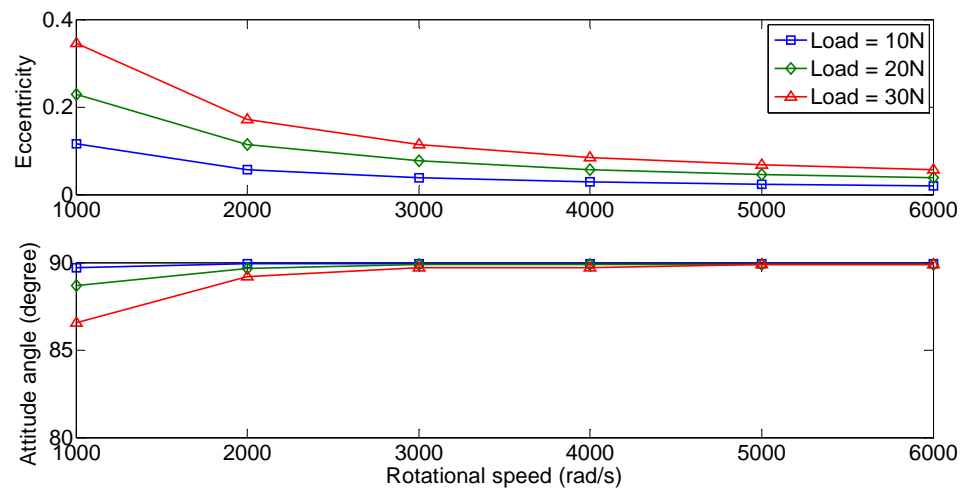


Figure 3. 3. Inner equilibrium positions under different external loads

Figure 3.3 shows inner equilibrium positions, i.e. eccentricity and attitude angle (the deviation from the vertical of the line which connects the centre of the ring from the centre of the shaft), under different external loads exerted on the shaft. Compared to outer equilibrium position, impact of the external load on the inner equilibrium position is much weaker. The journal appears to be rotating at a small eccentricity within a wide range except for 1000rad/s, at which speed, inner equilibrium position deviates the centre of the bearing obviously with 0.12, 0.23 and 0.35 inner eccentricities and 90° , 89° , 87° attitude angles under 10N, 20N and 30N external loads.

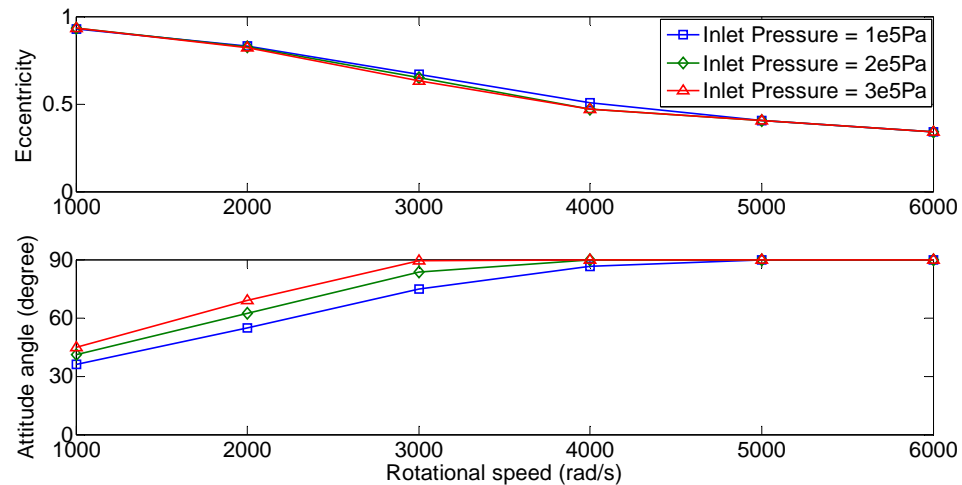


Figure 3. 4. Outer equilibrium positions under different lubricant inlet pressure

Figure 3.4 reveals the outer equilibrium positions under different lubricant feed pressures. It can be seen that the influence of the lubricant inlet pressure is mainly reflected in the attitude angles. The higher the feed pressure provided, the lower the journal speed that the attitude angles reach 90° .

The influence of lubricant feed pressure on the pressure distribution of the inner film has not been considered. As a result, the inner eccentricities will not be changed under different supply pressure.

3.3.2 Oil film continuity

Inside the bearing clearance, the oil film is generally not continuous but with the cavitation area where the oil film cannot bear the external load. The influences of the external load and the lubricant feed pressure on oil film continuity are discussed in this section.

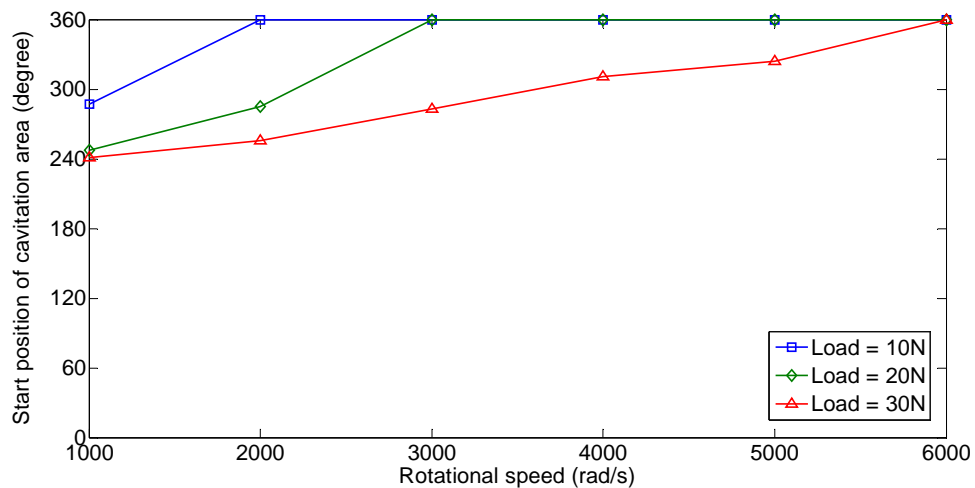


Figure 3. 5. The start positions of the cavitation area in outer oil film under 10N, 20N and 30N external loads within 6000rad/s of the journal speed

Figure 3.5 shows the starting positions of the cavitation area in the outer oil film under different external loads. Under light loads, such as 10N and 20N, the cavitation area will not appear until the journal speed is below 2000rad/s and 3000rad/s, whereas under a high load, such as 30N, the cavitation area exists in the whole speed range of 1000 to 6000rad/s. This is because the ring rotates at a larger outer eccentricity when a higher external load is exerted.

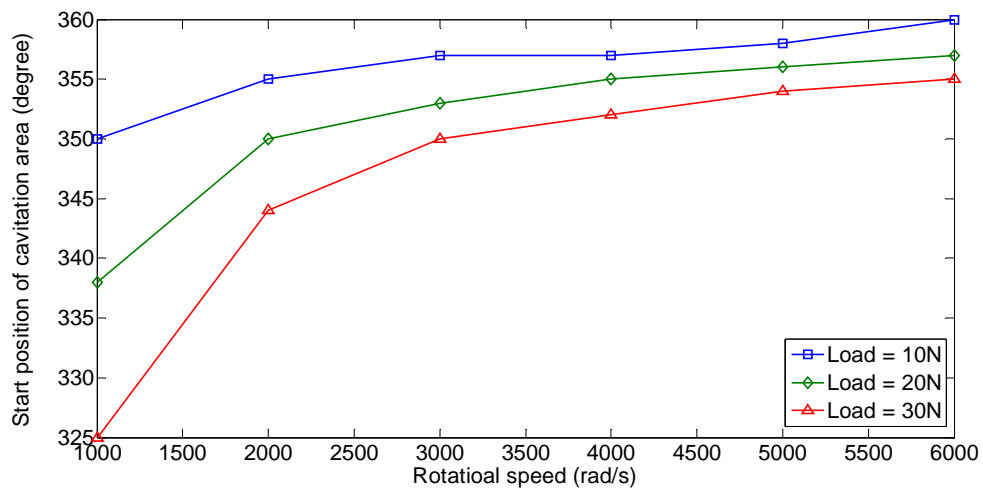


Figure 3. 6. The start positions of the cavitation area in the inner oil film under 10N, 20N and 30N external loads within 6000rad/s of the journal speed

A similar situation can be observed for the starting positions of the cavitation area in the inner oil film, as shown in Figure 3.6. Moreover, the cavitation area exists within the whole 6000rad/s speed range, despite such an area being much less than that in the outer oil film.

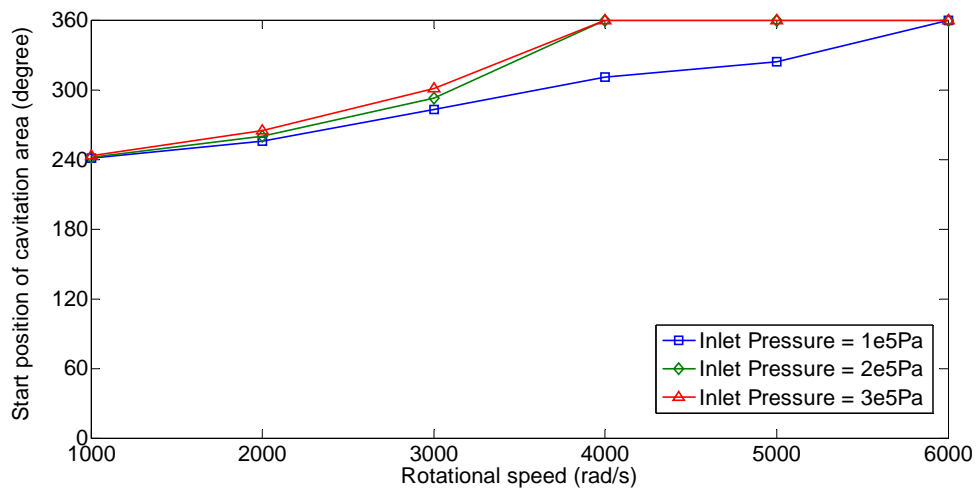


Figure 3. 7. The start positions of the cavitation area in the outer oil film under different lubricant inlet pressure

Figure 3.7 shows the starting position of the cavitation area in the outer oil film under

different lubricant inlet pressures. It clearly shows that by increasing inlet pressure, at a relatively low speed, the cavitation phenomenon could be avoided. On the other hand, the cavitation area appears at the same position at 1000rad/s even under different supply pressures. The effect of the lubricant feed pressure is mainly reflected in the speed range between 3000rad/s and 6000rad/s journal speed.

3.3.3 Inner oil film lubrication

The inner clearance of the floating ring bearing is lubricated through the holes evenly distributed on the ring. As a result, the oil flow rate depends on the pressure difference on both sides of the supply hole. When the pressure in the outer film is higher than that of the inner film, lubricant is supplied to the inner clearance, otherwise the lubricant would flow out from the inner oil film.

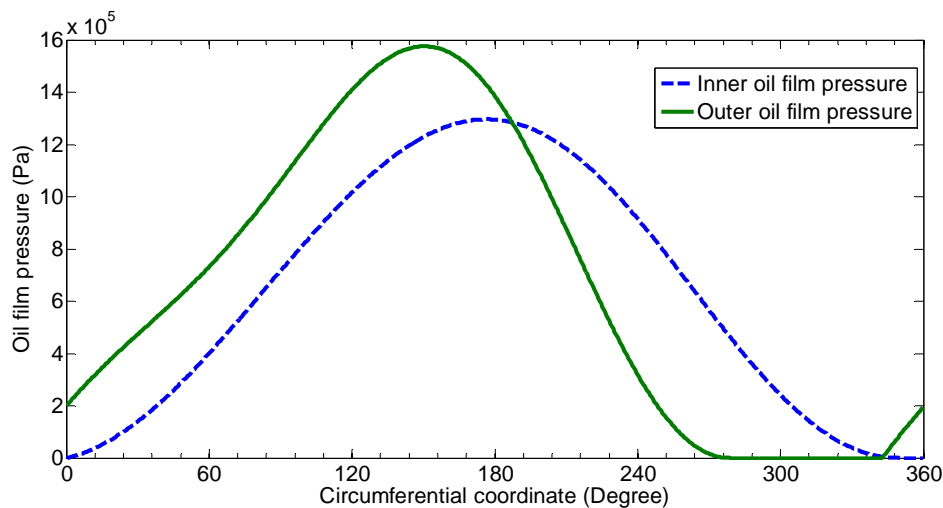


Figure 3. 8. Circumferential pressure distribution in the outer and inner oil films at a journal speed of 3000rad/s under 2×10^5 Pa lubricant feed pressure

Figure 3.8 shows the circumferential pressure distribution in the outer and inner oil films.

On the top of the bearing shell, i.e. 0° , where lubricant supply hole locates, the oil film pressure in the outer film is the same as the inlet pressure. Ruptures occur at 280° of the outer oil film where oil film pressure becomes zero. At the position near the supply hole, the oil film resumes to be continuous in the outer clearance. For the inner oil film, the inner eccentricity is very small as a result of the thinner clearance and the higher rotational speed. As a result, the cavitation phenomenon is almost non existent in the inner oil film. Compared to the inner oil film, the peak value of the outer oil film pressure is higher because a higher load is supported by the outer oil film.

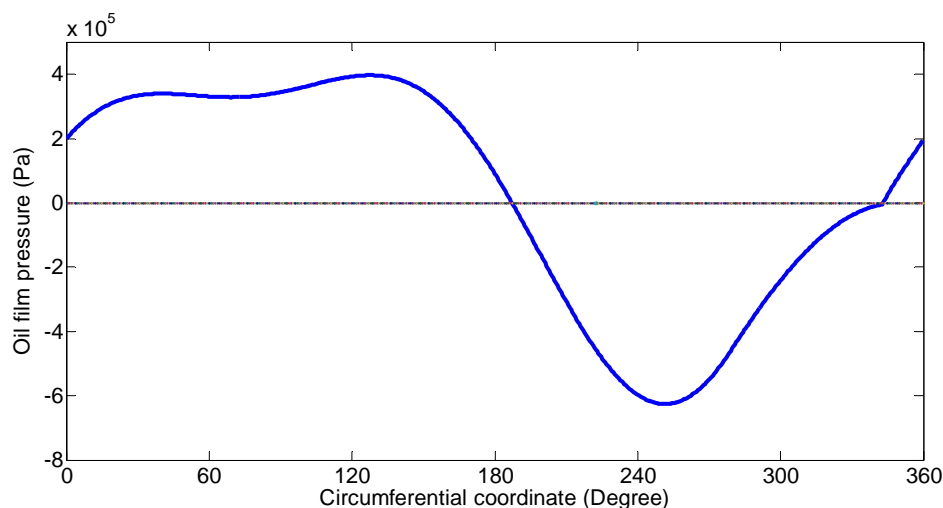


Figure 3. 9. The pressure difference between the outer and inner oil film in the circumferential direction

Figure 3.9 reveals the pressure difference between the outer and inner oil film in the circumferential direction. Positive pressure difference values are shown from the position of the lubricant supply hole to 187° . In this area, the outer oil film pressure is higher than that of the inner oil film and the lubricant is supplied into the inner oil film. Between 187° and 343° , the pressure difference appears as negative values which demonstrate the

lubricant flow out from the inner oil film. Lubricant is re-supplied into the inner oil film after 343° because of the lubricant supply.

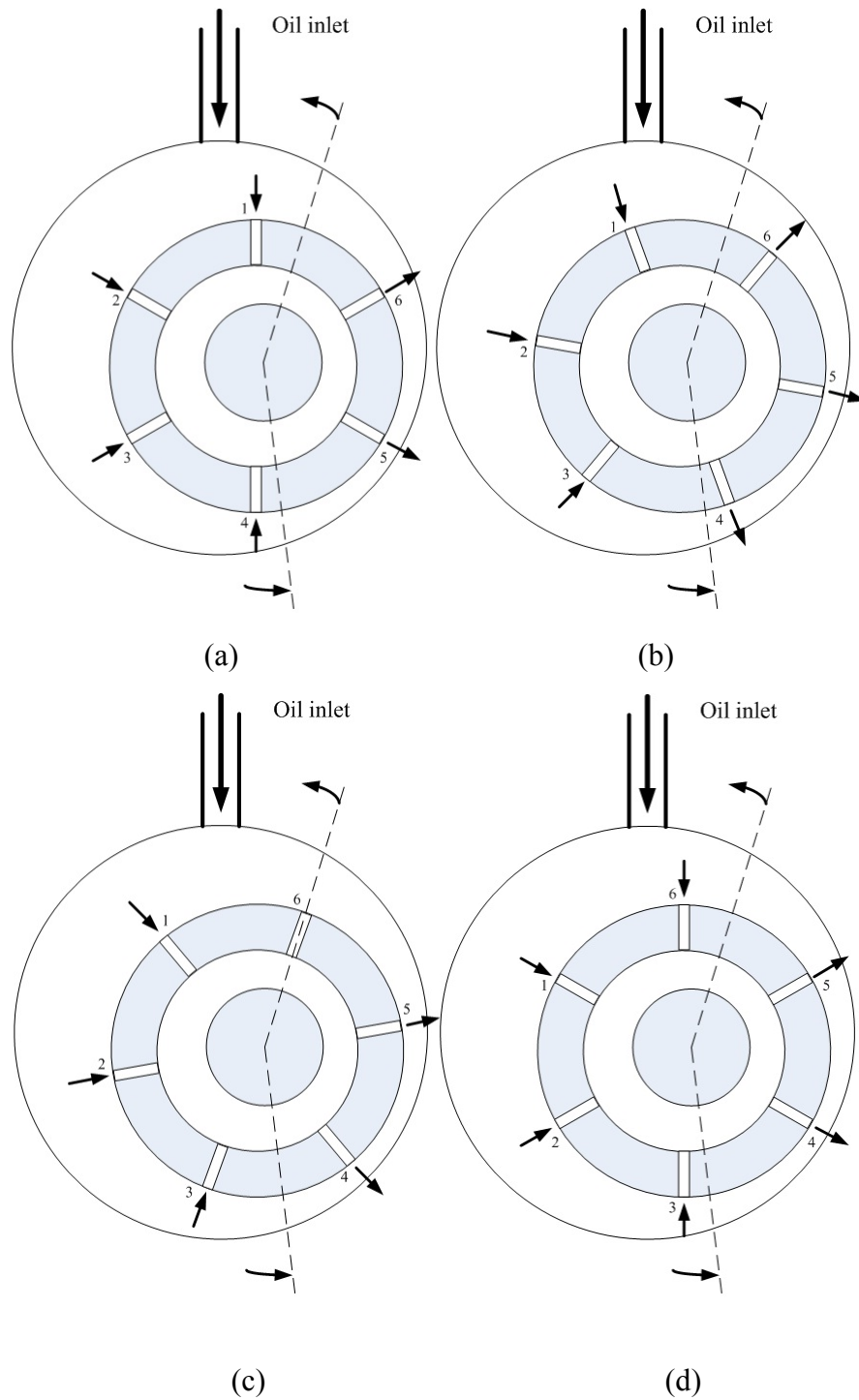


Figure 3. 10. Inner oil film lubrication as the ring spins: (a) 0° (b) 20° (c) 40° (d) 60°

Figure 3.10 illustrates the inner oil film lubrication as the ring spins in a counterclockwise direction. In this case, there are six holes evenly distributed on the ring. The two dash lines represent the boundary between the positive and negative pressure difference areas. On the left hand side of the boundary, the outer oil film pressure is higher than that of the inner oil film. On the right hand side of the boundary, the outer oil film pressure is lower than that of the inner oil film. Figure 3.10(a) shows the case that the 1st hole is on the top. The first four holes, 1st to 4th, are located in the positive pressure difference area where the lubricant flow is supplied into the inner oil film and at the 5th and 6th holes, the lubricant flow out. As the ring spins 20°, as shown in Figure 3.10(b), the 4th hole enters the negative pressure difference area and the lubricant flow the out inner oil film through the 4th, 5th and 6th holes. As the ring spins 20° further, as shown in Figure 3.10(c), the 6th hole reaches the boundary. Theoretically no pressure difference exists between the two sides of the hole and there is no lubricant flowing through this hole. Figure 3.10(d) shows the case as the ring spins 60°. The same situation can be seen in Figure 3.10(a).

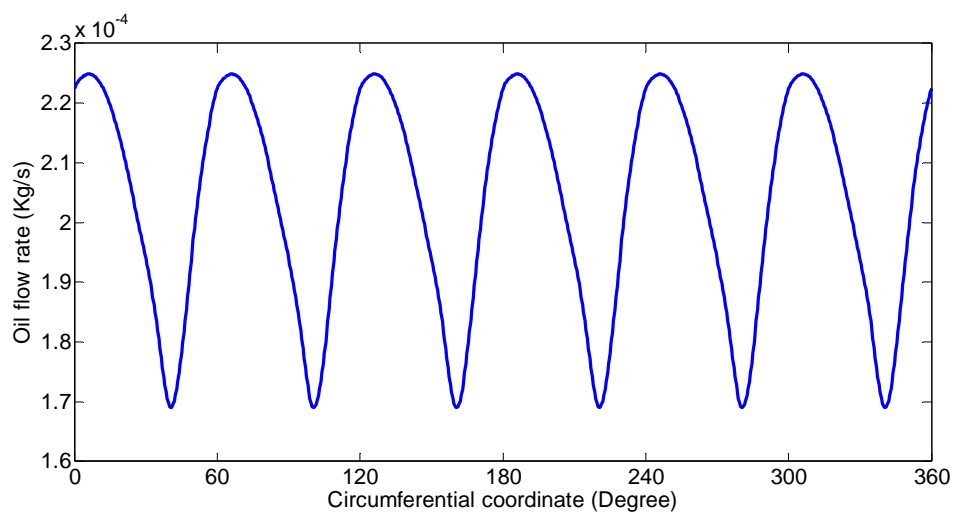
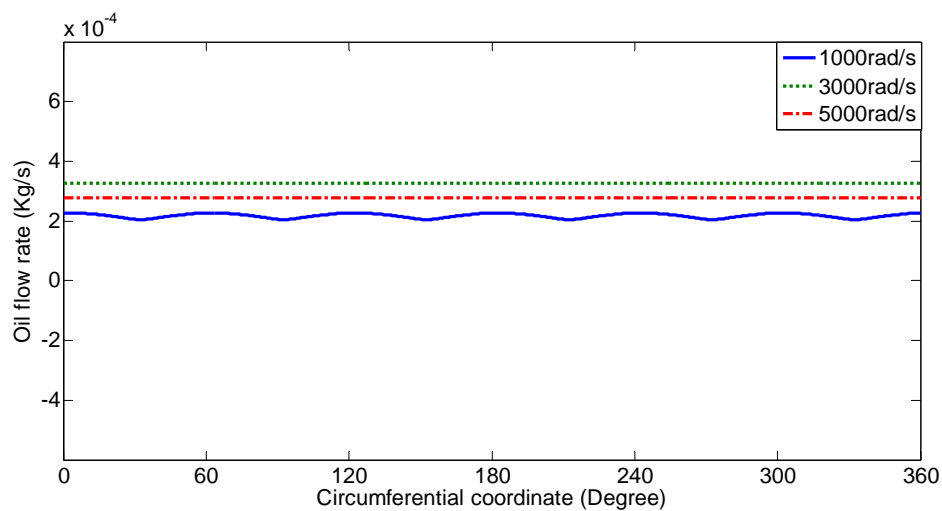


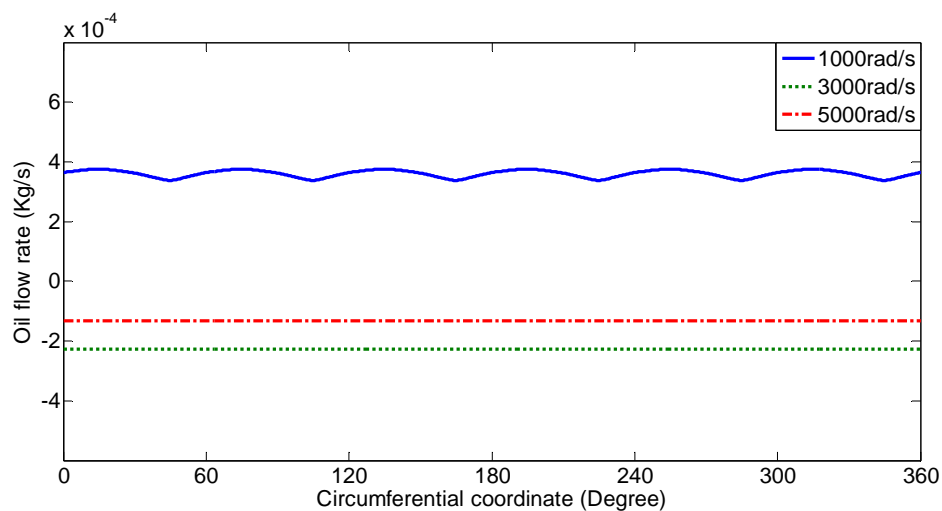
Figure 3. 11. The oil flow rate supplied to the inner oil film in one revolution of the ring

Figure 3.11 shows the oil flow rate supplied into the inner oil film. We see that the oil flow rate shows a periodic change each 60° due to the six holes evenly distributed on the ring. In each cycle, the maximum oil flow rate emerges at the position of 15° . As the ring spins further, the oil flow rate declines until 40° , where the oil flow rate reaches the bottom and then increases again until the end of the cycle.

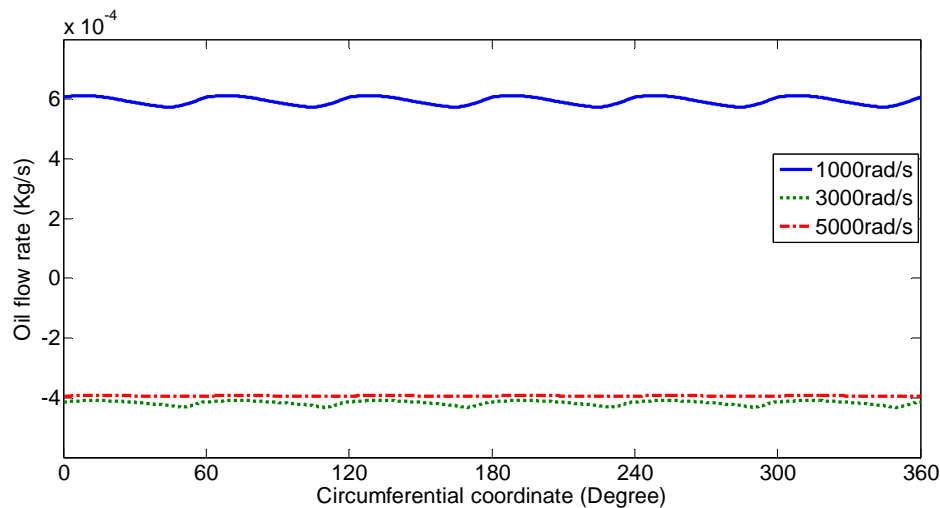
3.3.4 Effects of external load on the oil flow rate into the inner oil film



(a)



(b)



(c)

Figure 3. 12. The oil flow rate into the inner oil film in one revolution of the ring at journal speeds of 1000rad/s, 3000rad/s and 5000rad/s under 10N, 20N and 30N external loads:

(a)10N load (b)20N load (c)30N load

Figure 3.12 shows the oil flow rates into the inner oil film in each revolution of the ring at journal speeds of 1000rad/s, 3000rad/s and 5000rad/s under different external loads. The inlet pressure is assumed to be 10^5 Pa in this section. When a 10N load is exerted on the shaft, as is shown in Figure 3.12(a), the oil flow rate is at its lowest at 1000rad/s which fluctuates around 2.1kg/s. As the journal speed is increased to 3000rad/s, the outer eccentricity becomes smaller and the cavitation area shrinks, meaning that more lubricant could be fed into the inner oil film. However, as the journal speed is increased further, to 5000rad/s, the oil flow rate drops compared to 3000rad/s. This is because the rising speed of the rotors enhances the oil film pressure in the inner and outer clearances and reduces the pressure difference between the two films. As a result, it becomes difficult for lubricant to be supplied into the inner oil film. Under 20N and 30N external loads exerted on the

shaft, as is shown in Figure 3.12(b) and (c), the negative oil flow rate can be seen at 3000 rad/s and 5000rad/s, which will cause a lubricant starvation. This phenomenon leads to the oil film thickness reducing, meaning that the oil film is unable to bear the same load as usual. On the other hand, the fluctuation of the oil flow rate at a higher speed is not as obvious as that of a lower one. This demonstrates that high speed rotation of the ring could weaken the influences of the holes' position on the inner oil film lubrication.

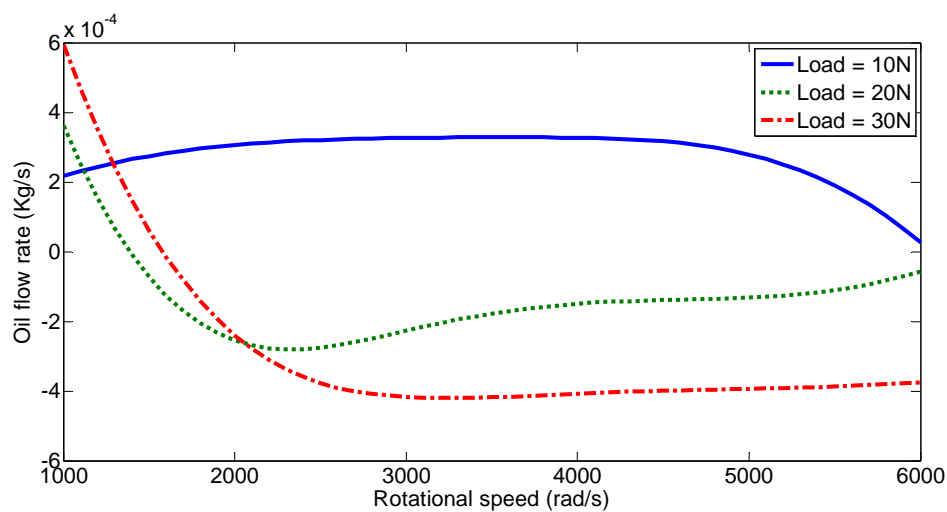
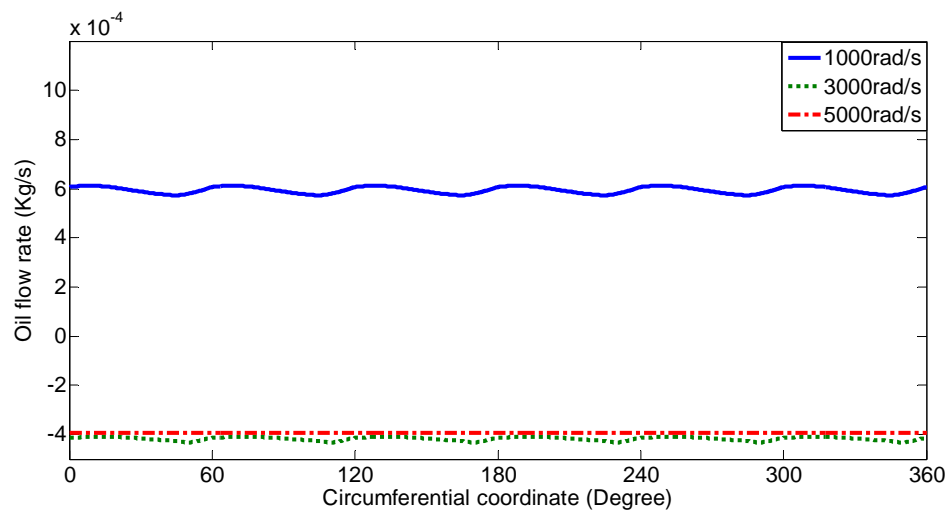


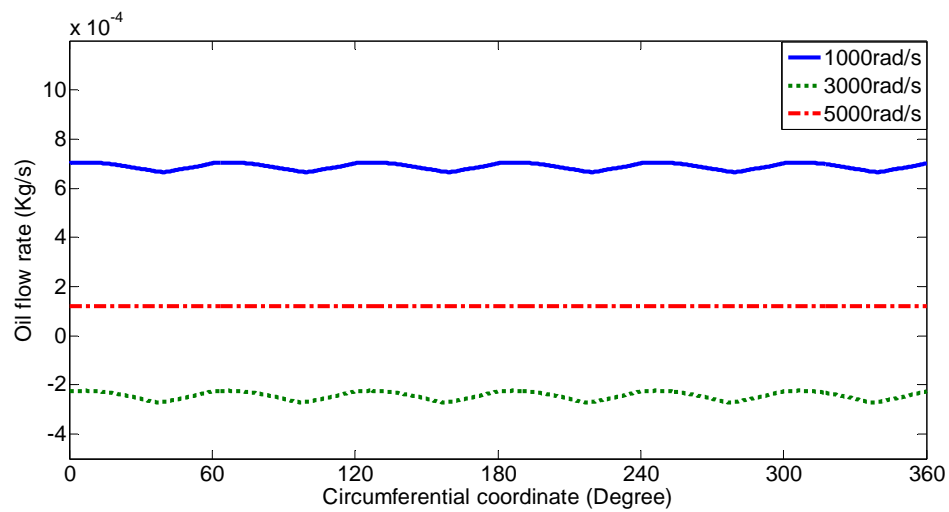
Figure 3. 13. The mean oil flow rate into inner the oil film under different external loads

Figure 3.13 shows the effects of the external load on the mean oil flow rate into the inner oil film within 6000rad/s of the journal speed. Under 10N external load, the oil flow rate keeps positive values within the whole speed range except for a slight drop at a speed higher than 5000rad/s. A similar trend can be seen between the oil flow rates under 20N and 30N loads. At the lower speed range, the oil flow rates show positive values but decline dramatically as the journal speed increases. At about 1500rad/s, the starved lubrication will occur and will last for a wide range of speeds. This phenomenon could be alleviated as the journal speed is increased.

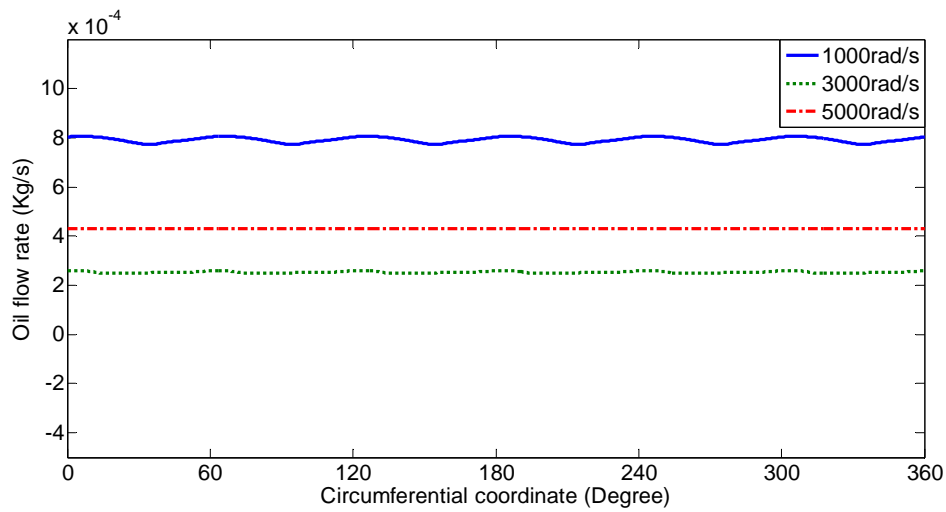
3.3.5 Effects of inlet pressure on the oil flow rate into the inner oil film



(a)



(b)



(c)

Figure 3. 14. The oil flow rate into the inner oil film in a revolution of the ring at journal speeds of 1000rad/s, 3000rad/s and 5000rad/s under 10^5 Pa, 2×10^5 Pa and 3×10^5 Pa inlet pressure: (a) 10^5 Pa (b) 2×10^5 Pa (c) 3×10^5 Pa

Figure 3.14 shows the oil flow rate into the inner oil film in each revolution of the ring at the journal speed of 1000rad/s, 3000rad/s and 5000rad/s under different inlet pressure. The external load is assumed to be 30N in this simulation. Under 10^5 Pa inlet pressure, as shown in Figure 3.14(a), the oil flow rate is 6×10^{-4} kg/s at 1000rad/s. The starved lubrication occurs at 3000rad/s and 5000rad/s journal speeds. By increasing the inlet pressure to 2×10^5 Pa, as is shown in Figure 3.14(b), the starved lubrication is eliminated at a journal speed of 5000rad/s. This phenomenon still occurs at 3000rad/s but it has been alleviated compared to the case of 10^5 Pa inlet pressure. By increasing the inlet pressure further to 3×10^5 Pa, as is shown in Figure 3.14(c), the starved lubrication disappears for all three speeds. On the other hand, the fluctuation of the oil flow rate becomes slightly as the inlet pressure is increased. This shows that a higher inlet pressure can reduce the influences

of ring rotation on inner oil film lubrication.

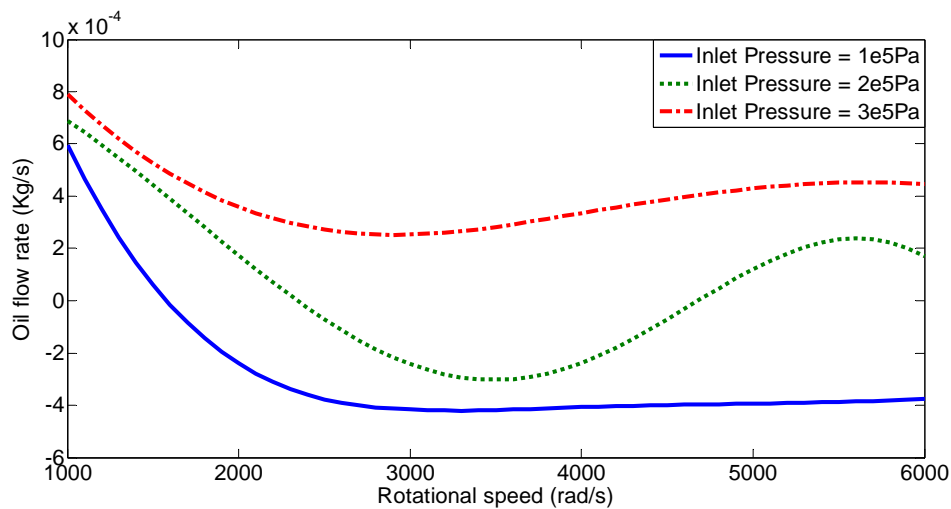


Figure 3. 15. The mean oil flow rate into the inner oil film under

10^5 Pa, 2×10^5 Pa and 3×10^5 Pa inlet pressure

Figure 3.15 reveals the effects of inlet pressure on the mean oil flow rate into the inner oil film within the range of 0 to 6000rad/s of journal speed. With a relative lower speed range, the mean flow rates decline sharply from 6×10^{-4} kg/s, 7×10^{-4} kg/s and 8×10^{-4} kg/s under 10^5 Pa, 2×10^5 Pa and 3×10^5 Pa inlet pressure. When the journal speed exceeds 3000rad/s, the mean oil flow rate into the inner oil film increases especially under higher inlet pressures such as 2×10^5 Pa and 3×10^5 Pa. We can observe that the starved lubrication occurs in a wide speed range higher than 1500rad/s under 10^5 Pa inlet pressure. Under 2×10^5 Pa inlet pressure, the starved lubrication occurs only within the speed range of 2300rad/s and 4500rad/s journal speeds, and this phenomenon disappears completely within the whole speed range of 6000rad/s journal speed under 3×10^5 Pa inlet pressure. We can conclude that enhancing the inlet pressure can effectively improve the inner oil film lubrication, and that the starved lubrication can be completely eliminated when the inlet

pressure is high enough.

3.4 Summary

In this chapter, the steady state Reynolds Equations regarding two oil films of the floating ring bearing have been derived based on the infinitely long bearing theory. Analytical expressions of oil film pressure distribution have been obtained in which oil inlet pressure and cavitation situation have been taken into account.

Under different external loads and oil inlet pressure, the equilibrium positions of journal and ring along with the cavitation areas of two oil films have been simulated. It is found that heavy external loads could result in large outer eccentricity but the influence to inner eccentricity is not obvious which is reflected only within the lower speed range. Oil inlet pressure mainly affects the outer attitude range. On the other hand, external load could extend cavitation areas in both outer and inner oil films, which could be shrinking at high speed while increasing oil inlet pressure.

Inner oil film lubrication procedure has been studied and the effects of external loads and oil inlet pressure on oil flow rate into the inner oil film have been investigated. It is found that heavier external load could reduce oil flow rate into the inner oil film within a wide speed range even might lead to inner film oil starvation, although the flow rate is initially larger at low speed. On the other hand, increasing oil inlet pressure could improve effectively the inner oil film lubrication.

CHAPTER FOUR

THEORETICAL MODELLING FOR A TURBOCHARGER ROTOR SYSTEM

The rotor system plays a key role in a turbocharger which determines whether the turbocharger will work normally or not. In addition, the dynamic characteristics of the bearing can also affect the rotor motion to a large degree. Most of the faults associated with turbochargers are related to their rotor bearing systems. In this chapter, a theoretical model has been developed for the turbocharger rotor bearing system using the Finite Element method in order to investigate the dynamic performance of the turbocharger rotor system.

Nomenclature of Section 4.1

m_d	Mass of the disk (kg)	θ_{yB}	Rotation angle of B end of shaft segment in y direction (rad)
J_d	Diameter moment of inertia of the disk (kgm^2)	s	Coordinate in shaft segment (m)
J_p	Polar moment of inertia of the disk (kgm^2)	l_s	Length of shaft segment (m)
x_d	Displacement of the disk in x direction (m)	r_s	Radius of shaft segment (m)
y_d	Displacement of the disk in y direction (m)	μ_s	Mass of the unit length (kg/m)
θ_x	Rotation angle in x direction (rad)	J_{ds}	Diameter moment of inertial of the unit length (kgm^2/m)
θ_y	Rotation angle in y direction (rad)	J_{ps}	Polar moment of inertial of the unit length (kgm^2/m)
T_d	Kinetic energy (J)	T_s	Kinetic energy of shaft segment (J)
x_A	Displacement of A end of shaft segment in x direction (m)	V_s	Potential energy of shaft segment (J)
y_A	Displacement of A end of shaft segment in y direction (m)	EI	Flexural rigidity (N/m^2)
x_B	Displacement of B end of shaft segment in x direction (m)	c_{xx}	Damping coefficients (Ns/m)
		c_{xy}	
		c_{yx}	
		c_{yy}	
		k_{xx}	Stiffness coefficients (N/m)
		k_{xy}	
		k_{yx}	

y_B	Displacement of B end of shaft segment in y direction (m)	k_{yy}			
θ_{xA}	Rotation angle of A end of shaft segment in x direction (rad)		x_{sj}	Displacement of the journal in x direction (m)	
θ_{yA}	Rotation angle of A end of shaft segment in y direction (rad)		y_{sj}	Displacement of the journal in y direction (m)	
θ_{xB}	Rotation angle of B end of shaft segment in x direction (rad)				

Nomenclature of Section 4.2

$m_{1...6}$	Mass of the nodes (kg)	$[M]$	System mass matrix
$k_{1...5}$	Stiffness coefficients of shaft segments (N/m)	$[M_R]$	Mass matrix of the ring
$c_{1...5}$	Damping coefficients of shaft segments (Ns/m)	$[K]$	System stiffness matrix
$x_{1...6}$	Displacement of the nodes in x direction (m)	$[C]$	System damping matrix
$y_{1...6}$	Displacement of the nodes in y direction (m)	$\{U\}$	System displacement vector
Ω	Rotational speed (rad/s)	$\{U_R\}$	Displacement vector of the ring
e_ξ	Eccentricities in the rotating	$\{W\}$	System dead weight

e_η	coordinate system	$\{W_R\}$	Dead weight of the ring
m_{imb}	Imbalance mass (kg)	$\{F_u\}$	Imbalance centrifugal force
F_{x_imb}	Imbalance centrifugal force in x direction (N)	$\{P\}$	Lubricant feed pressure
F_{y_imb}	Imbalance centrifugal force in y direction (N)	$\{Fh_{inner}\}$	Inner oil film force
		$\{Fh_{outer}\}$	Outer oil film force

Nomenclature of Section 4.3

Fh_x	Oil film force in x direction (N)	R_o	Outer radius of the ring (m)
Fh_y	Oil film force in y direction (N)	R_i	Inner radius of the ring (m)
Fh_{xo}	Original oil film force in x direction (N)	R_J	Radius of the journal (m)
Fh_{yo}	Original oil film force in y direction (N)	C_o	Outer bearing clearance (m)
Δx	Micro displacement in x direction (m)	C_i	Inner bearing clearance (m)
Δy	Micro displacement in y direction (m)	L	Bearing length (m)
$\Delta \dot{x}$	Micro velocity in x direction (m/s)	Ω_R	Rotational speed of the ring (rad/s)
$\Delta \dot{y}$	Micro velocity in y direction (m/s)	x_i	Dimensionless displacement of the

			journal in x direction
ϕ	Attitude angle (degree)	y_i	Dimensionless displacement of the journal in y direction
θ	Circumferential coordinate (degree)	x_R	Dimensionless displacement of the ring in x direction
μ	Lubricant viscosity (PaS)	y_R	Dimensionless displacement of the ring in y direction
P_o	Pressure distribution of outer oil film (Pa)	h_o	Dimensionless thickness of outer oil film
P_i	Pressure distribution of inner oil film (Pa)	h_i	Dimensionless thickness of inner oil film
X	Journal displacement in x direction (m)	τ_o	Dimensionless time
Y	Journal displacement in y direction (m)	τ_i	
X_R	Ring displacement in x direction (m)	p_o	Dimensionless outer oil film pressure
Y_R	Ring displacement in y direction (m)	p_i	Dimensionless inner oil film pressure
Z	Axial coordinate system (m)		

Nomenclature of Section 4.4

F_{imp}	Impact force (N)	ζ	Displacement of the rotor (m)
F_{rub}	Rub force (N)	f	Friction coefficient
kr	Radial stiffness (N/m)		

A turbocharger is a rotating machine of high speed and light load. The rotational speed can easily reach 140,000r/min or higher. Whether the turbocharger is able to work safely at such high speeds largely depends upon its dynamic performance. In this chapter, a dynamic model has been developed for the turbocharger rotor system using the theory of finite element method to provide a foundation for modal analysis, critical speeds calculation, bending vibration and stability analysis.

4.1 Finite Element Analysis of the Rotor System

4.1.1 Finite element method

As the rotor system is usually comprised of impellers, shaft segments with distributed mass and elasticity, bearings, etc, it can be discretized into a number of units, such as the disk, the shaft segment and the bearing along the axial direction. Through the unit analysis, the relationship between the nodal force and nodal displacement can be established. The rotor system motion equation is formed by combining all units. As a consequence, it is possible to transfer a continuous rotor system into a system with multiple degrees of freedom. The critical speeds and force response of the system can then be obtained by solving a group of linear equations.

4.1.2 Motion equations of the unit

(I) Rigid disk unit

Assuming the mass, diameter moment of inertia and polar moment of inertia of a rigid disk unit to be m, J_d, J_p respectively, the unit displacement vector is expressed by:

$$\{u_{1d}\} = [x, \theta_y]^T \quad \text{and} \quad \{u_{2d}\} = [y, -\theta_x]^T.$$

The kinetic energy of a rigid disk unit is given by:

$$T_d = \frac{1}{2} \{\dot{u}_{1d}\}^T [M_d] \{\dot{u}_{1d}\} + \frac{1}{2} \{\dot{u}_{2d}\}^T [M_d] \{\dot{u}_{2d}\} + \Omega \{\dot{u}_{1d}\}^T [J] \{\dot{u}_{2d}\} + \frac{1}{2} J_p \Omega^2 \quad (4.1)$$

$$\text{where } [M_d] = \begin{bmatrix} m_d & 0 \\ 0 & J_d \end{bmatrix}, \quad [J] = \begin{bmatrix} 0 & 0 \\ 0 & J_p \end{bmatrix}$$

Using the Langrange equation [135], the motion differential equation of a rigid disk unit can be expressed by

$$\begin{aligned} [M_d] \{\ddot{u}_{1d}\} + \Omega [J] \{\dot{u}_{2d}\} &= \{Q_{1d}\} \\ [M_d] \{\ddot{u}_{2d}\} - \Omega [J] \{\dot{u}_{1d}\} &= \{Q_{2d}\} \end{aligned} \quad (4.2)$$

where $[M_d]$, $\Omega [J]$ are the mass matrix and the gyroscopic matrix of the unit, and $\{Q_{1d}\}$, $\{Q_{2d}\}$ are the corresponding generalized forces.

(II) Shaft segment unit

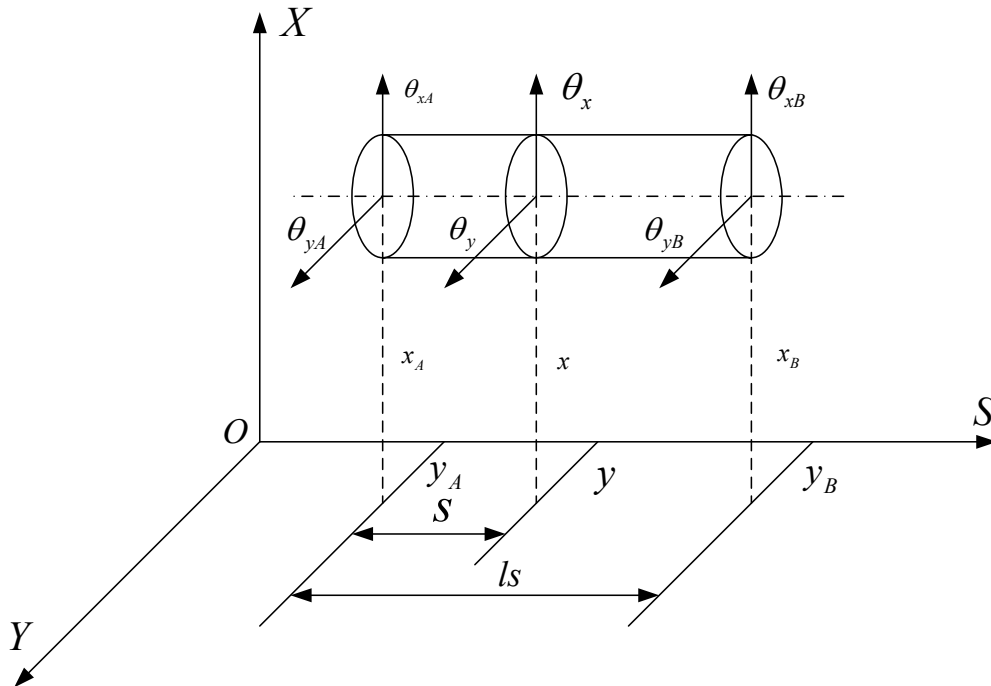


Figure 4. 1. An elastic shaft segment unit in Finite Element analysis

Figure 4.1 shows an elastic shaft segment unit. Nodal displacements on both ends of the unit are expressed by $\{u_{1s}\} = [x_A \quad \theta_{yA} \quad x_B \quad \theta_{yB}]^T$ and $\{u_{2s}\} = [y_A \quad -\theta_{xA} \quad y_B \quad -\theta_{xB}]^T$. According to the theory of the beam unit, the interpolation function of the displacement matrix is expressed by:

$$[N] = [N_1(s) \quad N_2(s) \quad N_3(s) \quad N_4(s)] \quad (4.3)$$

where $N_1(s) = 1 - 3\left(\frac{s}{l_s}\right)^2 + 2\left(\frac{s}{l_s}\right)^3$

$$N_2(s) = l_s \left[\frac{s}{l_s} - 2\left(\frac{s}{l_s}\right)^2 + \left(\frac{s}{l_s}\right)^3 \right]$$

$$N_3(s) = 3\left(\frac{s}{l_s}\right)^2 - 2\left(\frac{s}{l_s}\right)^3$$

$$N_4(s) = l_s \left[-\left(\frac{s}{l_s}\right)^2 + \left(\frac{s}{l_s}\right)^3 \right]$$

For a circular cross-section of a shaft segment with length l and radius r , with μ, j_d, j_p denoting mass, diameter moment of inertia and polar moment of inertia of the unit length of the shaft segment. The kinetic energy T_s and potential energy V_s of the unit are expressed by:

$$\begin{aligned} T_s = & \frac{1}{2} \{\dot{u}_{1s}\}^T ([M_{sT}] + [M_{sR}]) \{\dot{u}_{1s}\} + \frac{1}{2} \{\dot{u}_{2s}\}^T ([M_{sT}] + [M_{sR}]) \{\dot{u}_{2s}\} + \Omega \{\dot{u}_{1s}\}^T [J_s] \{\dot{u}_{2s}\} \\ & + \frac{1}{2} j_{ps} l_s \Omega^2 \end{aligned} \quad (4.4)$$

$$V_s = \frac{1}{2} \{u_{1s}\}^T [K_s] \{u_{1s}\} + \frac{1}{2} \{u_{2s}\}^T [K_s] \{u_{2s}\} \quad (4.5)$$

Where $[M_{sT}], [M_{sR}], \Omega[J_s], [K_s]$ denote the translational inertia matrix, rotational inertia matrix, gyroscopic matrix and stiffness matrix of the unit respectively, and are represented as follows:

$$[M_{sT}] = \int_0^{l_s} \mu [N]^T [N] ds = \frac{\mu l_s}{420} \begin{bmatrix} 156 & 22l_s & 54 & -13l_s \\ 22l_s & 4l_s^2 & 13l_s & -3l_s^2 \\ 54 & 13l_s & 156 & -22l_s \\ -13l_s & -3l_s^2 & -22l_s & 4l_s^2 \end{bmatrix} \quad (4.6)$$

$$[M_{sR}] = \int_0^{l_s} j_{ds} [N']^T [N'] ds = \frac{\mu r_s^2}{120l_s} \begin{bmatrix} 36 & 3l_s & -36 & 3l_s \\ 3l_s & 4l_s^2 & -3l_s & -l_s^2 \\ -36 & -3l_s & 36 & -3l_s \\ 3l_s & -l_s^2 & -3l_s & 4l_s^2 \end{bmatrix} \quad (4.7)$$

$$[J_s] = \int_0^{l_s} j_{ps} [N']^T [N'] ds = \frac{\mu r_s^2}{60l_s} \begin{bmatrix} 36 & 3l_s & -36 & 3l_s \\ 3l_s & 4l_s^2 & -3l_s & -l_s^2 \\ -36 & -3l_s & 36 & -3l_s \\ 3l_s & -l_s^2 & -3l_s & 4l_s^2 \end{bmatrix} \quad (4.8)$$

$$[K_s] = \int_0^{l_s} EI [N'']^T [N''] ds = \frac{EI}{l_s^3} \begin{bmatrix} 12 & 6l_s & -12 & 6l_s \\ 6l_s & 4l_s^2 & -6l_s & 2l_s^2 \\ -12 & -6l_s & 12 & -6l_s \\ 6l_s & 2l_s^2 & -6l_s & 4l_s^2 \end{bmatrix} \quad (4.9)$$

Using the Lagrange equation, the motion differential equation of the shaft segment unit is expressed by

$$\begin{aligned} [M_s] \{\ddot{u}_{1s}\} + \Omega [J_s] \{\dot{u}_{2s}\} + [K_s] \{u_{1s}\} &= \{Q_{1s}\} \\ [M_s] \{\ddot{u}_{2s}\} - \Omega [J_s] \{\dot{u}_{1s}\} + [K_s] \{u_{2s}\} &= \{Q_{2s}\} \end{aligned} \quad (4.10)$$

where the mass matrix $[M_s] = [M_{sT}] + [M_{sR}]$ and $\{Q_{1s}\}, \{Q_{2s}\}$ are generalized force vectors.

(III) The bearing unit

Ignoring the influence of the bearing bases, the effects of the bearing on the rotor system are determined only by the hydrodynamic forces. If the hydrodynamic fluid force is linearized, it can be expressed by a polynomial of stiffness and damping coefficients, given by:

$$\begin{Bmatrix} Q_{1d} \\ Q_{2d} \end{Bmatrix} = - \begin{bmatrix} c_{xx} & c_{xy} \\ c_{yx} & c_{yy} \end{bmatrix} \begin{Bmatrix} \dot{x}_{sj} \\ \dot{y}_{sj} \end{Bmatrix} - \begin{bmatrix} k_{xx} & k_{xy} \\ k_{yx} & k_{yy} \end{bmatrix} \begin{Bmatrix} x_{sj} \\ y_{sj} \end{Bmatrix} \quad (4.11)$$

The elements of the two coefficient matrices denote stiffness and damping coefficients of a bearing unit in horizontal and vertical directions.

4.2 Modeling of a Turbocharger in Rotordynamics

A turbocharger rotor system consists of turbine and compressor impellers linked by a shared shaft supported by a pair of floating ring bearings. The physical model of a turbocharger rotor system is shown in Figure 4.2(a). The turbocharger rotor system has been modeled as six rigid disks linked by elastic shaft segments using the Finite Element method, which is shown in Figure 4.2(b).

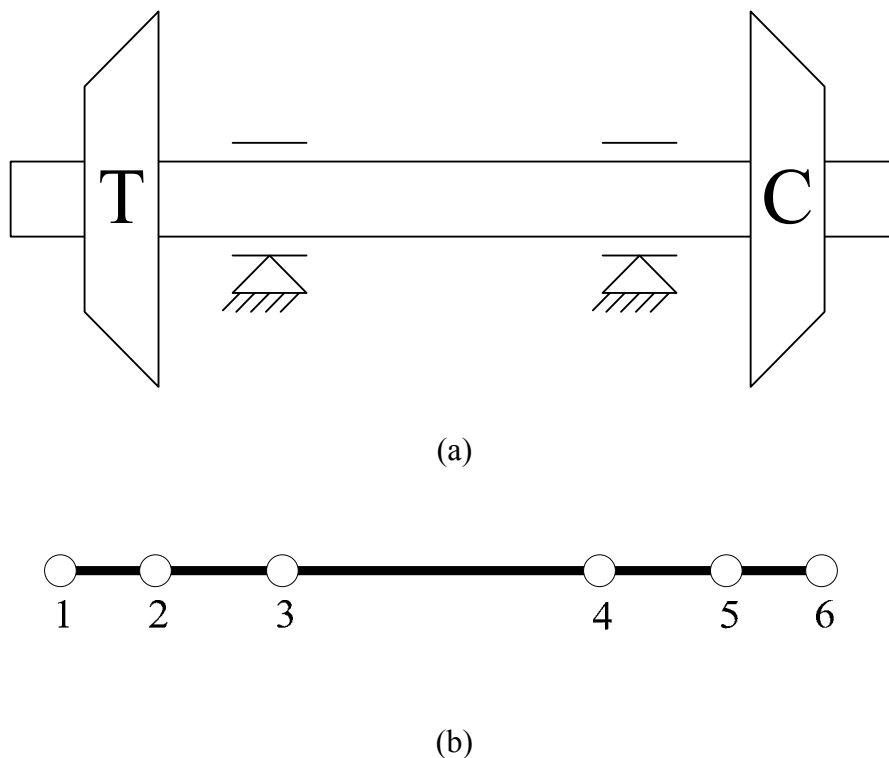


Figure 4. 2. The model of a turbocharger rotor system:

(a) Physical model (b) Finite element model

The system mass, stiffness and damping matrices are formed as follows:

It is assumed that the system mass is distributed on the mass nodes, thus the system mass matrix becomes diagonalised.

$$[M] = \begin{bmatrix} m_1 & & & & & \\ & m_2 & & & & \\ & & m_3 & & & \\ & & & m_4 & & \\ & & & & m_5 & \\ & & & & & m_6 \end{bmatrix} \quad (4.12)$$

where $\{m_1, \dots, m_6\}$ denote the mass of the discretized mass nodes.

Assuming the materials of the turbocharger shaft to be uniformed, the stiffness and damping matrices can be expressed by.

$$[K] = \begin{bmatrix} k_1 & -k_1 & & & & \\ -k_1 & k_1 + k_2 & -k_2 & & & \\ & -k_2 & k_2 + k_3 & -k_3 & & \\ & & -k_3 & k_3 + k_4 & -k_4 & \\ & & & -k_4 & k_4 + k_5 & -k_5 \\ & & & & -k_5 & k_5 \end{bmatrix} \quad (4.13)$$

$$[C] = \begin{bmatrix} c_1 & -c_1 & & & & \\ -c_1 & c_1 + c_2 & -c_2 & & & \\ & -c_2 & c_2 + c_3 & -c_3 & & \\ & & -c_3 & c_3 + c_4 & -c_4 & \\ & & & -c_4 & c_4 + c_5 & -c_5 \\ & & & & -c_5 & c_5 \end{bmatrix} \quad (4.14)$$

where $\{k_1, \dots, k_5\}$, $\{c_1, \dots, c_5\}$ denote the stiffness and damping coefficients of the shaft segments respectively.

As far as the turbocharger rotor system is concerned, the primary exciting forces for the system bending vibration include the static and dynamic loads. Static loads denote the

lubricant feed pressure acting on the ring, the dead weight, etc. Dynamic loads denote the forces with varied values, such as the rotor imbalance, the hydrodynamic fluid forces, etc. Hydrodynamic fluid forces will be detailed in Section 4.4.

In the following section, the rotor imbalance centrifugal force is studied as follows. Rotor imbalance is the most common defect for automotive turbochargers, because as the shaft spins, the trajectory of the disk can deviate from its centerline.

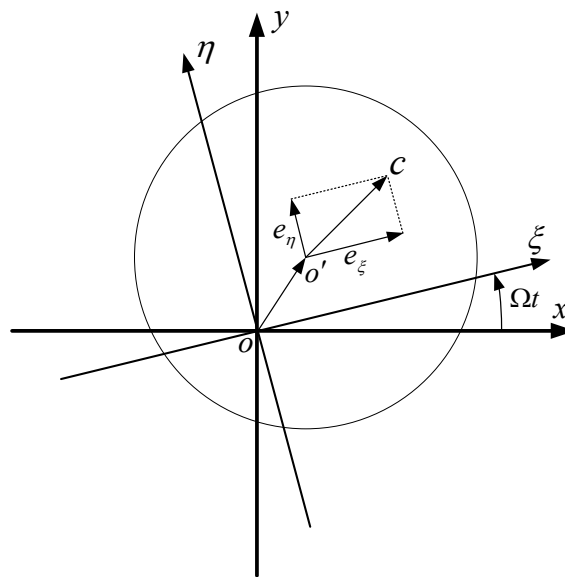


Figure 4. 3. Rotating disk with an imbalance mass

Figure 4.3 illustrates a disk rotating at the rotational velocity Ω with an imbalance mass m located at position c . The coordinate system XOY is a fixed system while $\xi O \eta$ is a rotating coordinate system. o' is the geometrical centre of the disk, and e_ξ, e_η represent eccentricities in the rotating coordinate system. Therefore if rotating at a rotational velocity Ω , centrifugal forces caused by the rotor imbalance mass m in X, Y directions can be expressed as follows:

$$F_{x_imb} = m_{imb} e_{\xi} \Omega^2 \cos \Omega t - m_{imb} e_{\eta} \Omega^2 \sin \Omega t \quad (4.15)$$

$$F_{y_imb} = m_{imb} e_{\xi} \Omega^2 \sin \Omega t + m_{imb} e_{\eta} \Omega^2 \cos \Omega t \quad (4.16)$$

Using matrices of mass [M], stiffness [K] and damping [C], the motion differential equation for the turbocharger rotor system is expressed as:

$$[M]\{\ddot{U}\} + [C]\{\dot{U}\} + [K]\{U\} = \{W\} + \{F_u\} + \{Fh_{inner}\} \quad (4.17)$$

where $\{U\} = \{x_1, \dots, x_6, y_1, \dots, y_6\}$ represent displacements vectors of the nodes in the horizontal and vertical directions, i.e. the X and Y directions. On the right hand side of the equation, the primary exciting forces include the imbalance centrifugal forces $\{F_u\}$, the hydrodynamic forces of the inner oil film $\{Fh_{inner}\}$ and the dead weight $\{W\}$.

The motion of the ring is determined by the outer and inner hydrodynamic fluid forces, the dead weight of the ring and the lubricant feed pressure. Therefore, the motion equation for the ring is given by:

$$[M_R]\{\ddot{U}_R\} = \{Fh_{outer}\} - \{Fh_{inner}\} + \{W_R\} + \{P\} \quad (4.18)$$

where U_R represents the displacement vector of the ring, and M_R is the mass matrix of the ring. The exciting force vectors include the hydrodynamic forces of the two oil films, the lubricant feed pressure and the dead weight.

Since the displacements of the shaft and the floating ring affect each other, equations (4.17) and (4.18) should be solved simultaneously. The motion equation for the turbocharger rotor system is then expressed in equation (4.19).

$$\begin{bmatrix} [M] & [0] \\ [0] & [M_R] \end{bmatrix} \begin{Bmatrix} \ddot{U} \\ \ddot{U}_R \end{Bmatrix} + \begin{bmatrix} [C] & [0] \\ [0] & [0] \end{bmatrix} \begin{Bmatrix} \dot{U} \\ \dot{U}_R \end{Bmatrix} + \begin{bmatrix} [K] & [0] \\ [0] & [0] \end{bmatrix} \begin{Bmatrix} U \\ U_R \end{Bmatrix} = \{F\}$$

$$\{F\} = \begin{Bmatrix} F_u \\ 0 \end{Bmatrix} + \begin{Bmatrix} W \\ W_R \end{Bmatrix} + \begin{Bmatrix} 0 \\ P \end{Bmatrix} + \begin{Bmatrix} Fh_{inner} \\ Fh_{outer} - Fh_{inner} \end{Bmatrix} \quad (4.19)$$

4.3 Hydrodynamic Fluid Forces in the Model

Hydrodynamic fluid force is generally expressed by a set of linear stiffness and damping coefficients. This approach is generally applied in the calculation of the critical speeds, the mode shapes, etc. However, the linear force model is not ideal for describing the nonlinear dynamic behaviors, such as rotor system instability. Both linear and nonlinear force models have been studied and described in sections 4.3.1 and 4.3.2 respectively.

4.3.1 Linear force model

Two oil films have been modelled as a mass-spring-damping model connected in series with the oil film forces expressed by a set of stiffness and damping coefficients.

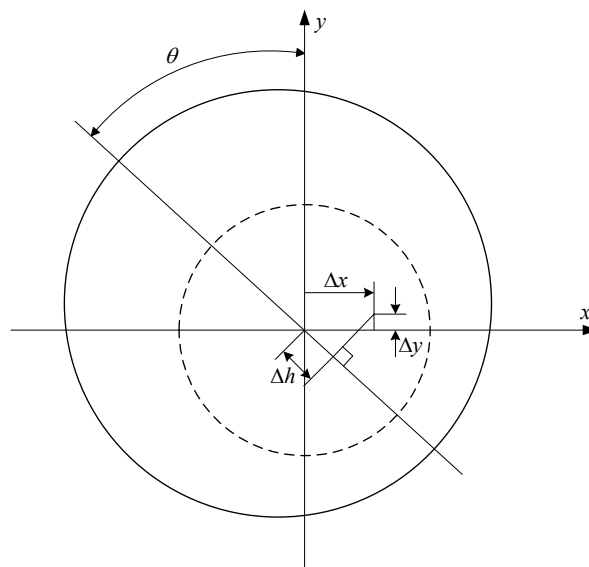


Figure 4. 4. Weak disturbance exerted on the journal

As shown in Figure 4.4, the journal is assumed to deviate from its static equilibrium position due to a weak disturbance and the oil film forces impacting on the journal will be

changed. The oil film force can be expressed in Taylor series form, as shown in equations (4.20) and (4.21) after neglecting the high order terms.

$$Fh_x = Fh_{x0} + \frac{\partial Fh_x}{\partial x} \Big|_0 \Delta x + \frac{\partial Fh_x}{\partial y} \Big|_0 \Delta y + \frac{\partial Fh_x}{\partial \dot{x}} \Big|_0 \Delta \dot{x} + \frac{\partial Fh_x}{\partial \dot{y}} \Big|_0 \Delta \dot{y} \quad (4.20)$$

$$Fh_y = Fh_{y0} + \frac{\partial Fh_y}{\partial x} \Big|_0 \Delta x + \frac{\partial Fh_y}{\partial y} \Big|_0 \Delta y + \frac{\partial Fh_y}{\partial \dot{x}} \Big|_0 \Delta \dot{x} + \frac{\partial Fh_y}{\partial \dot{y}} \Big|_0 \Delta \dot{y} \quad (4.21)$$

where Fh_x and Fh_y are the oil film forces in the x and y directions, and Fh_{x0} , Fh_{y0} are the original oil film forces in the x and y directions while the journal remains at its static equilibrium position.

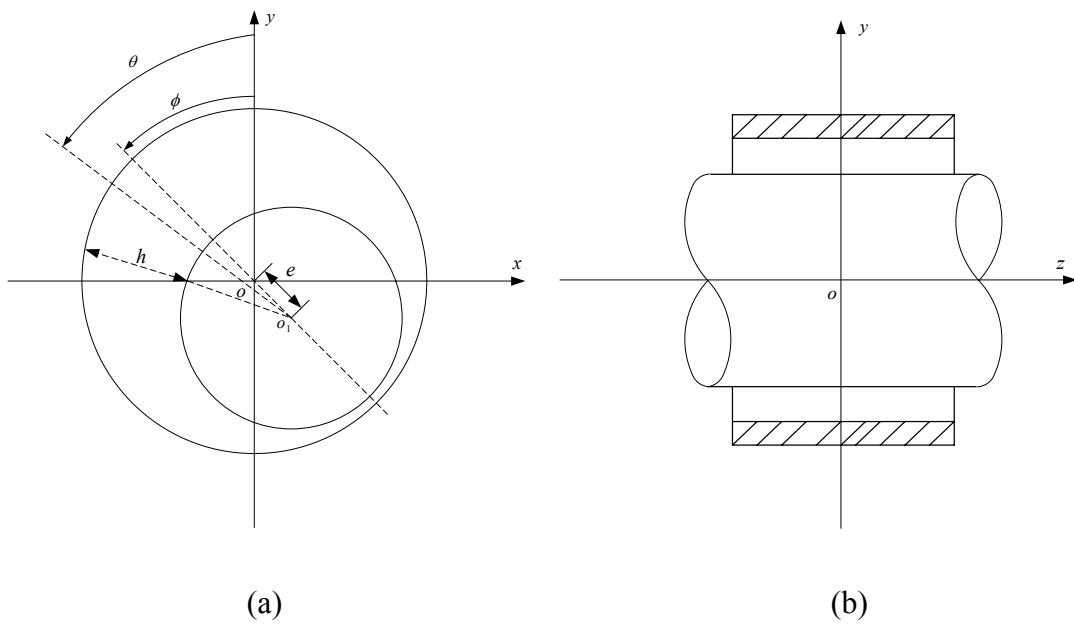


Figure 4. 5. Geometrical structure and system coordinates of the journal bearing

Figure 4.5 shows the system coordinate of a journal bearing in the radial and axial planes, where o and o_1 are the centers of the bearing and journal, e is the eccentricity of the journal, ϕ is the attitude angle and θ is the angle starting from the y-axis.

It has been assumed that at the static equilibrium position of the journal, the micro

displacements Δx and Δy and micro velocities $\Delta \dot{x}$ and $\Delta \dot{y}$ are exerted on the journal.

This allows the relationship between the weak disturbance of oil film force and the micro displacement to be determined. Oil film thickness, h , can be written as:

$$h = h_0 + \Delta h = h_0 + \Delta x \sin \theta - \Delta y \cos \theta \quad (4.22)$$

Oil film pressure, p , is then expressed as follows:

$$p = p_0 + \Delta p = p_0 + \frac{\partial p}{\partial x} \Delta x + \frac{\partial p}{\partial y} \Delta y + \frac{\partial p}{\partial \dot{x}} \Delta \dot{x} + \frac{\partial p}{\partial \dot{y}} \Delta \dot{y} \quad (4.23)$$

Substituting equations (4.22) and (4.23) into the Reynolds equation, four ordinary differential equations are derived as follows:

$$\frac{1}{R^2} \frac{\partial}{\partial \theta} \left(\frac{h_0^3}{12\mu} \frac{\partial \left(\frac{\partial p}{\partial x} \right)}{\partial \theta} \right) = \frac{1}{2} \Omega \left(\cos \theta - 3 \frac{\sin \theta}{h_0} \frac{\partial h_0}{\partial \theta} \right) - \frac{h_0^3}{4\mu R^2} \frac{1}{\partial \theta} \frac{\partial p_0}{\partial \theta} \frac{\partial}{\partial \theta} \left(\frac{\sin \theta}{h_0} \right) \quad (4.24)$$

$$\frac{1}{R^2} \frac{\partial}{\partial \theta} \left(\frac{h_0^3}{12\mu} \frac{\partial \left(\frac{\partial p}{\partial y} \right)}{\partial \theta} \right) = \frac{1}{2} \Omega \left(\sin \theta + 3 \frac{\cos \theta}{h_0} \frac{\partial h_0}{\partial \theta} \right) + \frac{h_0^3}{4\mu R^2} \frac{1}{\partial \theta} \frac{\partial p_0}{\partial \theta} \frac{\partial}{\partial \theta} \left(\frac{\cos \theta}{h_0} \right) \quad (4.25)$$

$$\frac{1}{R^2} \frac{\partial}{\partial \theta} \left(\frac{h_0^3}{12\mu} \frac{\partial \left(\frac{\partial p}{\partial \dot{x}} \right)}{\partial \theta} \right) = \sin \theta \quad (4.26)$$

$$\frac{1}{R^2} \frac{\partial}{\partial \theta} \left(\frac{h_0^3}{12\mu} \frac{\partial \left(\frac{\partial p}{\partial \dot{y}} \right)}{\partial \theta} \right) = -\cos \theta \quad (4.27)$$

Finite difference numerical approaches can then be applied to solve the above equations,

and the results $\frac{\partial p}{\partial x}, \frac{\partial p}{\partial y}, \frac{\partial p}{\partial \dot{x}}, \frac{\partial p}{\partial \dot{y}}$ are then integrated to calculate the dynamic coefficients

of the oil film.

$$k_{xx} = -R \int_{-\frac{L}{2}}^{\frac{L}{2}} \int_A \frac{\partial p}{\partial x} \sin \theta d\theta \quad (4.28)$$

$$k_{yx} = R \int_{-\frac{L}{2}}^{\frac{L}{2}} \int_A \frac{\partial p}{\partial x} \cos \theta d\theta \quad (4.29)$$

$$k_{xy} = -R \int_{-\frac{L}{2}}^{\frac{L}{2}} \int_A \frac{\partial p}{\partial y} \sin \theta d\theta \quad (4.30)$$

$$k_{yy} = R \int_{-\frac{L}{2}}^{\frac{L}{2}} \int_A \frac{\partial p}{\partial y} \cos \theta d\theta \quad (4.31)$$

$$c_{xx} = -R \int_{-\frac{L}{2}}^{\frac{L}{2}} \int_A \frac{\partial \dot{p}}{\partial \dot{x}} \sin \theta d\theta \quad (4.32)$$

$$c_{yx} = R \int_{-\frac{L}{2}}^{\frac{L}{2}} \int_A \frac{\partial \dot{p}}{\partial \dot{x}} \cos \theta d\theta \quad (4.33)$$

$$c_{xy} = -R \int_{-\frac{L}{2}}^{\frac{L}{2}} \int_A \frac{\partial \dot{p}}{\partial \dot{y}} \sin \theta d\theta \quad (4.34)$$

$$c_{yy} = R \int_{-\frac{L}{2}}^{\frac{L}{2}} \int_A \frac{\partial \dot{p}}{\partial \dot{y}} \cos \theta d\theta \quad (4.35)$$

where L is the length of the bearing and A is the integration field.

The dynamic coefficients of the inner and outer fluid films are then obtained, and substituted into the oil film force expression. The hydrodynamic fluid forces can then be calculated.

4.3.2 Nonlinear force model

In order to investigate nonlinear behaviours of a turbocharger rotor system, a nonlinear hydrodynamic fluid force model has been developed and is described in this section. The Capone oil film force model has been extended to the floating ring bearing.

The dimensionless form of the Reynolds equation for the outer fluid film is expressed by:

$$\frac{\partial}{\partial \theta} \left(h_o^3 \frac{\partial p_o}{\partial \theta} \right) + \left(\frac{R_o}{L} \right)^2 \frac{\partial}{\partial z} \left(h_o^3 \frac{\partial p_o}{\partial z} \right) = \frac{\partial h_o}{\partial \theta} + 2 \frac{\partial h_o}{\partial \tau_o} \quad (4.36)$$

where dimensionless parameters are

$$h_o = 1 - x_R \cos \theta - y_R \sin \theta, \quad z = \frac{Z}{L}, \quad x_R = \frac{X_R}{C_o}, \quad y_R = \frac{Y_R}{C_o}, \quad \tau_o = \Omega_R t, \quad p_o = \frac{P_o}{K_o},$$

$$K_o = 6\mu\Omega_R \left(\frac{R_o}{C_o} \right)^2$$

where h_o is the thickness of the outer film, C_o is the outer clearance, R_o is the radius of the outer ring, L is the bearing length, Ω_R is the rotational speed of the floating ring, μ is the lubricant viscosity. $h_o, x_R, y_R, z, \tau_o, p_o$ represent the dimensionless parameters.

The infinitely short bearing theory was used to solve the dimensionless Reynolds equations, and the pressure gradient in the angular direction was ignored. It was assumed that the lubricant was incompressible and that the viscosity was constant during the simulation. Consequently, the theoretical solutions of the differential equation for the outer and inner fluid films are given by

$$p_o = \frac{1}{2} \left(\frac{L}{D_o} \right)^2 \left[\frac{(x_R - 2\dot{y}_R) \sin \theta - (y_R + 2\dot{x}_R) \cos \theta}{(1 - x_R \cos \theta - y_R \sin \theta)^3} \right] (4z^2 - 1) \quad (4.37)$$

By integrating the oil film pressure in the outer oil film land, the hydrodynamic fluid forces of the outer film can be expressed as follows.

$$\begin{aligned} \begin{Bmatrix} Fh_{outer_x} \\ Fh_{outer_y} \end{Bmatrix} &= -\mu\Omega_R \left(\frac{R_o^2}{C_o^2} \right) \left(\frac{L^2}{D_o^2} \right) (R_o L) \frac{\sqrt{(x_R - 2\dot{y}_R)^2 + (y_R + 2\dot{x}_R)^2}}{(1 - x_R \cos \theta - y_R \sin \theta)} \\ &\quad \begin{Bmatrix} 3x_R V_o - \sin \alpha_o G_o - 2 \cos \alpha_o F_o \\ 3y_R V_o - \cos \alpha_o G_o - 2 \sin \alpha_o F_o \end{Bmatrix} \\ V_o &= \frac{2 + (y_R \cos \alpha_o - x_R \sin \alpha_o) G_o}{(1 - x_R^2 - y_R^2)} \end{aligned}$$

$$G_o = \frac{\pi}{\sqrt{1-x_R^2-y_R^2}} - \frac{2}{\sqrt{1-x_R^2-y_R^2}} \tan^{-1} \left(\frac{y_R \cos \alpha_o - x_R \sin \alpha_o}{\sqrt{1-x_R^2-y_R^2}} \right)$$

$$F_o = \frac{(x_R \cos \alpha_o + y_R \sin \alpha_o)}{(1-x_R^2-y_R^2)}$$

$$\alpha_o = \tan^{-1} \left(\frac{y_R + 2\dot{x}_R}{x_R - \dot{y}_R} \right) - \frac{\pi}{2} \text{sign} \left(\frac{y_R + 2\dot{x}_R}{x_R - \dot{y}_R} \right) - \frac{\pi}{2} \text{sign}(y_R + 2\dot{x}_R) \quad (4.38)$$

The dimensionless Reynolds equation for the inner film is expressed by

$$\frac{\partial}{\partial \theta} \left(h_i^3 \frac{\partial p_i}{\partial \theta} \right) + \left(\frac{R_J}{L} \right)^2 \frac{\partial}{\partial z} \left(h_i^3 \frac{\partial p_i}{\partial z} \right) = \frac{\partial h_i}{\partial \theta} + 2 \frac{\partial h_i}{\partial \tau_i} \quad (4.39)$$

where dimensionless parameters are

$$h_o = 1 - x_R \cos \theta - y_R \sin \theta, \quad z = \frac{Z}{L}, \quad x_i = \frac{X_i}{C_i}, \quad y_i = \frac{Y_i}{C_i}, \quad \tau_i = \left(\Omega_J + \frac{R_i}{R_J} \right) t, \quad p_i = \frac{P_i}{K_i},$$

$$K_i = 6\mu \left(\Omega_J + \frac{R_i}{R_J} \Omega_R \right) \left(\frac{R_J}{C_i} \right)^2$$

By integrating inner film pressure in the inner oil film land, the hydrodynamic forces could be expressed as follows:

$$\begin{aligned} \begin{Bmatrix} Fh_{inner-x} \\ Fh_{inner-y} \end{Bmatrix} &= -\mu \left(\Omega_J + \frac{R_i}{R_J} \right) \left(\frac{R_J^2}{C_i^2} \right) \left(\frac{L^2}{D_i^2} \right) (R_J L) \frac{\sqrt{(x_i - 2\dot{y}_i) + (y_i + 2\dot{x}_i)}}{(1 - x_i \cos \theta - y_i \sin \theta)} \\ &\quad \begin{Bmatrix} 3x_i V_i - \sin \alpha_i G_i - 2 \cos \alpha_i F_i \\ 3y_i V_i - \cos \alpha_i G_i - 2 \sin \alpha_i F_i \end{Bmatrix} \\ V_i &= \frac{2 + (y_i \cos \alpha_i - x_i \sin \alpha_i) G_i}{(1 - x_i^2 - y_i^2)} \\ G_i &= \frac{\pi}{\sqrt{1-x_i^2-y_i^2}} - \frac{2}{\sqrt{1-x_i^2-y_i^2}} \tan^{-1} \left(\frac{y_i \cos \alpha_i - x_i \sin \alpha_i}{\sqrt{1-x_i^2-y_i^2}} \right) \\ F_i &= \frac{(x_i \cos \alpha_i + y_i \sin \alpha_i)}{(1-x_i^2-y_i^2)} \\ \alpha_i &= \tan^{-1} \left(\frac{y_i + 2\dot{x}_i}{x_i - \dot{y}_i} \right) - \frac{\pi}{2} \text{sign} \left(\frac{y_i + 2\dot{x}_i}{x_i - \dot{y}_i} \right) - \frac{\pi}{2} \text{sign}(y_i + 2\dot{x}_i) \end{aligned} \quad (4.40)$$

It can be seen that hydrodynamic forces of the inner and outer oil films are calculated using different normalization standard Reynolds equations, thus the results could not be calculated directly for these. As a result, it is necessary to unify the normalization standard. Throughout this thesis, the outer oil film has been chosen as the standard. Parameters of relative displacement between the journal and the floating ring are given by:

$$x_i = (x - x_R) \frac{C_o}{C_i}, \quad y_i = (y - y_R) \frac{C_o}{C_i}, \quad h_i = 1 - (x - x_R) \frac{C_o}{C_i} \cos \theta - (y - y_R) \frac{C_o}{C_i} \sin \theta$$

$$\dot{x}_i = (\dot{x} - \dot{x}_R) \frac{\Omega_R}{\left(\Omega_J + \frac{R_i}{R_J} \Omega_R \right)}, \quad \dot{y} = (\dot{y} - \dot{y}_R) \frac{\Omega_R}{\left(\Omega_J + \frac{R_i}{R_J} \Omega_R \right)}$$

Initially, the hydrodynamic fluid forces are calculated, and then converted it into the outer

film standard by multiplying by a coefficient $\left(\frac{\Omega_J}{\Omega_R} + \frac{R_i}{R_J} \right) \frac{R_J^2 C_o^2}{R_o^2 C_i^2}$

Substitution of the hydrodynamic fluid forces of the two films into the system motion equations allows a numerical approach to be utilized for calculation of the bending vibration of the turbocharger rotor system.

4.4 Rub-impact Force

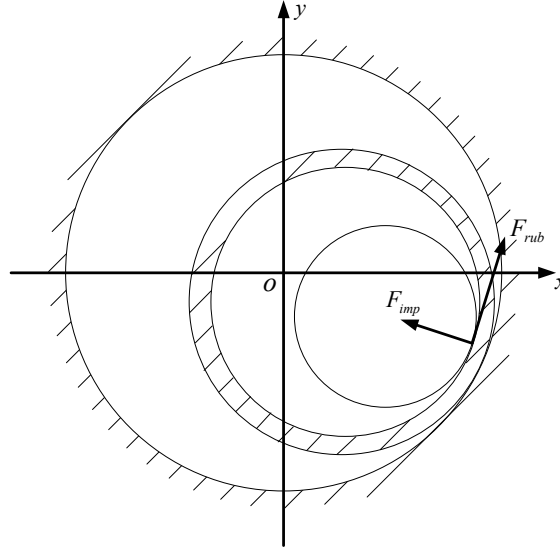


Figure 4. 6. Rub-impact dynamics model of the floating ring bearing

The rotor rub-impact phenomenon is very complex and involves many factors. A simplified dynamic model has been derived to simulate the phenomenon. Once the rotor touches the bearing, a rub force in the tangential direction and an impact force in the radial direction will be exerted on the rotor until the process is complete.

Figure 4.6 shows the rotor rub-impact force model, F_{imp} , F_{rub} denote the impact and rub forces respectively. The impact force depends upon the elastic deformation of the stator and the rub force can then be expressed according to the friction law. The rub and impact forces are expressed as follows:

$$F_{imp} = kr(\zeta - (C_i + C_o)) \quad (4.41)$$

$$F_{rub} = f \cdot F_{imp} \quad (4.42)$$

where kr is the radial stiffness coefficient of the floating ring and f is the friction

coefficient between the journal and the ring.

4.5 Summary

In this chapter, a theoretical model is developed for the turbocharger rotor system to simulate its bending vibration according to the finite element theory. The exciting forces which are taken into account include rotor imbalance, lubricant feed pressure, hydrodynamic forces of the floating ring bearing and the dead weight of the rotor. Furthermore, both linear and nonlinear hydrodynamic force models are studied for the modal analysis and stability analysis respectively. The rub-impact phenomenon is also investigated.

CHAPTER FIVE

CALCULATION OF CRITICAL SPEEDS AND MODE SHAPES OF A TURBOCHARGER ROTOR SYSTEM

As far as a rotor system is concerned, the critical speed is one of the most important parameters. Once critical speeds are reached, the resonance occurs which may damage the entire rotor system. Preventing the working speed from reaching critical speed and guaranteeing safe operation is crucial for a turbocharger rotor system whose service speed covers a quite wide speed range. In this chapter, the critical speeds and mode shapes of the turbocharger rotor system have been calculated and analyzed based on the mathematical model.

The motion of a turbocharger rotor system is generally dominated by the forced vibration caused by the rotor imbalance and the self-excited vibration, which is caused by hydrodynamic fluid forces. Once the rotational velocity approaches the natural frequency, the rotor begins to resonate, dramatically increasing the system vibration. This speed is known as the critical speed. For a rotor system with a series of natural frequencies, there are a series of corresponding rotational speeds.

In order to guarantee safe operation and to prevent working speeds from approaching critical speeds, modal analysis has been carried out in this chapter for a turbocharger rotor system based on the mathematical model. Firstly, a free rotor system has been analyzed, ignoring the effects of the bearing and gyroscopic effects; Critical speeds and mode shapes of a turbocharger rotor system were then studied, taking into account the influences of floating ring bearings and gyroscopic effects.

5.1 Modal Analysis for a Free Rotor

By ignoring the influences of the bearings and the gyroscopic effects, the frequency characteristic equation of a free rotor is expressed by:

$$[M]\{\ddot{U}\} + [K]\{U\} = \{0\} \quad (5.1)$$

The mass matrix $[M]$ and stiffness matrix $[K]$ are formed using the finite element method.

$$[M] = \begin{bmatrix} [M_1] & 0 \\ 0 & [M_1] \end{bmatrix} \quad (5.2)$$

$$[M1] = \begin{bmatrix} m_1 & & & & & & \\ & Jd_1 & & & & & \\ & & m_2 & & & & \\ & & & Jd_2 & & & \\ & & & & m_3 & & \\ & & & & & Jd_3 & \\ & & & & & & m_4 \\ & & & & & & & Jd_4 \\ & & & & & & & & m_5 \\ & & & & & & & & & Jd_5 \\ & & & & & & & & & & m_6 \\ & & & & & & & & & & & Jd_6 \end{bmatrix}$$

$$[K] = \begin{bmatrix} [K_1] & 0 \\ 0 & [K_1] \end{bmatrix} \quad (5.3)$$

$$[K_1] = \begin{bmatrix} k_{1_11} & k_{1_12} & & & & \\ k_{1_21} & k_{1_22} + k_{2_11} & k_{2_12} & & & \\ & k_{2_21} & k_{2_22} + k_{3_11} & k_{3_12} & & \\ & & k_{3_21} & k_{3_22} + k_{4_11} & k_{4_12} & \\ & & & k_{4_21} & k_{4_22} + k_{5_11} & k_{5_12} \\ & & & & k_{5_21} & k_{5_22} \end{bmatrix}$$

$$[k_{i_11}] = \begin{bmatrix} \frac{12EI_i}{l_i^3} & \frac{6EI_i}{l_i^2} \\ \frac{6EI_i}{l_i^2} & \frac{4EI_i}{l_i} \end{bmatrix} \quad [k_{i_12}] = \begin{bmatrix} -\frac{12EI_i}{l_i^3} & \frac{6EI_i}{l_i^2} \\ -\frac{6EI_i}{l_i^2} & \frac{2EI_i}{l_i} \end{bmatrix}$$

$$[k_{i_21}] = \begin{bmatrix} -\frac{12EI_i}{l_i^3} & -\frac{6EI_i}{l_i^2} \\ \frac{6EI_i}{l_i^2} & \frac{2EI_i}{l_i} \end{bmatrix} \quad [k_{i_22}] = \begin{bmatrix} \frac{12EI_i}{l_i^3} & -\frac{6EI_i}{l_i^2} \\ -\frac{6EI_i}{l_i^2} & \frac{4EI_i}{l_i} \end{bmatrix}$$

$$\{U\} = [U_1 \quad U_2]^T \quad (5.4)$$

$$\{U_1\} = [x_1 \quad \theta_{y1} \quad x_2 \quad \theta_{y2} \quad x_3 \quad \theta_{y3} \quad x_4 \quad \theta_{y4} \quad x_5 \quad \theta_{y5} \quad x_6 \quad \theta_{y6}]$$

$$\{U_2\} = [y_1 \quad -\theta_{x1} \quad y_2 \quad -\theta_{x2} \quad y_3 \quad -\theta_{x3} \quad y_4 \quad -\theta_{x4} \quad y_5 \quad -\theta_{x5} \quad y_6 \quad -\theta_{x6}]$$

The solution form of the frequency characteristic equation is assumed as:

$$\{U\} = \{U_o\} e^{j\omega_n t} \quad (5.5)$$

Substitute equation (5.5) into equation (5.1)

$$(-\omega_n^2 M + K)\{U_o\} = \{0\} \quad (5.6)$$

The natural frequencies and mode shapes of the free rotor can be obtained by solving the eigenvalues of the characteristic equation (5.6). The results can be found in Section 5.3.

5.2 Modal Analysis for a Turbocharger Rotor System

In this section, the critical speeds and mode shapes of the turbocharger rotor system are studied and both the influences of floating ring bearings and the gyroscopic effects are taken into account. The two oil films of the floating ring bearing can be simplified as a mass-spring-damping model. In the critical speed calculation, it is reasonable to ignore the damping effects and consider the support as isotropic when the stiffness and equivalent mass of the support are approximately similar in all directions [136]. Figure 5.1(a) shows the support model on one plane, where k_1 and k_2 denote the equivalent stiffness coefficients of the inner and outer oil films, m_R denotes the equivalent mass of the ring.

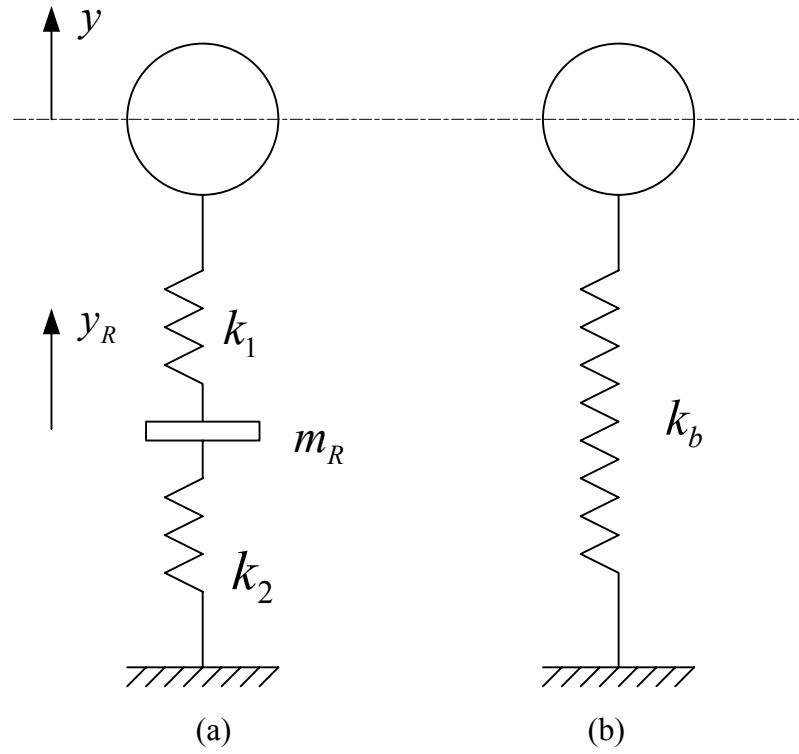


Figure 5. 1. Dynamic coefficients simplification of the floating ring bearing

The model has been simplified to an elastic support model shown in Figure 5.1(b). The motion equation of the equivalent mass is expressed as follows:

$$m_R \ddot{y}_R = k_1 (y - y_R) - k_2 y_R \quad (5.7)$$

The solution form of the equation (5.7) is assumed to

$$y_R = A e^{j\omega t} \quad (5.8)$$

where ω is the whirling frequency.

$$\ddot{y}_R = -A \omega^2 e^{j\omega t} = -\omega^2 y_R \quad (5.9)$$

Substitute the equation (5.9) into the equation (5.7)

$$y_R = \left(\frac{k_1}{k_1 + k_2 - m_R \omega^2} \right) y \quad (5.10)$$

The displacement relationship of the ring and the journal is established by the equation

(5.10) on one plane. The equivalent stiffness coefficient k_b in Figure 5.1(b) can therefore be expressed by

$$k_b = \frac{k_1(k_2 - m_R \omega^2)}{k_1 + k_2 - m_R \omega^2} \quad (5.11)$$

Taking into account the floating ring bearings and the gyroscopic effects of the rigid disk, the frequency characteristic equation of the turbocharger rotor system is given as:

$$[M]\{\ddot{U}\} + \Omega[J]\{\dot{U}\} + [K]\{U\} = \{0\} \quad (5.12)$$

$$[M] = \begin{bmatrix} [M_1] & 0 \\ 0 & [M_1] \end{bmatrix} \quad (5.13)$$

$$[M_1] = \begin{bmatrix} m_1 & & & & & \\ & Jd_1 & & & & \\ & & m_2 & & & \\ & & & Jd_2 & & \\ & & & & m_3 & \\ & & & & & Jd_3 \\ & & & & & & m_4 \\ & & & & & & & Jd_4 \\ & & & & & & & & m_5 \\ & & & & & & & & & Jd_5 \\ & & & & & & & & & & m_6 \\ & & & & & & & & & & & Jd_6 \end{bmatrix}$$

$$[J] = \begin{bmatrix} 0 & [J_1] \\ [-J_1] & 0 \end{bmatrix} \quad (5.14)$$

$$[J_1] = \begin{bmatrix} 0 & & & & & \\ & J_{p1} & & & & \\ & & 0 & & & \\ & & & J_{p2} & & \\ & & & & 0 & \\ & & & & & J_{p3} \\ & & & & & & 0 \\ & & & & & & & J_{p4} \\ & & & & & & & & 0 \\ & & & & & & & & & J_{p5} \\ & & & & & & & & & & 0 \\ & & & & & & & & & & & J_{p6} \end{bmatrix}$$

$$[K] = \begin{bmatrix} [K_1] & 0 \\ 0 & [K_1] \end{bmatrix} \quad (5.15)$$

$$[K_1] = \begin{bmatrix} k_{1_11} & k_{1_12} & & & & \\ k_{1_21} & k_{1_22} + k_{2_11} & k_{2_12} & & & \\ & k_{2_21} & k_{2_22} + k_{3_11} + k_b & k_{3_12} & & \\ & & k_{3_21} & k_{3_22} + k_{4_11} + k_b & k_{4_12} & \\ & & & k_{4_21} & k_{4_22} + k_{5_11} & k_{5_12} \\ & & & & k_{5_21} & k_{5_22} \end{bmatrix}$$

$$[k_{i_11}] = \begin{bmatrix} \frac{12EI_i}{l_i^3} & \frac{6EI_i}{l_i^2} \\ \frac{6EI_i}{l_i^2} & \frac{4EI_i}{l_i} \end{bmatrix} \quad [k_{i_12}] = \begin{bmatrix} -\frac{12EI_i}{l_i^3} & \frac{6EI_i}{l_i^2} \\ -\frac{6EI_i}{l_i^2} & \frac{2EI_i}{l_i} \end{bmatrix}$$

$$[k_{i_21}] = \begin{bmatrix} -\frac{12EI_i}{l_i^3} & -\frac{6EI_i}{l_i^2} \\ \frac{6EI_i}{l_i^2} & \frac{2EI_i}{l_i} \end{bmatrix} \quad [k_{i_22}] = \begin{bmatrix} \frac{12EI_i}{l_i^3} & -\frac{6EI_i}{l_i^2} \\ -\frac{6EI_i}{l_i^2} & \frac{4EI_i}{l_i} \end{bmatrix}$$

$$\{U\} = [U_1 \quad U_2]^T \quad (5.16)$$

$$\{U_1\} = [x_1 \quad \theta_{y1} \quad x_2 \quad \theta_{y2} \quad x_3 \quad \theta_{y3} \quad x_4 \quad \theta_{y4} \quad x_5 \quad \theta_{y5} \quad x_6 \quad \theta_{y6}]$$

$$\{U_2\} = [y_1 \quad -\theta_{x1} \quad y_2 \quad -\theta_{x2} \quad y_3 \quad -\theta_{x3} \quad y_4 \quad -\theta_{x4} \quad y_5 \quad -\theta_{x5} \quad y_6 \quad -\theta_{x6}]$$

The solution form of the equation (5.12) is assumed to

$$\{U\} = \{U_o\}e^{\lambda t} \quad (5.17)$$

Equation (5.17) is then substituted into equation (5.12)

$$(\lambda^2[M] + \lambda\Omega[J] + [K])(U_o) = \{0\} \quad (5.18)$$

The eigenvalue of the equation (5.18) should be purely imaginary, $\lambda = j\omega_n$. $\omega_n > 0$ corresponds to the natural frequency of the synchronous forward precession and $\omega_n < 0$ corresponds to the natural frequency of synchronous backward precession. Where the gyroscopic effect is concerned, the natural frequency ω_n will be determined not only by system parameters, but also by the rotational speed, Ω .

5.3 Simulation and Analysis

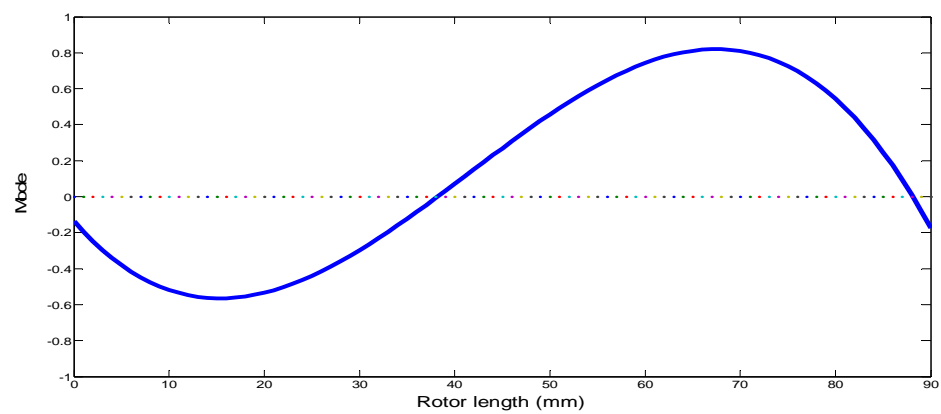
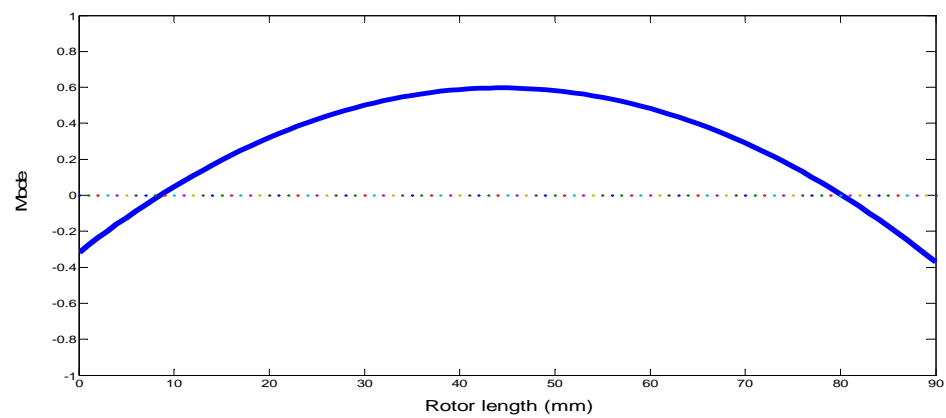
Table 5.1 lists the simulation parameters of the turbocharger rotor system for modal analysis, which is estimated according to the parameters of the GJ90C turbocharger. Based on the given parameters, the natural frequencies and mode shapes of a free rotor have been calculated. A finite element model with six mass nodes can theoretically provide twelve natural frequencies and twelve vibration modes. In this section, the first four orders natural frequencies and the corresponding mode shapes are listed.

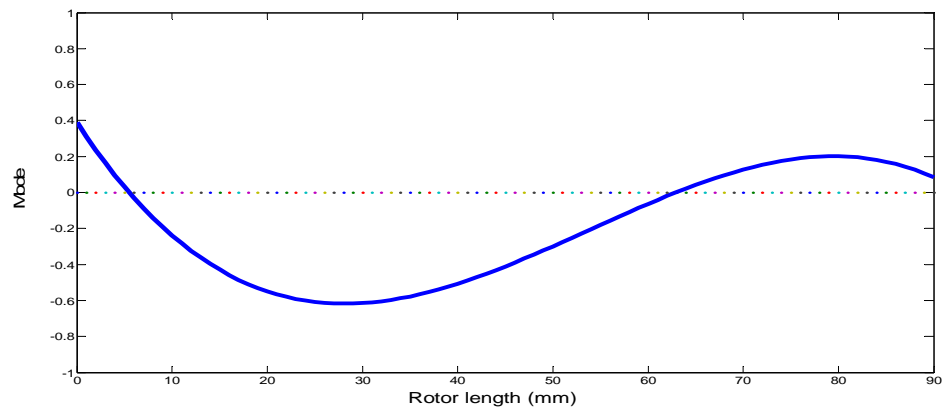
Table 5. 1. Parameters of a turbocharger rotor system for modal analysis

Parameters	Values
Mass	$m_1 = 0.01\text{kg}$, $m_2 = 0.06\text{kg}$ $m_3 = 0.015\text{kg}$, $m_4 = 0.02\text{kg}$ $m_5 = 0.07\text{kg}$, $m_6 = 0.01\text{kg}$
Moment of inertia	$Jd_1 = 0.2 \times 10^{-6} \text{kgm}^2$, $Jd_2 = 9 \times 10^{-6} \text{kgm}^2$ $Jd_3 = 0.2 \times 10^{-6} \text{kgm}^2$, $Jd_4 = 0.2 \times 10^{-6} \text{kgm}^2$ $Jd_5 = 8 \times 10^{-6} \text{kgm}^2$, $Jd_6 = 0.2 \times 10^{-6} \text{kgm}^2$ $Jp_1 = 0.1 \times 10^{-6} \text{kgm}^2$, $Jp_2 = 16 \times 10^{-6} \text{kgm}^2$ $Jp_3 = 0.1 \times 10^{-6} \text{kgm}^2$, $Jp_4 = 0.1 \times 10^{-6} \text{kgm}^2$ $Jp_5 = 14 \times 10^{-6} \text{kgm}^2$, $Jp_6 = 0.1 \times 10^{-6} \text{kgm}^2$
Radius of shaft segments	$r_1 = 5 \times 10^{-3} \text{m}$, $r_2 = 5 \times 10^{-3} \text{m}$ $r_3 = 4 \times 10^{-3} \text{m}$, $r_4 = 7 \times 10^{-3} \text{m}$ $r_5 = 7 \times 10^{-3} \text{m}$
Length of shaft segments	$l_1 = 5 \times 10^{-3} \text{m}$, $l_2 = 25 \times 10^{-3} \text{m}$ $l_3 = 30 \times 10^{-3} \text{m}$, $l_4 = 25 \times 10^{-3} \text{m}$ $l_5 = 5 \times 10^{-3} \text{m}$
Young's modulus	$E = 205\text{GPa}$

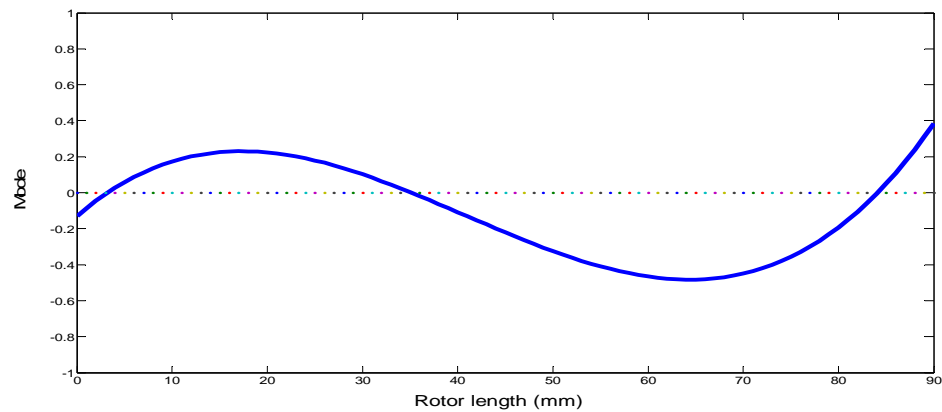
Table 5. 2. Natural frequencies of a free rotor

Order	Natural frequency
1	1730Hz
2	5045Hz
3	11975Hz
4	18193Hz





(c)



(d)

Figure 5. 2. Mode shapes of a turbocharger free rotor: (a) The first order (b) The second order (c) The third order (d) The fourth order

Table 5.2 shows the first four orders of natural frequencies of a free rotor according to the simulation parameters listed in Table 5.1. We can see that the natural frequencies are quite high especially for the higher orders while neglecting the support and gyroscopic effects. Figure 5.2 shows the first four orders mode shapes of a free rotor system. It can be seen that all four orders are bending modes. The fourth order mode shape already shows the trend of transforming into the local mode.

While considering gyroscopic effects on the turbocharger rotor system, the natural frequency will be related to the rotational speed of the shaft. Each speed corresponds to a

series of natural frequencies, half of which represent synchronous forward precession and half of which represent synchronous reverse precession. Table 5.3 lists the first ten orders of natural frequencies for the turbocharger rotor every 500rad/s within the speed range of 8000rad/s as the equivalent stiffness coefficient of the floating ring bearing is assumed to be 10^4 N/m.

Table 5. 3. First ten orders of natural frequencies of a turbocharger rotor system

Speed (rad/s)	Forward precession (Hz)					Reverse precession (Hz)				
0	11976	5046	1732	52	20	-11976	-5046	-1732	-52	-20
500	11997	5094	1769	53	25	-11955	-4997	-1695	-52	-16
1000	12019	5143	1808	53	31	-11934	-4950	-1659	-52	-13
1500	12040	5193	1847	53	37	-11913	-4904	-1623	-52	-11
2000	12063	5244	1887	53	44	-11893	-4858	-1589	-52	-9
2500	12085	5295	1927	53	55	-11873	-4813	-1555	-50	-8
3000	12108	5347	1968	53	61	-11853	-4769	-1521	-50	-7
3500	12131	5400	2010	53	68	-11833	-4725	-1489	-50	-6
4000	12154	5454	2052	53	76	-11814	-4682	-1457	-50	-5
4500	12177	5508	2095	53	85	-11794	-4640	-1427	-50	-5
5000	12201	5563	2138	53	93	-11775	-4598	-1396	-50	-4
5500	12225	5619	2182	53	101	-11756	-4557	-1367	-50	-4
6000	12250	5676	2227	53	110	-11738	-4517	-1338	-50	-4
6500	12274	5733	2272	53	118	-11720	-4477	-1311	-50	-4
7000	12300	5791	2317	53	127	-11701	-4438	-1283	-50	-3

7500	12325	5850	2363	53	135	-11683	-4399	-1257	-50	-3
8000	12351	5909	2410	53	143	-11667	-4361	-1231	-50	-3

It can be seen from Table 5.3 that natural frequencies increase as the rotational speed is raised, as a result of the gyroscopic effects. As far as the turbocharger working speed range is concerned, the fifth and the above orders of natural frequencies are too high to be taken into account. As a result, only the first four orders natural frequencies are considered and these higher orders have been disregarded.

In order to study effects of the bearing on the performance of the turbocharger shaft motion, different equivalent stiffness coefficients have been given in order to simulate the different bearing stiffness. Figures 5.3 to 5.8 illustrate both Campbell diagrams and mode shapes at 8000rad/s rotor angular velocity under the stiffness coefficients as 10^{10} , 10^7 and 10^4 N/m.

In Campbell diagrams, the dashed line represents the line on which the rotational speed is equal to the natural frequencies, i.e. $\Omega = \omega_n$. It can be seen from Campbell diagrams (Figures 5.3, 5.5, 5.7) that the natural frequencies of the turbocharger rotor system emerge in pairs, one of them being the forward precession frequency and the other being the reverse precession frequency. However, the system natural frequency rises as the bearing stiffness increases. When the equivalent bearing stiffness coefficient is assumed as 10^{10} N/m, the $\Omega = \omega_n$ line will intersect only with the first pair of natural frequencies, showing that two critical speeds of the rotor system exist. When the stiffness coefficient decreases to 10^7 N/m, the first two orders of natural frequencies intersect with the $\Omega = \omega_n$ line which illustrates that the rotor system has four critical speeds, double forward speeds and double reverse speeds. When the stiffness coefficient further decreases to 10^4 N/m, the $\Omega = \omega_n$

line will also intersect with the third reverse frequency line, a line which demonstrates the existence of the third reverse critical speed besides the above four speeds.

From Figure 5.4, it can be seen that the first forward and the reverse modes are bending modes while the others are elastic gyroscopic modes when the bearing stiffness is assumed to be relatively high, i.e. 10^{10} N/m. As is shown in Figure 5.6, as the bearing stiffness decreases to 10^7 N/m, rigid body conical modes emerge, which is shown in both the first forward and reverse modes. The second forward and reverse modes, however, are approximately translational modes and the others are bending and gyroscopic modes respectively. The same trends can be observed as the bearing stiffness further decreases to 10^4 N/m as is shown in Figure 5.7. Both mode shapes are rigid shapes (conical modes and translational modes respectively). The third forward and reverse modes are bending modes and the fourth are gyroscopic modes.

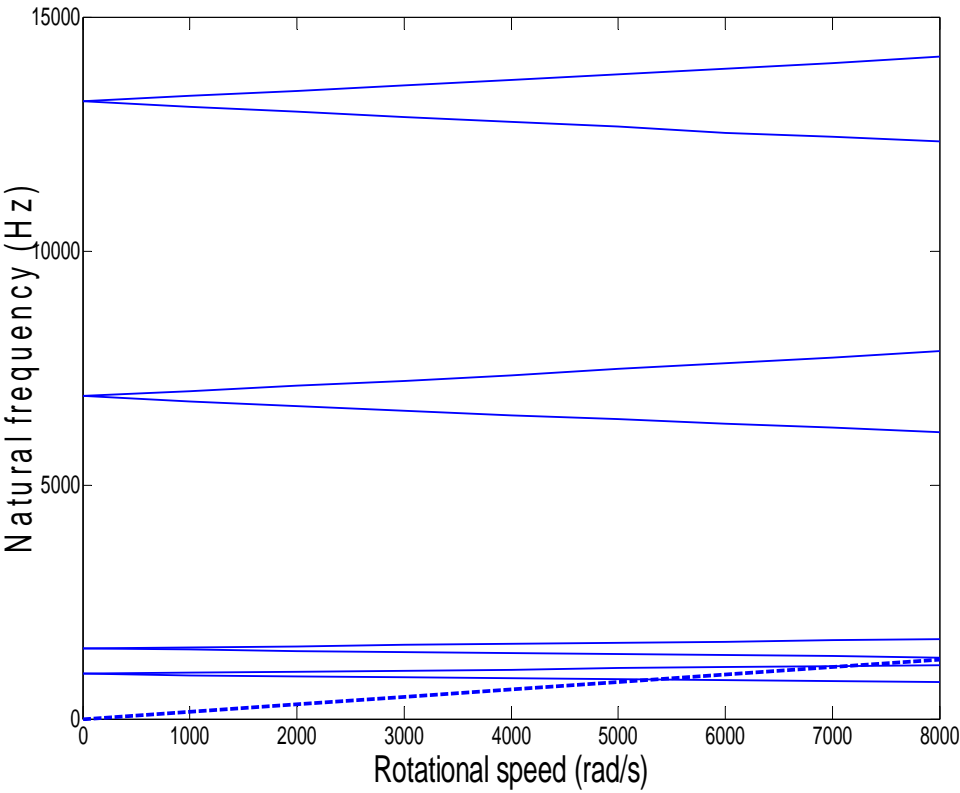
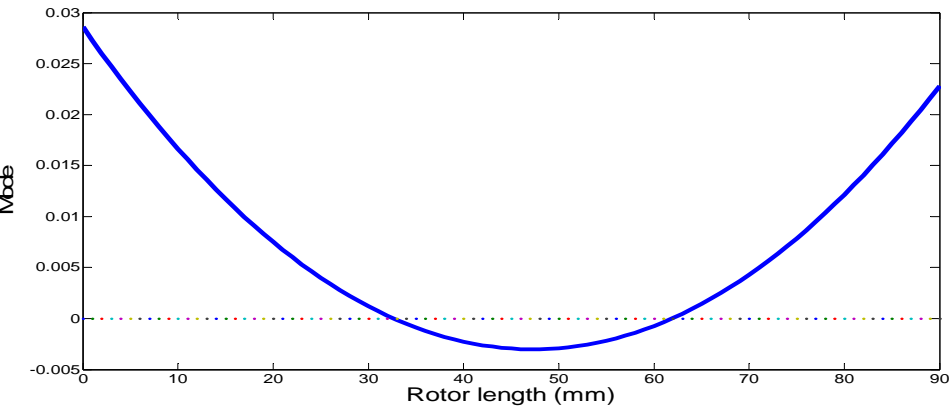
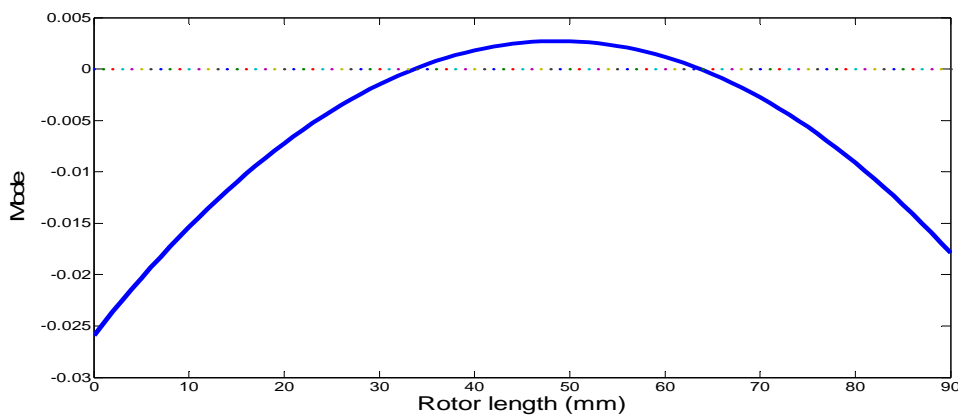


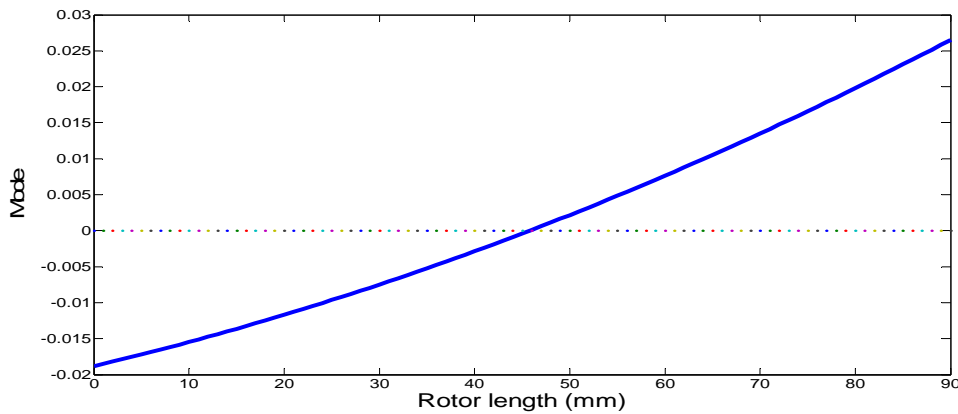
Figure 5. 3. A Campbell diagram of the turbocharger rotor system with an equivalent stiffness coefficient of 10^{10} N/m



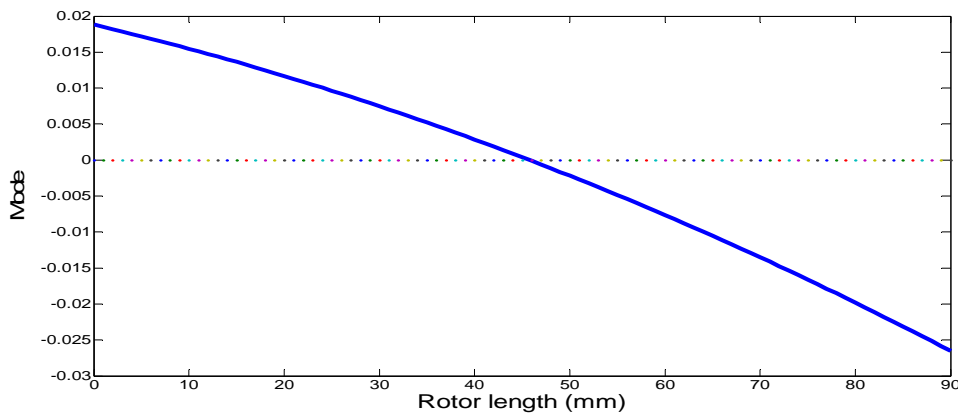
(a) The first forward mode



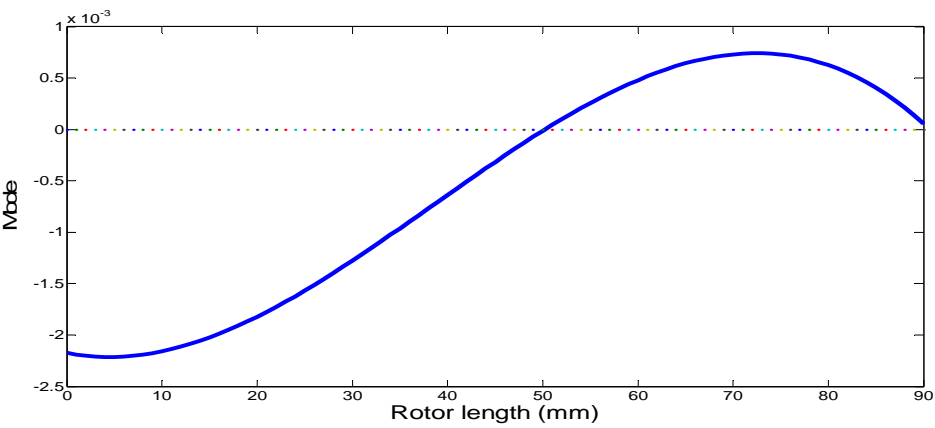
(b) The first reverse mode



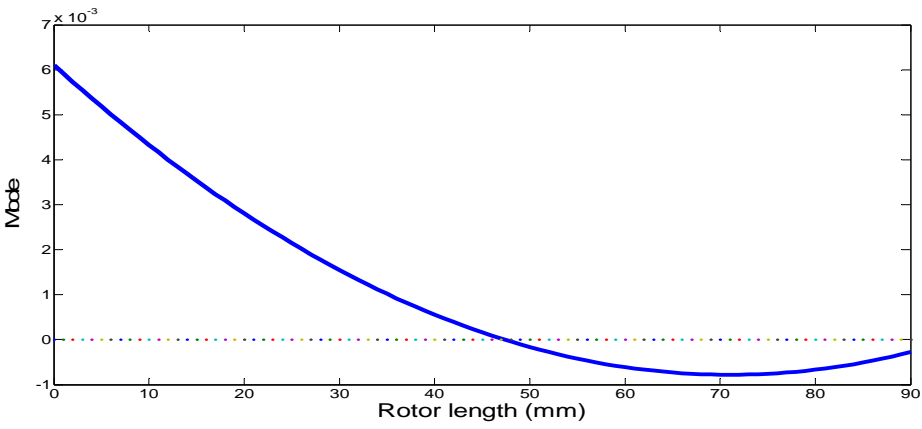
(c) The second forward mode



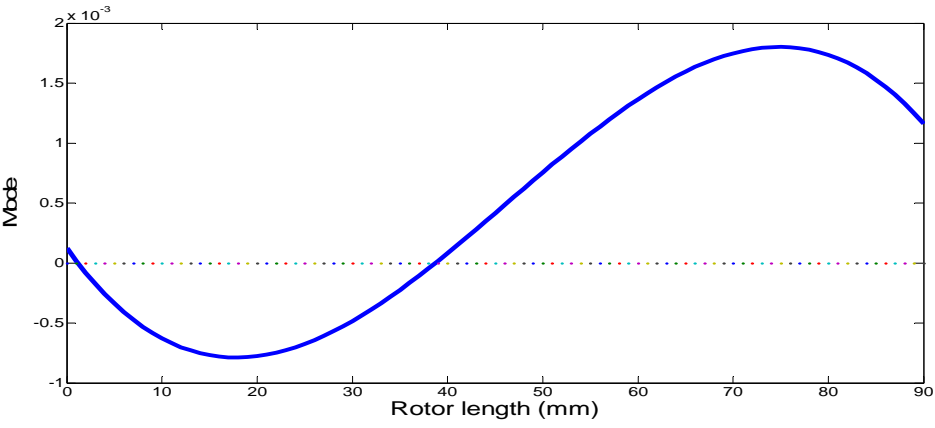
(d) The second reverse mode



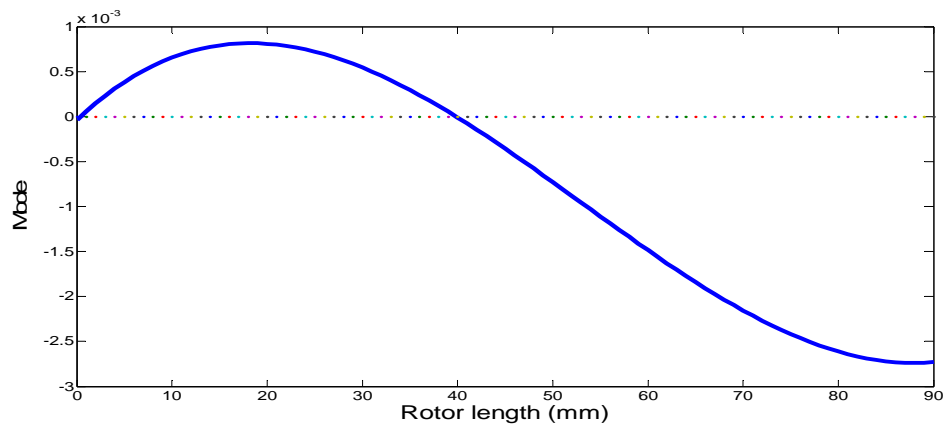
(e) The third forward mode



(f) The third reverse mode



(g) The fourth forward mode



(h)

Figure 5. 4. Turbocharger mode shapes with an equivalent bearing stiffness coefficient of 10^{10} N/m at the rotational speed of 8,000 rad/s

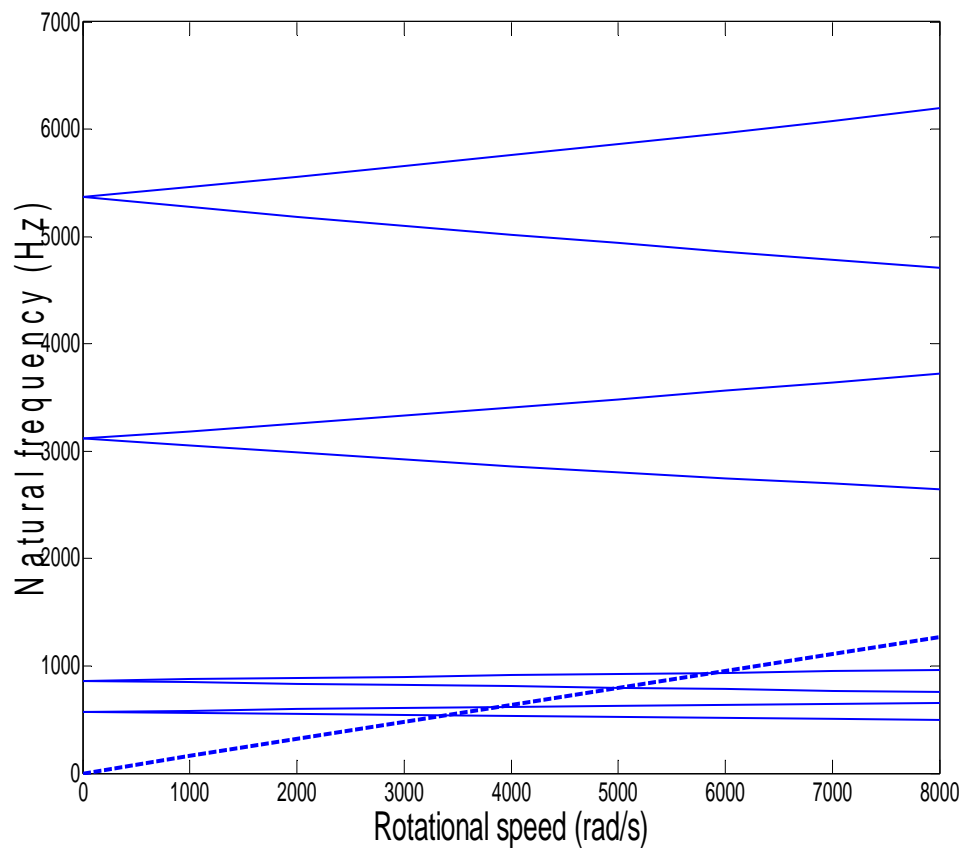
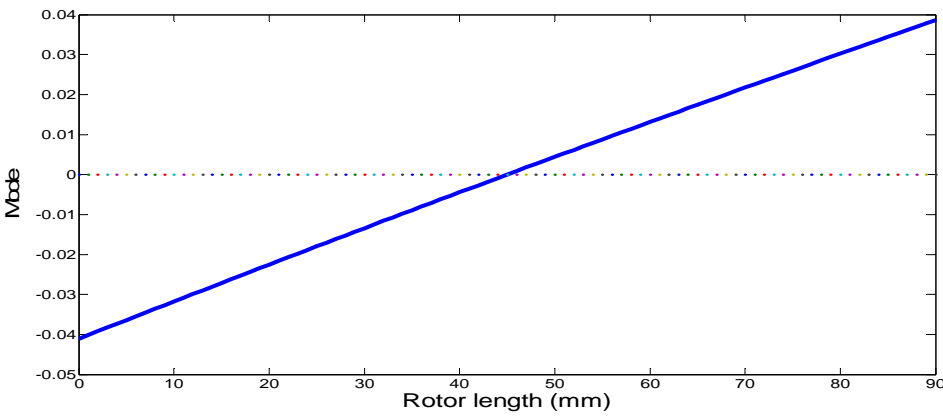
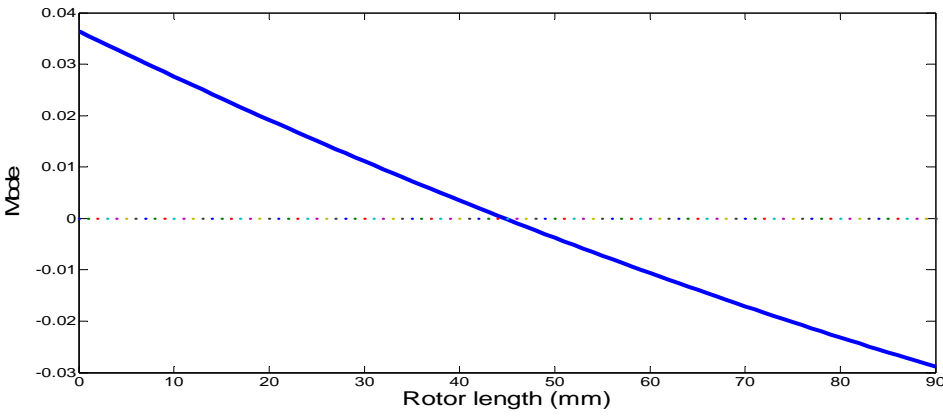


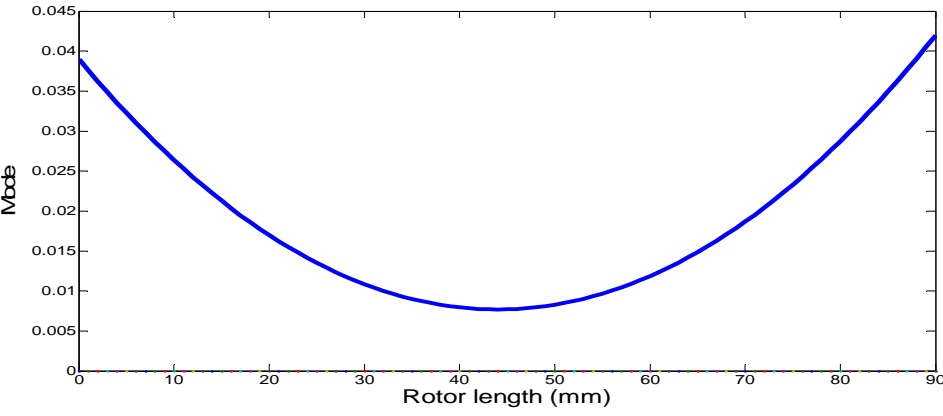
Figure 5. 5. A Campbell diagram of the turbocharger rotor system with an equivalent stiffness coefficient of 10^7 N/m



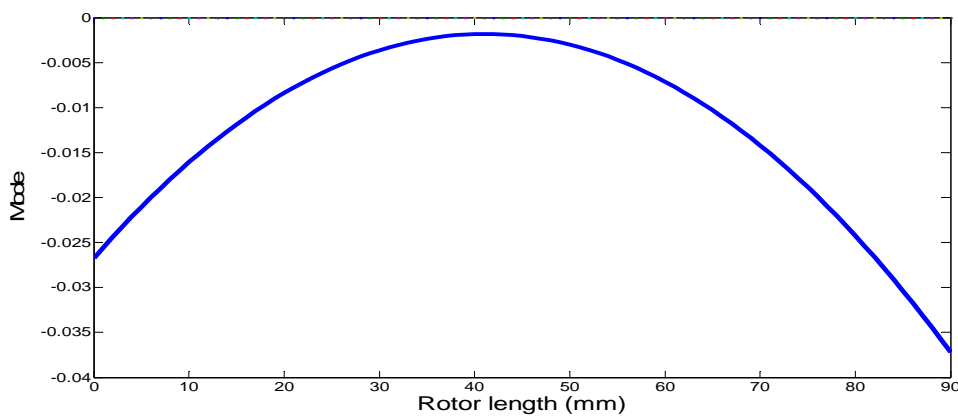
(a) The first forward mode



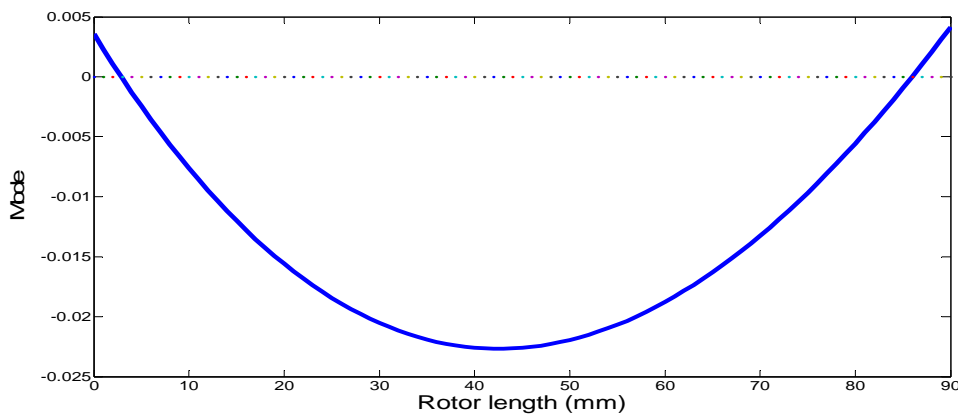
(b) The first reverse mode



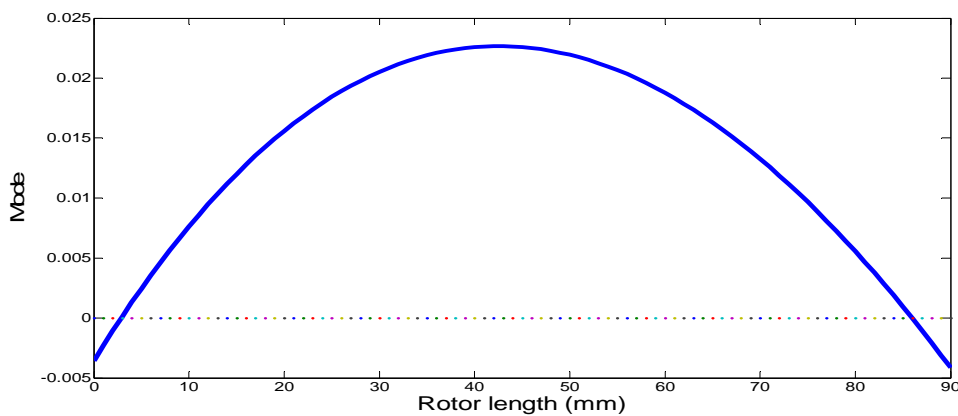
(c) The second forward mode



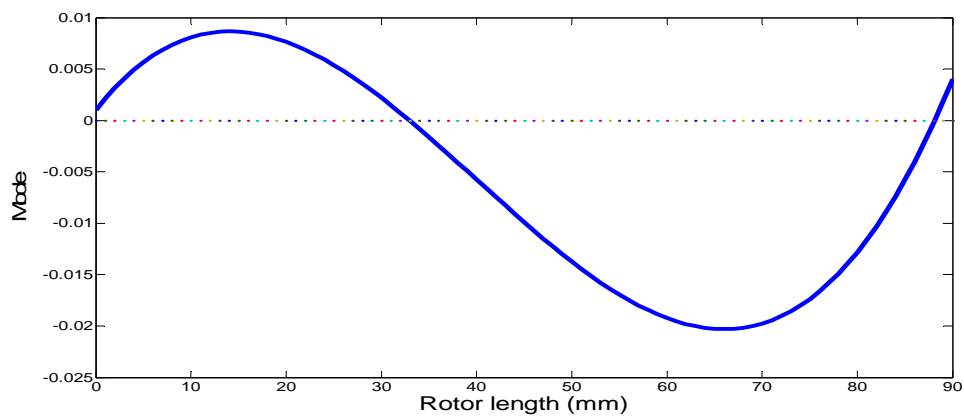
(d) The second reverse mode



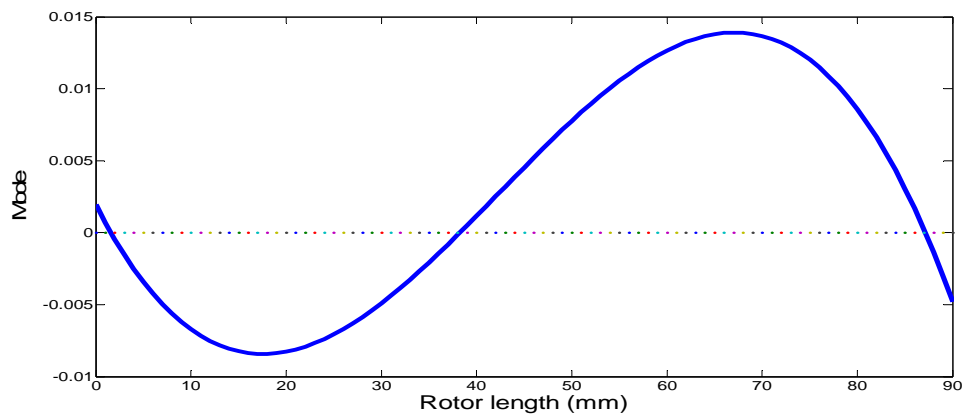
(e) The third forward mode



(f) The third reverse mode



(g) The fourth forward mode



(h) The fourth reverse mode

Figure 5. 6. Turbocharger mode shapes with an equivalent bearing stiffness coefficient of 10^7 N/m at the rotational speed of 8,000 rad/s

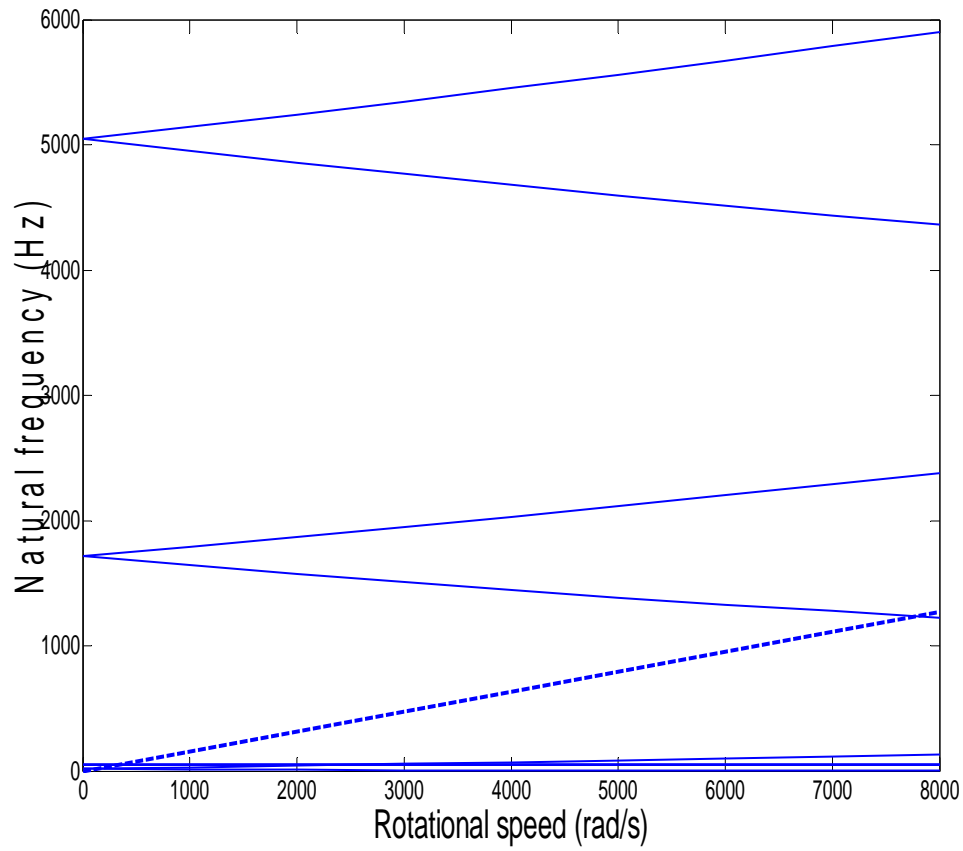
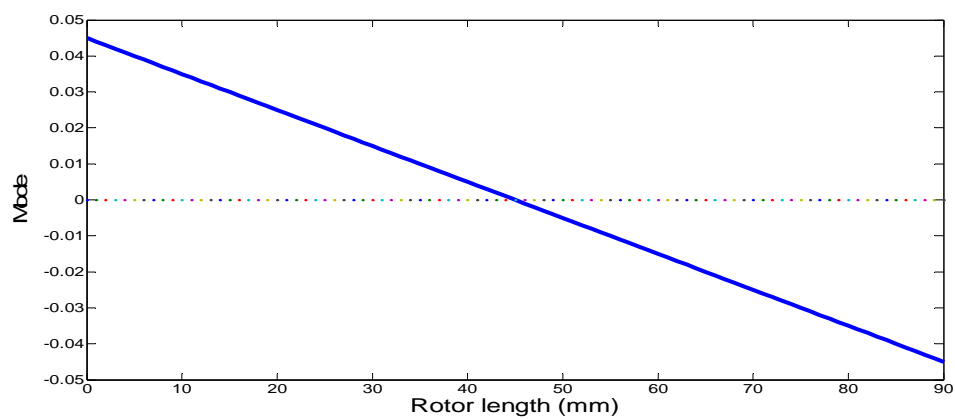
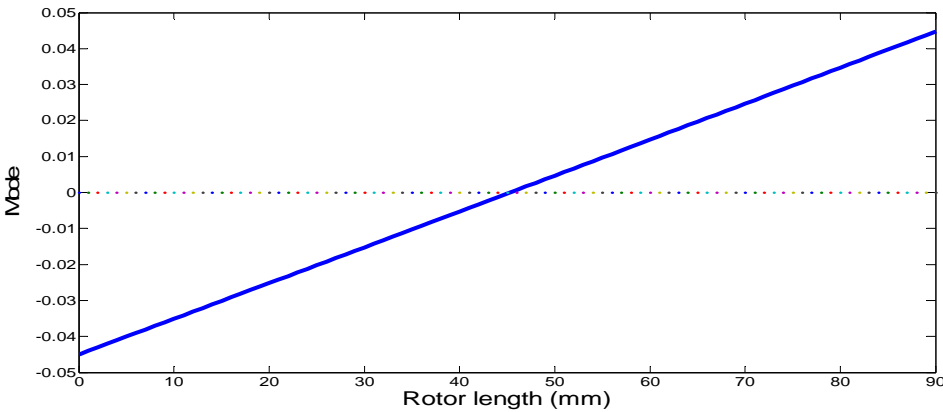


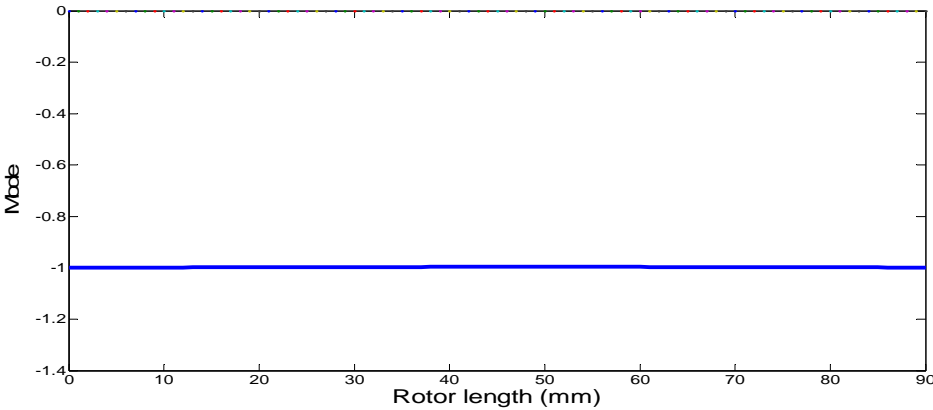
Figure 5. 7. A Campbell diagram of the turbocharger rotor system with an equivalent stiffness coefficient of 10^4 N/m



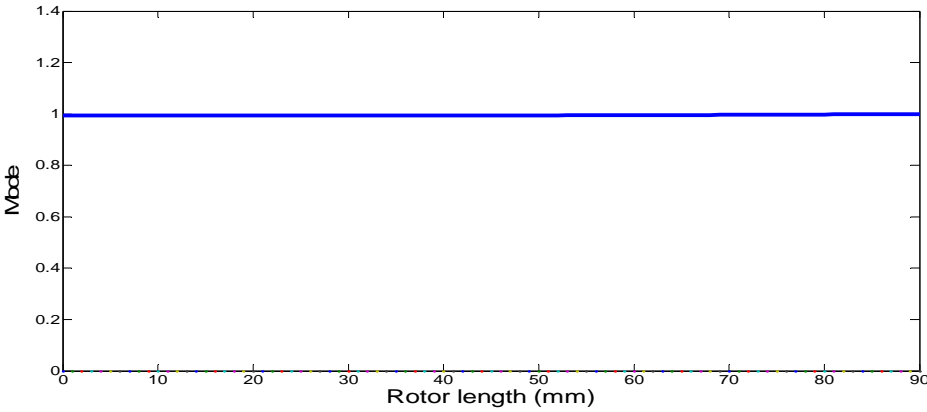
(a) The first forward mode



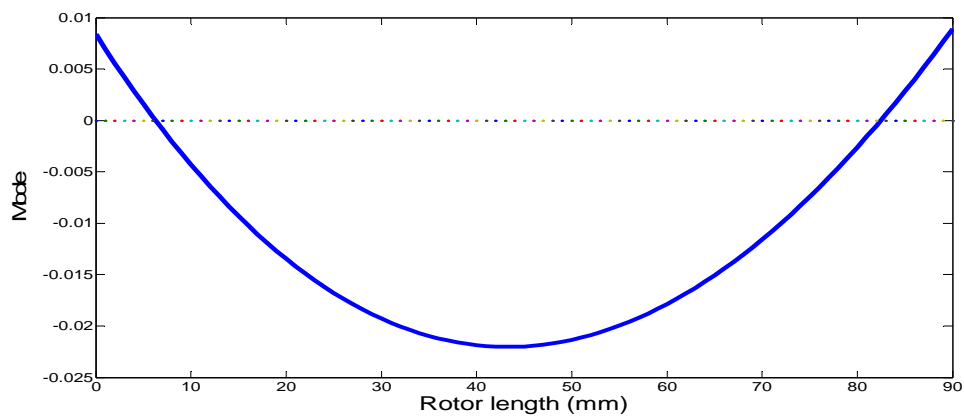
(b) The first reverse mode



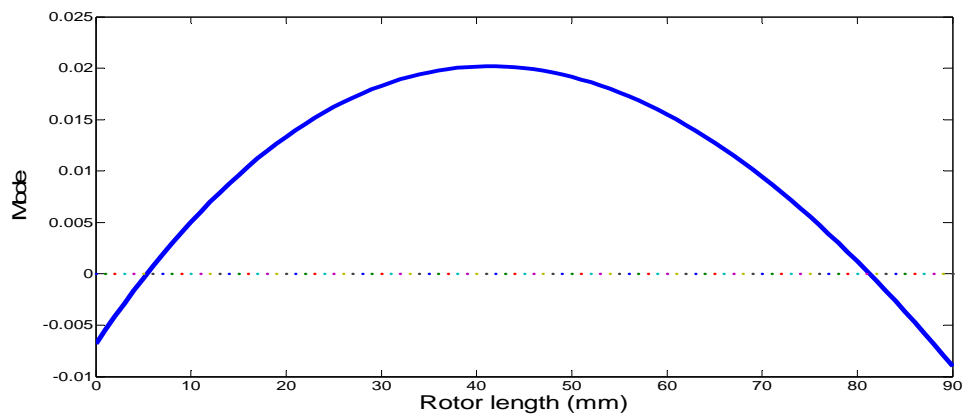
(c) The second forward mode



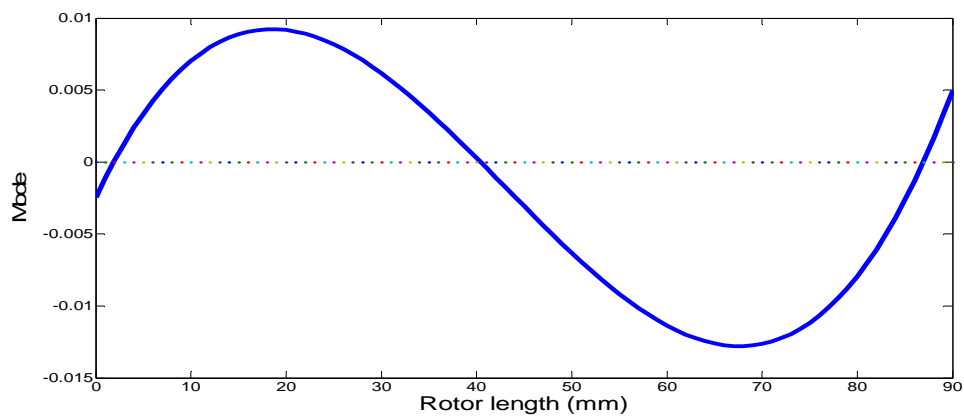
(d) The second reverse mode



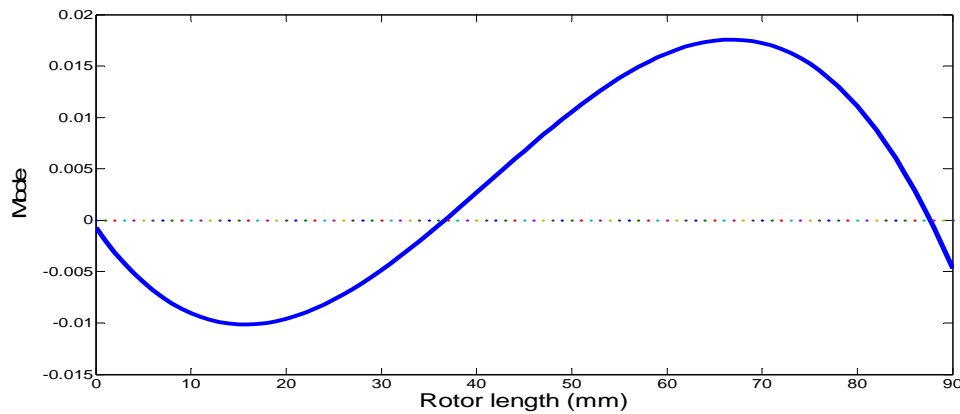
(e) The third forward mode



(f) The third reverse mode



(g) The fourth forward mode



(h) The fourth reverse mode

Figure 5. 8. Turbocharger mode shapes with an equivalent bearing stiffness coefficient of 10^4 N/m at the rotational speed of 8,000 rad/s

The mode shapes of a rotor correspond to its natural frequencies. As the rotor works at critical speeds, the corresponding mode shapes will be excited. It can be deduced from the simulation results that the conical mode can be excited at a low speed. As the rotational speed is further increased, translational mode and bending mode can be excited successively. If increasing the speed further, the local mode might occur. However, not all of those mode shapes will be excited, even if the rotor speed can cover the corresponding critical speeds, which also depends on the stiffness and damping of the support.

5.4 Summary

In this chapter, modal analysis is carried out for a free rotor and a turbocharger rotor system based on the mathematical model. The critical speeds and mode shapes are calculated. The effect of the stiffness of the support on the critical speed and the mode shapes are analyzed.

CHAPTER SIX

STABILITY ANALYSIS OF A TURBOCHARGER ROTOR SYSTEM UNDER MULTI-FIELD COUPLED FORCES

The system vibration and the stability are the key issues for a rotor bearing system. In addition, instability is one of the most common faults that might threaten the system security. In this chapter, the stability characteristics of a turbocharger rotor system have been investigated based on the simulation results. The effects of the rotor imbalance, lubricant viscosity, bearing clearances and lubricant feed pressure on the stability of the turbocharger rotor system have been studied.

6.1 Introduction to the motion of the Turbocharger Rotor System

The turbocharger rotor system is supported on a pair of hydrodynamic floating ring bearings which comprise of inner and outer fluid films in series. The stability characteristic is governed by the coupling of the rotor dynamics and the fluid dynamics. Compared to the single film journal bearing, two oil films inside floating ring bearings affect each other that makes the stability analysis of a turbocharger rotor system more complicated.

In this chapter, the developed mathematical dynamics model of a turbocharger rotor system has been introduced in which the rotor imbalance, the hydrodynamic fluid force, the lubricant feed pressure and the dead weight have been considered. The nonlinear hydrodynamic fluid forces have been expressed by extending the Capone hydrodynamic force model. Following model development, the bending vibration of the turbocharger rotor system has been calculated by the numerical integration. Based on the simulation results, the effects of rotor imbalance, lubricant viscosity, bearing clearances and lubricant feed pressure on the stability of the turbocharger rotor system have been studied. The stability of the two films and the dynamic performances of the rotor system have been concluded.

6.2 Stability Analysis of a Turbocharger Rotor System

6.2.1 Stability characteristics of the floating ring bearing

The objective of the stability analysis of a journal bearing is to study the instability phenomenon under the high speed lubricant flow. The journal centreline generally works

steadily at the static equilibrium position until the shaft velocity reaches a certain value when the journal centreline will be whirling around the static equilibrium position. In the case of small perturbation, the trajectory of the journal appears to be similar to the ellipse, while in the case of large perturbation, the trajectory deviates from the ellipse and performs a more complex locus.

Compared to single film journal bearings, the floating ring bearings of turbochargers comprise of double oil films. The outer film is formed by the fixed bearing shell and the ring, and the inner oil film is formed by the journal and the ring. According to the theory of fluid lubrication, we see that the oil film is formed between a fixed surface and a rotating surface running at the sum rotational velocity. Theoretically speaking, the whirling frequency should be around 50% of the ring's velocity when the instability occurs in the outer oil film and the whirling frequency should be around 50% of the sum of the journal and ring when the instability occurs in the inner oil film. However, due to the interaction of two films and the influences of working conditions, the stability discipline of the floating ring bearing is more complex than it appears.

In the following sections, the effects of the rotor imbalance, lubricant viscosity, bearing clearances and lubricant feed pressure on the stability of the turbocharger rotor system have been studied based on the simulation results. It should be noted that the simulation speed range is between 0 and 8000rad/s.

6.2.2 Influences of the rotor imbalance

Rotor imbalance is the most common fault for the rotor systems. The centrifugal forces

caused by the rotor imbalance can excite the synchronous motion, the angular frequency of which is approximately the same as the shaft velocity. In addition, the rotor imbalance can also affect the stability of the rotor system. Table 6.1 lists simulation parameters in the rotor imbalance analysis.

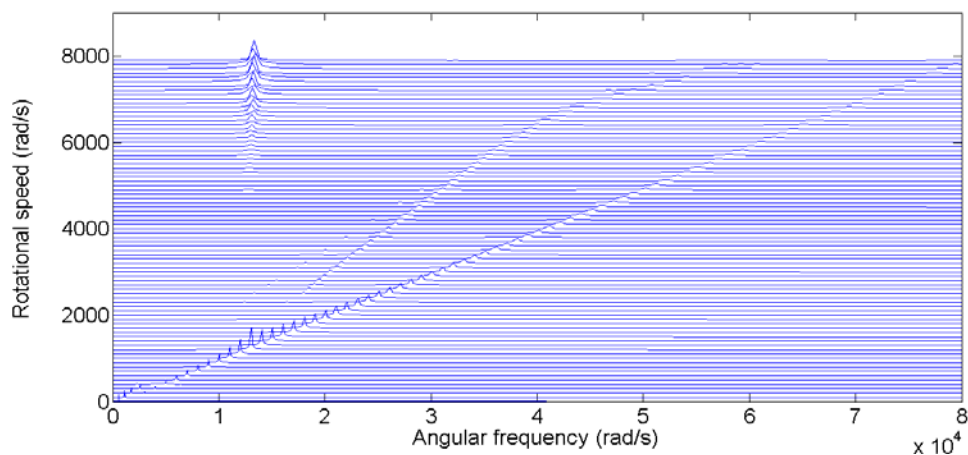
Table 6. 1. Simulation parameters in the rotor imbalance analysis

Parameters	Values
Lubricant viscosity	15cp
Outer radius of the ring	9mm
Inner radius of the ring	5mm
Outer clearance of the bearing	80 μ m
Inner clearance of the bearing	20 μ m
Static load on floating ring	0

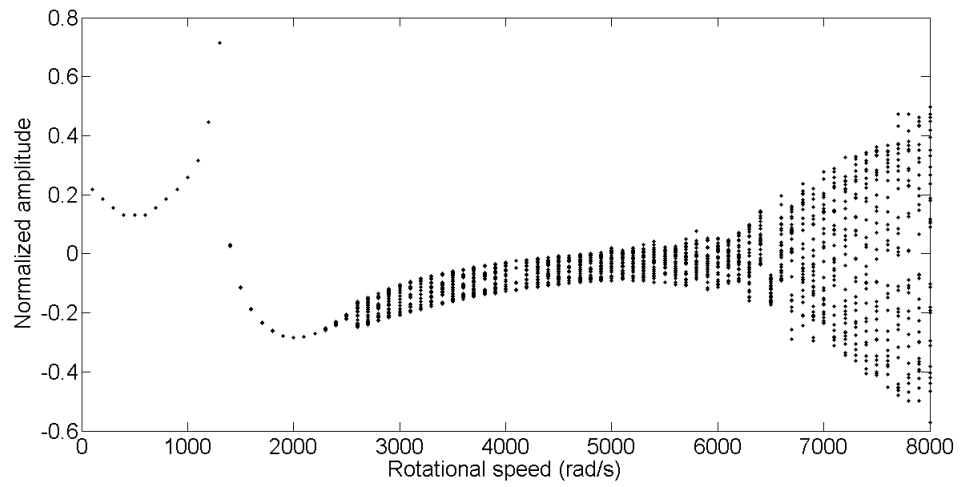
The rotor imbalance is assumed to be exerted on the turbine node in the theoretical model.

The following figures are based on the predicted displacements of the turbocharger shaft.

Normalized angular frequency denotes the frequency ratio relative to the shaft velocity.

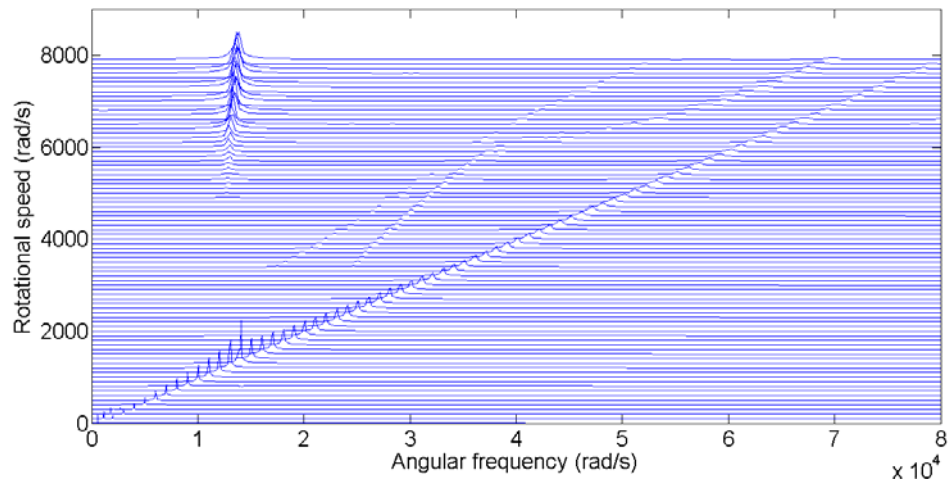


(a)

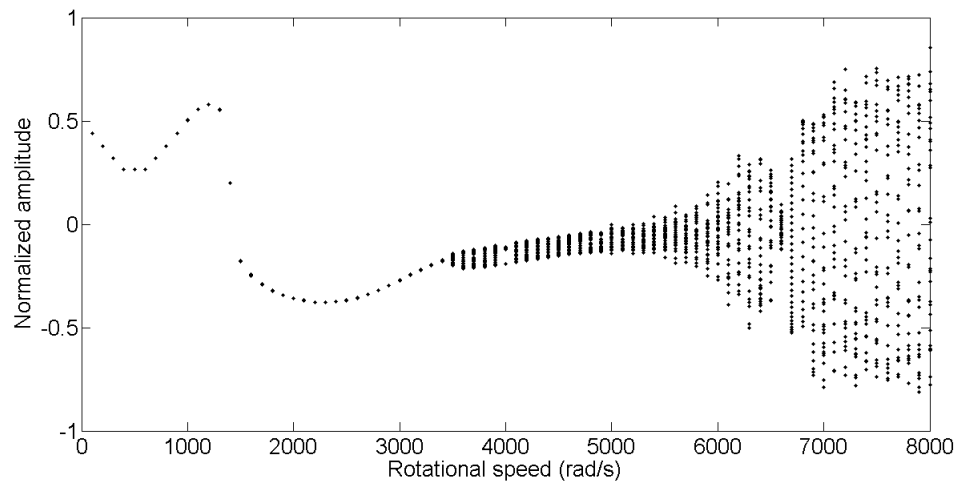


(b)

Figure 6. 1. Displacement of the turbocharger shaft under 10^{-5} kgm rotor imbalance at the turbine impeller: (a)Waterfall diagram (b)Bifurcation diagram

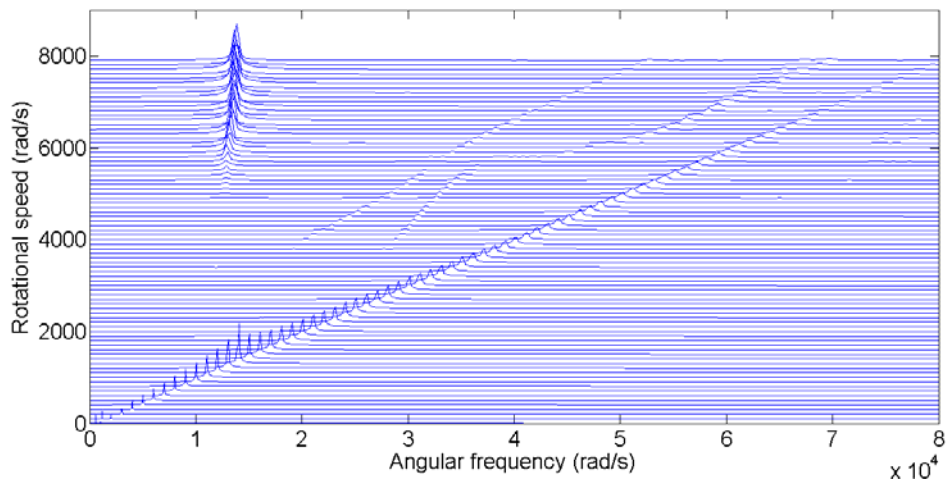


(a)

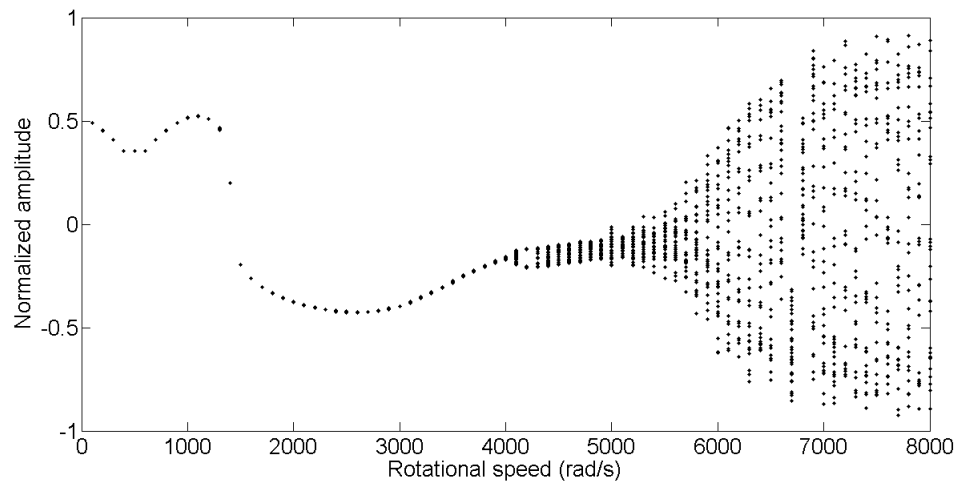


(b)

Figure 6.2. Displacement of the turbocharger shaft under 2.5×10^{-5} kgm rotor imbalance at the turbine impeller: (a) Waterfall diagram (b) Bifurcation diagram



(a)

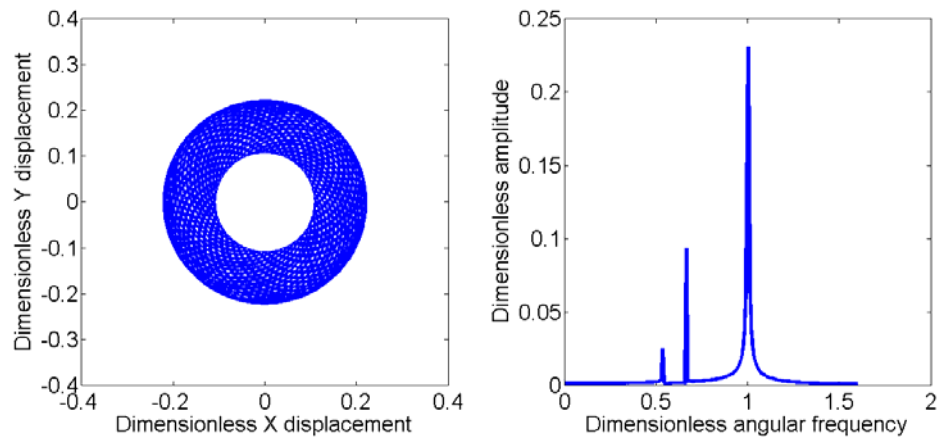


(b)

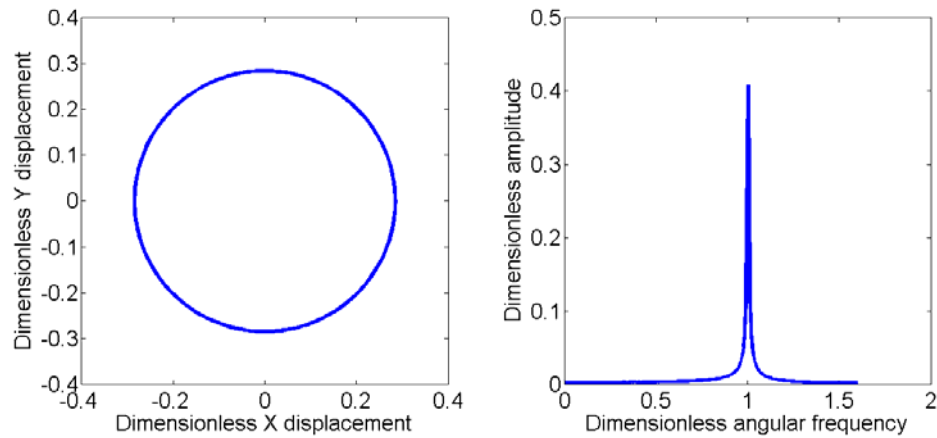
Figure 6. 3. Displacement of the turbocharger shaft under 5×10^{-5} kgm rotor imbalance at the turbine impeller: (a)Waterfall diagram (b)Bifurcation diagram

Figures 6.1 to 6.3 show the waterfall and global bifurcation diagrams of the displacement of the turbocharger shaft under 2.5×10^{-5} kgm , 2.5×10^{-5} kgm and 5×10^{-5} kgm rotor imbalance at the turbine impeller respectively. It can be seen from Figure 6.1 that the synchronous component exists within the whole speed range. It dominates the displacement of turbocharger rotor system until 2600rad/s, at which the instability occurs in the inner oil film. As the rotational speed is increased to approximate 6700rad/s, the instability in outer oil film commences to be excited. Compared to the inner oil film instability, the amplitude of the rotor system under outer oil film instability is larger. As is shown in Figure 6.2, the synchronous component appears and dominates the rotor system displacement below 3500rad/s under 2.5×10^{-5} kgm , when the instability in the inner oil film is excited. At approximate 6000rad/s and over, the instability occurs in the outer oil film. Under 5×10^{-5} kgm , as is shown in Figure 6.3, the turbocharger shaft shows

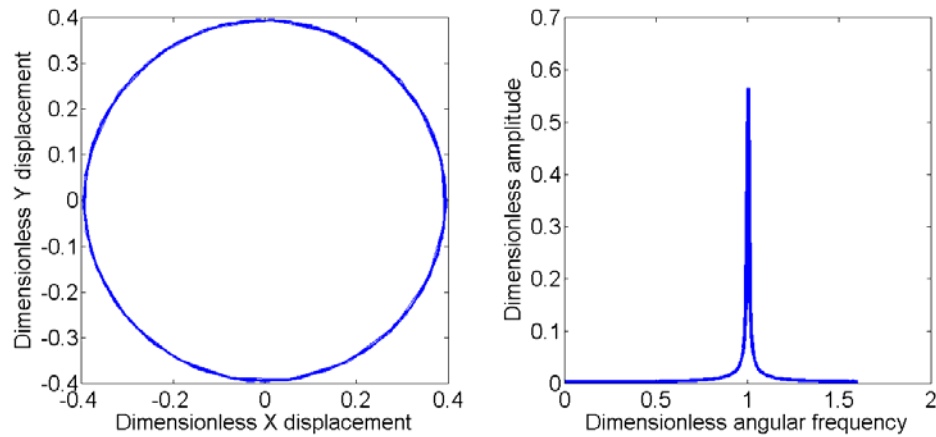
periodical motion below 4100rad/s. The instability commences to occur at approximate 4100rad/s in the inner oil film. The outer film instability occurs at over 5000rad/s and persists until a high speed.



(a)



(b)



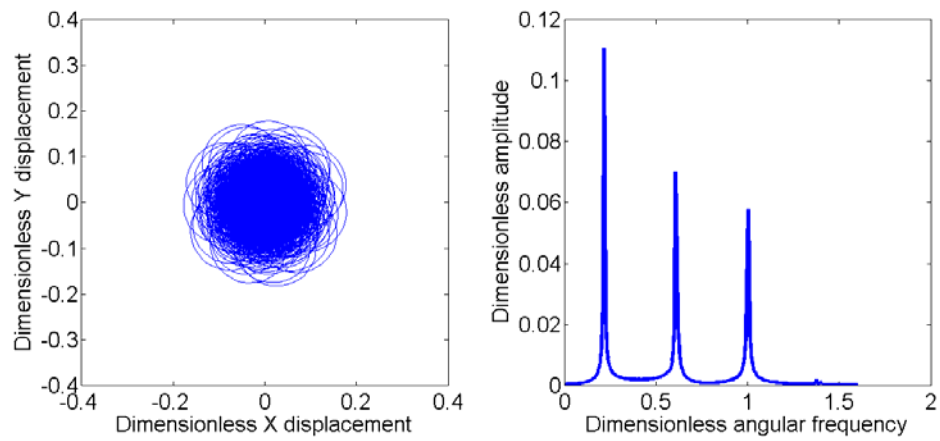
(c)

Figure 6. 4. The spectrum and trajectory of the turbocharger shaft at 3000rad/s:

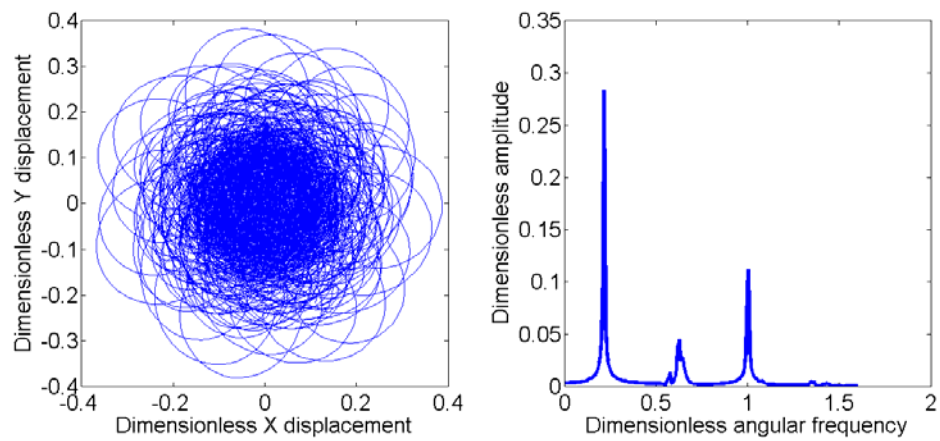
(a) under 10^{-5} kgm rotor imbalance (b) under 2.5×10^{-5} kgm rotor imbalance

(c) under 5×10^{-5} kgm rotor imbalance

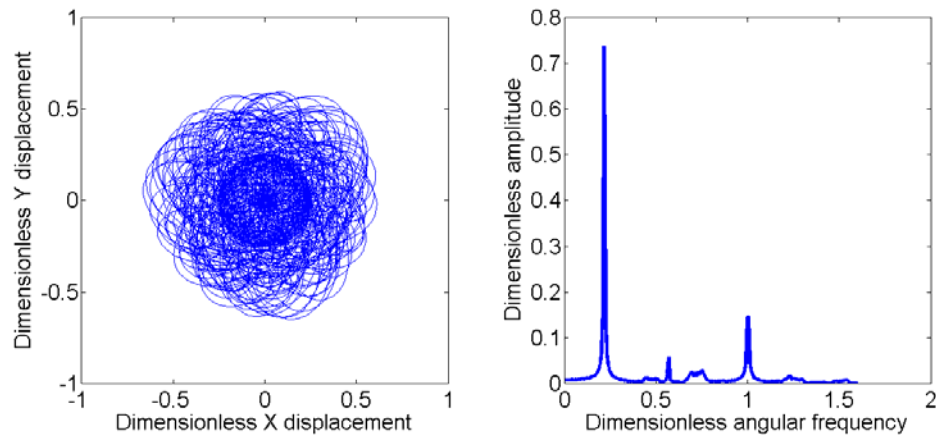
Figure 6.4 shows the trajectory and spectrum of the turbocharger shaft at 3000rad/s. It can be seen that the system shows periodical motion under 2.5×10^{-5} kgm and 5×10^{-5} kgm rotor imbalance. Under 10^{-5} kgm rotor imbalance, a subsynchronous component is excited with the frequency of 60% of the shaft speed, which illustrates the appearance of the instability of the inner oil film.



(a)



(b)



(c)

Figure 6. 5. The spectrum and trajectory of the turbocharger shaft at 6000rad/s:

(a) under 10^{-5} kgm rotor imbalance (b) under 2.5×10^{-5} kgm rotor imbalance

(c) under 5×10^{-5} kgm rotor imbalance

Figure 6.5 show the spectrum and trajectory of the turbocharger shaft at 6000rad/s. Turbocharger rotor system perform the irregular trajectories under three rotor imbalance at such a high speed. Under 2.5×10^{-5} kgm and 5×10^{-5} kgm rotor imbalance, the instability of outer oil film dominates the system motion. Under 10^{-5} kgm rotor imbalance, both the synchronous and two subsynchronous components exist simultaneously with similar amplitudes

It can therefore be concluded that the rotor imbalance can lead to the appearance of the synchronous component in the turbocharger rotor system, the angular frequency of which is equal to the shaft velocity. The larger rotor imbalance, the larger amplitude of the rotor system appears especially at a relatively low speed range. The centrifugal force can inhibit the appearance of the instability in the inner oil film. However, the instability in outer oil

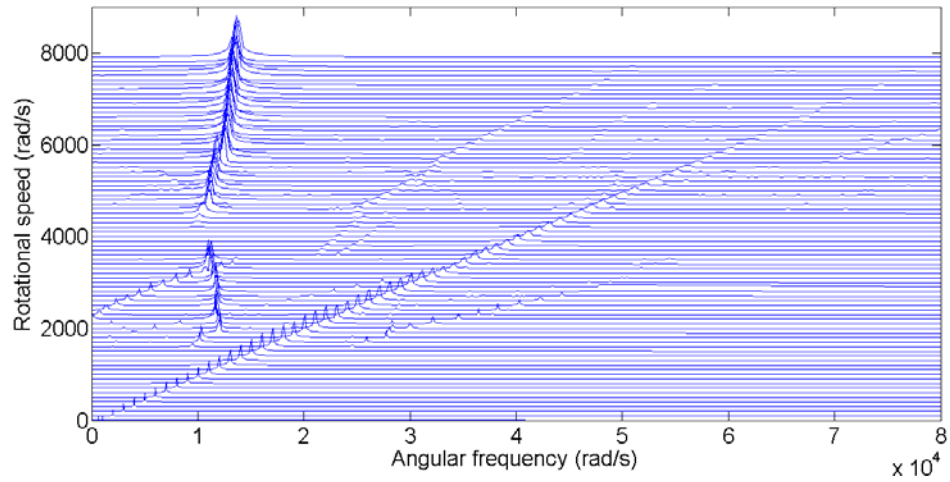
film can be excited at a lower speed, when the amplitude of the rotor system becomes larger.

6.2.3 Influences of the lubricant viscosity

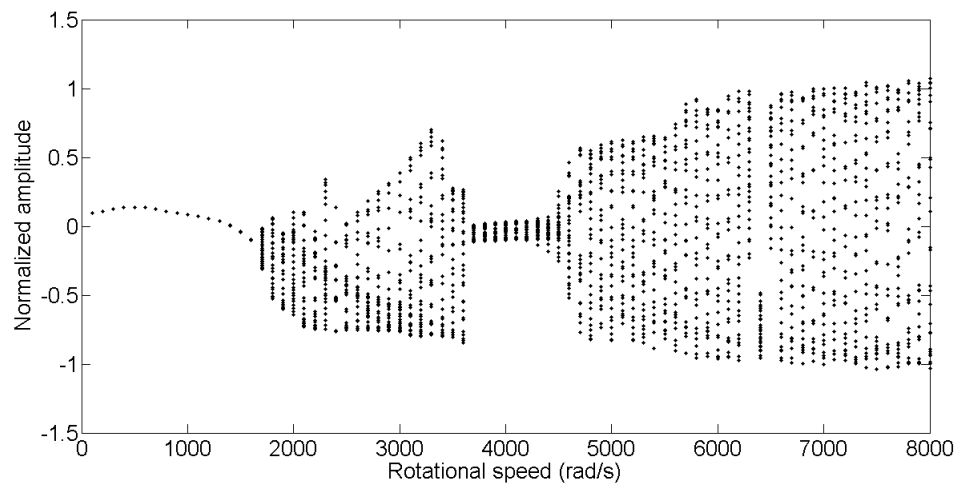
The lubricant viscosity affects the characteristics of the lubricant flow in the bearing clearances which might influence the oil film pressure distribution and the hydrodynamic fluid forces around the shaft and the ring. Therefore, the stability of the turbocharger rotor system will be affected. Table 6.2 lists the simulation parameters in the lubricant viscosity analysis.

Table 6. 2. Simulation parameters in the lubricant viscosity analysis

Parameters	Values
Outer radius of the ring	9mm
Inner radius of the ring	5mm
Outer clearance of the bearing	80μm
Inner clearance of the bearing	20μm
Imbalance on turbine node	2.5×10^{-5} kgm
Static load on floating ring	0



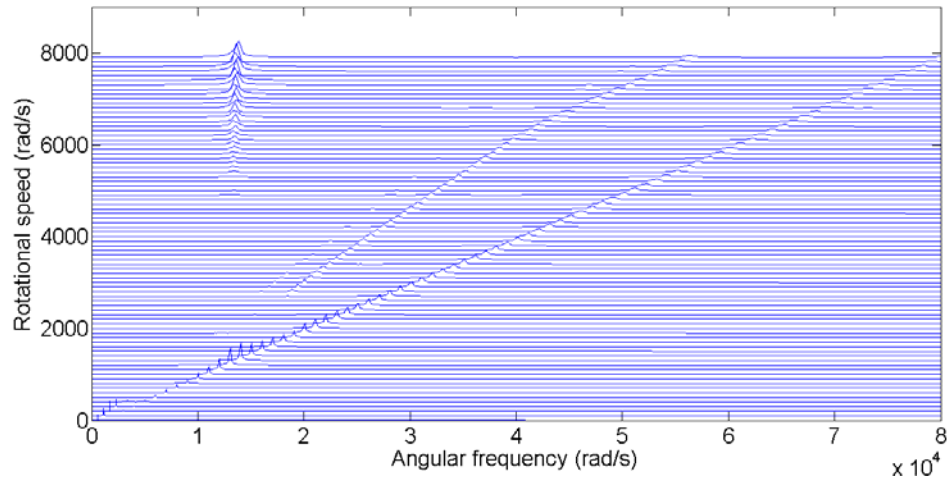
(a)



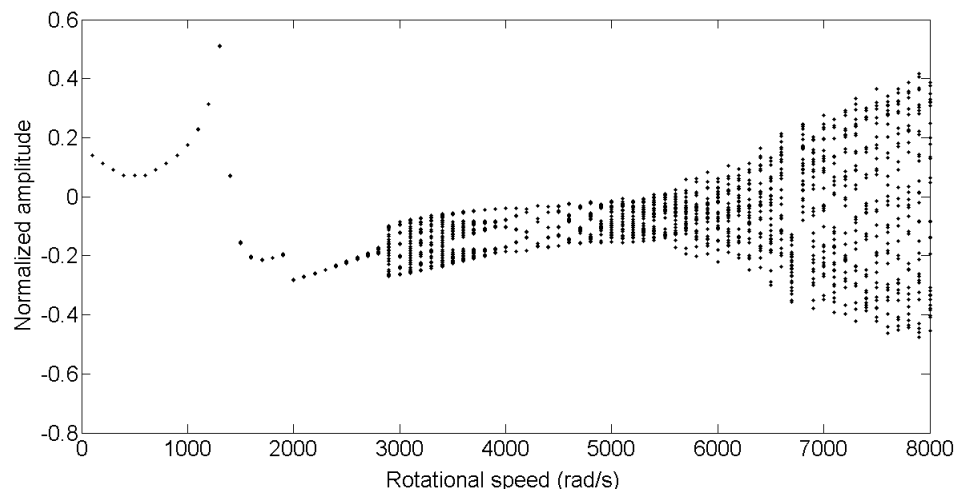
(b)

Figure 6. 6. Displacement of the turbocharger shaft under 5cp lubricant viscosity:

(a)Waterfall diagram (b)Bifurcation diagram



(a)



(b)

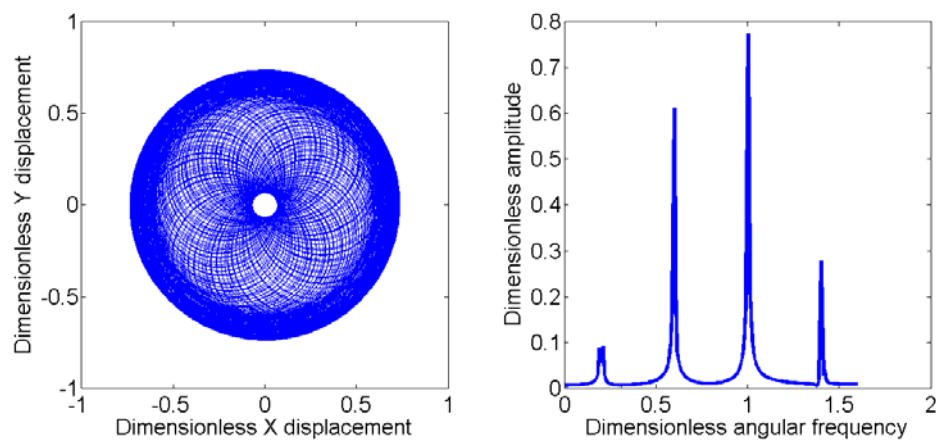
Figure 6. 7. Displacement of the turbocharger shaft under 35cp lubricant viscosity:

(a)Waterfall diagram (b)Bifurcation diagram

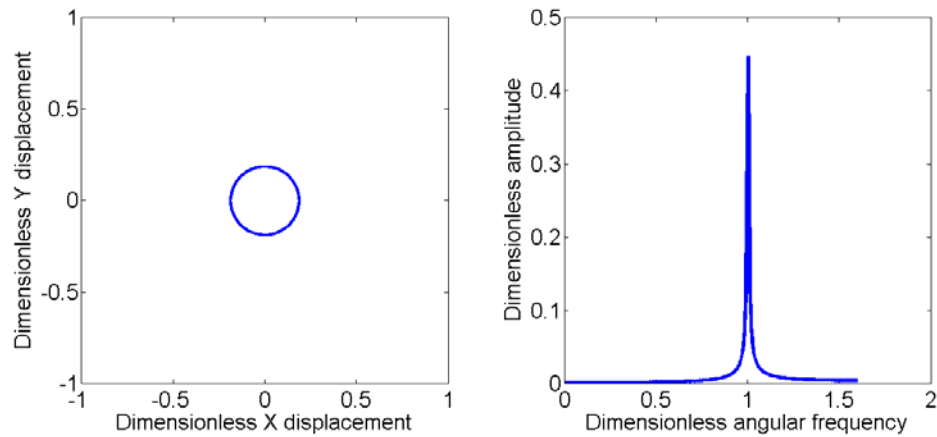
Figures 6.6 and 6.7 illustrate the waterfall and bifurcation diagrams of the displacement of the turbocharger shaft under 5cp and 35cp lubricant viscosities respectively. From Figure 6.6, it can be seen that the dominant displacement for the turbocharger shaft is the synchronous component. The instability commences to occur at 1700rad/s in the inner oil film. Within the speed range of 1700rad/s to 3600rad/s, system motion is dominated by the

inner oil film instability. Moreover, the frequency of the instability is nearly locked rather than increase as the rotational speed is increased. Over approximate 4500rad/s, the instability is excited in the outer oil film. Under 35cp lubricant viscosity, as shown in Figure 6.7, turbocharger shaft performs a periodical motion below 2900rad/s when the instability is excited in the inner oil film. The instability in the outer oil film occurs at approximate 6700rad/s.

Figure 6.8 shows the trajectory and spectrum of the turbocharger shaft at 2000rad/s. Under 5cp lubricant viscosity, the rotor system performs a period doubling motion that includes both the synchronous and subsynchronous component simultaneously. The angular frequency of the subsynchronous component is approximately 60% of the shaft velocity. Under 35cp lubricant viscosity, the rotor system performs periodic motion, demonstrating that the instability still does not occur.



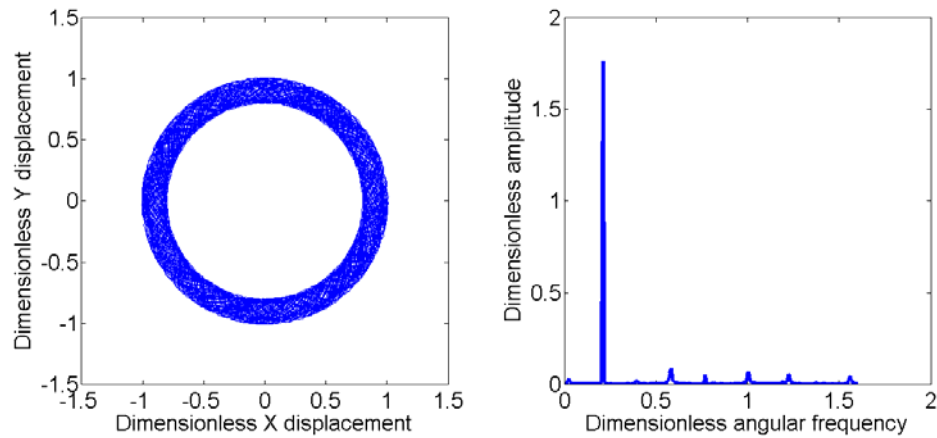
(a)



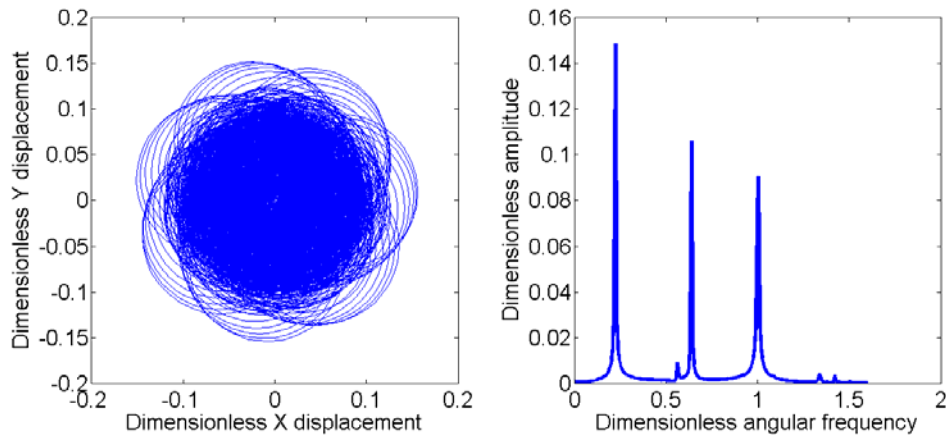
(b)

Figure 6. 8. The spectrum and trajectory of the turbocharger shaft at 2000rad/s:

(a)under 5cp lubricant viscosity (b)under 35cp lubricant viscosity



(a)



(b)

Figure 6. 9. The spectrum and trajectory of the turbocharger shaft at 6000rad/s:

(a)under 5cp lubricant viscosity (b)under 35cp lubricant viscosity

Figure 6.9 shows the spectrum and trajectory of the turbocharger shaft at 6000rad/s. Under 5cp lubricant viscosity, the motion of the turbocharger shaft is dominated by the subsynchronous component with the frequency of 20% of the shaft speed, which illustrates the instability occurs in the outer oil film. Under 35cp lubricant viscosity, the turbocharger shaft performs an irregular trajectory. Both the synchronous and two subsynchronous components exist simultaneously, but the amplitudes of them are much smaller compared to case of low lubricant viscosity.

Compared to the simulation results of 15cp, which is described in section 6.2.1, 5cp and 35cp lubricant viscosities, it can be concluded that the instability in both inner and outer oil films can be inhibited by a higher lubricant viscosity. Under a lower lubricant viscosity, instabilities of both oil films are excited at the lower speeds, when the system shows a dramatic motion. Under a higher viscosity, the instabilities occur at higher speeds,

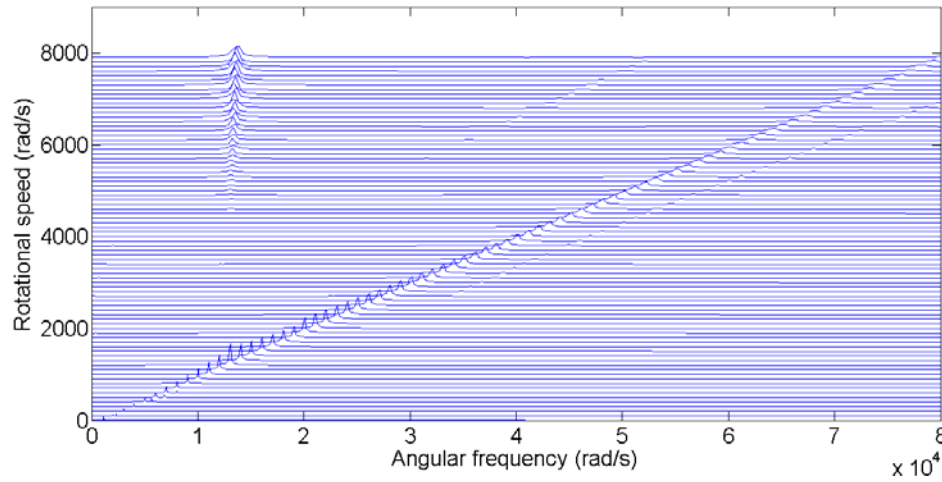
especially for the inner oil film instability. The amplitude under oil film instabilities are also inhibited.

6.2.4 Influences of bearing clearances

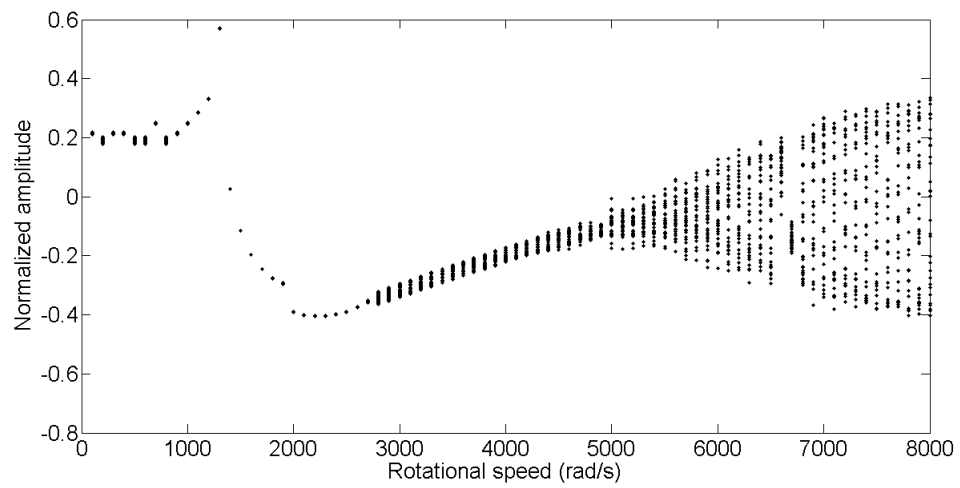
Under extreme working conditions, wear is a common fault for turbocharger hydrodynamic bearings. Due to dry friction during start-up and rub-impact phenomenon under high load, etc, bearing clearances may be changed after long term usage. In this section, the affects of inner and outer bearing clearances on the stability of the turbocharger rotor system are studied respectively. Table 6.3 lists simulation parameters in bearing clearances analysis.

Table 6. 3. Simulation parameters in the bearing clearances analysis

Parameters	Values
Lubricant viscosity	15cp
Outer radius of the ring	9mm
Inner radius of the ring	5mm
Outer clearance of the bearing	80 μ m ; 90 μ m ; 100 μ m
Inner clearance of the bearing	15 μ m ; 20 μ m ; 25 μ m
Rotor imbalance on turbine mass node	2.5×10^{-5} kgm
Static load on floating ring	0



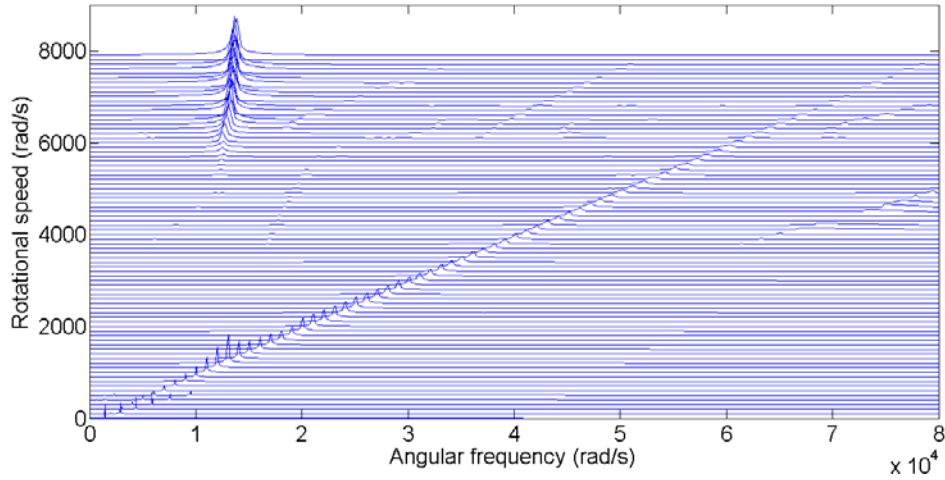
(a)



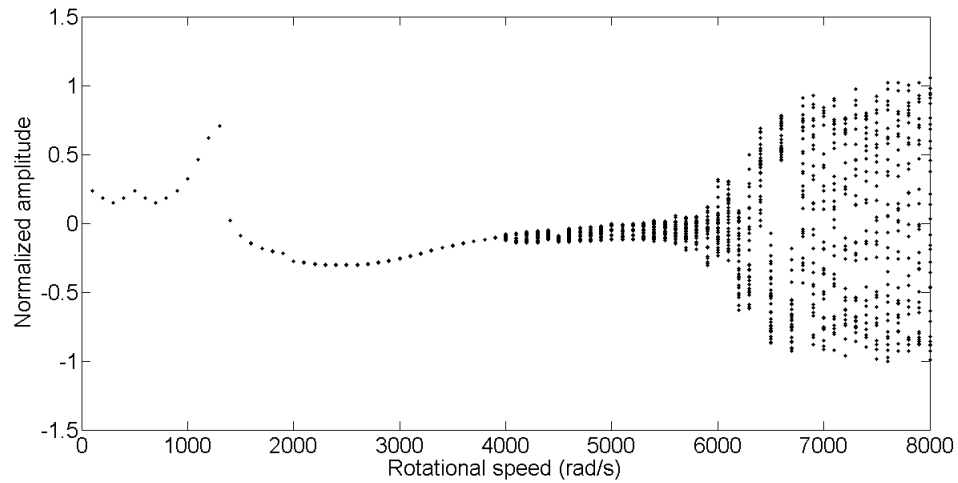
(b)

Figure 6. 10. Displacement of the turbocharger shaft under $15\mu\text{m}$ inner bearing clearance:

(a)Waterfall diagram (b)Bifurcation diagram



(a)



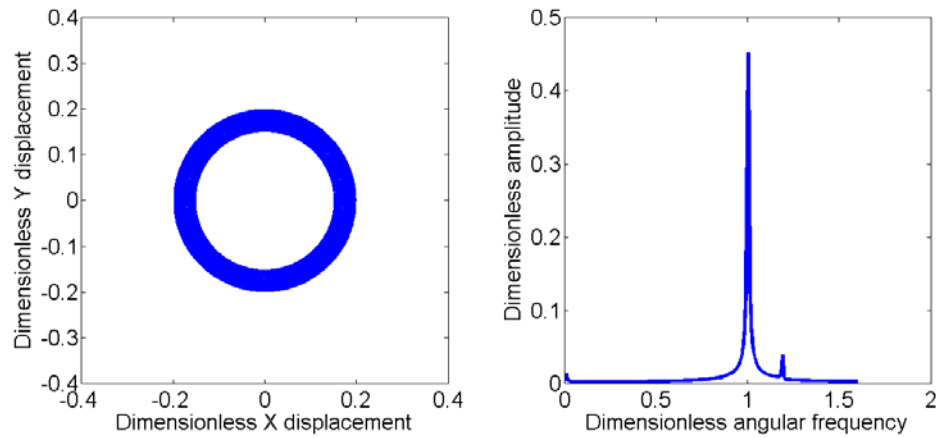
(b)

Figure 6. 11. Displacement of the turbocharger shaft under 25 μ m inner bearing clearance:

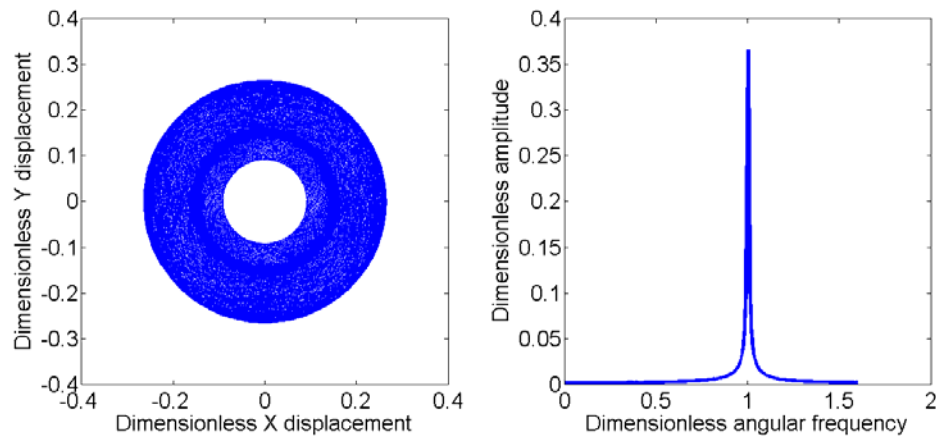
(a)Waterfall diagram (b)Bifurcation diagram

Figures 6.10 and 6.11 show the waterfall and bifurcation diagrams of the displacement of turbocharger shaft under 15 μ m and 25 μ m inner bearing clearances respectively. It can be seen from Figure 6.10 that under 15 μ m inner bearing clearance, the instability does not occur until the shaft speed reaches 2800rad/s, while the outer oil film enters instability at

5000rad/s.



(a)



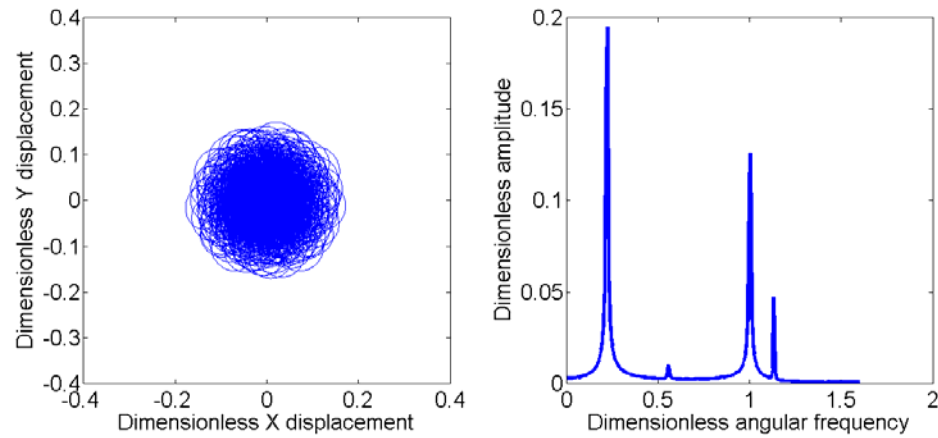
(b)

Figure 6. 12. The spectrum and trajectory of the turbocharger shaft at 3000rad/s:

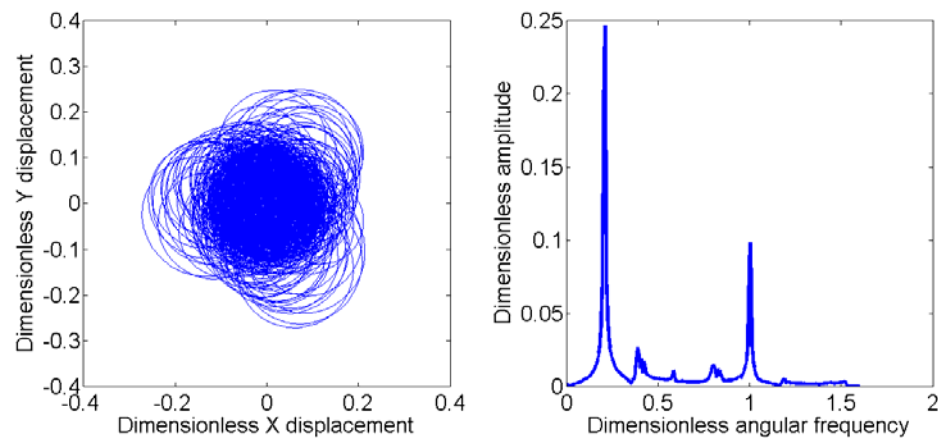
(a)under15 μ m inner bearing clearance (b)under25 μ m inner bearing clearance

Under 25 μ m inner bearing clearance, as shown in Figure 6.11, the rotational speed, at which the inner oil film instability occurs, is increased to 4000rad/s. The speed of outer oil film instability is also increased to 5900rad/s. On the other hand, under 25 μ m inner bearing clearance, the amplitude of the shaft motion during outer oil film instability is much larger

than that under $15\mu\text{m}$ inner bearing clearance.



(a)



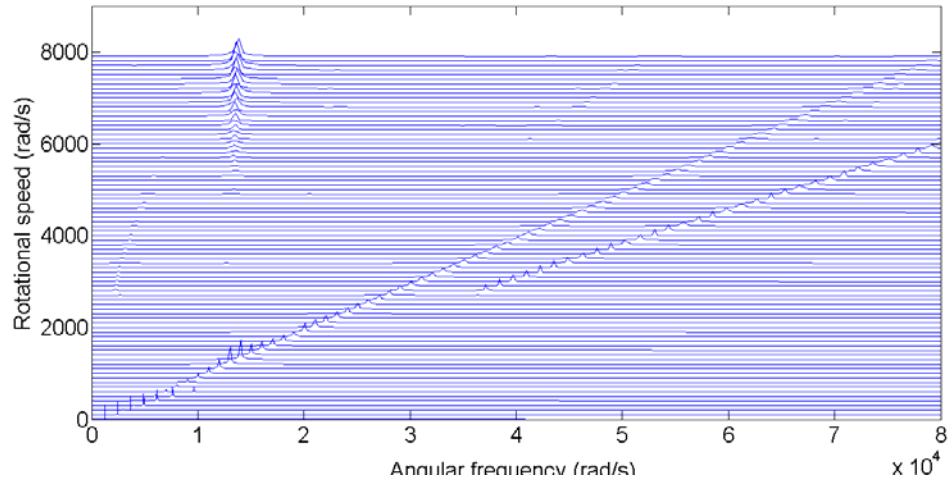
(b)

Figure 6. 13. The spectrum and trajectory of the turbocharger shaft at 6000rad/s:

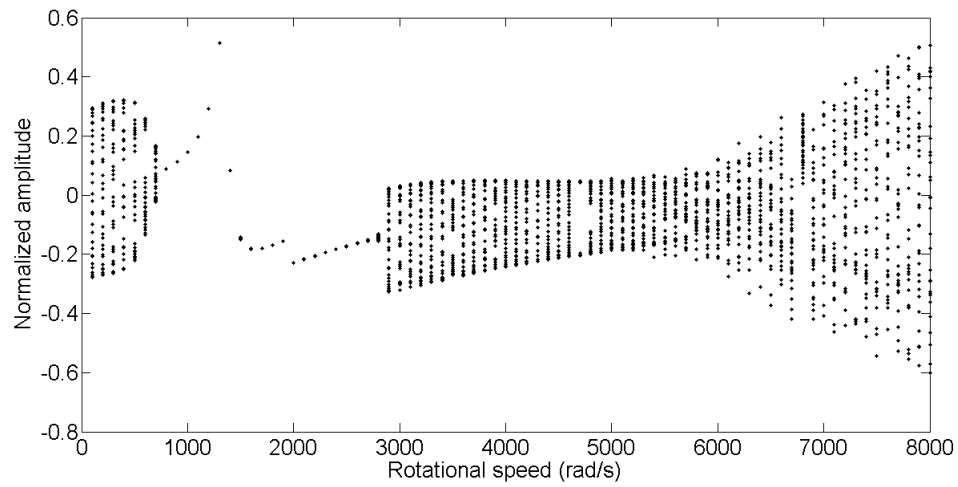
(a)under $15\mu\text{m}$ inner bearing clearance (b)under $25\mu\text{m}$ inner bearing clearance

Figure 6.12 shows the spectrum and trajectory of the turbocharger shaft at 3000rad/s. Turbocharger shaft performs a periodical motion under either or $25\mu\text{m}$ inner bearing clearance. The synchronous component dominates the system motion. At 6000rad/s, as shown in Figure 6.13, instabilities occur in the outer oil film under either or $25\mu\text{m}$ inner

bearing clearance. Trajectories become irregular. Under larger inner clearance, the amplitude of rotor system is larger.



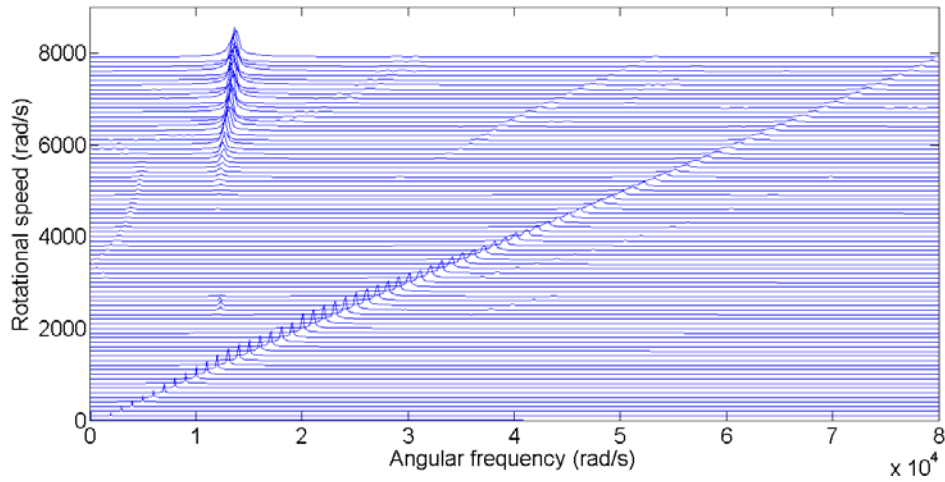
(a)



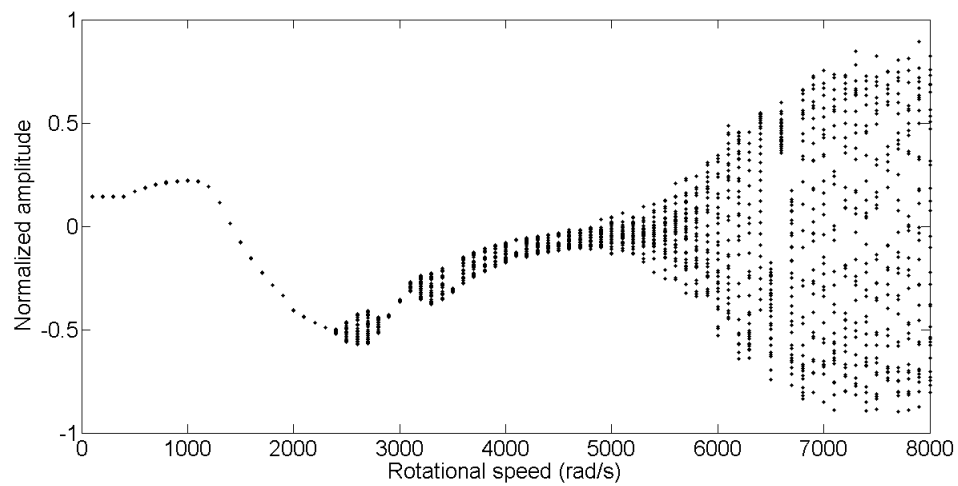
(b)

Figure 6. 14. Displacement of the turbocharger shaft under $70\mu\text{m}$ outer bearing clearance:

(a)Waterfall diagram (b)Bifurcation diagram



(a)



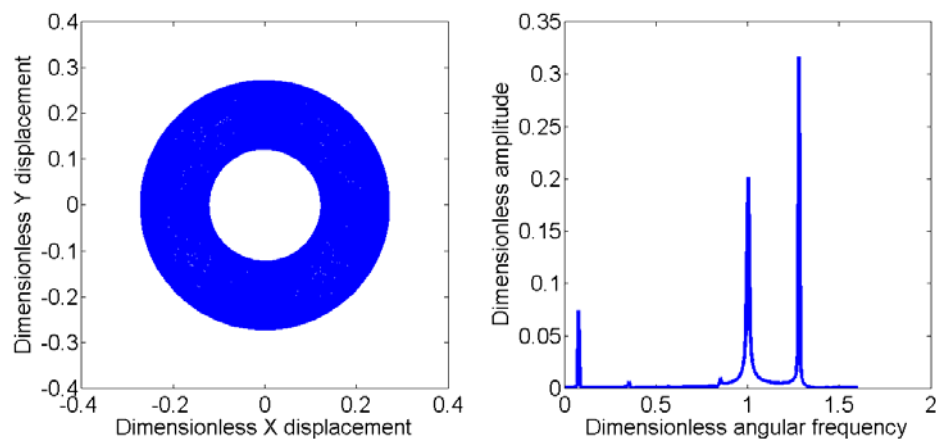
(b)

Figure 6. 15. Displacement of the turbocharger shaft under $90\mu\text{m}$ inner bearing clearance:

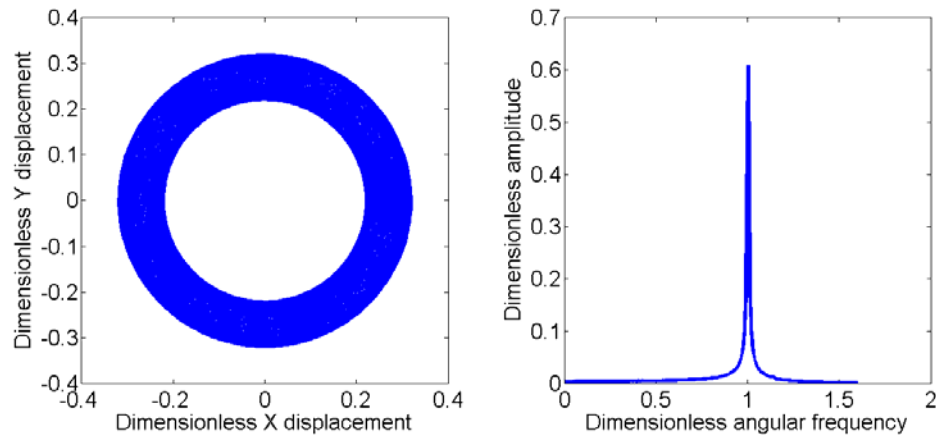
(a)Waterfall diagram (b)Bifurcation diagram

Figures 6.14 and 6.15 show the waterfall and bifurcation diagrams of the displacement of the turbocharger shaft under $70\mu\text{m}$ and $90\mu\text{m}$ outer bearing clearances respectively. When under $70\mu\text{m}$ outer bearing clearance, as shown in Figure 6.14, the turbocharger shaft performs a periodical motion within the speed range of 800rad/s to 2800rad/s , while

instability occurs in the inner oil film below 800rad/s. While the rotational speed is increased to 2800rad/s, a high order harmonic component is excited and persists until a high speed. Outer oil film instability commences to occur at approximate 6000rad/s. However, the inner oil film instability is not obvious within the whole speed range. Under 90 μ m outer bearing clearance, as shown in Figure 6.15, the synchronous component dominates the motion of turbocharger rotor system below 2500rad/s, when the instability commences to occur in the inner oil film. When the speed is higher than 4900rad/s, outer oil film instability is excited.



(a)

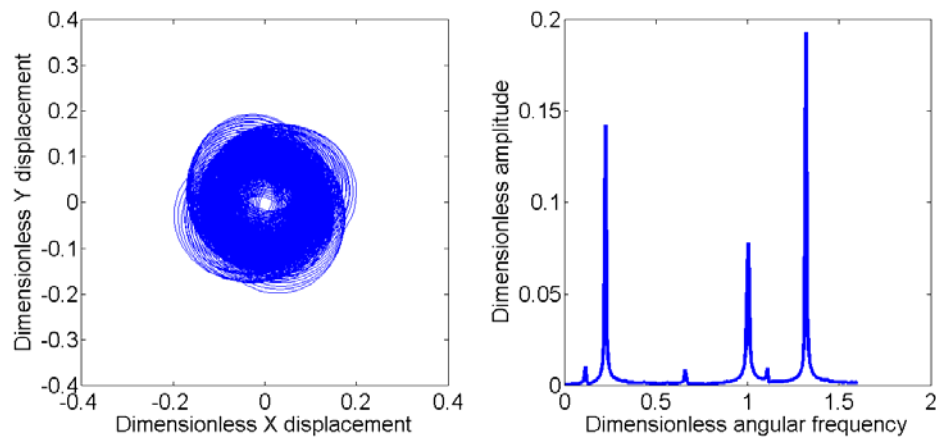


(b)

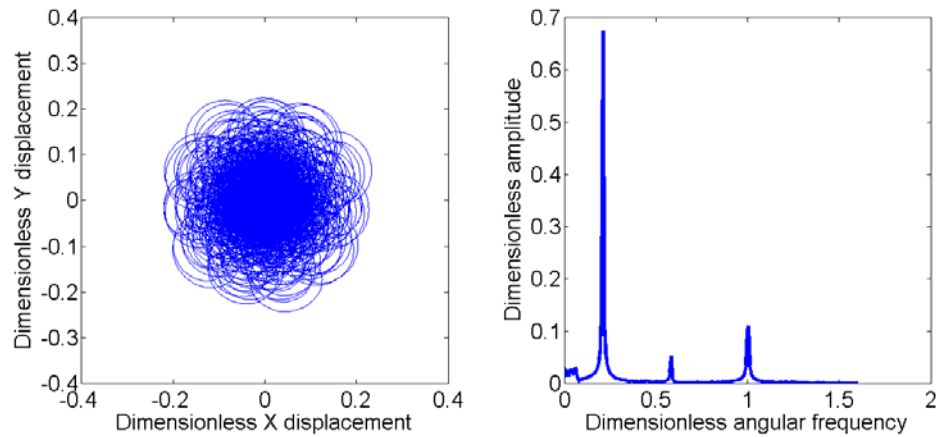
Figure 6. 16. The spectrum and trajectory of the turbocharger shaft at 3000rad/s:

(a)under 70 μ m outer bearing clearance (b)under 90 μ m outer bearing clearance

Figure 6.16 shows the spectrum and the trajectory of the turbocharger shaft at 3000rad/s. Under 70 μ m outer bearing clearance, besides the synchronous component, a high order harmonic component is also excited, which frequency is approximate 1.3 times of the shaft speed, while under 90 μ m outer bearing clearance, only the synchronous component exists.



(a)



(b)

Figure 6. 17. The spectrum and trajectory of the turbocharger shaft at 6000rad/s:

(a)under 70 μ m outer bearing clearance (b)under 90 μ m outer bearing clearance

Figure 6.17 shows the spectrum and the trajectory of the turbocharger shaft at 6000rad/s. Under 90 μ m outer bearing clearance, the subsynchronous component due to the outer oil film instability is more obvious than that under 70 μ m outer bearing clearance.

According to the simulation results, it can be concluded that either inner or outer bearing clearances can affect the stability discipline of two oil films. As the inner clearance is increased, the inner oil film instability will occur at a higher rotational speed, but the outer oil film instability will be excited at a lower rotational speed. On the other hand, as the outer clearance is decreased, the hydrodynamic forces become larger, which inhibit the appearance of the instability in both inner and outer oil films. A high order harmonic component might also be excited by a thinner outer clearance.

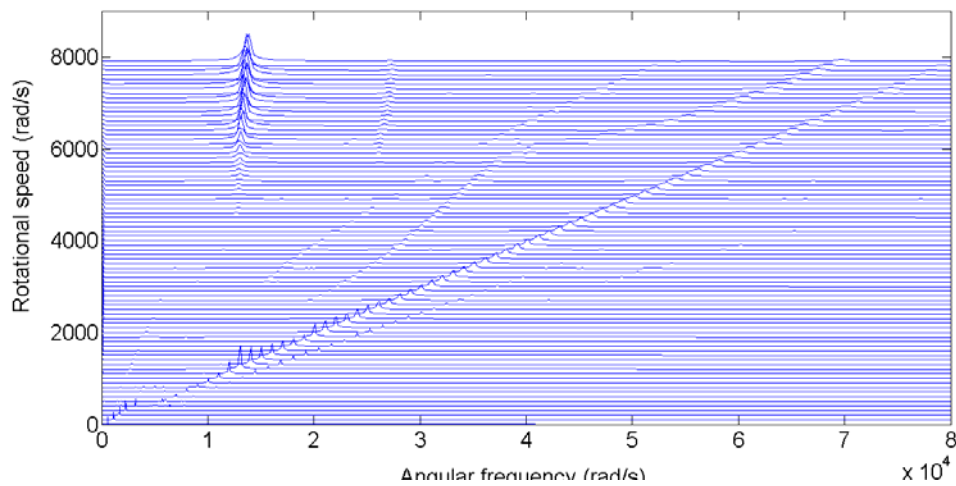
6.2.5 Influences of the lubricant feed pressure

For the lubrication of the floating ring bearings, the lubricant is supplied into the outer film

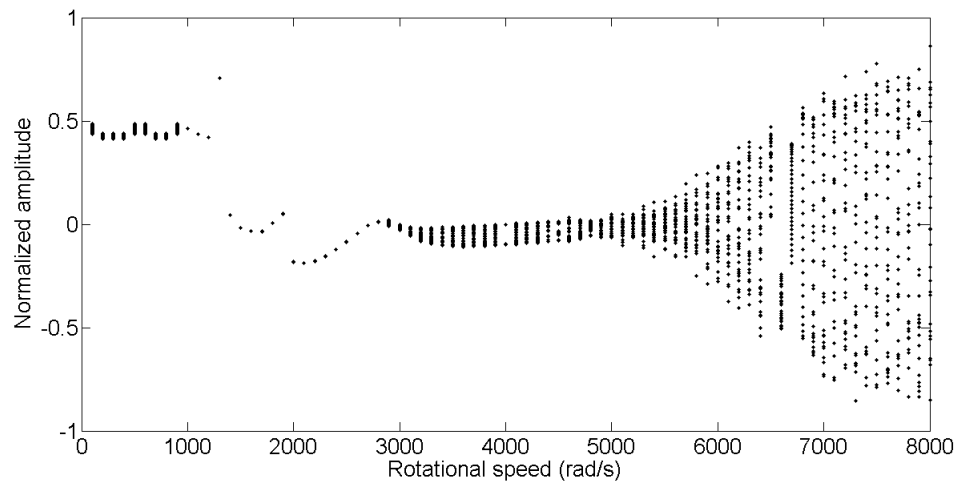
through a hole on the top of the bearing shell, meaning that the feed pressure can be simulated as a static load on the ring. Table 6.4 lists the simulation parameters in the lubricant feed pressure analysis.

Table 6. 4. Simulation parameters in the lubricant feed pressure analysis

Parameters	Values
Lubricant viscosity	15cp
Outer radius of the ring	9mm
Inner radius of the ring	5mm
Outer clearance of the bearing	80 μ m
Inner clearance of the bearing	20 μ m
Rotor imbalance on turbine impeller	2.5×10^{-5} kgm



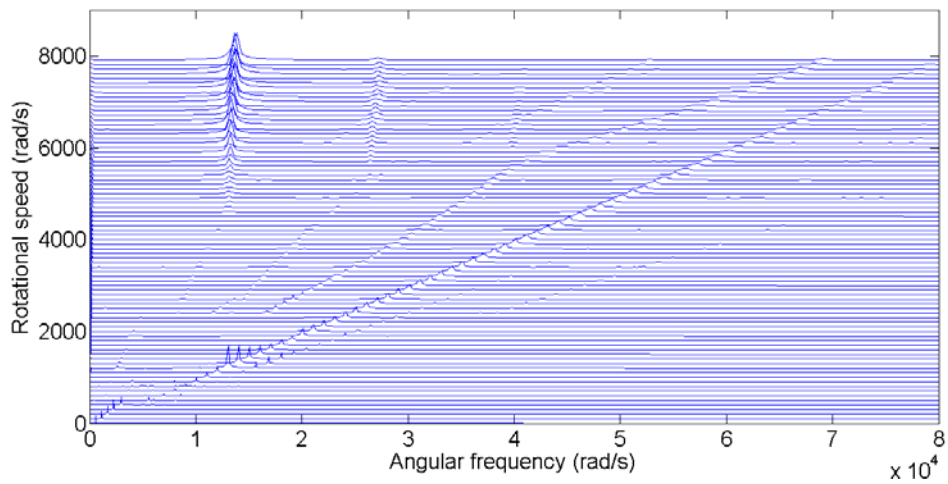
(a)



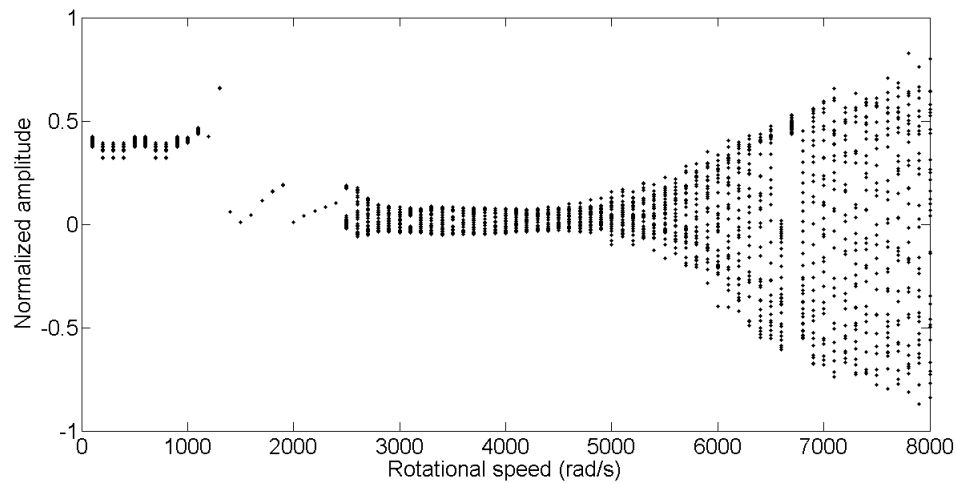
(b)

Figure 6. 18. Displacement of the turbocharger shaft under 2N static load on the ring:

(a)Waterfall diagram (b)Bifurcation diagram



(a)



(b)

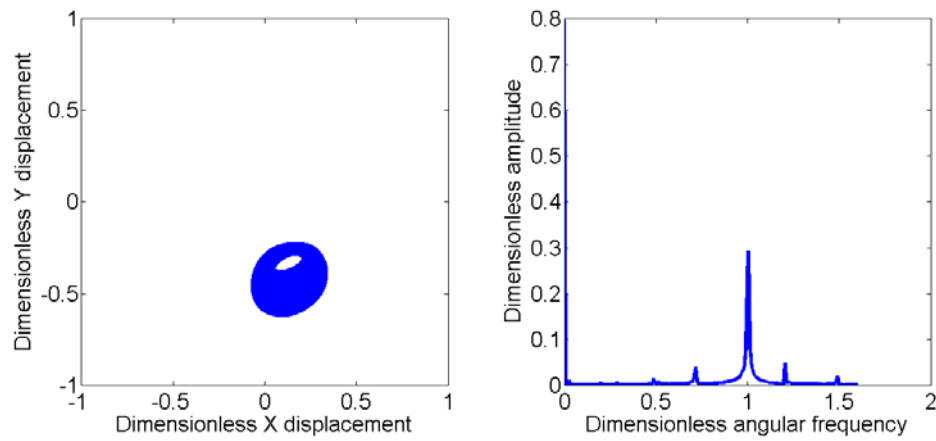
Figure 6. 19. Displacement of the turbocharger shaft under 5N static load on the ring:

(a)Waterfall diagram (b)Bifurcation diagram

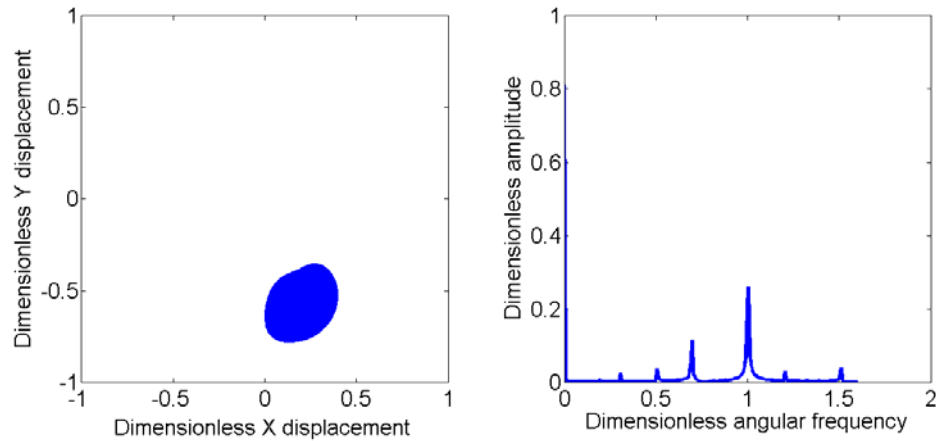
Figures 6.18 and 6.19 show the waterfall and bifurcation diagrams of the displacement of the turbocharger shaft under 2N and 5N static loads on the ring respectively. Under 2N static load on the ring, as is shown in Figure 6.18, the turbocharger shaft performs at a steadily periodic motion below 3000rad/s. The subsynchronous component occurs from approximate 3000rad/s, when the doubling period bifurcation occurs. This shows the appearance of the instability in the inner oil film. The outer oil film instability occurs at 5300rad/s and dominates the system motion up until a very high speed is reached. Under 5N static load, as shown in Figure 6.19, the subsynchronous component appears from 2500rad/s, when the rotor system shows a doubling period motion. The outer oil film instability dominates the system motion over 5000rad/s shaft speed.

Figure 6.20 shows the spectrum and trajectory of the turbocharger shaft at 3000rad/s. Under 2N static load, only the synchronous component can be seen in the spectrum that

demonstrates the turbocharger shaft performs a periodical motion. Under 5N static load, the inner oil film instability occurs that excites a subsynchronous component with the frequency of 60% of the shaft speed. Due to the effect of the static load exerted on the ring, the trajectory of the shaft is under the centre of the bearing.



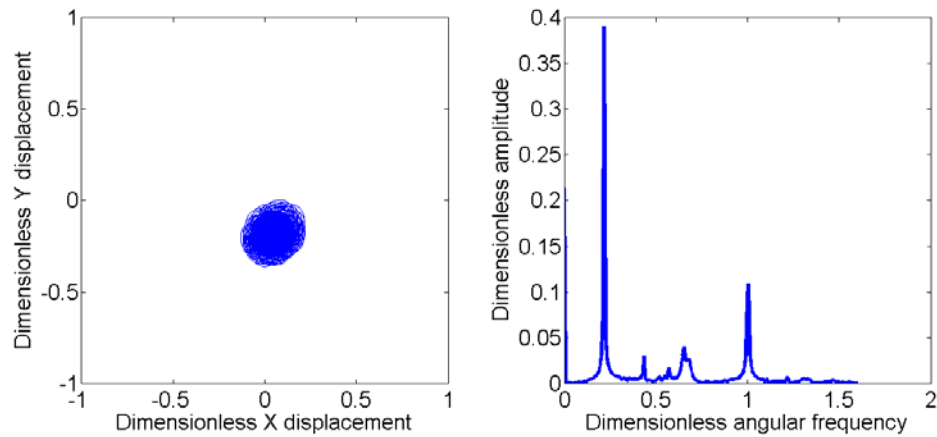
(a)



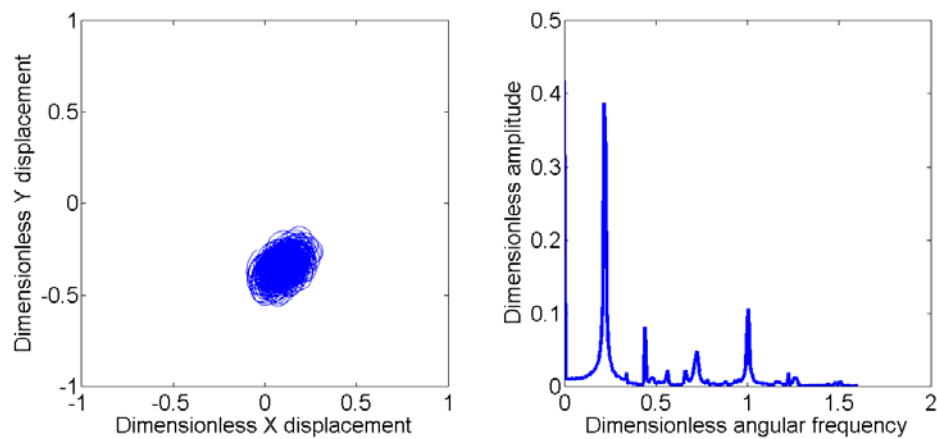
(b)

Figure 6. 20. The spectrum and trajectory of the turbocharger shaft at 3000rad/s:

(a)under 2N static load (b)under 5N static load



(a)



(b)

Figure 6. 21. The spectrum and trajectory of the turbocharger shaft at 6000rad/s:

(a)under 2N static load (b)under 5N static load

Figure 6.21 shows the spectrum and trajectory of the turbocharger shaft at 6000rad/s. The similar motions are shown in the cases of 2N and 5N static loads. Instabilities in the outer oil film have been excited under both outer bearing clearances.

According to the simulation results, it can be concluded that the lubricant feed pressure exerts a static load on the ring. It can excite the instability at a lower rotational speed in

both inner and outer bearing clearances.

6.3 Summary

In this chapter, the stability characteristic of the floating ring bearing is introduced. According to the simulation results, the effects of the rotor imbalance, lubricant feed pressure, bearing clearances and lubricant feed pressure on the stability of the turbocharger rotor system are analysed.

The rotor imbalance can lead to the appearance of the synchronous component in the turbocharger rotor system, the angular frequency of which is equal to the shaft velocity. The larger rotor imbalance, the larger amplitude of the rotor system appears especially at a relatively low speed range. The centrifugal force can inhibit the appearance of the instability in the inner oil film. However, the instability in outer oil film can be excited at a lower speed, when the amplitude of the rotor system becomes larger.

The lubricant viscosity can inhibit the instability in both inner and outer oil films. Under a lower lubricant viscosity, instabilities of both oil films are excited at the lower speeds, when the system shows a dramatic motion. Under a higher viscosity, the instabilities occur at higher speeds, especially for the inner oil film instability. The amplitude under oil film instabilities is also inhibited.

Either inner or outer bearing clearance can affect the stability discipline of two oil films. As the inner clearance is increased, the inner oil film instability will occur at a higher rotational speed, but the outer oil film instability will be excited at a lower rotational speed. On the other hand, as the outer clearance is decreased, the hydrodynamic forces become

larger, which inhibit the appearance of the instability in both inner and outer oil films. A high order harmonic component might also be excited by a thinner outer clearance.

The lubricant feed pressure exerts a static load on the ring. It can excite the instability at a lower rotational speed in both inner and outer bearing clearances.

CHAPTER SEVEN

TURBOCHARGER TEST RIG DEVELOPMENT

In order to validate the developed theoretical model, the related experimental data are required. In this chapter, a turbocharger test rig has been developed. The motion of a turbocharger rotor system can be monitored under different working conditions.

7.1 Introduction to the Turbocharger Test Rig

A turbocharger test rig has been designed and developed to monitor the shaft motion and validate the developed dynamics model of the turbocharger. A turbocharger test rig can generally be categorized into ‘hot air driven’ and ‘cold air driven’ in terms of the driven style. In the hot air driven style, the compressed air is heated in a combustion chamber and then delivered into the turbocharger. A close loop system is generally also used in this style in which the compressed air is recycled and delivered to the combustion chamber. In the cold air driven style, the driving force is directly provided by an air compressor or a fan. An open loop system is generally applied in this driven style. The air from the compressor of the turbocharger is directly discharged into the atmosphere.

As the thermal effects of exhaust gases on the performances of the turbocharger shaft motion have not been involved and the cost of the test rig establishment of a hot air driven is very high, a cold air driven style is adopted in this test rig.

The test rig comprises of the turbocharger, the air resource system, the lubrication system, the pipeline system, the sensors and the signal acquisition system. The block diagram of the turbocharger test rig is shown in Figure 7.1.

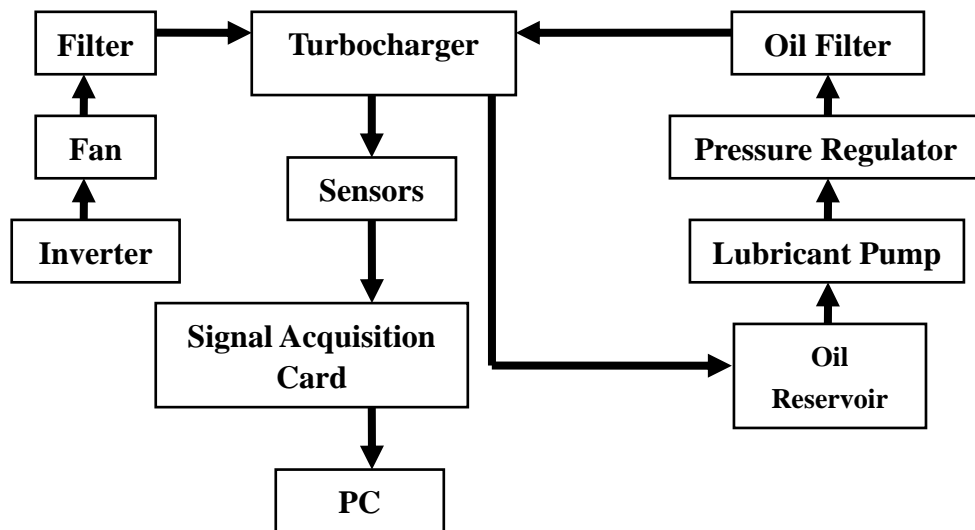


Figure 7. 1. The block diagram of the turbocharger test rig

7.2 The Turbocharger

A commercial automotive turbocharger GJ90C has been purchased for this test, as shown in Figure 7.2. The GJ90C turbocharger is designed for the Styer WD615.68 (1491-310, 1891-310) series engine. The typical specifications are listed as follows:

- The material of the GJ90C turbocharger casing satisfies an extensive range of temperature requirements.
- A reasonable structure of the compressor and turbine impellers guarantees a normal application.
- Supported by the floating ring bearing.
- Good reliability under both high temperature and high rotational speed.
- The minimum airflow should be more than 0.2kg/s and the lubrication feed pressure

should be around 0.3MPa.



Figure 7. 2. The GJ90C turbocharger

7.3 Air Resource System

Either an air compressor or a fan could provide an air resource for the turbocharger. The air compressor compresses fresh air in a chamber and then drives the rotating turbine impeller, the speed of which can be controlled by a valve [137~139]. However, this approach makes it difficult to maintain the output air pressure as a result of the limited volume of the air compressor chamber. In this test rig, a fan is adopted to provide a steady and adjustable air resource for the turbocharger. Although the mean output air pressure is lower when compared to an air compressor, a fan can drive the turbocharger steadily at a certain rotational speed and also has the advantage of being cheaper.

The flow rate of the fan is mainly determined by the diameter of the impeller, the rotational speed and the blade shape, while the output pressure depends upon the diameter of impeller, the rotational speed, the density and the blade shape. The empirical formulas [140] are given as follows:

$$Q = \bar{Q} \frac{\pi}{4} D_2^2 v_2 \quad (7.1)$$

$$H = 0.000334 \bar{H} D_2^2 v_2^2 \quad (7.2)$$

where Q, H denote the output flow rate (m^3/s) and pressure (Pa), D_2, v_2 denote the diameter (m) and the rotational speed of the impeller (rad/s) respectively, \bar{Q}, \bar{H} are the coefficients of the flow rate and the pressure.

According to the specification of the GJ90C turbocharger, a 5.5kw fan has been utilized with a maximum air flow and output pressure of $1500 \text{ m}^3/\text{h}$ and 5kPa respectively.

An inverter has also been installed to control the motor speed of the fan. In addition, the inverter can also protect the whole device in case of the current, voltage or load exceeding their secure thresholds. A DZB200 general inverter has been purchased from Fuling Inverter Company China, which can output a maximum of 80Hz for the motor and drive with the fan rotating at a maximum speed of 4400r/min. According to the output flow rate and pressure, it can be estimated that the turbocharger working speed can therefore theoretically reach 30000r/min. The real maximal speed, however, will also depend upon numerous factors including the turbocharger, hose, etc.

7.4 Lubrication System

A turbocharger is lubricated by the engine lubrication system in vehicles. In this test rig, an

independent lubrication system is required for the lubrication and heat transfer of the bearings. Figure 7.3 shows the block diagram of the lubrication system, including a lubrication pump, an oil reservoir, a pressure regulator, an oil filter and the interface.

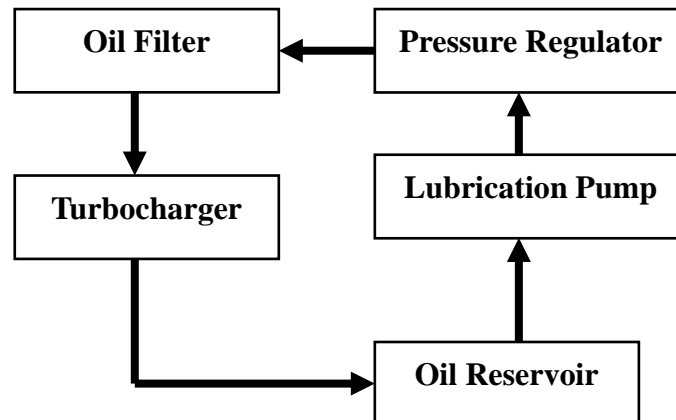


Figure 7. 3. The block diagram of the lubrication system

The lubricant is pumped from an oil reservoir into the turbocharger by the pump. After lubrication and heat transfer, the lubricant returns back to the reservoir. The pressure and flow rate of the lubricant can be controlled by the pressure regulator. To prevent the impurity from destroying the floating ring bearing, an oil filter is installed at the outlet of the pump.

A CB-B gear pump has been adopted as the lubrication pump in the test rig, as is shown in Figure 7.4. The rated speed is 1450rpm and the maximum displacement of the pump is 15L/min. The hydraulic control valve, Tescom 44-52-12243V, as shown in Figure 7.5, is installed to control the lubricant feed pressure towards the turbocharger. The output and inlet pressure of the valve are 2-100PSIG (0.014MPa-0.069MPa) and 400PSIG (2.7MPa) respectively. According to the typical specification of the pump and the length of the

lubricant pipe, the volume of the oil reservoir is designed to be 30L.



Figure 7. 4. CB-B gear lubrication pump



Figure 7. 5. Tescom 44-52-12243V Hydraulic control valve

7.5 Pipeline System

In this test rig, the pipeline system includes an air pipeline and a lubricant pipeline.

The air pipeline links the output of the fan with the inlet of the turbocharger. Equation (7.3) is the formula of the flow rate in the pipeline. It can be seen that under the same flow velocity, the larger the area of cross section is, the higher the volume of air that will pass through. Therefore the diameter of the pipeline should be large enough for the air flow pass through, otherwise the damping of the pipeline will affect the driven effects. In addition, the curvature radius of the hose should also be large enough to ensure good ventilation.

$$Q = Sv \quad (7.3)$$

where Q denotes the flow rate (m^3/s), S denotes the area of the cross-section of the pipeline (m^2) and v denotes the flow velocity (m/s).

The lubricant pipeline, as a circulation system (see Figure 7.3), delivers the lubricant to the turbocharger and returns it back to the oil reservoir. The Lubricant pipeline and the turbocharger are assembled by a flange. According to the geometrical parameters of the inlet and the return lubricant supply holes of the GJ90C turbocharger, a pair of assembly flanges have been designed, which are shown in Appendix A. Figure 7.6 shows the photograph of the assembly flanges between the lubricant pipe and the turbocharger.



Figure 7. 6. A photograph of the assembly flanges between the lubricant pipe and the turbocharger

7.6 Sensors and Installation

The test rig aims to investigate the turbocharger shaft motion under different working conditions. Therefore, vibration sensors and rotational speed sensors should be installed for measurement purposes.

Common vibration sensors include the piezoelectric accelerometer, the inertial electromagnetic sensor and the eddy current displacement transducer [141]. Different sensors are

fitted for different measurement conditions. In the case of analyzing damage or fault caused by inertia forces, acceleration should be selected as the primary measurement parameter; in the case of investigating the vibration intensity and condition, velocity should be selected as the primary measurement parameter; in the case of the measurement of the object position, displacement should be selected as the primary measurement parameter.

As far as the bending vibration of the turbocharger rotor system is concerned, a non-contact type sensor should be chosen due to the high speed rotation. In addition, the material of the GJ90C turbocharger shaft, 41NiCrMo22, is not a magnetizer but an electrical conductor on the surface of which the eddy current can be formed. Therefore, the eddy current displacement transducer is used to measure the bending vibration of the turbocharger rotor system.

The turbocharger shaft motion shows characteristics such as low amplitude and high frequency. Therefore, the frequency response is a critical criterion in the selection of vibration sensors, because even the fundamental frequency of the turbocharger shaft is approximately 2-3KHz. KAMAN KD2306 1U1, a kind of high precision eddy current displacement transducer is adopted in the test rig, shown in Figure 7.7. KAMAN precision products' model KD2306 is a non-contact, linear, analog displacement measuring system. The system operates on a traditional inductive bridge circuit, which can be used for a precisely static and dynamic measurement of conductive targets. Table 7.1 lists its typical specification.



Figure 7. 7. KAMAN KD2306 1U1 eddy current displacement transducer

Table 7. 1. The typical specification of a KD2306 1U1 eddy current displacement

	transducer
Sensor type	KD2306 1U1
Resolution	0.01%Fs
Frequency response	50KHz
Nonlinearity	<1%Fs
Thermal sensitivity standard	0.1%Fs/° F
Compensated	0.02%Fs/° F
Standard measuring range	1mm
Target material	Non-magnetic

The installation of eddy current displacement transducers should satisfy the following requirements: Firstly, sensors should be fixed on the turbocharger casing in order to eliminate the effects of the base vibration of the test rig and only extrude the shaft motion.

Secondly, the precision of the adopted eddy current displacement transducers is high, inevitably meaning that it has a very short measuring range (approximately 1mm). It is therefore necessary to design a mechanical component to help the sensor to approach the measuring position without touching the rotating shaft. Thirdly, a cylindrical surface should be chosen as the measuring position in order to avoid positioning it out of the sensor's range as the shaft spins.

According to the above requirements, a cylindrical surface at the shaft end on the compressor impeller side has been chosen as the measuring position. Two slots have been milled in a perpendicular position for the placement of the displacement transducer, which is shown in Appendix B.

A pair of mechanical components have been designed to fix the eddy current displacement transducers on the casing, which is shown in Appendix C. The components include upper and lower plates. The upper plate is used to adjust the axial position of the sensor by sliding along the slot and the lower plate is used to control the radial position of the sensor. The sensors are fixed by a pair of locknuts and the long hole is used to guide the wire of the sensor away from the compressor impellers.



Figure 7. 8. A photograph of the eddy current displacement transducers installed on the turbocharger

The rotational speed is monitored by a cylindrical photoelectric sensor BR100_DDT_P, as shown in Figure 7.9, manufactured by Autonics China. The typical specification of the speed sensor is listed in Table 7.2.



Figure 7. 9. A BR100_DDT_P cylindrical photoelectric sensor

Table 7. 2. Typical specification of the BR100_DDT_P photoelectric sensor

Sensor	BR100_DDT_P
Range	100mm
Type	Diffuse
Differential range	<20%
Response time	Max. 1ms

Light sensitive tape must be adhered to the rotating parts to reflect the light emitted from the photoelectric sensor. The tape could directly be adhered to the impeller, but the lubricant leakage from the turbocharger's central casing towards the two sides as result of the pressure difference will lead to the belt to drop, especially at a high rotational speed. In order to overcome the difficulty of the tape placement, a speed nut has been designed, shown in Figure 7.10. The thread in the middle of the nut matches the shape of the shaft end so that the nut can be assembled with the shaft and will spin synchronously. Light sensitive tape is adhered to the nut, facing the speed sensor. It should be noted that the thread in the middle of the nut is machined as reverse thread so that the fit between the shaft and the nut will be increasingly tight as the shaft spins in order to prevent the nut from being thrown out.



Figure 7. 10. The speed nut for the light sensitive belt placement

The cylindrical photoelectric sensor is fixed on a universal bracket facing the speed nut, as shown in Figure 7.11.



Figure 7. 11. The rotational speed sensor fixed on a universal bracket

7.7 Signal Acquisition System

A USB-6251 BNC signal acquisition card is used to collect signals, as shown in Figure 7.12.

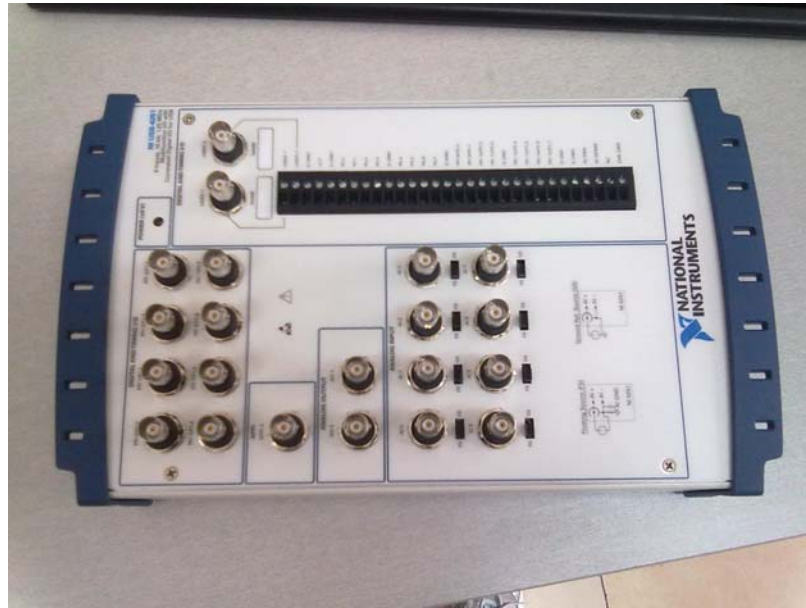


Figure 7. 12. USB-6251 BNC signal collection card

The parameters of the NI USB-6251 are listed as follows:

- 8 differential BNC analog inputs (16 bit), 1.25MS/s single channel (1MS/s aggregate)
- 2 BNC analog outputs (16 bit, 2.8MS/s); 2.4 digital I/O (8 clocked, 8 BNC); 32-bit counters
- Uses mass termination version with SCC signal conditioning
- NI signal streaming for bidirectional high speed data streams over USB; OEM version available
- Compatible with Labview, ANSI C/C++, C#, Visual Basic, Net and Visual Basic 6.0
- NI-DAQmx driver software and NI Labview signal Express LE interactive data-logging software

The 1.25MS/s sampling rate of the single channel makes it possible to collect signals within a wide frequency band. As a result, subsynchronous, synchronous and the higher orders harmonics components of displacement signals can be acquired. As well as this eight differential BNC analog inputs make it possible to monitor multiple signals simultaneously. Therefore, the NI USB-6251 signal acquisition card is completely satisfactory for the requirements of this test rig.

The graphic programming language Labview 2010 professional version is used to program in order to achieve signal collection.

7.8 The Entire Test Rig



Figure 7. 13. A photograph of the turbocharger test rig

Figure 7.13 shows a photograph of the turbocharger test rig that includes the tested

turbocharger, the lubrication system, the pipeline system, the sensors and the signal acquisition system. This test rig is designed for the monitor of turbocharger rotor system motion. Through a pair of eddy current displacement transducers installed in a perpendicular direction, both the rotor system motion in two directions and the shaft trajectory can be collected simultaneously. In addition, the rotational speed of the tested turbocharger can be controlled by adjusting the output frequency of the inverter. Therefore, the rotor system motion in the steady-state at different rotational speeds and in the process of the acceleration and deceleration can be obtained by adjusting the shaft speed, monitored by the cylindrical photoelectric sensor. The lubricant feed pressure can be manually controlled by a pressure regulator. As well as this, by port expansion, this test rig can also be used for the investigation of the performance of the turbocharger in other areas, such as the air fluid, thermal effects, materials, etc.

CHAPTER EIGHT

EXPERIMENTAL RESULTS AND ANALYSIS

Following the turbocharger test rig development, the motion of the turbocharger rotor system has been monitored under various working conditions. The dynamic performances and stability of the turbocharger rotor system have been investigated according to the experimental data and simulation results.

Following the establishment of the turbocharger test rig, signals of the displacement of the turbocharger shaft at the compressor impeller side have been collected. The dynamic performance and the stability of the turbocharger rotor system have then been discussed based on the experimental data and simulation results.

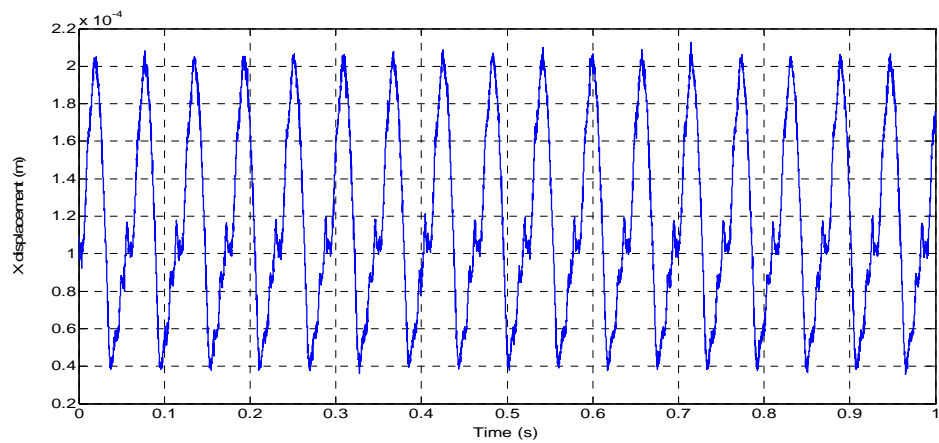
8.1 Introduction to the Experiment Procedure

The procedure of the experiment has been briefly introduced as follows:

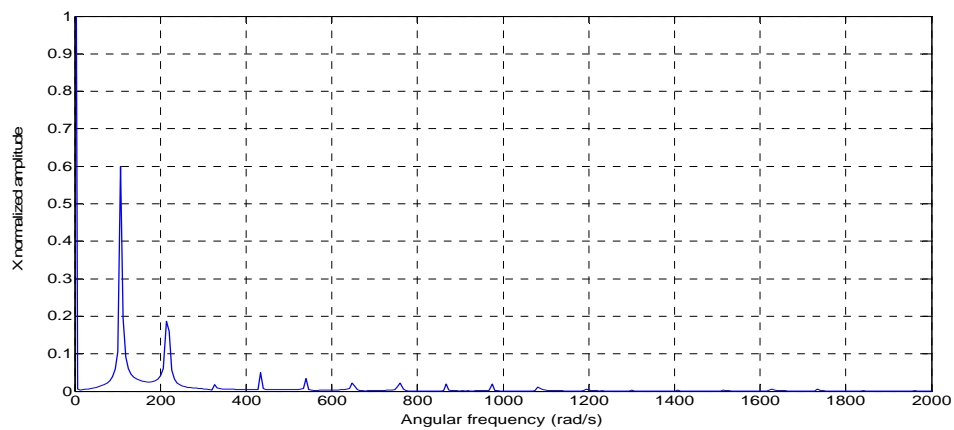
- (I) Before the experiment, the speed nut with light sensitive tape adhered is loaded onto the turbocharger shaft end facing the cylindrical photoelectrical sensor.
- (II) A hose is placed on the turbine impeller end of the turbocharger to recycle the leaked lubricant.
- (III) In order to avoid the appearance of dry friction of the floating ring bearing, the lubrication gear pump must be working in advance in order to fully lubricate the bearing.
- (IV) The rotational speed of the fan is controlled by adjusting the output frequency of the inverter.
- (V) Even though the turbocharger works steadily at a given speed, speed fluctuation will inevitably appear as a result of the unstable air flow.
- (VI) After the experiment, the fan should be shut down first and then the lubrication system should be switched off until the turbocharger has stopped rotating in order to prevent the floating ring bearing failing as a result of dry friction and the remaining heat.

8.2 Experimental Results and Analysis

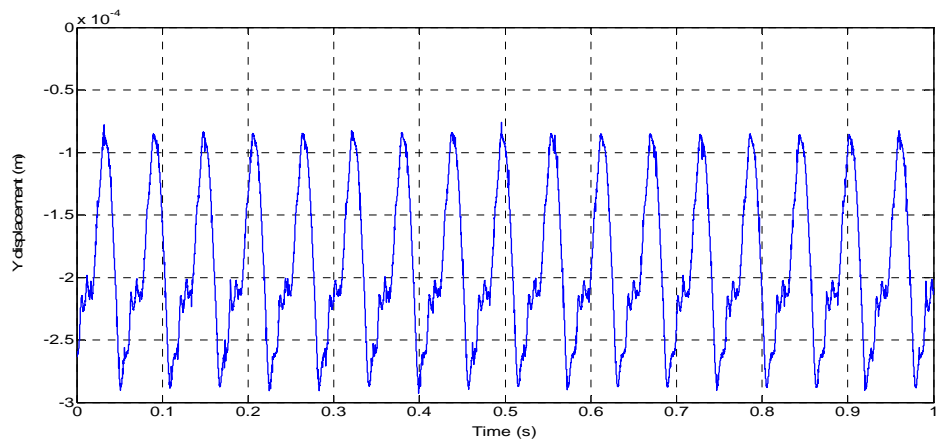
Signals from the turbocharger shaft end motion at the compressor impeller side in X and Y directions within the speed range of 20,000r/min have been collected.



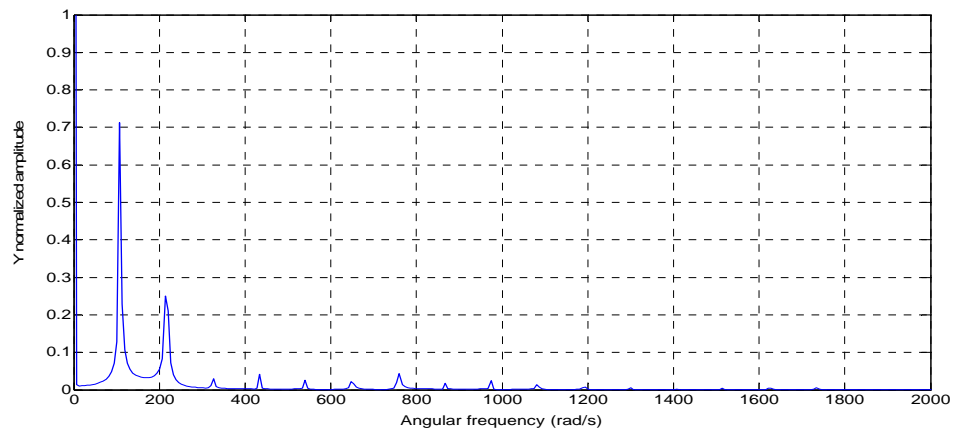
(a)



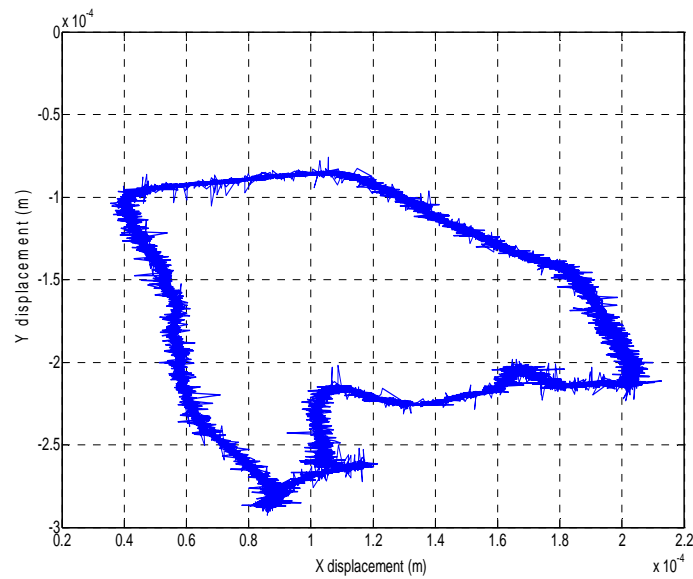
(b)



(c)



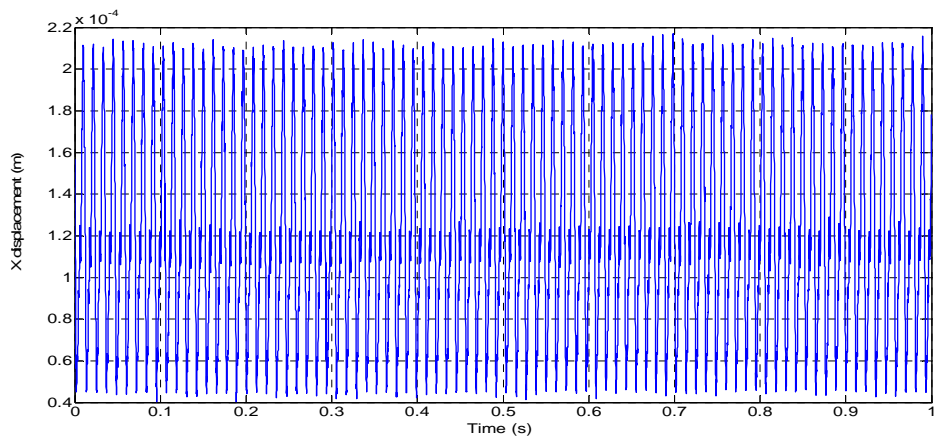
(d)



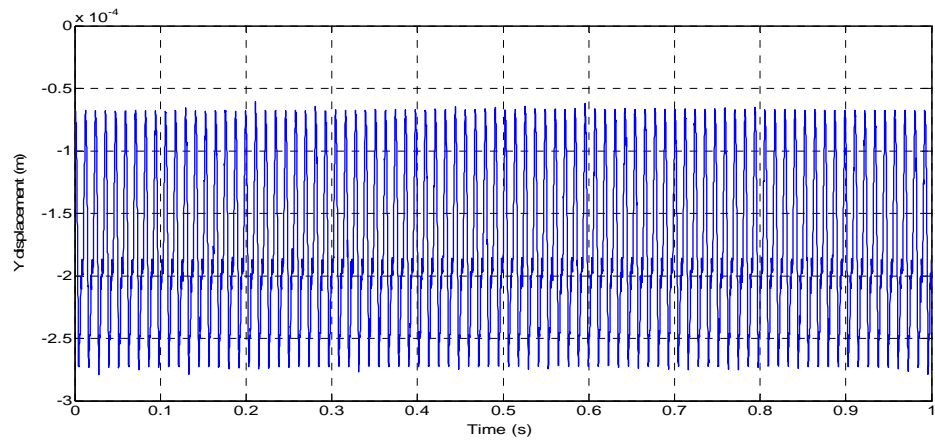
(e)

Figure 8. 1. The turbocharger shaft end motion at the compressor impeller side at 1,000r/min rotational speed: (a)X displacement (b)Spectrum of X displacement (c)Y displacement (d)Spectrum of Y displacement (e)Trajectory

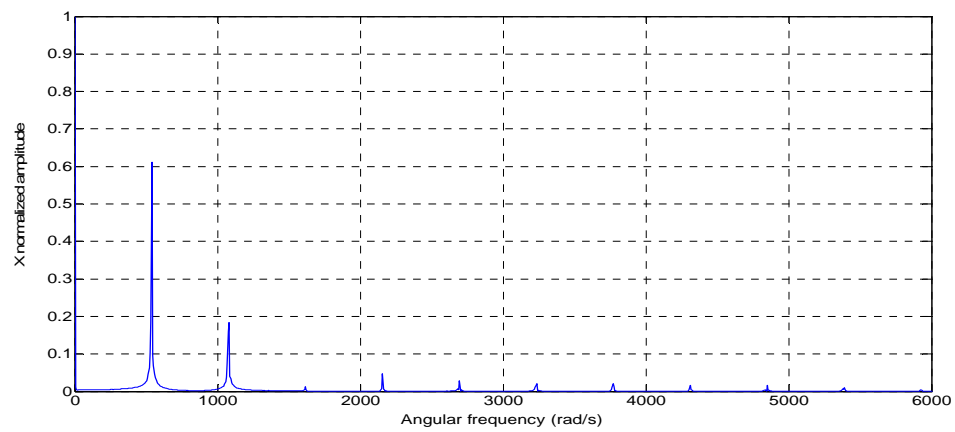
Figure 8.1 shows the turbocharger shaft end motion at the compressor impeller end within one second at 1,000r/min ($\approx 100\text{rad/s}$) rotational speed. The turbocharger shaft can be seen to perform the periodic motion in X and Y directions. The displacement signals obtained are not smooth but with glitches at some places, and the irregular shaft trajectory demonstrates the existence of these glitches. The spectrum diagrams illustrate that shaft motion comprises of the synchronous component, the second order harmonic component and a series of slightly higher orders components. The subsynchronous component does not emerge at this speed. Due to the lubricant feed pressure, however, the shaft is whirling below the central position of the bearing.



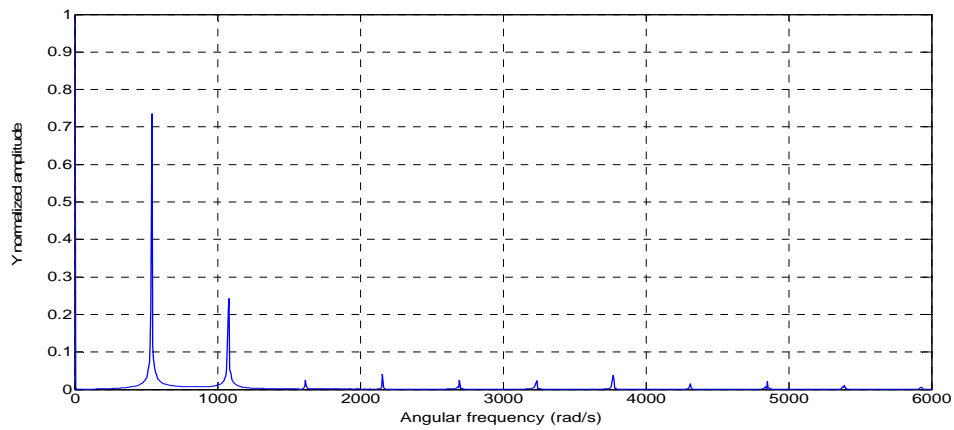
(a)



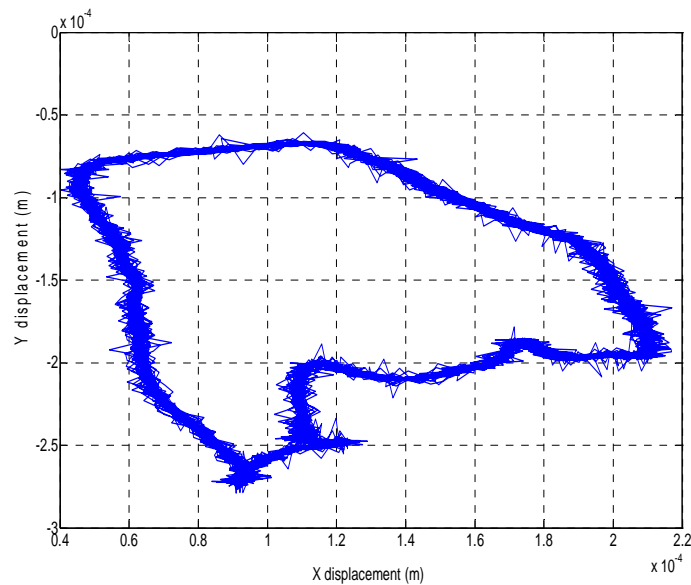
(b)



(c)



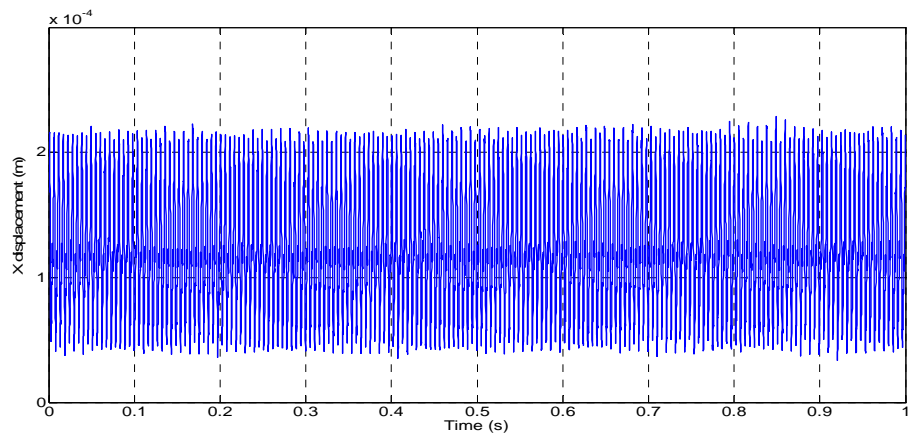
(d)



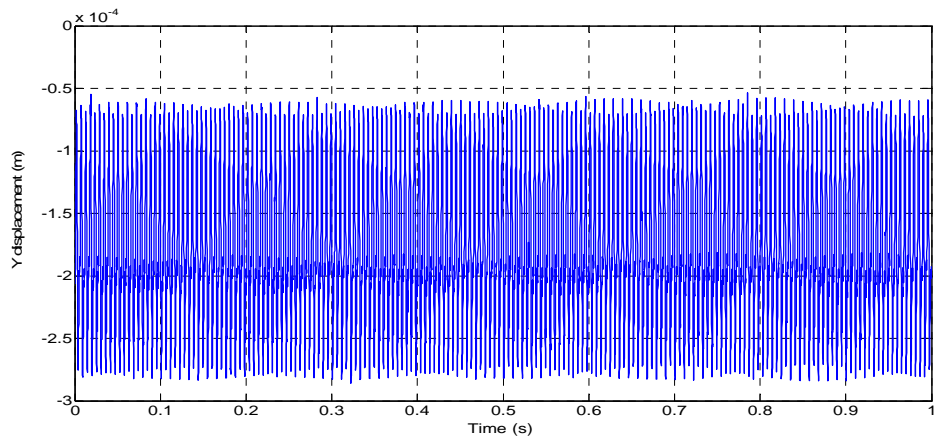
(e)

Figure 8. 2. The turbocharger shaft end motion at the compressor impeller side at 5,000r/min rotational speed: (a)X displacement (b)Spectrum of X displacement (c)Y displacement (d)Spectrum of Y displacement (e)Trajectory

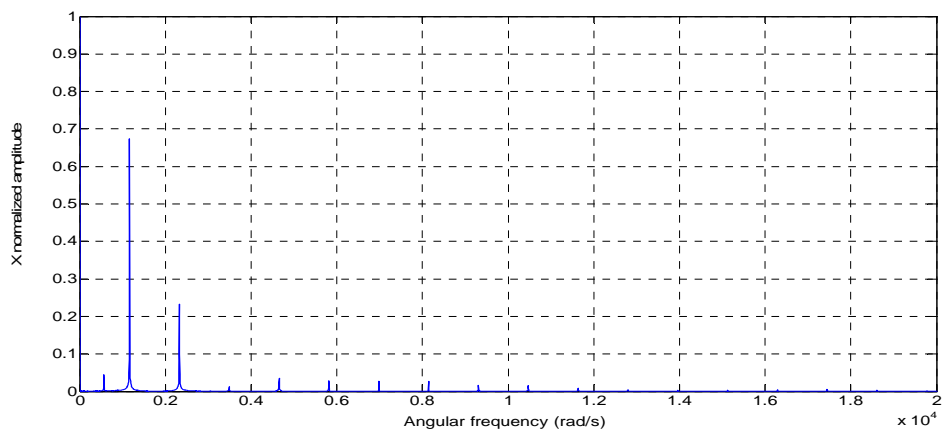
As is shown in Figure 8.2, similar experimental results can be observed when the rotational speed is increased to 5,000r/min ($\approx 500\text{rad/s}$), except for the slight increase of the amplitude in both directions as a result of the larger rotor imbalance centrifugal force.



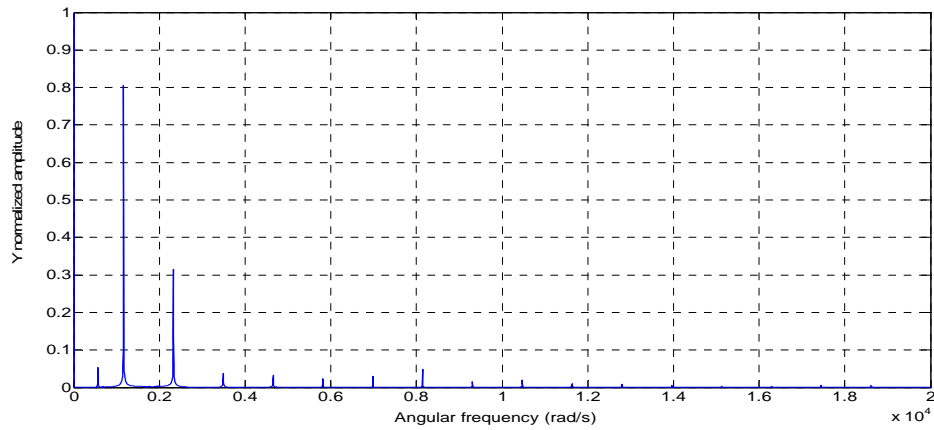
(a)



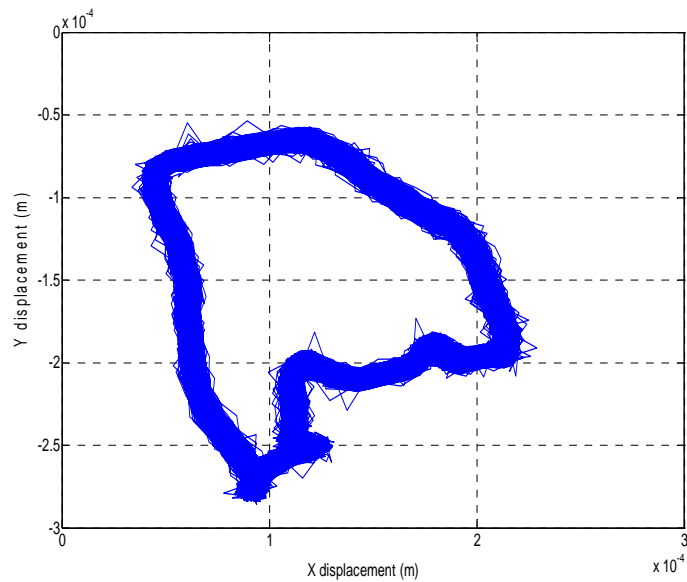
(b)



(c)



(d)

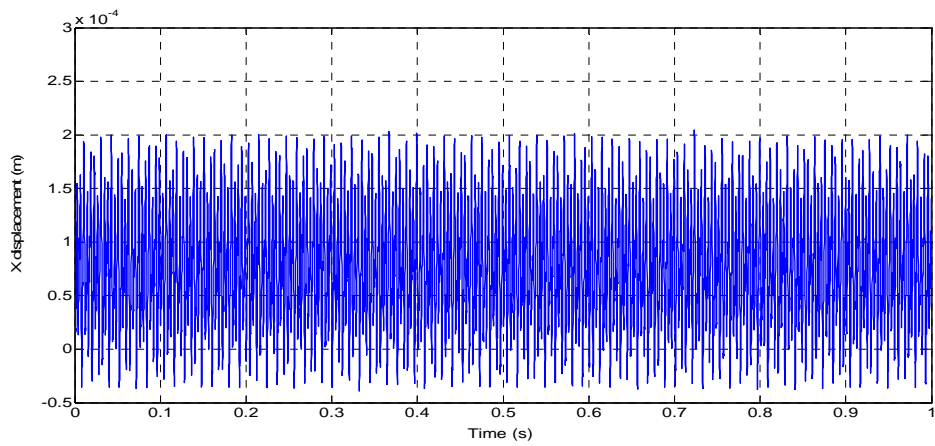


(e)

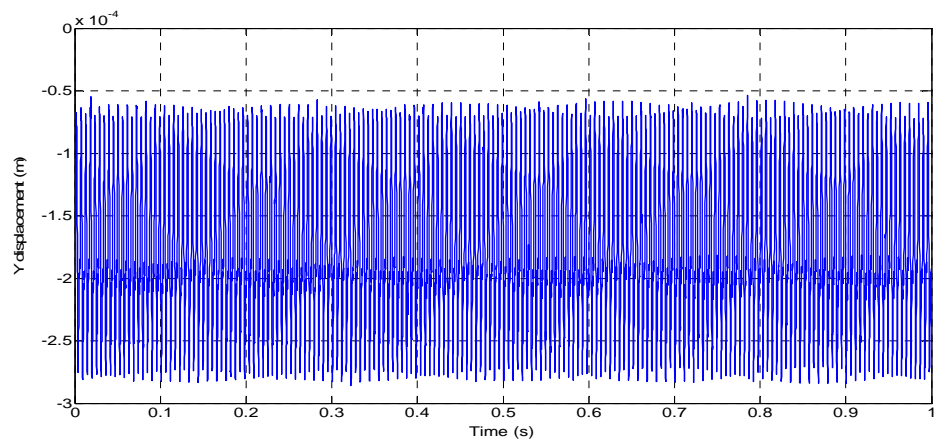
Figure 8. 3. The turbocharger shaft end motion at the compressor impeller side at 11,000r/min rotational speed: (a)X displacement (b)Spectrum of X displacement (c)Y displacement (d)Spectrum of Y displacement (e)Trajectory

The rotational speed of the turbocharger was increased further to 11,000r/min ($\approx 1,100\text{rad/s}$) with the shaft motion being shown in Figure 8.3. It can be seen that besides the synchronous and such high orders harmonic components, the subsynchronous

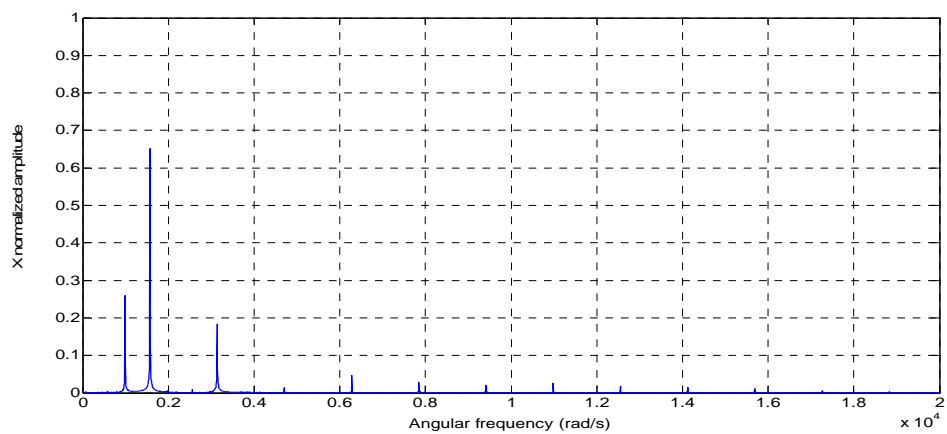
component starts to appear which angular frequency is approximately half of the shaft speed.



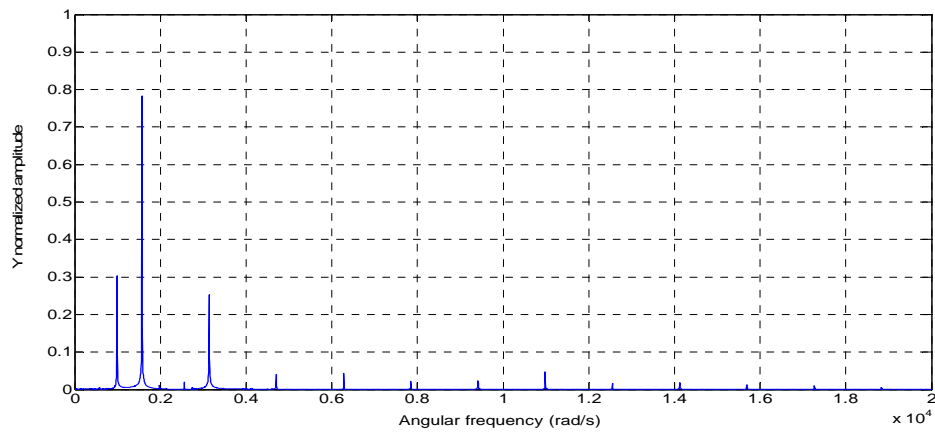
(a)



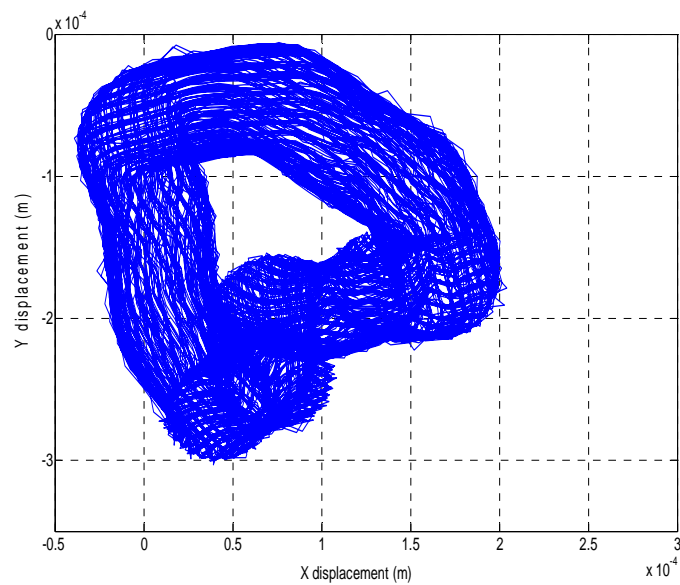
(b)



(c)



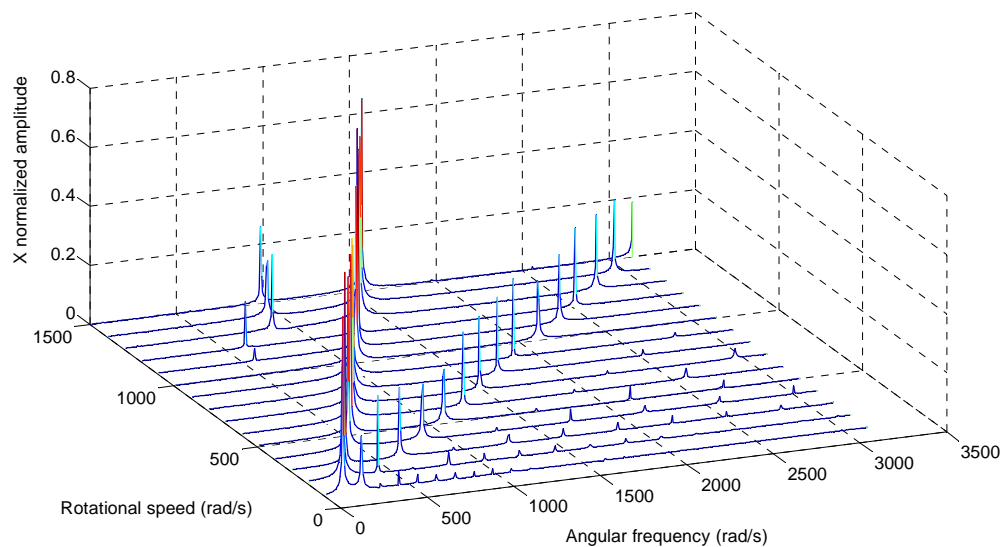
(d)



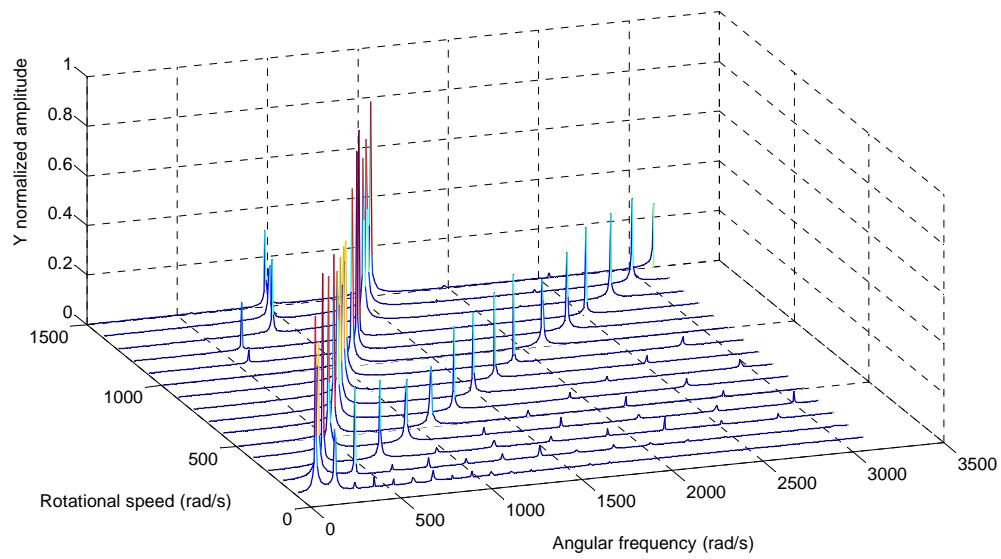
(e)

Figure 8. 4. The turbocharger shaft end motion at the compressor impeller side at 15,000r/min rotational speed: (a)X displacement (b)Spectrum of X displacement (c)Y displacement (d)Spectrum of Y displacement (e)Trajectory

Figure 8.4 show the shaft motion as the turbocharger rotates steadily at 15,000r/min ($\approx 1,500\text{rad/s}$) rotational speed. The previously subsynchronous component has been replaced by another component whose angular frequency is 987rad/s , which is approximately one sixth of the shaft speed. The amplitude of the subsynchronous component increases sharply, when compared to at the amplitude at lower rotational speed. The shaft is whirling within a larger area.



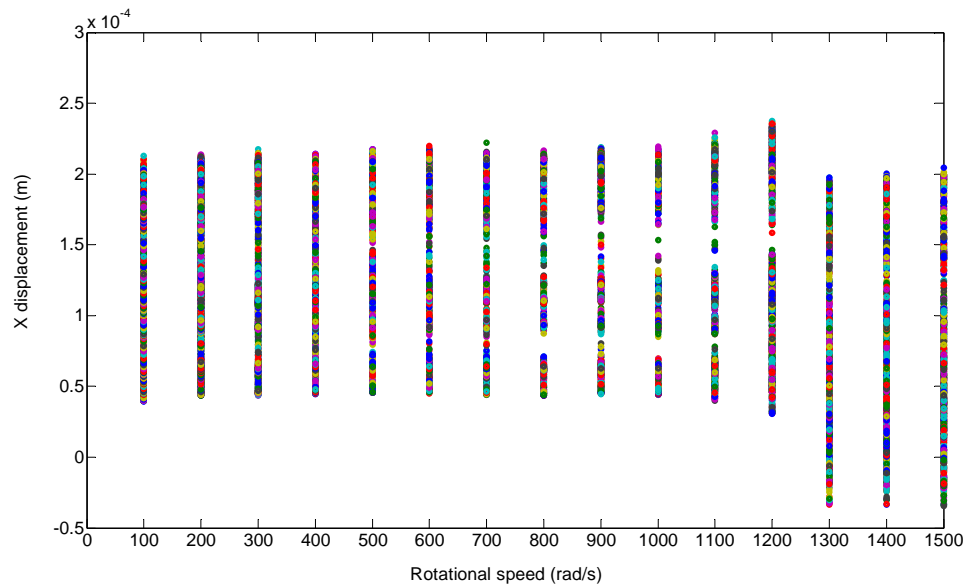
(a)



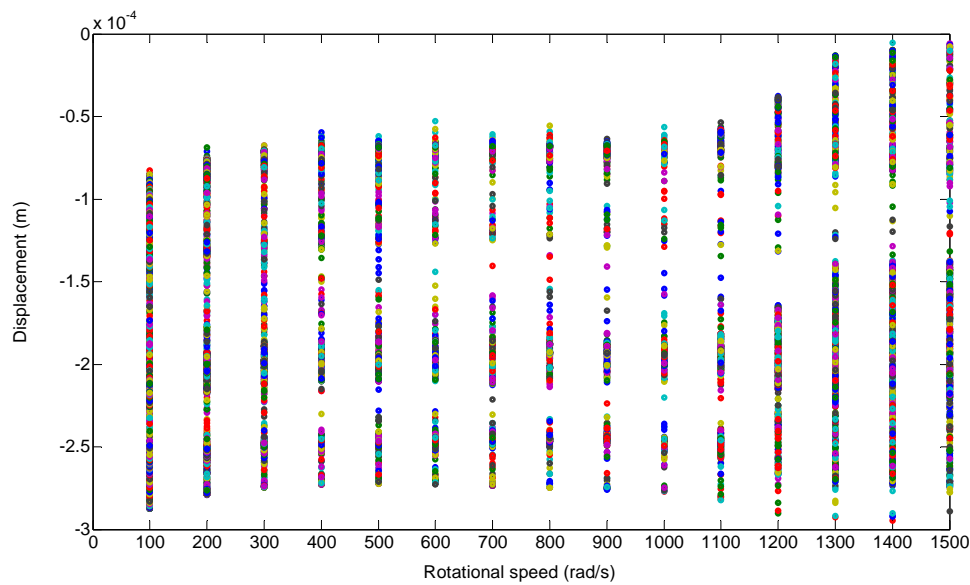
(b)

Figure 8. 5. Waterfall diagrams of the turbocharger shaft end motion at the compressor side:

(a)X displacement (b)Y displacement



(a)



(b)

Figure 8. 6. Bifurcation diagrams of the turbocharger shaft end motion at the compressor side: (a)X displacement (b)Y displacement

Figures 8.5 and 8.6 show waterfall and bifurcation diagrams of the turbocharger shaft motion. Within the measuring speed range, the synchronous component exists and dominates the vibration which demonstrates the effects of the residual rotor imbalance. This is different to the simulation results, the second order harmonic component exists within the speed range which amplitude does not obviously change as increasing rotational speed. This shows that as well as rotor imbalance centrifugal forces, hydrodynamic fluid forces and the dead weight, there should also be another exciting force affecting the motion of the turbocharger rotor system.

From the spectrum diagram we see that the second order harmonic component can come as a result of the following things: Firstly, the appearance of an axial crack on the rotor, a kind of misalignment, could excite a stable second order harmonic component; secondly, the

bolts may have loosened or a crack may have occurred on the base; thirdly, the rub-impact phenomenon - once the rotors touch the stators, a series of harmonic vibration components can be caused; fourthly, concentricity deviation between the disks may lead to the appearance of the second harmonic component.

Within the speed range of the measurement, the appearance of the subsynchronous components at which the angular frequencies are approximately $1/2$ and $1/6$ of the shaft speed shows the oil whirling phenomenon occurring in the fluid films inside the floating ring bearing; this also supports the simulation results at the relatively low speed range.

According to the simulation and experimental results, we can see that the rotational speed at which subsynchronous components occur as well as the sequence in which the instability of the two oil films emerge, depends upon parameters such as the rotor system eccentricity, the phase difference between the rotor imbalance, the bearing clearances, the lubricant viscosity and the feed pressure.

Rotor system instability can be illustrated using a typical procedure as an example: At low speed range, the inner oil film is crucial to the rotor system motion. When the rotational speed reaches a critical value, the damping of the outer film cannot inhibit the excitation from the inner oil film. At that time, oil whirl and whip phenomenon will then occur in the inner oil film. The whirling frequency is generally approximately one third of the shaft speed and will slightly increase as the rotational speed rises. In addition, the amplitude of the subsynchronous component will be larger than that of the synchronous component. If the rotational speed is increased yet further, the outer oil film will gradually replace the inner oil film to dominate the rotor system motion. Once a critical value is reached, the

outer oil film can no longer inhibit the inner film. The second bifurcation occurs and the rotor system becomes unstable once again. As mentioned above, the instability procedure is determined by the parameters of the rotor system which can affect not only the angular velocity at which subsynchronous components occur, but also the sequence in which oil film instabilities emerge.

8.3 Summary

In this chapter, the procedure of the experiment is briefly introduced. Then, the experimental data regarding bending vibration of the turbocharger rotor system are collected within the speed range of 1000 to 20000 r/min. The stability characteristics of turbocharger rotor system are analyzed through the experimental and simulation results.

CHAPTER NINE

CONCLUSIONS AND FUTURE WORK

In this chapter, the achievements of this research project are summarized. The findings and conclusions are presented. The contributions to knowledge have been summarized separately and proposals for future research to develop this area of work are discussed.

9.1 Review of Research Objectives and Achievements

The objectives of this research project and key achievements are described below:

Objective 1: To conduct a full literature review of current research in the areas of fluid lubrication, rotordynamics and turbocharger rotordynamics.

Achievement 1: Publications associated with research on fluid lubrication were reviewed and linear and nonlinear models of the hydrodynamic forces were summarized and compared. The classical models of nonlinear hydrodynamic forces are listed in Section 2.1. The theory and background of three areas of rotordynamics were introduced, namely: critical speeds, forced response and stability analysis. General approaches to the research of rotordynamics are given in Section 2.2.

Literature associated with rotordynamics research of the turbocharger, which is a flexible rotor system supported by floating ring bearings, were reviewed and are presented in Section 2.3. Background theory related to the research of the turbocharger rotordynamics were introduced, including: the nonlinear theory of the vibration system, the modal synthesis method and the numerical calculation approach; and are presented in Sections 2.4, 2.5 and 2.6 respectively.

Objective 2: To investigate the fluid lubrication of the floating ring bearing system.

Achievement 2: The analytical expressions of the oil film pressure distribution in the floating ring bearing were derived using the infinitely long bearing theory, taking into account the oil inlet pressure and cavitation area – see Section 3.2.

The equilibrium positions of the journal and ring, in terms of the eccentricity and attitude angle, were simulated. The influences of external loads and oil inlet pressure on the oil flow rate into the inner clearance were investigated analytically based on the simulation results shown in Section 3.3.

Objective 3: To develop a theoretical dynamics model for the turbocharger rotor system.

Achievement 3: Using the finite element method, a finite element model was developed for the turbocharger rotor system. The shaft was modeled as a series of beam elements and the turbine and compressor wheels were modeled as rigid disks. The dimensionless form of the Capone hydrodynamic force model was extended into the floating ring bearing with double oil films. The adaptive time step Runge-kutta approach was introduced to numerically integrate the second order system motion equation as shown in Section 4.2.

Objective 4: To analyze the dynamic performance of the turbocharger rotor system and to calculate the critical speeds and mode shapes.

Achievement 4: Modal analysis was carried out on both a free rotor system as in Section 5.2 and a turbocharger rotor system as in Section 5.3. Influences of the support and gyroscopic effects were ignored in the free rotor system analysis, whilst the turbocharger rotor system analysis took into account the support of the floating ring bearings and gyroscopic effects. The studies of the critical speeds and mode shapes were based on the simulation results shown in Section 5.4.

Objective 5: To study the effects of working conditions on the dynamic performance and stability of the turbocharger rotor system.

Achievement 5: Dynamic performance and stability of the turbocharger rotor system was simulated under various parameters. Parameters investigated included: the trajectory, the spectrum, the waterfall and bifurcation diagrams, effects of the rotor imbalance, lubricant viscosity and feed pressure and bearing clearances (results provided in Section 6.2).

Objective 6: To construct a turbocharger test rig to validate and verify the theoretical model.

Achievement 6: A cold air driven turbocharger test rig was designed and assembled, as described in Chapter 7. Following test rig development, the experimental data associated with the bending vibration of the turbocharger shaft was acquired, as given in Section 8.2. The experimental and simulation results were then used to determine the stability of the turbocharger rotor system in Section 8.3.

9.2 Conclusions

Conclusion 1: Based on the infinitely long bearing form of the steady-state Reynolds Equation, the analytical expressions of the oil film pressure distribution in two clearances of the floating ring bearing have been derived. These expressions take into account the influences of the oil inlet pressure and cavitation area and the lubrication model has been described.

Conclusion 2: The equilibrium positions of the journal and ring in terms of the eccentricity and attitude angle have been simulated under different external loads and oil inlet pressures. It was found that heavy external loads could result in larger outer eccentricities but the effect on inner eccentricity was inconclusive and was only observed in the lower speed range. The oil inlet pressure primarily affected the outer range of the attitude angle, but the external load could extend the cavitation areas in both the outer and inner oil film causing shrinkage of the cavitation area at high speeds when the oil inlet pressure is increased.

Conclusion 3: The lubrication of the inner oil film of the floating ring bearing was studied. The effects of external loads and oil inlet pressures on the oil flow rate into the inner bearing clearance were investigated. It was found that a heavier external load could reduce the oil flow rate into the inner oil film across a wide speed range. These conditions could lead to inner film oil starvation even if the initial flow rate was higher at lower speed. However, increasing oil inlet pressure effectively improved the inner oil film lubrication.

Conclusion 4: Modal analysis was carried out on a free rotor system ignoring the influence of support and gyroscopic effects. Calculation results showed that all four orders of mode shapes were bending modes in which the fourth order already showed the trend of transforming into the local mode.

Conclusion 5: Modal analysis was carried out on the turbocharger rotor system, taking into account the effects of the floating ring bearing and gyroscopic effects. The characteristic

equation of the turbocharger rotor system was derived and critical speeds and mode shapes of the turbocharger rotor system were calculated. The results showed that the critical speed increased as the shaft speed is increased due to gyroscopic effects. It was then demonstrated, through the Campbell diagram that the critical speeds of the turbocharger rotor system would increase as the stiffness coefficient of the bearing increased. This condition could also affect the mode shapes of the rotor system.

Conclusion 6: Studies of the influence of the rotor imbalance on the stability of the turbocharger shaft motion concluded that the rotor imbalance could lead to the appearance of the synchronous component for the turbocharger rotor system, the angular frequency of which was equal to the shaft velocity. The centrifugal force can inhibit the appearance of the instability in the inner oil film. However, the instability in outer oil film can be excited at a lower speed, when the amplitude of the rotor system becomes larger.

Conclusion 7: Studies of the influence of the lubricant viscosity on the stability of the turbocharger shaft motion concluded that the lubricant viscosity can inhibit the instability in both inner and outer oil films. Under a lower lubricant viscosity, instabilities of both oil films are excited at the lower speeds, when the system shows a dramatic motion. Under a higher viscosity, the instabilities occur at higher speeds, especially for the inner oil film instability. The amplitude under oil film instabilities is also inhibited.

Conclusion 8: An investigation of the influence of the bearing clearances on the stability of

the turbocharger shaft motion concluded that either inner or outer bearing clearance can affect the stability discipline of two oil films. As the inner clearance is increased, the inner oil film instability will occur at a higher rotational speed, but the outer oil film instability will be excited at a lower rotational speed. On the other hand, as the outer clearance is decreased, the hydrodynamic forces become larger, which inhibit the appearance of the instability in both inner and outer oil films. A high order harmonic component might also be excited by a thinner outer clearance.

Conclusion 9: The lubricant feed pressure exerts a static load on the ring. It can excite the instability at a lower rotational speed in both inner and outer bearing clearances.

Conclusion 10: The displacement signals of the turbocharger shaft end at the compressor side were collected within the speed range 0~15,000r/min. The experimental data showed that the synchronous component and second order harmonic component existed within the entire measuring speed range. Apart from glitches in the data observed at the measuring position, it is concluded that the synchronous component is caused by the residual rotor imbalance. A number of reasons have been identified which could excite the second order harmonic component of the turbocharger rotor system. Both simulation and experimental data were used to study the stability characteristics of the turbocharger rotor system supported by the floating ring bearing.

9.3 Contribution to Knowledge

Contribution 1: Static performance of the fluid lubrication of the turbocharger floating ring bearings.

Most commercial turbochargers use the floating ring bearings to support the rotor system. The application of floating ring bearings not only decreases the relative speed between the journal and the bearing shell, but also inhibits self-excited vibration. It is difficult to study the static performance of the fluid lubrication of floating ring bearings, due to the interaction of the inner and outer oil films.

In this thesis, the Reynolds Equation has been extended to study both the inner and outer oil films of the floating ring bearing. The analytical expressions for the oil film pressure distribution have been obtained by taking into account the oil inlet pressure, and the Reynolds boundary condition, when numerically solving the Reynolds Equations. Based on the results obtained, the rotational velocity of the shaft and the equilibrium positions for the journal and ring have been deduced under different external loads and lubricant feed pressures. Furthermore, during this work the conditions at which a rupture could occur between the divergent wedge of the oil films, was determined.

Contribution 2: Effects of ring rotation on the fluid lubrication of the inner oil film of the floating ring bearings.

The outer clearance of the floating ring bearing was lubricated through the supply hole located on top of the bearing shell, whilst lubrication of the inner clearance was determined

by the pressure difference between the two oil films. Rotation of the ring also significantly affected the lubrication of the inner oil film.

In this thesis, a lubrication model for the floating ring bearing was developed and used to study the effects of the rotation of the ring rotation on the oil flow rate into the inner bearing clearance. The relationship of the oil flow rate and the rotational velocity of the journal were obtained under different external loads and lubricant feed pressures. Furthermore, trigger conditions and solution approaches for oil starvation have been simulated and mean oil flow rates into the inner bearing clearance, have been determined.

Contribution 3: Nonlinear hydrodynamic forces.

The primary exciting forces of the turbocharger rotor system bending vibration include rotor imbalance and hydrodynamic forces, the latter of which demonstrate highly nonlinear characteristics. The standard method used to resolve this, is linearization using the perturbation method. Although this method is suitable for the calculation of critical speeds and mode shapes of the rotor system, it is inadequate for describing the bending vibration and nonlinear behaviors.

In this thesis, the Capone hydrodynamic force model has been extended to simulate the dynamic performance of the floating ring bearing. The analytical expression for the hydrodynamic forces of the two oil films have been derived based on the dimensionless form of the Reynolds Equations. The calculations have been normalized by using a multiplication coefficient for the two oil films.

Contribution 4: Stability analysis of the turbocharger rotor system.

A turbocharger rotor system can be viewed as a rotor bearing system with double disks supported by a pair of floating ring bearings. The dynamic performance and stability of the system depends on the working conditions, but studies are complicated by the interaction and nonlinear behavior of the inner and outer oil films.

In this thesis, the motion of the turbocharger shaft was simulated within a shaft speed range of 0 to 8000rad/s under different rotor imbalance, lubricant viscosity, bearing clearance and lubricant feed pressure conditions - numerical integration approaches were used. The influences of the structural parameters and working conditions on the stability of the turbocharger rotor system were obtained from the spectra, trajectory, bifurcation and waterfall diagrams.

9.4 Future Work

Future work 1: In this research, the lubricant flow in the floating ring bearing was simplified as a laminar flow. However, turbulent flow sometimes occurred in the bearing clearance when the Reynolds number exceeded 4000 and conventional fluid lubrication theory based on laminar flow could not be applied.

To date, the standard approach for studying turbulent flow lubrication is to introduce a modified form of the Reynolds Equation using an empirical coefficient. This approach is clearly inappropriate for describing such a complex phenomenon. Therefore, it is recommended that turbulent flow lubrication theory and its impact on displacement of the rotor system should be investigated in more depth.

Future work 2: In the dynamics model which has been developed, the exciting forces for the vibration of the turbocharger rotor system included the rotor imbalance, hydrodynamic forces, lubricant feed pressure and the dead weight. However, potential faults, such as the crack, loosening of the base, fatigue fracture, etc, have not been considered. These faults could occur individually or simultaneously as coupled faults.

To date, the majority of rotor fault research has been based on the Jeffcott rotor model. It is, therefore, necessary to carry out an in depth analysis of the stability for a multi-span rotor bearing system with coupled faults.

Future work 3: Stability analysis of a rotor bearing system is an important industrial application. It is therefore insufficient to observe only the trend of the stability characteristics of the system. In order to understand the capability of the rotor system to withstand actual working conditions, it is also necessary to quantify the degree of stability of the system and this should form part of a future research study.

Future work 4: Throughout this research, the influence of rotational velocity fluctuation has been ignored in both theoretical modeling and experimental study. But in practice, a turbocharger is driven by the exhaust discharged from the engine cylinders. The intermittent nature of the engine exhaust results in the driven force being a series of gas pulses rather than a steady flow and this will inevitably lead to a bending-torsional coupled vibration of the rotor system. This effect on the stability of the rotor bearing system

requires deeper investigation.

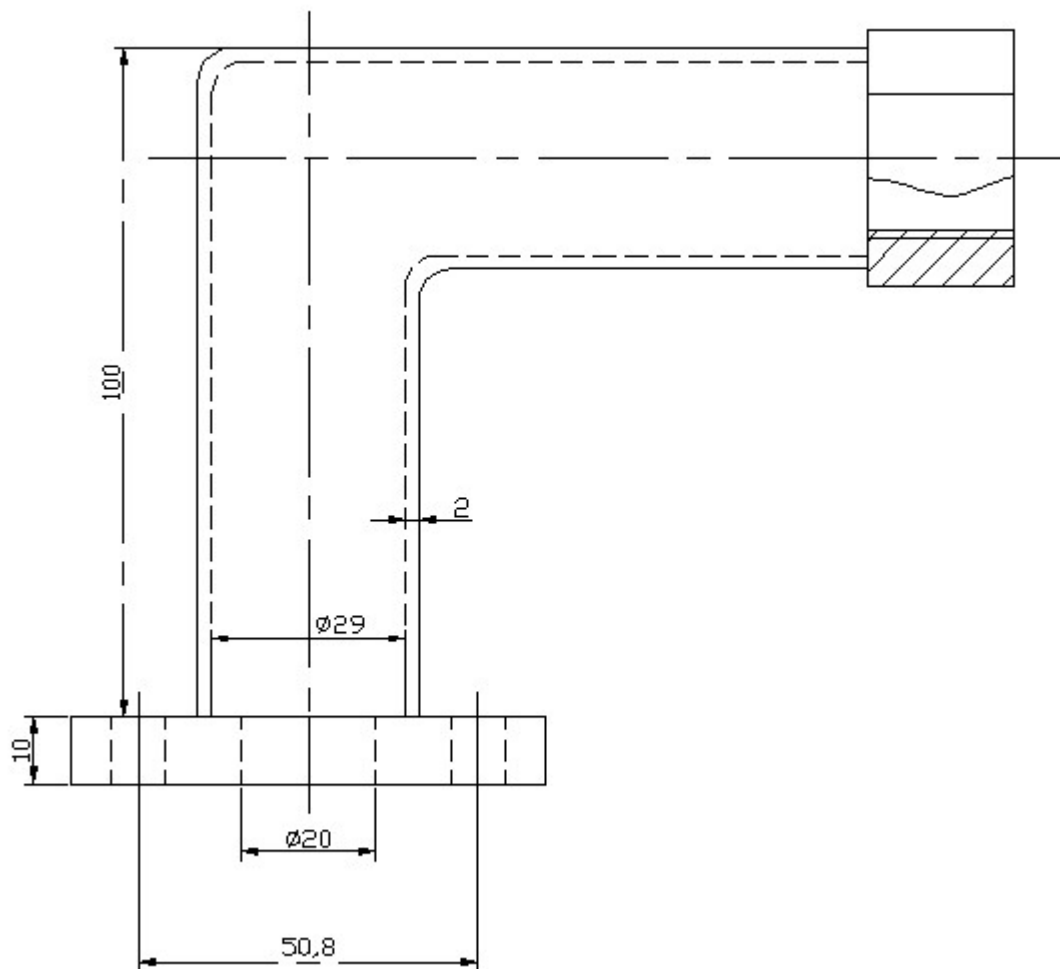
Future work 5: In the dynamics model of the turbocharger rotor system developed in this research, the turbine impeller and the compressor impeller were modeled as rigid disks. Modeling ignored the elasticity of the disk, as well as the effect which the geometrical shape of the impellers had on the dynamic performance of the turbocharger rotor system. Although simplification of the model made the study more convenient, the accuracy of the model was inevitably affected. Therefore, it is recommended that a more comprehensive model is developed in the future.

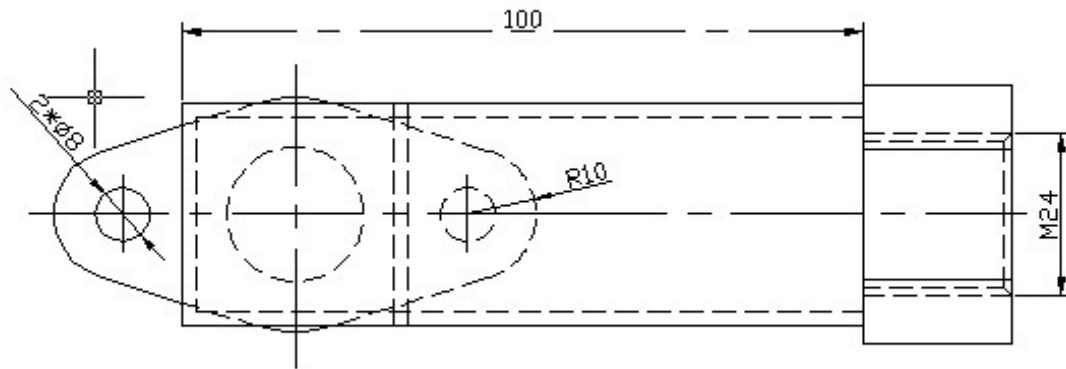
Future work 6: Due to reasons of security and high cost, this turbocharger test rig was a cold air driven system. The air supply was provided by a fan, making it difficult for the turbocharger to be driven at higher rotational velocities. For future work, it is recommended that a combustion chamber is installed in the test rig and high temperature and high pressure air supplies are used to extend the speed range of the turbocharger.

Appendices

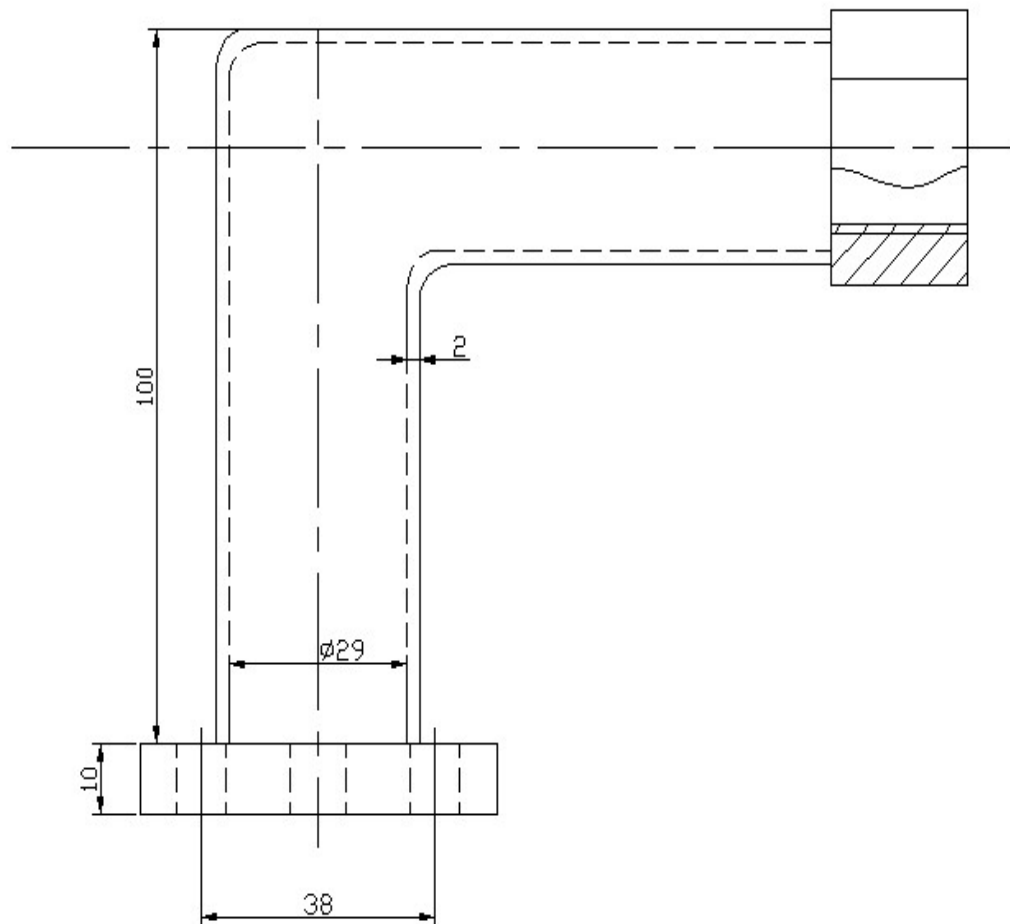
Appendix A

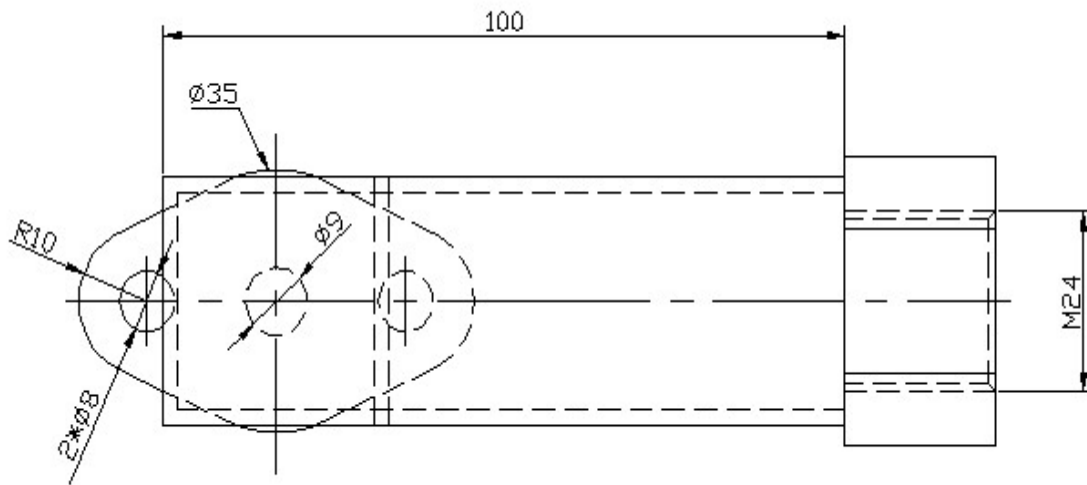
The design of the lubricant flanges in the test rig is shown in Appendix A. The unit in this Figure A is mm.





(a)



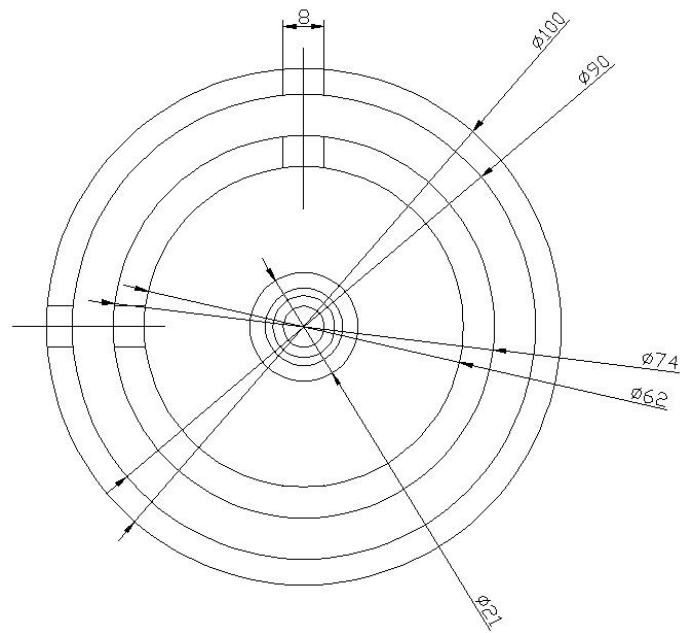


(b)

Figure A. The lubricant flange in the test rig: (a)Return flange (b)Inlet flange

Appendix B

The slots which are milled in a perpendicular position on turbocharger casing for the placement of the displacement transducers are shown in Appendix B. The unit in Figure B is mm.



(a)

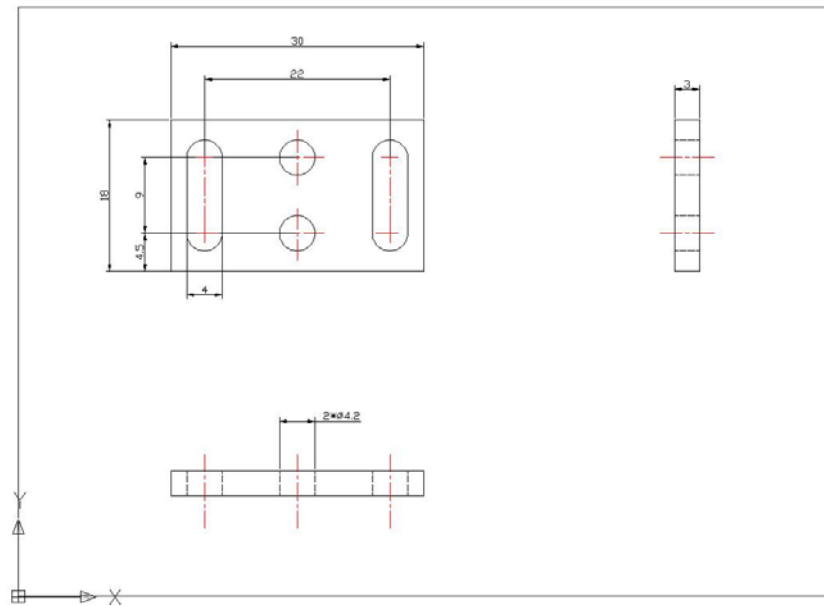


(b)

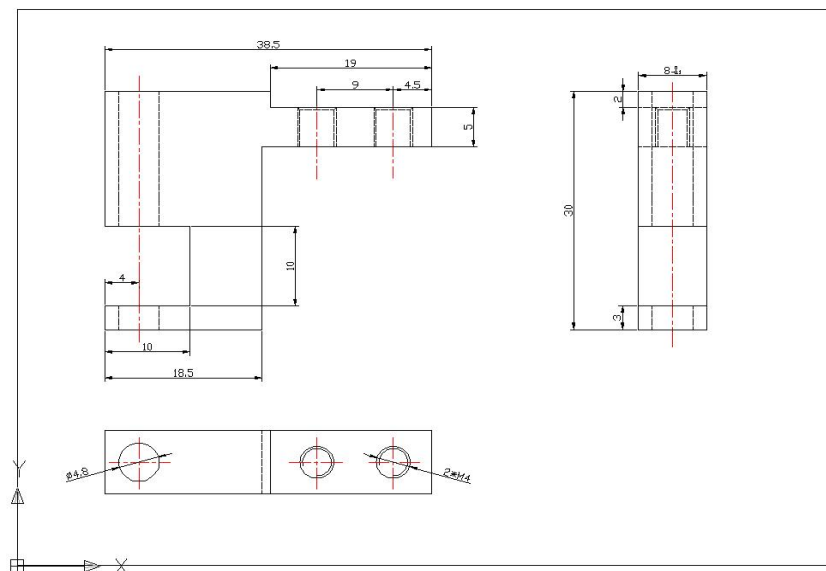
Figure B. Two slots milled on the turbocharger casing in a perpendicular direction

Appendix C

The design of mechanical components to fix the eddy current displacement transducers on the casing is shown in Appendix C. The unit in Figure C is mm.



(a) Upper plate



(b) Lower plate

Figure C. Fixed mechanical components for eddy current displacement transducers

Reference

1. A. Muszynska. *Rotordynamics*. CRC press, 2005. ISBN: 0824723996, 9780824723996.
2. Miller JK. *Turbo: Real world high-performance turbocharger systems*. CarTech Inc, 2008. ISBN: 13 978-1-932494-29-7.
3. Shaw C and Nussdorfer T. An analysis of the full-floating ring bearing. NACA Report 1947; 866: 95-107.
4. Tower. Proc. Instn. Mech. Engrs 1885: 36-58.
5. Reynolds O. On the theory of lubrication and its application to Mr. Beauchamp Tower's experiments including an experimental determination of the viscosity of olive oil. Phil. Trans 1886; 177(1): 157-234.
6. Sommerfeld A. Zur hydrodynamischen theoric der Schmiermittelreibunh. Z. Math. U. Physik 1904; 50: 97-106.
7. Dubois GB and Ocvirk FW. Analytical derivation and experimental evaluation of short bearing approximation for full journal bearing. NACA Report 1953: 1157.
8. Kinsbury A. Trans. ASME 1931. 53: 59.
9. Christopherson. Proc. IMechE 1942. 142.
10. Ocvirk KW. NACAT Report 1959. 2808.
11. Szczygieski WM and Schweltzer G. Dynamics of a high speed rotor touching a boundary. Proc. Dynam. Of Multibody Systems IUTAM/AFTOMM Symp. Udlna,

- Italy, 1986, pp: 287-298.
12. Rankine MWJ. On the dynamical principles of the motion of velocipedes. *The Engineer* 1869; 28: 79, 129, 153, 157.
 13. Jeffcott HH. The lateral vibration loaded shafts in the neighborhood of a whirling speed. – The effect of want of balance. *Philosophical Magazine* 1919; 6: 37.
 14. Rao JS. *Rotor Dynamics*. New Age International, 1996. ISBN: 8122409776, 9788122409772.
 15. Yang JF, Yang K, Yu DR, etc. Research on the nonlinear oil film forces of journal bearings. *Chin J Vib Eng* 2005; 18(1): 118-123.
 16. Meng ZQ, Xu H and Zhu J. A database method of nonlinear oil film force based on Poincare transformation. *Chin J Tribol* 2001; 21(3): 223-227.
 17. Gardner M, Myers C and Savage M. Analysis of limit-cycle response in fluid-film journal bearing using the method of multiple scales. *Q J Mech Appl Math* 1985; 38: 27-45.
 18. Russo M and Russo R. Parametric excitation instability of rigid unbalanced rotor in short turbulent journal bearing. *Proc. IMechE, Part C: J Mech Eng Sci* 1993; 207: 149-160.
 19. Adams ML and Abu-Mahfouz IA. Exploratory research on chaos concepts as diagnostic tools for assessing rotating machinery vibration signatures. In: *Proceedings of IFOMM Fourth International Conference on Rotor Dynamics*, Chicago, USA, 1994, pp: 29-39.
 20. Yuan XY and Zhu J. Study on the nonlinear stability of unbalanced rotor bearing

- systems. Chin J Vib Shock 1996; 15(1).
21. Chen YS, Ding Q and Meng Q. Stability analysis of the low-frequency vibration of a nonlinear rotor. Chin J Appl Mech 1998; 15(1).
 22. Zhao JY and Huhn EJ. Subharmonic, quasi-periodic and chaotic motions of a rigid rotor supported by an eccentric squeeze film damper. J Mech Eng Sci 1993; 207: 382-392.
 23. Zhao JY, Linnett IW and Mclean LJ. Sub-harmonic and quasi-periodic motions of an eccentric squeeze film damper-mounted rigid rotor. J Vib Acoust 1994; 116: 357-363.
 24. Chen WJ, Gunter EJ. Introduction to dynamics of rotor-bearing systems. Trafford Publishing, 2005. ISBN: 1412051908, 9781412051903.
 25. Bannwart AC, Cavalca KL and Daniel GB. Hydrodynamic bearings modeling with alternate motion. Mech Res Common 2010; 37(6): 590-597.
 26. Zhang W, Zheng TS, Ma JM, et al. Modeling of the transient nonlinear hydrodynamic force and the expression. Prog Nat Sci 2002; 12: 255-260.
 27. Chen L, Zheng TS and Zhang W. A variation approximate solution for nonlinear oil-film forces of sliding bearing. Chin J Appl Sci 2002; 19(3).
 28. Meng G, Guo Y and Hahn EJ. The influence of fluid inertia forces on the sudden unbalance responses of squeeze film damper supported rotors. Proc. IMechE, Part J: J Eng Tribol 1998; 212: 353-357.
 29. Meng G and Gasch R. Stability and stability degree of a cracked flexible rotor supported on journal bearings. Trans. ASME, J Sound Vib 2000; 122: 116-125.
 30. Meng G and Zhang WM. Stability, bifurcation and chaos of a high speed rub-impact

- rotor system in MEMS. *Sens Actuators A* 2006; 127: 163-178.
31. Leng XL, Meng G, Zhang T, et al. Bifurcation and chaos response of a cracked rotor with random disturbance. *J Sound Vib* 2007; 299: 621-632.
 32. Wang JX and Meng G. Study of the vibration control of a rotor system using a magnetorheological fluid damper. *J Vib Control* 2005; 11: 263-276.
 33. Cheng M, Meng G and Jing JP. Numerical and experimental study of a rotor-bearing-seal system. *Mech Mach Theory* 2007; 42: 1043-1057.
 34. American Petroleum Institute. API Standard 617. 7th ed. 2002, 6.
 35. American Petroleum Institute. API Standard 612. 4th ed. 1995, 6.
 36. Prohl MA. A general method for calculating critical speed of flexible rotors. *Trans. ASME, J Appl Mech* 1945; 12: 142-148.
 37. Lund JW. Stability and damped critical speed of a flexible rotor in fluid-film bearings. *Trans. ASME, J End Ing* 1974; 96: 509-517.
 38. Horner GC and Pilkey WD. The Riccati transfer matrix method. *Trans. ASME, J Mech Des* 1978; 100: 297-302.
 39. Kim D and David JW. An improved method for stability and damped critical speeds of rotor-bearing systems. *Trans. ASME, J Vib Acoust* 1990; 102: 112-119.
 40. Guo L and Sheng XM. An improved method for critical speed of rotor bearing system. *Lubr Eng* 1998; 3: 33-36.
 41. Ozguven HN and Ozkan ZL. Whirl speeds and unbalance response of multibearing rotors using finite element. *Trans. ASME, J Vib Acoust Stress Reliab Des* 1984; 106: 72-79.

42. Childs DW and Graviss K. A note on critical-speed solutions for finite element based rotor models. Trans. ASME, J Mech Des 1982; 104: 412-416.
43. Jia XM. The calculation and analysis of unbalance vibration of 200MW steam turbine rotor system. Turbine Tech 2000; 42.
44. Shiraki K, Ingaki T and Kanki H. Transverse vibration of a general cracked rotor bearing system. Trans. ASME, J Mech Des 1982; 104: 343.
45. Verhoeven J. Excitation force identification of rotating machines using operational rotor/stator amplitude data and analytical synthesized transfer functions. J Vib Acoust 1988; 110(3): 307-314.
46. Irretier H. Mathematical foundations of experimental modal analysis in rotor dynamics. Mech Syst Sig Process 1999; 13: 183-191.
47. Greenhill LynM and Cornejo GA. Critical speeds resulting from unbalance excitation of backward whirl modes. In: *Proceedings of ASME of Design Engineering Technical Conference*. Boston, USA, 1995, Vol. 3. pp: 991-1000.
48. Hong SW and Park JH. An efficient method for the unbalance response analysis of rotor bearing systems. J Sound Vib 1997; 200: 491-504.
49. Jun OS and Kim JO. Free bending vibration of a multi-step rotor. J Sound Vib 1999; 224: 625-642.
50. Chasalevris AC and Papadopoulos CA. A continuous model approach for cross-coupled bending vibrations of a rotor-bearing system with a transverse breathing crack. Mech Mach Theory 2009; 44: 1176-1191.
51. Ehrich FF. Some observations of chaotic vibration phenomena in high-speed

- rotordynamics. Trans. ASME. J Vib Acoust 1991; 113: 50-57.
52. Parkinson AG. Second order vibration of flexible shafts. Proceedings Royal Society of London 1965; 259: 1-31.
 53. Lin YH and Lin SC. Optimal weight design of rotor systems with oil film bearings subjected to frequency constraints. Finite Elem Anal Des 2001; 37: 777-798.
 54. Aleyaasin M, Ebrahimi M and Whalley R. Vibration analysis of distributed-lumped rotor systems. Comput Meth Appl Mech Eng 2000; 189: 545-558.
 55. Firoozian R and Zhu H. A hybrid method for the vibration analysis of rotor-bearing system. Proc. IMechE, Part C: J Mech Eng Sci 1991; 205: 131-137.
 56. Hagg AC. Some dynamic properties of oil film journal bearings. Trans. ASME, J Eng 1956; 3: 302-306.
 57. Sternlicht B. Elastic and damping properties of cylindrical journal bearings. Trans. ASME, J Basic Eng 1959; 81: 101-108.
 58. Lund JW. Spring and damping coefficients for the tilting pad journal bearing. Trans. ASME, J Tribol 1964; 7: 342-352.
 59. Lund JW. Calculation of stiffness and damping properties of gas bearing. Trans. ASME, J Lubr Tech 1968; 90: 793-803.
 60. Glienicke J. Experimental investigation of the stiffness and damping coefficients of turbine bearings and their application to instability prediction. *In: Journal Bearings for Reciprocating and Turbomachinery, IME Symposium in Nottingham*, pp: 122-135, 1966.
 61. Yang JF, Yang K and Yu DR. Nonlinear dynamic oil film pressure distribution of

- sliding bearings. Chi J Power Eng 2005; 25: 4.
62. Yang JF, Yang K and Yu DR. Characteristics of nonlinear dynamic oil film forces and the decomposition of π oil film forces. Chi J Power Eng 2005; 25: 6.
63. Yang JF, Liu ZS and Yu DR. Research on nonlinear oil film force and its stability of journal bearing. Power Eng 2004; 24.
64. Yang JF, Yang K and Yu DR. Nonlinear film-force of journal bearing. Journal of Harbin Institute of Technology 2003; 35.
65. Yang JF and Liu ZS. Research on nonlinear oil film force and its stability of journal bearing. Vib Eng 2004; 24.
66. Zhang YM, Wen BC and Liu QL. Sensitivity of rotor-stator systems with rubbing. Mech Struct Mach 2002; 30: 203-211.
67. Zhang YM, Wen BC and Leung Andrew YT. Reliability analysis for rotor rubbing. Trans. ASME, J Vib Acoust 2002; 124: 58-62.
68. Zhang YM, Wen BC and Liu QL. Reliability sensitivity for rotor-stator systems with rubbing. J Sound Vib 2003; 259: 1059-1107.
69. Tang BX, Zhu EH and Wen BC. High-speed balancing. J Mech Strength 1992; 1.
70. Ting Q and Chen YS. Non-stationary motion and instability of a shaft/casing system with rubs. J Vib Control 2001; 7: 327-338.
71. Goldman P and Muszynska A. Chaotic behavior of rotor/stator systems with rubs. Trans. ASME, J Eng Gas Turbines Power 1994; 116: 692-701.
72. Chu F and Zhang Z. Bifurcation and chaos in rub-impact jeffcott rotor system. J Sound Vib 1998; 210: 1-18.

73. Chang-Jian CW and Chen CK. Chaos and bifurcation of a flexible rub-impact rotor supported by oil film bearings with non-linear suspension. *Mech Mach Theory* 2007; 42: 312-333.
74. Chang-Jian CW and Chen CK. Bifurcation and chaos of a flexible rotor supported by turbulent journal bearings with non-linear suspension. *Trans. ImechE, Part J: J Eng Tribol* 2006; 220: 549-561.
75. Chang-Jian CW and Chen CK. Nonlinear dynamic analysis of a flexible rotor supported by micropolar fluid film journal bearings. *Int J Eng Sci* 2006; 44: 1050-1070.
76. Chang-Jian CW and Chen CK. Bifurcation and chaos analysis of a flexible rotor supported by turbulent long journal bearings. *Chaos Solitons Fractals* 2007; 34: 1160-1179.
77. Fu YM, Zheng YF and Zhu SJ. Analysis of the chaotic motion for a rotor system with a transverse crack. *Acta Mech Solida Sin* 2003; 16: 74-80.
78. Gadangi RK, Palazzolo AB and Kim J. Transient analysis of plain and tilt pad journal bearings including fluid film temperature effects. *Trans. ASME, J Tribol* 1996; 118: 423-430.
79. Chen YS. Nonlinear bifurcation of rotor-bearing system. *J Vib Eng* 1996; 9: 266-275.
80. Tatara A. An experimental study on the stability effect of floating bush journal bearings. *JSME Bulletin* 1970; 13: 859-863.
81. Tanaka M and Hori Y. Stability characteristics of floating bush bearings. *Trans. ASME, J Lubr Tech* 1972; 94: 248-259.

82. Hill HC. Sliper bearings and vibration control in small gas turbine. Trans. ASME, Soc Mech Engrs 1950; 80: 1756-1764.
83. Dworski J. High-speed rotor suspension formed by full floating hydrodynamic radial and thrust bearings. Trans. ASME, J Eng Power 1964; 86: 149-160.
84. Tondl A. *Some problems of rotordynamics*. Chapman and Hall, London, 1965, pp: 155-160, 200-201.
85. Rohde SM and Ezzat HA. Analysis of dynamically loaded floating ring bearings for automotive applications. Trans. ASME, J Lubr Tech 1980; 102: 271-277.
86. Trippett R and Dennis FC. High-speed floating-ring bearing test and analysis. Trans. ASLE 1983; 27: 73-81.
87. Tanaka M. A theoretical analysis of stability characteristics of high speed floating bush bearings. In: *Proceedings of the 6th International Conference on Vibration in Rotating Machinery*, ImechE Conference Transaction, Oxford, Uk, Sept. 1996, Paper C500/087/96: 133-142.
88. Howard SA. Rotordynamic design analysis of an oil-free turbocharger. NASA Conference Publication, n 10193/2, Applied Life Models, Design, Vibration Control, Mechanical Components, Tribology, 1997, pp: 36.
89. Howard SA. Rotordynamics and design methods of an oil-free turbocharger. Trans. Tribol 1999; 42: 174-179.
90. Walton JF, Heshmat H and Tomaszewski MJ. Testing of a small turbocharger/turbojet sized simulator rotor supported on foil bearings. In: *Proceedings of ASME Turbo Expo*, Vienna, Austria, 2004, v6: Microturbines and Small Turbomachinery; Structures and

- Dynamics; General; Structural Mechanics and Vibration; Unsteady Aerodynamics; Rotordynamics: 67-73.
91. Aretakis N, Mathioudakis K, Kefalakis M, et al. Turbocharger unstable operation diagnosis using vibroacoustics measurements. Trans. ASME, J Eng Gas Turbine Power 2004; 126: 840-847.
 92. Chen H, Hakeem I and Martinez-Botas RF. Modelling of a turbocharger turbine under pulsating inlet conditions. Proc. IMechE, Part A: J Power Eng 1996; 210: 397-408.
 93. Kreuz-Ihli T, Filsinger D, Shulz A, et al. Numerical and experimental study of unsteady flow field and vibration in radial inflow turbines. J Turbomach 2000; 122: 247-254.
 94. Peat KS, Torregrosa AJ, Broatch A, et al. An investigation into the passive acoustic effect of the turbine in an automotive turbocharger. J Sound Vib 2006; 295: 60-75.
 95. Payri F, Benajes J and Reyes M. Modelling of a supercharger turbines in internal-combustion diesel engines. Int J Mech Sci 1995; 38: 853-869.
 96. Payri F, Desantes JM and Broatch A. Modified impulse method for the measurement of the frequency response of acoustic filters to weakly nonlinear transient excitations. J Acoust Soc Am 2000; 107: 731-738.
 97. W Thomson. *Theory of vibration with applications*. Taylor & Francis, 2004. ISBN: 0748743804, 9780748743803
 98. Padmanabhan C and Singh R. Analysis of periodically excited non-linear systems by a parametric continuation technique. J Sound Vib 1995; 184(1): 35-38.
 99. Sundararajan P and Noah ST. An algorithm for response and stability of large order non-linear systems-applications to rotor systems. J Sound and Vib 1998; 214(4):

- 695-723.
100. Cherfils L. A parallel and adaptive continuation method for semilinear bifurcation problems. *Comput Meth Appl Mech Eng* 1998; 163: 247-259.
 101. Blair KB, Krousgrill CM and Farris TN. Harmonic balance and continuation techniques in the dynamic analysis of Duffing's equation. *J Sound Vib* 1997; 202(5): 717-731.
 102. Hu HY. Numerical scheme of locating the periodic response of non-smooth non-autonomous systems of high dimension. *Comput Meth Appl Mech Eng* 1995; 123(1): 53-62.
 103. Zheng HP and Chen YS. A method evaluating stability degree of periodic solution based on perturbing response data in a non-autonomous system. *Chin J Appl Sci* 2002; 19(2): 75-77.
 104. Zheng HP and Chen YS. A numerical method on estimation of stable regions of rotor systems supported on lubricated bearings. *Appl Math Mech* 2002; 23(10): 991-996.
 105. Roose D, Lust K, Champneys A, et al. A Newton-Picard shooting method for computing periodic solution of large-scale dynamical system. *Chaos Solitons Fractals* 1995; 5(10): 1913-1925.
 106. Van Noorden TL, Verduyn Lunel SM and Blik A. Acceleration of the determination of periodic states of cyclically operated reactors and separators. *Chem Eng Sci* 2002; 57: 1041-1055.
 107. Tiesinga G, Wubs FW and Veldman AEP. Bifurcation analysis of incompressible flow in a driven cavity by the Newton-Picard method. *J Comput Appl Math* 2002; 140:

- 751-772.
108. Hurty WC. Vibrations of structural systems by component mode synthesis. J Eng Mech Div 1960; 86: 51-69.
 109. Gladwell GML. Branch mode analysis of vibrating system. J Sound Vib 1964; 1: 41-59.
 110. Tran DM. Component mode synthesis methods using interface modes: Application to structures with cyclic symmetry. Comput Struct 2001; 79: 209-222.
 111. Tran DM. A comparison of component mode synthesis methods for cyclic structures. ASME, Dyn Syst Contr Div 2000; 68: 23-30.
 112. Meirovitch L. *Computational methods in structural dynamics*. Springer, 1980.
 113. Craig RR and Chang CJ. Free-interface methods of substructure coupling for dynamic analysis. AIAA J 1976; 14: 1633-1635.
 114. Craig RR. *Substructure coupling for dynamic analysis*. Washington: National Aeronautics and Space Administration, 1977.
 115. Craig RR. Review of time-domain and frequency-domain component mode synthesis method. J Modal Anal 1985; 2(2): 59-72.
 116. Kuhar EJ and Stahle CV. Dynamic transformation method for modal synthesis. AIAA J 1974; 12: 672-678.
 117. Kubomura K. Theory of substructure modal synthesis. Trans. ASME, J Appl Mech 1982; 49: 903-909.
 118. Kubomura K. A collection of technical papers: AIAA/ASME/ASCE/AHS 26th Structures, Structural Dynamics & Materials Conference, Orlando, April 15-17, 1985.

119. Kubomura K. Component mode synthesis for damped structures. AIAA J 1987; 25: 740-745.
120. Curnier A. On three modal synthesis variants. J Sound Vib 1983; 90: 527-540.
121. Engels RC. Convergence improvement for component mode synthesis. AIAA J 1992; 30: 490-495.
122. Farhatt C and Geradin M. On a component mode synthesis method and its application to incompatible substructures. Comput Struct 1994; 51: 459-473.
123. Thonon C, Geradin M, Cardonna A, et al. Unification of the impedance and component mode formulations in the assembling of flexible structures. Application to linear systems. Report VA-144. LTAS, University de Liege, 1995.
124. Ohayon R, Sampaio R and Soize C. Dynamic substructuring of damped structures using singular value decomposition. Trans. ASME, J Appl Mech 1997; 64: 292-298.
125. Bourquin F and Hennezel F. Intrinsic component mode synthesis and plate vibrations. Comput Struct 1992; 44: 315-324.
126. Bourquin F. Component mode synthesis and eigenvalues of second-order operators: discretization and algorithm. Math Model Number Annual 1992; 26: 385-423.
127. Minnicino II MA and Hopkins DA. Overview of reduction methods and their implementation into finite-element local-to-global techniques. ARL-TR-3340. Army Research Laboratory. Aberdeen Proving Ground, MD 21005-5069, 2004.
128. Bathe KJ and Wilson EL. *Numerical methods in finite element analysis*. New Jersey, Prentice-hall, Inc. Englewood Cliffs, 1976.
129. Press WH, Teukolsky SA, Vetterling WT, et al. Numerical recipes in C. Press of

- Cambridge University, 1992.
130. Palm WJ. *Mechanical vibration*. John Wiley, USA, 2007.
 131. Griffiths DV and Smith IM. *Numerical methods for engineers*. Chapman & Hall/CRC, 2006. ISBN: 1584884010, 9781584884019.
 132. Dahlquist G and Bjorck A. *Numerical methods in scientific computing*. SIAM, 2008. ISBN: 0898716446, 9780898716443.
 133. Song Y, Li XS and Gu CW. CFD analysis of the load capacity and oil feeding characteristics of floating bush bearings with bush rotation being considered. *J Eng Thermophys* 2010; 31: 951-954.
 134. Andres LS and Kerth J. Thermal effects on the performance of floating ring bearings for turbochargers. *J Eng Tribol* 2004; 218: 437-450.
 135. Forsyth AR. *Calculus of variations*. New York: Dover, 1960, pp: 17-20 and 26.
 136. Lund JW. Sensitivity of the critical speeds of a rotor to changes in the design. *Trans. ASME, J Mech Des* 1980; 102: 115-121.
 137. Zima S. Development of turbocharger test rig. *MTZ* 1993; 54: 218-222.
 138. Zhong HG, Liu K and Wen GZ. Test rig and test technology of turbocharger for vehicles. *Gas Turbine Experiment and Research* 2003; 16: 37-44.
 139. Holt C, Andres LS, Sahay S, et al. Test response and nonlinear analysis of a turbocharger supported on floating ring bearings. *J Vib Acoust* 2005; 127: 107-115.
 140. Warsi ZUA. *Fluid dynamics: theoretical and computational approaches*. Taylor & Francis, 2006. ISBN: 0849333970, 9780849333972.
 141. Fraden J. *Handbook of modern sensors: Physics, Designs, and Application*. Springer,

2010. ISBN: 1441964657, 9781441964656.